A Comparison of Continuum and Cell-based Models of Colorectal Cancer

Alexander C. Walter, MMath

Thesis submitted to The University of Nottingham
for the degree of Doctor of Philosophy

March, 2009

Abstract

Colorectal cancer is thought to originate in the epithelial cells that line the colorectal crypt and, in most cases, is associated with a mutation in Wnt-signalling pathway. These mutations cause cells to alter their proliferative behaviour, make their cytoskeleton less deformable and increase their levels of cell-cell and cell-substrate adhesion.

In this thesis we develop three different types of models for the proliferation and movement of epithelial cells in a colorectal crypt. We use these models to investigate how changing the cell adhesion, cytoskeleton and proliferation properties of mutant cells affects their ability to establish a mutant population within the crypt.

First we develop a continuum model of two cell populations, normal and mutant, using a spatially-varying source term to model Wnt-dependent proliferation and using Darcy's law to describe cell movement down pressure gradients. We distinguish between mutant cells and normal cells by assuming the former have a spatially independent source term, representing proliferation, and a different viscosity to normal cells, to model changes in their cytoskeleton and levels of adhesion. The model is solved analytically by an asymptotic expansion of the variables and numerically using a collocation method. The results show that the ability of mutant cells to remain in the crypt depends on the position of the initial mutation and their viscosity: the further up the crypt a cell suffers a mutation the more rigid and adhesive the cell must be for a mutation to persist.

We then consider a discrete cell-centre model based on the work of Meineke *et al.* [109]. Cell-cell interaction forces are modelled by springs and are balanced by a viscous drag term. Adaptations to [109] include unpinning of stem cells from the bottom of the crypt, dependence of cell-drag on cell size, dependence of cell-cell interaction forces on their area of contact and the inclusion of mutant cells. Using agile software engineering techniques, the software environment, CHASTE, is developed and used to solve the model numerically and to reproduce experimental findings such as crypt homoeostasis and monoclonality. The results again reveal that increasing the drag on the mutant cells increases the likelihood of a mutant population establishing itself within the crypt.

The third approach is a discrete cell-vertex model. The model decouples cell-cell adhesion forces from cell deformation forces and movement is determined by a free-energy gradient balanced by a viscous drag term. Numerical simulations show that the model can generate similar results to the cell-centre model, and reveal that increased cell-cell adhesion of the mutant cells increases the likelihood of the mutant population invading the crypt.

Finally the three models are compared in terms of their suitability for modelling epithelial tissue.

Contents

Acknowledgements

Firstly, I'd like to thank my supervisors Helen and Oliver, for their help, guidance and patience over the past few years. Thanks also to Integrative Biology for funding the research in this thesis. My thanks also go to "Team Chaste" — my partner-in-crime/ science Gary, Ozzy, Phil, Axel, Pras, Jon, Joe and Lee for making it so much fun to work on; and to Dave Gavaghan and all at the DTC for a great year and some invaluable training at the beginning of the PhD.

I'd also like to thank all the Postgrads in Pope C9 for all their help and making it such an enjoyable experience.

Finally I'd like to thank Mum, Dad, Ralf, Frank and the rest of my family and friends (especially the old Sherwood hall '99 crew, Dave and Dan) for all the support over the years.

Chapter 1

Literature review

1.1 Introduction and motivation

Colorectal cancer [45, 168] is the third most common cancer in terms of incidence and the second most common cause of cancer-related death in the UK. In 2005, in the UK alone, 36,766 patients were diagnosed with colorectal cancer [168] and in 2006, 15,957 patients died from colorectal cancer [168].

Mathematical modelling has played an important role in the understanding of cancer, dating back to Armitage and Doll [10], who, in 1954, predicted the number of mutations needed for cancer to develop. In this thesis, we aim to increase the understanding of the early stages of colorectal cancer by using a variety of theoretical approaches to model the proliferation and movement of epithelial cells that line the colorectal crypt. We compare the insight that each approach provides and discuss its strengths and weaknesses. In the remainder of this chapter, we introduce the relevant biological information on the physiology of the colon and early stages of colorectal cancer (§1.2) and review some mathematical modelling approaches that could be (or have been) used to model the colorectal crypt (§1.3).

1.2 Biological background

Like many cancers, colorectal cancer is generally a disease of old age [2]. It requires several genetic mutations [51] (around six) within the colonic cells to develop a carcinoma. These mutations lead to changes in the behaviour of the cells which result in major structural changes including buckling of the colorectal crypts. To understand how these mutations lead to colorectal cancer, in this section

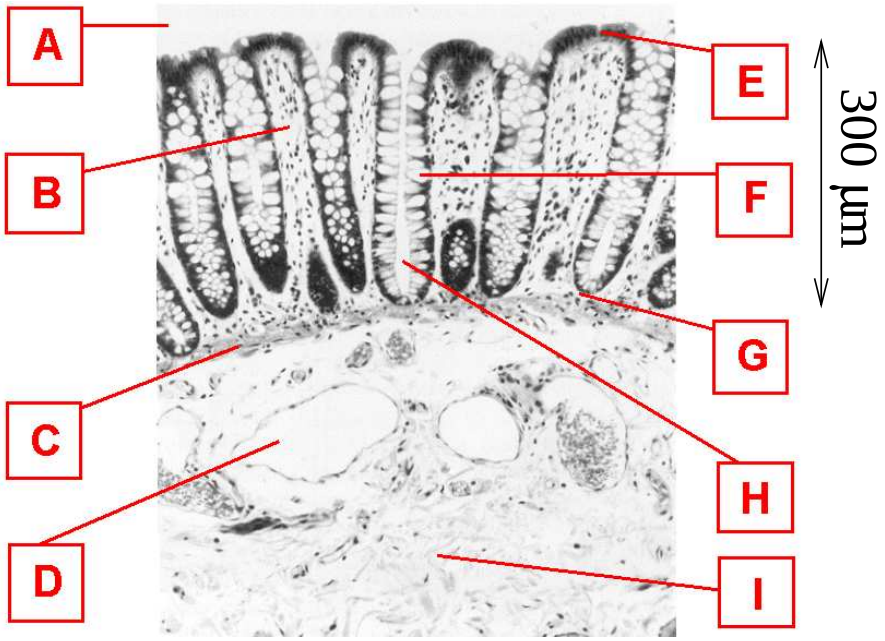

Figure 1.1: Section of normal human colon. A = intestinal lumen; B = lamina propria; C= lamina muscularis mucosae; D = blood vessel; E = surface epithelium; F = Goblet cell; G = stem cells; H = crypt lumen; I = submucosa. Image taken from the School of Medicine (University of Leeds)[119].

we first describe the function of normal gut tissue (§1.2.1). We then describe how mutations can lead to morphological changes and later to colorectal cancer (§1.2.2).

1.2.1 Normal tissue

Gut function

The large intestine (large bowel) is the penultimate stage in the digestive tract and is approximately 1.5m long and 7.5cm wide [140]. It is comprised of the cecum, the colon and the rectum [104] and its main function is to first absorb and then to pass into the bloodsteam primarily water and nutrients from the material that passes through it. Absorption takes place through a layer of epithelial cells that line the inside of the large intestine. Throughout the large intestine the internal surface has a number of folds, which increase the surface area available for absorption of nutrients [140].

The structure of the inner surface of the colon is shown in figure 1.1. The outer layer of the colon is a smooth muscle layer, the muscularis externa (below the tissue shown in figure 1.1). The main function of the muscularis externa is to move matter along the large intestine through peristaltic

contractions. Inside the muscularis externa is the submucosa (marked I in figure 1.1), which contains vessels that provide the main blood supply to the large intestine. Inside the submucosa another layer of muscle (the muscularis mucosae, C in figure 1.1) separates the submucosa from the inner-most part of the large intestine, the mucosa. Embedded in the mucosa are many intestinal glands or crypts.

Crypts

When the colon is viewed internally, it appears as a pitted surface. These pits are the test-tube-shaped colorectal crypts that supply the epithelial cells covering the internal surface of the colon. It is estimated that there are approximately 10^7 crypts in an adult human colon [118], each crypt containing $1000 - 4000$ epithelial cells [118]. The crypts are embedded in the surrounding stroma and are about 300μm (40-60 cells) [7, 137] in length and approximately 50μm [7] in diameter.

The epithelial cells toward the bottom of a crypt proliferate. All cells, except the stem cells at the bottom of the crypt, are believed to migrate up the crypt in response to the mitotic pressure [65] generated by proliferating cells beneath them (although it has also been suggested that active migration may play a role [116]). As these epithelial cells migrate up the crypt they proliferate less and differentiate (adapt to their final absorptive functional form, see figure 1.2). Once the cells reach the top of the crypt they migrate onto the luminal surface, perform their absorptive function and are shed into the lumen. The time taken for a cell at the base of the crypt to migrate up the crypt and be shed into the lumen is estimated to be 2-3 days in mouse [121] and 5-6 days in man [171].

Crypts can undergo fission, a process in which a crypt divides in two. This process happens regularly during postnatal growth [37] but is less prominent in later stages of life. Crypts lined with normal cells typically undergo symmetric crypt fission, whereas crypts with lined with mutated epithelial cells have been found to undergo asymmetric fission [131].

Cell types

We now introduce the different cell types found in the colorectal crypt.

It is widely accepted that cell replacement and production is accomplished by stem cells found at the base of the crypt [103]. The stem cells are a small population of relatively undifferentiated, cells that typically maintain their population size when they divide [128]. When a stem cell proliferates its offspring are usually a stem cell and a transit cell, although they can on occasion produce two stem cells. The progeny of stem cells have the ability to develop into any of the epithelial cells found

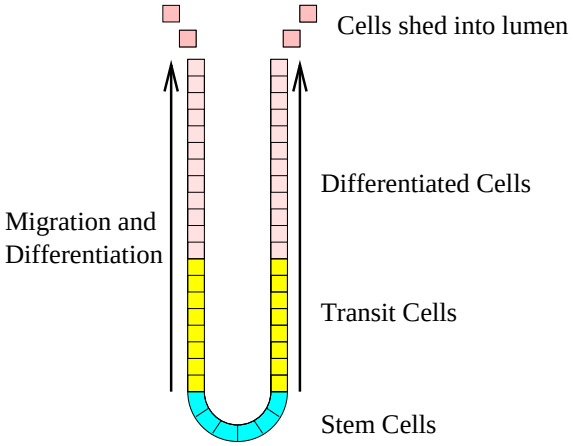

Figure 1.2: Schematic of a colorectal crypt. Stem cells (cyan) at the crypt base, proliferate to produce transit cells (yellow), which migrate up the crypt and differentiate into differentiated cells (pink). Cells are shed into the lumen at the top of the crypt.

in the colorectal crypt [128]. The stem cells retain their own strand of DNA in each chromosome and pass on the copied strands to their progeny [130] (although some dispute this hypothesis [87]). This reduces the risk of mutations in the DNA [93]. Stem cells are difficult to define and characterise either morphologically or using labelling techniques [92]. Consequently it is hard to determine their number [129]. However, it is estimated that there are 4-6 stem cells in each crypt [128], although some authors have put this figure as high as 64 [188]. It is thought the number of stem cells may fluctuate when the crypt undergoes fission and also in different regions of the gut [98]. It is also thought that stem cells do not proliferate as frequently as their progeny, with stem cells having an estimated cell-cycle time longer than 24 hours [2].

Situated directly above the stem cells (further up the crypt) are their progeny, the transit cells (see figure 1.2). It is thought that transit cells undergo 4-6 cell divisions as they move up the crypt [129] with a cell-cycle time slightly less than that of stem cells [13]. As the transit cells move upwards they proliferate less [103] and differentiate. Differentiation is defined as the change in a cell phenotype and is brought about by changes in gene expression [129]. One mechanism that is believed to regulate differentiation is extracellular signalling, i.e. the Wnt signalling pathway (see below).

Towards the top of the crypt and on the internal surface of the colon are fully differentiated cells, which do not proliferate (see figure 1.2). They migrate up the crypt onto the internal surface of the colon where they perform their absorptive function, passing water and nutrients from the lumen into the stroma and back into the bloodstream. Thereafter the fully differentiated cells are shed into the lumen [60]. It is thought that about 10^{10} epithelial cells are shed into the gut-lumen every day [132].

The Wnt signalling pathway

The structure of the epithelial cells in the crypt is maintained in part by the expression of the extracellular protein Wnt [126]. Wnt is a small, lipid-modified protein that plays many roles in mature tissues and in embryonic development [74]. For example, Wnt is implicated in tissue patterning through the control of cell proliferation [74]. In the crypt, extracellular Wnt is thought to be expressed by stromal cells with high levels of expression at the bottom of the crypt and at low levels at the top [60].

Wnt proteins bind to Frizzled receptors on the epithelial cell membrane and can activate one of three signalling pathways [74]; the canonical Wnt pathway, the noncanonical planar cell polarity (PCP) pathway, and the Wnt/Ca^{2+} pathway [41]. Our main concern is the canonical Wnt signalling pathway (see figure 1.3), in this pathway cells can be either in an "off" or "on" state, as described below.

"Off" state

In the absence of Wnt, the proteins Axin and GSk3β form a destruction complex with the protein APC (adenomatous polyposis coli) in the cell cytoplasm [74]. This complex binds to free cytoplasmic β-catenin, phosphorylates it and thereby marks it for degradation [19]. This stabilises β-catenin and prevents it entering the nucleus [19]. If β-catenin is located in the nucleus it forms a complex with the protein TCF that promotes the transcription of genes such as c-myc [111] and cyclinD1 [154, 162]. These proteins promote cell growth and the transcription of genes associated with DNA synthesis [58] and thereby contribute to cell proliferation [126]. In summary, in the absence of Wnt, β-catenin is degraded and does not enter the nucleus. As a result the cell does not transcribe the proteins needed for proliferation.

"On" state

By contrast, when Wnt is present, it binds to Frizzled receptors and the proteins Axin and GSk3β are drawn toward the cell membrane [19]. This inhibits the formation of the destruction complex and leads to an abundance of cytoplasmic β-catenin, some of which enters the nucleus, binds with TCF, leading to cell proliferation. In summary, the presence of Wnt increases the amount of β-catenin which can enter the nucleus to transcribe cMyc, cyclin-D and other target genes. In doing so Wnt signalling promotes proliferation.

In view of the above we deduce that the extracellular gradient of Wnt along the crypt axis results in higher rates of proliferation by cells at the bottom of the crypt (the stem cells and the transit cells) and low rates at the top of the crypt (the differentiated cells).

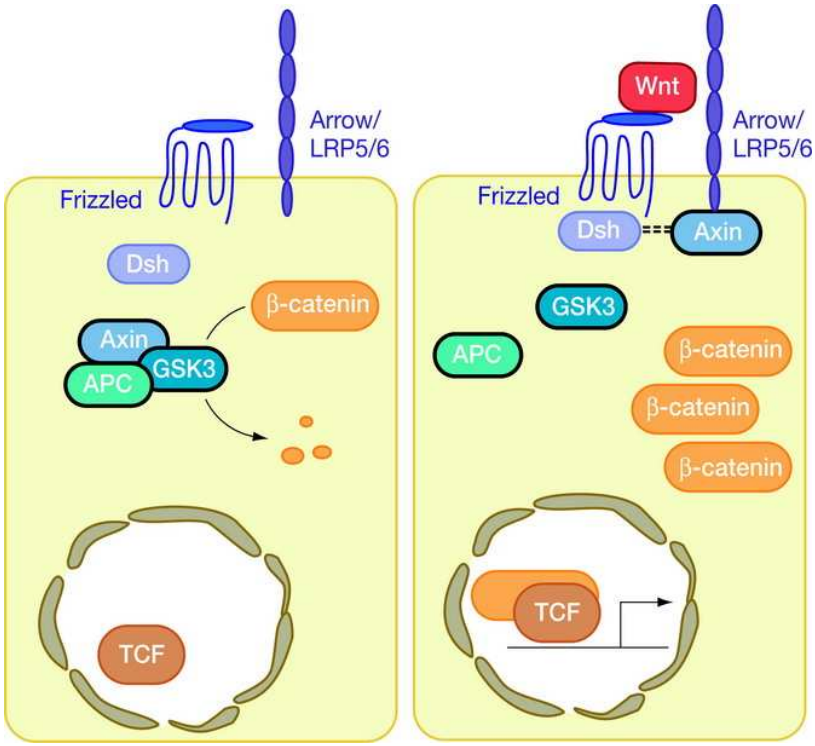

Figure 1.3: Schematic of the Wnt signalling pathway, taken from Logan and Nusse [96]. (Left) Wnt signalling pathway off. A destruction complex of APC, Axin and GSK3 is fromed and degrades β-catenin. (Right) Wnt signalling pathway on. Axin and GSK3 are drawn to the cell-membrane, so no destruction complex is formed. β-catenin becomes abundant and can enter the nucleus, where it binds with TCF, leading to the onset of proliferation.

The Wnt signalling pathway is thought to affect many other phenomena, not just cell proliferation [171]. Indeed β-catenin was initially identified for its role in cell adhesion [18]. As well as stimulating expression of proteins associated with proliferation, nuclear β-catenin is thought to activate the transcription of proteins associated with apoptosis (survivin) [23] and adhesion (Ephrin-B) [40].

Hinck *et al.* [66] found that high levels of β-catenin lead to stronger cell-cell adhesion [66]. This process occurs when β-catenin [117] binds with E-cadherin to form a complex near the cell surface [2]. Cadherins (such as E-cadherin) are transmembrane proteins that have a large extracellular polypeptide chain. These extracellular chains bind to extracellular cadherin chains from adjacent cells. For these bound cadherin chains to have an adhesive effect, they must be anchored inside the cell membrane. This is done by a complex comprising, amongst other proteins, β-catenin. It has been shown that increasing the number of anchored cadherins (which happens in the presence of increased β-catenin) increases cell-cell adhesion [40]. In summary, increased Wnt increases cytoplasmic β-

catenin levels which increases adhesion.

It has also been shown that migration and sorting of cells is affected by the level of β-catenin in a cell, through the expression of Ephrin ligands and EphB receptors [169]. Nuclear β-catenin leads to the transcription of proteins for EphB receptors and the down-regulation of proteins for the ligand Ephrin. EphB receptors control cell shape and migration through the remodelling of a cell's cytoskeleton and are also thought to regulate cell-to-substrate binding [15]. The expression of β-catenin in proliferating cells and low levels of β-catenin in differentiated cells leads to high levels of EphB receptors in proliferating cells and high levels of Ephrin ligands in differentiated cells [15]. On contact, EphB receptors and Ephrin ligands have a repulsive effect [83]. It is thought that this receptor-ligand interaction enables cells to sort themselves, with proliferating cells at the bottom of the crypt and differentiated cells at the top [15].

It is thought that APC, like β-catenin, may also be a multi-functional protein that affects cell proliferation and adhesion [18]. This is due to the high concentration of APC close to adherens junctions (adhesion proteins) on the cell membrane which are involved in the development of cadherin bonds [20]. However it is noted that the effects of APC could just be an indirect consequence of the Wnt signalling pathway [20].

Thus the Wnt signalling pathway is important in regulating cell proliferation, migration, sorting and differentiation in the colorectal crypt. It controls the distribution of epithelial cells in the crypt, with stem and transit cells at the bottom of the crypt and differentiated cells at the top.

1.2.2 Mutations and progression to cancer

Cancer is a multi-stage process that requires the accumulation of several genetic mutations, each of which successively alter the tissue's normal behaviour. These events are well documented in the adenoma-carcinoma sequence [75], originally defined by Fearon and Vogelstein [53], which describes the stepwise progression from normal to dysplastic epithelium with the accumulation of clonally selected genetic alterations [90].

One of the earliest mutations in colorectal cancer is often in APC or β-catenin [126]. This leads to a breakdown in the Wnt-signalling pathway and overproliferation of epithelial cells. The affected crypts become distorted (via crypt buckling) and can lead to an outgrowing "early adenoma" or polyp. Such an adenoma remains small until it suffers a mutation in the K-ras oncogene. K-ras proteins are signalling proteins that act as molecular switches, transducing signals from the cell surface to the cell membrane [141]. Mutations in K-ras are thought to cause the cell to proliferate continuously [25],

enable the adenoma to grow larger in size and to become an "intermediate adenoma"[6]. Further mutations in proteins such as Smad4 and Smad2, enable the tumour to grow further, often occur later in the development of an adenoma. At a yet later stage the gene $p53$ is often mutated and the adenoma becomes a carcinoma. $p53$ is an oncogene that is found mutated in over 50% of human tumours [54]. It is known as the "gatekeeper of the genome" [90] and its main function is to ensure that if DNA is damaged then the cell will not undergo mitosis [54]. When $p53$ is mutated, cells with damaged DNA may proliferate, allowing progeny to be produced with more mutations. Following loss of $p53$ the carcinoma accumulates successive mutations more rapidly, some allowing the cancer to spread or metastasise to other parts of the body.

Early mutations

Some 80% of all colorectal tumours show loss of APC function. Amongst those colorectal tumours that retain wild-type APC, around half show signs of mutations in β-catenin [60]. This finding lead to the discovery that unstabilised β-catenin, when β-catenin cannot be degraded by the APC complex, is an early event in colorectal cancer [19]. An APC mutation may render APC unable to bind to Axin [74] and prevent formation of the β-catenin destruction complex, leaving β-catenin unphosphorylated. Similarly a mutation in β-catenin can lead to a transcriptionally active β-catenin protein that cannot be degraded by the APC-based destruction complex [74]. Both of these mutations result in the cell behaving as if it is being continuously stimulated by Wnt, regardless of the Wnt level [74]. Cells with these mutations are termed adenomatous. These two types of mutations, loss of APC function and mutation in β-catenin, are found to be mutually exclusive [60], which is consistent with them having a similar effect on β-catenin stability.

It has been noted that for APC fully to lose its function, both alleles of the gene must be mutant [60], whereas destabilisation of β-catenin requires only a single mutation. However loss of APC function is far more common (80%) in colorectal cancer than β-catenin mutations (10%). One explanation for this phenomenon is that APC may have other tumour suppressor functions beside the degradation of β-catenin [139].

A disease commonly studied in colorectal cancer is Familial Adenomatous Polyposis (FAP) [81, 131]. FAP is a hereditary condition in which one of the two copies of APC has a germ-line mutation [84]. As a result its sufferers need only develop a single mutation in APC to lose APC function. This leads to the development of numerous polyps and consequently early onset of colorectal cancer. Many studies of the early stages of colorectal cancer are carried out on patients with FAP.

Loss of control of the Wnt signalling pathway leads to many effects, as APC and β-catenin interact

with many proteins, including cyclinD1 [154, 162], c-myc [111], survivin [23], EphB [40] and Ephrin-B [40]. Some of the most widely reported changes in behaviour are increased rates of proliferation and the crypt losing its proliferative hierarchy, so that cells proliferate throughout the entire crypt, rather than just at its base. As a result, the number of proliferating cells in the crypt increases and they are distributed widely throughout it (rather than just in the lower part of the crypt).

In addition to proliferation being affected when a cell becomes adenomatous, the cell experiences many other changes, as β-catenin and APC control many other proteins (as mentioned in above). Sansom *et al.* [141] note that loss of APC function also affects cell differentiation and migration. In [141], experimental evidence shows that adenomatous cells undergo cellular changes including increased cell packing and failure to migrate and differentiate.

Nathke [115] also noted decreased migration in cells lacking APC function and proposed that the lack of APC function affects the ability of the cytoskeleton to change shape, leading to decreased migration. Nathke also proposed that the number of Ephrins (which are involved in cell-cell adhesion) could change with a mutation in APC or β-catenin, which would also affect cell migration.

It is interesting to note that adenomas with β-catenin mutations tend to be less aggressive than those with APC mutations [116]. This may be related to the different levels of adhesion that the mutations cause. It has also been found that Ephrin, a protein associated with β-catenin and APC that plays a role in cell sorting, may suppress colorectal cancer in its later stages [14, 42].

Top-down or bottom-up morphogenesis?

When cells become adenomatous, they proliferate at an increased rate. However it is a matter of great debate how adenomatous cells form polyps [187]. Two mechanisms have been suggested (see figure 1.4): top-down and bottom-up morphogenesis. In top-down morphogenesis, an adenomatous epithelium is initiated by a mutation in a cell at the top of a crypt, that expands laterally and downwards and invades (adjacent) crypts containing normal epithelium. In bottom-up morphogenesis, the first adenomatous cell occurs at the base of the crypt; they increase in number through proliferation, until they eventually populate the entire crypt.

Different experimental results support each hypothesis. For example, it has been noted [105] that in adenomatous polyps, cells towards the top of the crypt proliferate more than cells toward the bottom. There is also evidence showing that adenomatous cells reside only at the top of crypts in adenomatous polyps [153]. These two pieces of evidence support top-down morphogenesis. However other evidence, such as the identification of fully adenomatous crypts, supports bottom-up

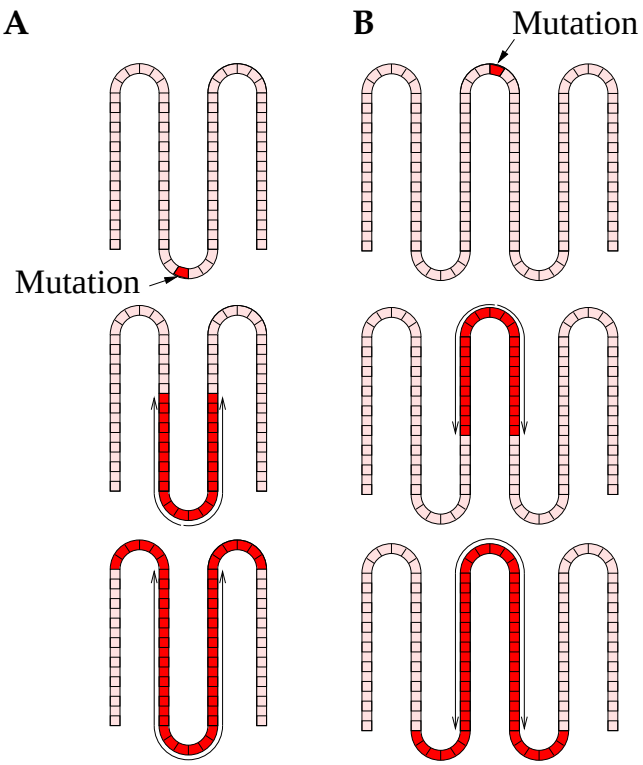

Figure 1.4: Schematic diagrams showing (A) bottom-up morphogenesis and (B) top-down morphogenesis. In (A) the initial mutant cell is at the base of the crypt and the mutant cells move upward to colonise the crypt (cell migration is indicated by the arrows). In (B) the initial mutation is in a cell near the top of the crypt and mutant cells invade downwards into the crypt.

morphogenesis [185].

To gain insight into this debate, firstly we have to ask where the initial adenomatous cell occurs. Komarova and Wang [80] developed a mathematical model that challenged the conventional thinking that differentiated cells could not be targets for APC mutations due to their short life span. It is widely accepted that the first APC mutation occurs in a stem cell [186], as any transit cells undergoing a mutation would not stay in the crypt long enough to establish a population of mutant cells [34]. Komarova and Wang predicted that it is unlikely that both APC mutations occur in the stem cell; they predict at least one APC mutation occurs in a differentiated cell. In their model, differentiated cells are defined as "not stem cells", so they include transit cells amongst their number. (It is unlikely that differentiated cells in the normal sense would suffer a genomic mutation as they do not proliferate [2].)

Shih *et al.* [153] presented strong experimental evidence supporting top-down morphogenesis. They

studied 35 small adenomas from patients with FAP, staining cells for β-catenin and genetically altered APC. They found that APC mutations were uniformly present in cells toward the top of the crypt, whereas cells at the bottom of the crypt were identical to those in the bases of normal crypts. Furthermore in none of the adenomas studied were any fully adenomatous crypts found. With this evidence the authors concluded that the adenomatous epithelium proceeded from the top of the crypt downwards, rather than from the bottom. Two theories were put forward to explain how this may happen: (i) the initial adenomatous cells reside at the top of the crypts; (ii) that the initial adenomatous cells originate in stem cells, migrate up the crypt and form the adenomatous mucosae in the intercryptal zones. A third explanation due to Lamprecht and Lipkin [85], and consistent with work by Komarova and Wang [80], proposed that a transit daughter cell is the primary target for a mutation.

Many authors have suggested that the initial mutation is at the crypt base, whose offspring populate all of the crypt, bottom-up morphogenesis, rather than top-down invasion of crypts [178, 185]. These fully mutant crypts then expand through crypt fission to form polyps. Preston *et al.* [131] presented strong evidence supporting bottom-up morphogenesis. They studied 40 small adenomas from non-FAP patients and 4 sections from FAP patients, staining for proliferative activity and β-catenin in both cases. They found cases of fully adenomatous crypts, where all the cells within the crypt, from top to bottom, showed signs of proliferation and nuclear β-catenin. They also observed a sharp cut-off between the adenomatous cells and the normal epithelia present in the inter-cryptal zones. They concluded that this fully adenomatous crypt must have emerged from a mutant cell at the bottom of the crypt proliferating to fill the entire crypt. They also found fully adenomatous crypts that showed signs of budding or asymmetric crypt fission. They concluded that the main mode of expansion in early adenomas is through crypt fission. However they conceded that top-down morphogenesis does occur, but as a later event since the only cases in which it was found involved larger adenomas.

It could be the case that both top-down and bottom-up morphogenesis can occur [46]. It may be that the experimental evidence in each case is found only evidence of one type of morphogenesis occurring. We believe that by mathematically modelling the colorectal crypt, we may be able to identify conditions under which each of these mechanisms may occur. This investigation forms the basis for the models presented in Chapters 2-4 of this thesis.

1.3 Review of relevant mathematical models

In this section we identify different mathematical techniques for modelling tissue growth and assess their merits. First, we note the behaviour that will be important for us to model.

As the colorectal crypt is regularly repeated many times within the colon, we take the crypt as the unit of interest. It is widely thought that the initial stage in colorectal cancer, in most cases, is a mutation in an epithelial cell within the crypt and we therefore model the epithelium.

We intend to capture behaviour seen in the crypt seen experimentally (detailed below). We will use these features to judge the advantages and disadvantages of different mathematical modelling techniques. One of the most important features is the differential proliferation of cells in a crypt arising due to changes in the levels of the protein Wnt or through mutations [74]. We also wish to incorporate cell migration into our model. Cells migrate from the base of the crypt onto the luminal surface, but mutations can change this behaviour, by changing the level of cell-substrate adhesion and increased rigidity of the cytoskeleton [116]. Another important feature is cell-cell adhesion which is known to vary with cell type and may be affected by mutations [141]. A further feature to be included is the changing cell size throughout its lifespan, particularly over a small time period around proliferation [2].

In summary the important features against which we judge the relative merits of the different models are proliferation, cell migration, cell-cell adhesion, cell-substrate adhesion and cell growth.

We discuss different types of mathematical modelling as follows. First we cover continuum models (§1.3.1) and discrete cell-level models (§1.3.2), attempts to combine the two (§1.3.3) and finally other types of models (§1.3.4).

Continuum models, in general, require fewer parameters to be estimated and have been used to study many types of tissue growth. Cell-level models can include a greater level of detail and have been used to describe the behaviour of various epithelia, including the epithelium of a colorectal crypt.

1.3.1 Continuum models

Continuum models have been widely used to describe cell growth and movement. The tissue is often modelled as a homogeneous medium and may be used to describe large tissues such as tumour spheroids. Continuum models can describe large scale features easily and can be adapted to many different geometric configurations.

Continuum models typically contain a mass balance which is often supplemented this with a constitutive law. An illustrative example, describing the changes in amounts of two phases of material, taken from King and Franks [79], is given below:

$$\frac{\partial \varrho_1}{\partial t} + \nabla \cdot (\varrho_1 \mathbf{v}_1) = \nabla \cdot (D_1 \nabla \varrho_1) + K_1 \varrho_1, \tag{1.1a}$$

$$\frac{\partial \varrho_2}{\partial t} + \nabla \cdot (\varrho_2 \mathbf{v}_2) = \nabla \cdot (D_2 \nabla \varrho_2) + K_2 \varrho_2, \tag{1.1b}$$

$$\varrho_1 + \varrho_2 = 1. \tag{1.1c}$$

ϱ_1, ϱ_2 are densities of two phases (for example, cells and water), $\mathbf{v}_1,\ \mathbf{v}_2$ are their velocities, $D_1,\ D_2$ their diffusion coefficients, $K_1,\ K_2$ their source terms and t represents time. Cell proliferation and death are modelled by source terms, with positive values representing cell proliferation and negative values representing cell death.

For 1D geometries (or geometries symmetric in all but one dimension) it is possible to solve (1.1) without introducing a constitutive law (see Ward and King [177], Araujo and McElwain [8] and Bertuzzi and Gandolfi [17]), as all changes in the unidirectional velocity field are caused by changes in volume associated with cell proliferation and death.

For models in two or more space dimensions, a constitutive law is needed. We now introduce different constitutive laws that have been used along with mass balance equations to describe the proliferation and movement of cells.

Darcy's Law

One of the simplest constitutive laws is Darcy's Law. Originally used to describe the flow of a viscous fluid through a porous medium. Darcy's law is defined as

$$\mathbf{v} = -\frac{\kappa}{\mu} \nabla p \tag{1.2}$$

where $\mathbf{v}$ is the velocity of the cells, p is the pressure, μ the viscosity of the cells and κ the effective permeability of the scaffold through which the cells are moving.

One of the earliest models to use Darcy's law as a constitutive assumption for tissue growth was developed by Greenspan [64] to describe tumour growth. With this constitutive assumption, Greenspan was able to describe nutrient dependent tumour growth. The model was used to predict conditions under which an avascular spherically-symmetric tumour could remain in a steady state.

A common implementation of Darcy's law is to assume that two phases, whether they be cells and water or normal cells and tumour cells, do not diffuse and are distinct, being separated by a moving boundary [44, 56, 100]. With this assumption and applying (1.2), (1.1) becomes

$$-\frac{\kappa}{\mu_1}\nabla^2 p_1 = K_1, \text{ for } \varrho_1 = 1, \ \varrho_2 = 0, \tag{1.3a}$$

$$-\frac{\kappa}{\mu_2}\nabla^2 p_2 = K_2, \text{ for } \varrho_1 = 0, \ \varrho_2 = 1. \tag{1.3b}$$

This implementation has led to models that are able to follow the movement of the boundary between the two phases. Various techniques have been used to solve this problem including finite difference methods [56] and boundary integral techniques [44, 100]. This may be an appropriate way of describing behaviour of two populations of cells, such as normal and mutant cells in a colorectal crypt.

Darcy's law has also been derived by using balance of momentum and making further assumptions about the cells in other models such as assuming the cells to be a viscous fluid and the tissue being spherically symmetric, as done by Breward *et al.* [26], Landman and Please [86] and Chen *et al.* [39]. Attempts have also been made to develop multiscale models, such as by Ribba *et al.* [135], while assuming a Darcy-constitutive law.

One of the advantages of using Darcy's law is that large movements of tissues can be modelled. In other models, including those that use linear elasticity, it is strictly possible only to model small displacements: this would be inappropriate for the crypt as there are large movements of cells. Another advantage of using Darcy's law is that it is simple. It is easy to implement analytically and numerically and it introduces few parameters. However the simplicity of Darcy's law can be a disadvantage as it is hard to directly model many of the properties mentioned at the beginning of §1.3, such as cell-cell and cell-stroma adhesion and cytoskeleton rigidity.

Stokes' Law

An alternative to Darcy's law is to model the movement of the cells with Stokes flow [79], which describes fluid flow where inertial forces are small compared to viscous forces. Stokes' Law models the cells as a Newtonian fluid and has been used to describe tissue growth in tumours [26, 32, 33], the growth of a freely suspended tissue [79] and in multiphase models of tissue growth focussing on the interaction between nutrient, cells and water [89, 97].

An advantage that models using Stokes flow share with those using Darcy's law is the ability to

model large deformations. The model is also reasonably simple to implement and contains few parameters. However, these models suffer from the same problems as Darcy models: they may be too simple to model the features that we require, such as cell adhesion and cytoskeleton rigidity, and have not been derived in a consistent way from cell-scale models.

Brinkman models

A combination of Stokes' Law and Darcy's Law has been used to describe tissue growth on a 1D domain has been described by Fozard *et al.* [55]. Here, a Brinkman-continuum model is used to approximate a cell-level model of a growing epithelium. Terms from Darcy's law represent the breaking and reforming of cell-substrate bonds and the terms from Stokes' law represent the internal cell viscosity. The model showed good agreement with cell-level models when internal cell viscosity was assumed to be minimal and the cells were assumed to be homogeneous.

Solid mechanics

In addition to modelling tissue as a fluid, other approaches model the tissue using the principles of solid mechanics including linear elasticity, non-linear elasticity and viscoelasticity.

Linear elasticity

Authors such as Jones *et al.* [77] and Roose *et al.* [138] used principles in thermal mechanics to develop linear elastic models for tissue growth. These models used parameters such as Young's modulus, the bulk modulus and a time-derivative of a linear stress-strain relationship to characterise mechanical properties of the tissue.

An advantage of these linear elasticity models is that they use parameters that could be measured by tensile testing of the tissue. However linear elasticity is not appropriate for modelling the epithelium in the crypt, which undergoes large displacements and the cells rearrange to a plastic deformation, rather than an elastic deformation. A further problem is that these models can lead to stress build-up since viscous stress relaxation is neglected.

Nonlinear elasticity

Some of the questions raised when using linear elasticity, such as the assumption that large deformations can be modelled by a derivative of a linear elasticity relationship, have been addressed by nonlinear elastic models of tissue growth [3, 4, 5, 136, 156]. The models, based on work by Rodriguez *et al.*, assume a non-linear strain-energy function and use a Lagrangian approach to model problems

where there are large deformations of tissues.

The advantage here is that large deformations can considered, although this does come at a cost as the models are more complex to solve and require greater estimation of parameters for which there is little experimental data [5]. These models also neglect plastic deformation, even for large deformations applied for long times. As with the linear elasticity models, this would be a problem when modelling the colorectal crypt epithelium. This weakness has been addressed by viscoelastic models of tissue growth such as that developed by MacArthur and Please [99], who assumed the tissue could be modelled as a Maxwell fluid.

Cell-cell adhesion models

An approach to modelling the interaction of two cell populations, paying particular attention to the role of cell-cell adhesion in a deterministic continuum framework, was developed by Armstrong *et al.* [11]. They considered two populations of cells with different levels of cell-cell adhesion and allowed cells to interact with near neighbours. The model developed in [11] shows the sorting and mixing of different cells types depends on the parameter regime used. Cells could sort from one another, engulf one another or freely mix with one another.

While this approach could include effects such as different levels of cell-cell adhesion; cell-substrate adhesion or the effect of changing cytoskeleton rigidity are not considered.

Summary of continuum models

Overall there are many advantages to using continuum models to model a colorectal crypt. First, they are generally fairly simple, and contain few parameters. It is relatively straightforward to include cell proliferation and death and to allow them to depend on a spatially-varying nutrient or protein. These effects can be incorporated by introducing a source term into the appropriate mass balance equations. This could be used to describe the Wnt-dependent proliferation hierarchy found in the colorectal crypt. Continuum models can, by assuming a constitutive law and using the balance of momentum to define cell velocity, model the migration of cells. It is also possible to incorporate heuristic mechanisms for cell-cell adhesion and cell-membrane adhesion by changing parameters in the constitutive law. In light of these benefits, we develop a continuum model, assuming Darcy's law, of the crypt in Chapter 2.

However there are several disadvantages to using this approach. Cells are not treated as distinct entities. As a result any measurements related to cells (such as cell size) are not explicitly defined.

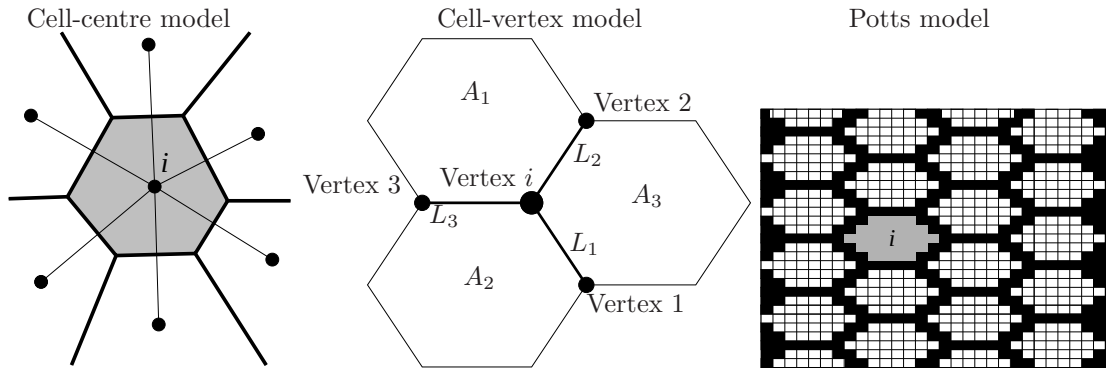

Figure 1.5: Figure showing three different cell-level models. (left) Cell-centre model where the movement of cell i is determined by interactions with neighbouring cells. (centre) Cell-vertex model, where the cell shape defined is by the cell's vertices. Vertex i moves in response to size and the shapes of the surrounding cells (1,2,3) which have areas, A_1, A_2, A_3. Lengths L_1, L_2, L_3 represent the distances from vertex i to vertices $1, 2, 3$ respectively. (right) Potts model, where cells comprise a set of lattice points, for example, cell i (shaded).

This causes difficulties when one attempts to incorporate sub-cellular features such as signalling pathways and protein-level models of cell-cell and cell-membrane adhesion. Another issue is whether there are enough cells within the crypt ($\sim$ 2000 cells) to justify modelling it as a continuum or whether each cell should be modelled as a discrete entity. With this in mind, in the next section we review several cell level models.

1.3.2 Cell-level models

Cell-level models treat each cell as a discrete entity that can interact with other cells. As such, it is possible to model in detail features such as proliferation and cell-cell adhesion. However cell-level models are computationally expensive to implement for large numbers of cells.

We separate our review of cell-based models into three main groups: models using centre-based dynamics, models using vertex-based dynamics and extended Potts models.

Cell-centre models

In these models, each cell is represented by the position and movement its centre (see figure 1.5 (left)). These models have been used for many biological problems, including modelling a colorectal crypt

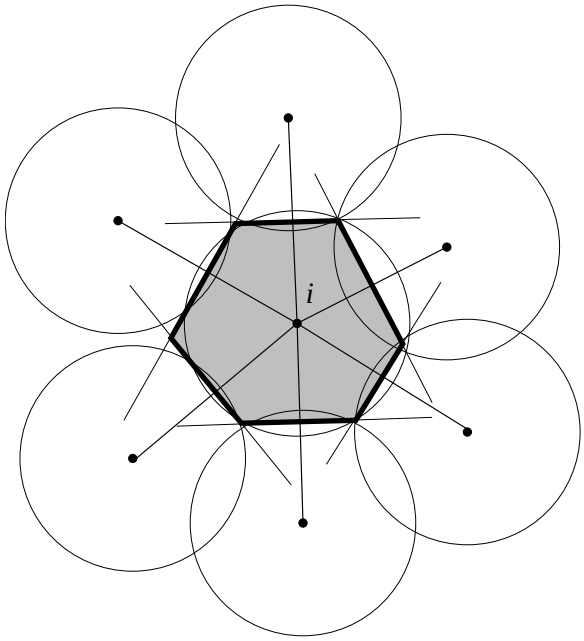

Figure 1.6: A Voronoi diagram to construct the polygonal shape of cell, i, shaded grey. From each point a circular wave is propagated at constant speed. Where the wavefronts collide a perpendicular bisector is drawn. These bisectors meet at the vertices of the polygonal cell(s).

[109]. Cell movement is often determined by a balance of forces acting on it. Various approaches have been developed for calculating the forces acting on a cell. These include modelling cell-cell connections with springs [109], and modelling the cells as deformable elastic spheres [147]. Inertial effects are assumed to be negligible and the cells' velocity is determined by balancing the cell-cell forces with a viscous drag term which models cell-substrate adhesion.

To represent the shapes of the cells, a Voronoi diagram may be used. A Voronoi diagram produces polygonal shapes for the cells by propagating a circular wave from each cell centre [181] (see figure 1.6). Where the wavefronts intersect, a chord is drawn between the two intersection points and extended past the inter-section. Points at which these lines intersect define the vertices of the polygonal cells.

The assumption that inertial effects are negligible and the forces from cell-cell interactions are balanced by a viscous drag term leads to the following equations of motion

$$\gamma_i \frac{d\mathbf{r}_i}{dt} = \sum_j \mathbf{F}_{ij}, \tag{1.4}$$

where $\mathbf{r}_i$ is the position of the centre of cell i, $\mathbf{F}_{ij}$ is the cell-cell interaction force between cell i and

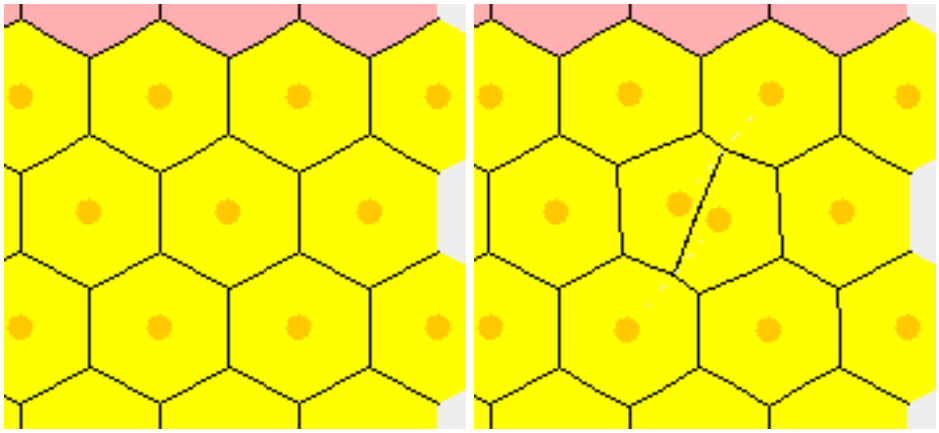

Figure 1.7: Schematic of cell birth in a cell-centre model, with (left) before cell birth and (right) after cell birth. New cell centre placed next to parent cell and two new daughter cells defined by a Voronoi diagram.

neighbouring cell j, $\sum_j$ is a sum over all neighbouring cells, γ_i is the drag coefficient on cell i and t is time.

A centre-based model for cell proliferation and movement of cells in an intestinal mouse crypt was developed by Meineke *et al.* [109]. The authors viewed the crypt as the 2D surface of a cylinder. The forces between the cells were modelled by linear springs connecting cells that share a common interface.

Cell movement within the crypt was driven by the proliferation of cells closer to the base of the crypt. To model proliferation, new-born cells were given a stochastically varying cell-cycle time and mitosis was modelled by placing a new cell centre in a random direction close to the dividing cell. The new cell shape was then defined by a Voronoi diagram (see figure 1.7). The spring connecting the new cell and its parent had a natural spring length that grew linearly over the first hour after mitosis.

The model considered three different cell types: stem cells (at the bottom of the crypt), transit cells (in the lower part of the crypt) and differentiated cells (toward the top of the crypt). Stem cells were fixed in position and had no restriction on the number of divisions they could undergo. They produced a new transit cell of generation 1 when undergoing mitosis. Transit cells proliferated three times; a transit cell of generation n produced two new transit cells of generation $n+1$, unless $n=3$ in which case the cell produced two differentiated cells. Differentiated cells could not proliferate.

At each time step the total force on each cell due to the springs was calculated and the movement

of the cells updated using (1.4). The new cell shapes were then defined by Voronoi tessellation.

Meineke *et al.* [109] found that this model gave results that agreed qualitatively with experimental evidence, with cells at the bottom of the crypt more densly packed than those at the top and the crypt retaining its proliferative structure, with cells proliferating toward the crypt base. However there are questions that need to be raised about this model. The main problem is the validity of modelling cell-cell interactions with springs. This does not take into account cell-cell adhesion being dependent on contact area between cells, as such cells with a small contact area can have a high attractive force if they are further than the natural spring length apart. The drag on the cells models the breaking and reforming of cell-stroma bonds and is assumed to be constant regardless of cell size. However, it is thought that the number of bonds formed is dependent on the area of contact between the cell and the substrate on which it moves, which Meineke *et al.*'s model does not reflect. We aim to address these weaknesses in Chapter 3.

A different type of centre-based model was developed by Schaller and Meyer Hermann [147] to simulate the growth of a tumour spheroid. This model does not suffer many of the same problems as Meineke *et al.*'s as a more complex mechanics system is used. In [147], the cells were modelled as 3D elastic deformable spheres. This assumption was made as the natural shape of a cell in solution is usually a sphere. The forces on each cell were composed of two parts from each neighbouring cell, a force due to deformation and a force due to adhesion. The decrease in size due to the neighbouring cells was calculated and the force due to deformation was calculated as a function of Young's modulus and Poisson ratio. The adhesive force was proportional to the contact surface area with each neighbouring cell. The cell shapes were calculated by a 3D Voronoi tessellation.

A cell-cycle model was applied in each cell where a cell could only pass into DNA-synthesis phase if the level of stress on the cell was low enough. When a cell underwent mitosis, at the end of its cell cycle, the natural volume of the cell was conserved in the two daughter cells with a reduction in natural radius. The natural size of the cell then increased, to simulate growth until the cell finished its growth phase.

Again, at each time step the forces on each cell were calculated and the movement of the cells determined according to (1.4). The cell shapes were defined by Voronoi tessellation. A similar model was also developed by Galle *et al.* [57] who modelled the growth dynamics of epithelial cell populations in vitro.

These models [57, 147] have many strengths as both cell-cell adhesion and cell deformation are included, although they do have added complexity compared to models such as Meineke *et al.*'s [109].

Drasdo and Loeffler [48, 49] also developed a cell-centre based model primarily concerned with the buckling of a colorectal crypt. The authors developed a model for a 1D chain of cells in 2D space. The cells were treated as deformable elastic circles. The force on each cell was composed of four parts: (i) the elastic deformation force between the cells; (ii) a shear force holding the crypt in shape; (iii) a force from the stroma and (iv) a force restricting any bending of the epithelium. The model included proliferation and allowed for variation in the size of the cells through the cell cycle. Whilst this model does simulate the buckling of a colorectal crypt well, it is probably not an ideal model for the proliferation and growth of cells in a colorectal crypt as it is only 1D. As such it could not model azimuthal movement of cells around the crypt as seen experimentally by Taylor *et al.* [161]. However this could be addressed by an extension of the model to 3D.

Other approaches to modelling the epithelium include work by Walker *et al.* [175]. They used agent-based modelling to replicate patterns of *in vitro* cell-growth and movement under different calcium concentrations. In [175] cells could migrate freely on the substrate if not bonded to other cells otherwise they moved in response to cell-deformation forces. The likelihood of cell-cell bonds forming was dependent on the levels of calcium available for cadherin-mediated bonding. The model also incorporated the social behaviour of cells by including the effects of contact-inhibited growth. The model replicated *in vitro* patterns of cells well and was also applied to wound-healing of tissue [174].

Others have also developed multiscale models based on cell-centre dynamics, including Ramis-Conde *et al.* [133], who used a modified Hertz model, where cells are assumed to be deformable elastic spheres, to model cell-cell interactions. The forces between the cells were defined by the gradient of a free energy which comprised terms conserving cell size and representing cell-cell adhesion interaction. The level of cell-cell adhesion was proportional to the number of adhesion molecules in contact. This was calculated by incorporating a protein-signalling model into each cell and assuming the adhesion proteins were spread evenly over the cell's surface.

The model was for a population of cells in 3D and had two viscous drag terms; one for the friction generated by the movement of a cell and one for the friction generated by cells moving past one another,

$$\underbrace{\gamma_i \frac{d\mathbf{r}_i}{dt}}_{\text{friction}} + \underbrace{\sum_j \Gamma_{ij}\left(\frac{d\mathbf{r}_i}{dt} - \frac{d\mathbf{r}_j}{dt}\right)}_{\text{cell-cell friction}} = \underbrace{\sum_j \mathbf{F}_{ij}}_{\text{forces}} + \underbrace{\mathbf{f}_i}_{\text{noise}} + \underbrace{\chi \nabla Q(t)}_{\text{chemotaxis}} . \tag{1.5}$$

Using this model, Ramis-Conde *et al.* [133] were able to study how intra-cellular effects can influence

the aggregation of a population of cells. This model has many strong points in that it is multiscale and includes many features such as cell-cell adhesion and cell deformation. With such a multiscale approach insight could be gained into how subcellular behaviour affects the behaviour the population of cells.

In summary, the cell-centre models can simulate cell proliferation and migration well. Some multiscale approaches include cell-cycle models, so it would be straight-forward to incorporate a Wnt-dependent (or any other nutrient/protein dependent) proliferation term into them. It is also easy to include different cell-cell adhesion levels in the models as some of the models already simulate cell-cell adhesion (for example [57, 133, 147, 175]). Another advantage of the centre-based cell models is that it is possible to vary cell-substrate adhesion by varying the drag coefficient in (1.4). Cell growth has also been incorporated into the models.

A disadvantage of the centre-dynamics models is their reliance on Voronoi tessellation. This means that the number of vertices and the shapes of the cells do not change smoothly [29]. Another disadvantage of these models is that they can be computationally expensive, with a new Voronoi diagram needing to be constructed at each time step.

Cell-vertex models

Cell-vertex models are a type of cell-level model that view the cells as polygons [70]. The dynamics of each cell is defined by the movement of its vertices (see figure 1.5 (centre)). These models are very good for modelling differential cell-cell adhesion. This is be an important feature to model in a crypt, as common mutations in colorectal epithelial cells are thought to affect cell-cell adhesion. Cell patterns described by vertex models can change flexibly and the cell shapes are thought to mimic cells closely [70]. In these models the movement of each vertex is determined either by the explicit forces on each vertex or a free energy function and the gradient of free energy is assumed to exert a force. Once again inertial effects are neglected in comparison to friction forces.

Vertex models were originally used to describe the behaviour of foams on a two-dimensional surface [114]. More recently, Weliky and Oster [181] developed a 2D cell-vertex model to describe the movement of epithelial cells in the Fundulus epiboly. The Fundulus epiboly, like the crypt epithelium, is a growing and moving epithelium, which grows to cover the embryo of a Fundulus, a fish.

In [181], to model the movement of cells, at each time step the force on each vertex was calculated. This comprised a membrane tension force and an expansive force representing the pressure the cell experienced. The force representing pressure ensured that each cell tended to a particular size and

the membrane tension force ensured cells tended to a particular surface area. As this was a 2D model membrane length corresponded to surface area and area corresponded to cell volume. In this model the cells did not proliferate and moved deterministically according to

$$\frac{d\mathbf{r}_i}{dt} = \frac{1}{\mu_i} \sum_j \mathbf{F}_{ij} \tag{1.6}$$

where $\mathbf{r}_i$ is the position of the ith cell vertex, $\mathbf{F}_{ij}$ is the force from surrounding cell j, $\sum_j$ is a sum over all cells that surround vertex i, μ the viscous drag coefficient on vertex i and t is time. In the model vertices to slide and, in certain circumstances, to merge. Using this model Weliky and Oster were able to reproduce the essential features of the Fundulus epiboly, where an epithelium of cells grew to cover a spherical embryo.

A different approach to modelling cell movement of a monolayer of epithelial cells was taken by Nagai and Honda [112]. In contrast to Weliky and Oster [181], the vertices move not in response to explicitly calculated forces but down gradients of a free energy function,

$$\frac{d\mathbf{r}_i}{dt} = -\frac{1}{\mu_i} \nabla U = -\frac{1}{\mu_i} \nabla (U_L + U_D) \tag{1.7}$$

where the free energy, U, comprised two parts; a cell-cell adhesion energy, U_L, and a cell-deformation energy, U_D. The cell-cell adhesion energy is proportional to the contact area between cells,

$$U_L = \sum_{\langle ij \rangle} \alpha_{ij} |\mathbf{r}_i - \mathbf{r}_j|, \tag{1.8}$$

where $\langle ij \rangle$ is the number of cell edges in the population and α_{ij} is a constant dependent on the two cell types that lie along the edge connecting vertices i and j.

The deformation energy, U_D, generates a force such that cells tend toward a natural area A_0,

$$U_D = \sum_{k=1}^{N} \beta h^2 \left(A_j - A_{0_k} \right)^2 \tag{1.9}$$

where N is the total number of cells, h is the cell height and β is a constant. The authors used this model to show that, independent of initial conditions, the cells would adopt a uniform pattern. An advantage of this model compared to the Weliky and Oster model [181] is that it permits contact-area-dependent cell-cell adhesion as well as cell-volume control. This model was applied to wound

healing in [113] and has also been extended to 3D by Honda *et al.* [70] by using polyhedra to represent the cells.

Brodland and Chen [27] used a cell-vertex model to describe the sorting of different cell types due to the cells' different adhesive properties. As mentioned before, this would be an important feature to include in a model of crypt epithelial cell movement, as cell-cell adhesion changes with cell mutations and cell position. The forces on each vertex comprised three forces that acted tangentially along the cell edges. Each of these forces were comprised of a contractile force from the membranes and microfilaments and an opposing adhesion force. The strength of the adhesion forces varied depending on the two cell types involved. The movement of each vertex was again defined by (1.6).

The main advantages of cell-vertex models is that they can describe the movement of a cell accurately, with the cells having meaningful shapes [29]. This would be useful when modelling the crypt epithelium, as cells only change in size in the early stages of their cell cycle. Another advantage of vertex based models is that it is easy to incorporate differential cell-cell adhesion terms (see [27]), which is thought to occur in the crypt epithelium. A further advantage of cell-vertex models is they have no need for a Delaunay triangulation or Voronoi diagram to be produced at each timestep. In light of these benefits, we develop a cell-vertex model for the proliferation and movement of cells in a crypt epithelium in Chapter 4.

One of the main disadvantages of vertex-based models is that it is not easy to include differential cell-substrate adhesion terms for different cells, as any change in drag terms on vertex movement would depend on all cells surrounding the vertex. Finally as vertex-based methods contain more information than centre-based methods they can be more computationally expensive.

Potts models

A third type of cell-level model used to describe the proliferation and movement of epithelial cells is the Potts model. Here, cells are defined as a set of lattice points (see figure 1.5 (right)). Changes in cell shape are controlled by a stochastic Monte-Carlo method based on free energy. These methods differ greatly from cell-centre and cell-vertex-based models that are lattice-free and usually deterministic, as Potts models are lattice-based and stochastic.

Potts models are based on ideas used to describe patterns in metals and soap froths. Potts models were originally used to describe epithelial cell movement by Graner and Glazier [62]. In [62], a epithelium of cells is initially discretised onto a lattice. In this model strong bonds exist between like cells and weak bonds between cells that are not alike. Also it is assumed that the volume of a cell

(represented by its surface area) had a target value it would tend to if unstressed. A Hamiltonian (energy function), H, is constructed to account for these two assumptions.

The model works in the following way. A lattice point is picked at random and a neighbour of that lattice point is also picked at random. The probability swapping of these two points is calculated. If the change leads to a decrease in free energy the change happens with probability 1; otherwise the change happens with probability $e^{-\Delta H/T}$, where T is the temperature and ΔH the change in free energy, determined by the deformation of the cells and the contact energy.

Using this model the sorting of a random distribution of cells into two distinct populations was achieved. This approach is relatively simple and computationally inexpensive and may be useful for studying mutant and normal populations. However there is no clear realisation of time, as time is measured by the number of Monte-Carlo timesteps.

The model described by Graner and Glazier [62] was extended in [61] to include tension in the membrane around the cells. This ensured that the length of the cell membrane of individual cells tended toward a set value, a useful property for keeping cells in realistic shapes. Using this model the authors were able to describe many different cell patterns that arise in biology by varying the cell-cell adhesion energies. Other extensions include that of Ouchi *et al.* [122] who introduced negative surface energies into the Hamiltonian, so that cells reduce their surface energy through binding.

Even though Potts models have no physical measurement of time, some authors [59, 144, 157, 166] have adapted Potts models to include time-dependent features such as proliferation. Stott *et al.* [157] developed a Potts model to describe the growth of an avascular tumour spheroid. They incorporated a nutrient-dependent growth term along with cellular automata to describe the growth and proliferation of the cells. The authors found that the Potts model produced similar results to those found in continuum models, e.g. [39]. A similar approach was used by Ghaemi and Shahrokhi [59].

Further applications of the Potts model have been carried out by Turner and Sherratt [165] who used it to study cancer invasion by cells with low adhesiveness. Also Chaturvedi *et al.* [38] developed a 3D Potts model along with a reaction-diffusion equation for nutrient and a cellular automaton for limb growth of chickens.

The main advantage of the Potts model is that it is simple to program and computationally inexpensive to run. It also does not require any constitutive laws to be supplied, so fewer parameters need to be estimated. Another advantage is that differential cell-cell adhesion and cell death can be easily incorporated.

The main disadvantage is there is no sense of time associated with the model. This means that it is hard to incorporate time-dependent proliferation, a feature that is important when modelling a colorectal crypt, as there is a large amount of cell growth. Even though some authors have cell cycles in their models [59, 166] it is unclear how they relate time to the number of Monte-Carlo steps. Also the lack of modelling dissipative effects means that cell-substrate adhesion is ignored in these models. This would also be important in the crypt, as we would want to include mutant cells with increased levels of cell-substrate adhesion. Another disadvantage of the Potts model is that it is lattice-based, requiring high spatial resolution for realistic cell shapes.

1.3.3 Homogenisation models

As continuum models have advantages of efficiency over cell-level models, but have disadvantages such as difficulties in parameter estimation, attempts have been made to derive continuum models from cell-level models. Bodnar and Velazquez [21, 22] developed an integro-differential equation for the movement of a 1D line of cells using a cell-centre approach, where the forces on each cell depended on distance from neighbouring cells. The model showed good correlation to the cell-level model for particular energy potentials.

Fozard *et al.* [55] have developed a continuum Brinkman-model by homogenising a 1D cell-vertex model. They found good agreement with the cell-vertex model when cells were homogeneous. There were difficulties associated with incorporating cell-birth and the model has yet to be extended to 2D.

Alber *et al.* [1] derived a continuous approximation (a Fokker-Planck equation for cell densities) from a 1D cellular Potts model. Good agreement with the cellular-Potts model was observed for cases when the grid spacing was small and the two models yielded similar results for cell distribution when chemotaxis was included. We note that the approaches detailed in this subsection would be useful in comparing cell-level and continuum models.

1.3.4 Other approaches to colorectal crypt modelling

As well as cell-based and continuum models, we also introduce other models that could be applied to the modelling of an epithelium in a colorectal crypt.

A modelling approach taken by Tomlinson and Bodmer [163], (in work extended by by D'Onofrio and Tomlinson [47] and Johnston *et al.* [76]) developed a spatially-averaged population model that

decomposed the crypt into three different cell types (stem, transit and differentiated) and predicted how the number of cells of each type changed over time. Whilst this model may give interesting results on the numbers of different cell types, it is not for our purposes as we are also interested in cell movement.

A comprehensive review of many of the approaches that have been used to model the colorectal crypt is given by van Leeuwen *et al.* [171] and a review of cell-based models is given by Brodland [29].

1.3.5 Conclusions

There are many different approaches to modelling cell proliferation and movement. Using the criteria outlined in §1.3, we conclude that continuum models have many strengths. They can model cell proliferation, death and migration and, to some extent, cell-substrate adhesion and are relatively simple. As a result they are often computationally inexpensive to implement and include few parameters, reducing the effort associated with parameter estimation. However it is unclear whether the number of cells within a colorectal crypt is too small for their implementation.

Cell-based models are particularly good for implementing cell-cell adhesion and cell migration and have the ability to track individual cells. Of the cell-level models, cell-centre-based models are better at modelling cell-substrate adhesion but less well suited to modelling cell growth, while cell-vertex models are particularly well suited to modelling cell-cell adhesion. Potts models are fast and well suited to modelling cell-cell adhesion but less well suited to modelling time-dependent features such as proliferation. Cell-based methods are better suited for small numbers of cells but they become computationally expensive for large numbers of cells. It may be questioned whether the number of cells in a crypt (~ 2000 cells) is too large for these methods.

1.3.6 Thesis objectives and structure

The aim of this thesis is to aid the understanding of the early stages of colorectal cancer by identifying the factors that determine whether a mutant population can establish itself within a crypt. To do this we consider three different approaches for modelling the proliferation and movement of epithelial cells in the colorectal crypt, as described in Chapters 2-4.

In Chapter 2, we develop a continuum model. We use a spatially-varying source term to model Wnt-dependent proliferation and a Darcy constitutive law to describe cell movement. The model is

solved using linear stability analysis to find approximate analytic solutions, and numerically using a collocation method.

In Chapter 3, we adapt the cell-centre model of the crypt described by [109]. We use agile computational methods and develop a framework for a multiscale model of colorectal cancer. We model cell-cell interactions by springs connecting neighbouring cells and include subcellular protein signalling models.

In Chapter 4, we develop a cell-vertex model. We model the movement of the vertices by using a free energy function comprised of a cell-deformation term and a contact-area dependent cell-cell adhesion term.

We conclude in Chapter 5 with a comparison of the three models and a discussion of their merits. A summary of the main results of the thesis is presented along with ideas for further work.

Chapter 2

Continuum model of the colorectal crypt

The aim of this chapter is to develop a continuum model that describes the proliferation and movement of epithelial cells in a colorectal crypt. The model can be used to investigate how interactions between spatially-varying cell proliferation, cell movement down pressure gradients and cell-cell adhesion affect the structure of the crypt.

2.1 Introduction

One of the major debates in the study of colorectal cancer [98, 186] concerns how a mutant cell and its progeny can colonise an entire crypt. Two hypotheses have been proposed. Shih *et al.* [153] argue that the first mutant cells occur at the top of the crypt and proceed downwards to fill the crypt, via "top-down morphogenesis". This view is supported by other authors including Lamprecht and Lipkin [85]. However other authors including Preston *et al.* [131] and Wong *et al.* [185], present experimental evidence to argue that the stem cells at the base of the crypt are the first to acquire a mutation. The crypt is then filled by mutant cells originating from the bottom of the crypt. This is "bottom-up morphogenesis".

In this chapter we develop and analyse a mathematical model in order to identify the conditions under which top-down and bottom-up morphogenesis of a mutant population (see §1.2.2 for further details) could occur in a colorectal crypt. Our model simulates the proliferation and migration of epithelial cells within a colorectal crypt.

We distinguish between two types of epithelial cells, so that we can see the effects of introducing a mutant cell population (cells with mutations in APC or β-catenin) into a normal cell population. The two cell populations are separated by a clearly defined interface, with no gaps or other material between the cells. The model is developed by combining the principle of mass balance with

Darcy's law for cell movement. This approach has been used by several other authors to model cell movement, notably Greenspan [64]. The model is similar to that described by Franks [56] but with cell populations having different viscosities. In our model viscosity embodies resistance to cell movement. It is a lumped parameter that accounts for the breaking and reforming of bonds to the stroma and neighbouring cells, as well as the reshaping of the cell's cytoskeleton. Cells with a larger number of bonds per surface area and having a cytoskeleton that is hard to reshape are assumed to have a higher viscosity than those with fewer bonds and a softer cytoskeleton.

The mass balance equation includes a spatially-varying source term to mimic the effects of the signalling protein Wnt on cell proliferation. Proliferation rates in normal colorectal crypts (where no mutant cells are present) are higher at the base of the crypt [103] where Wnt levels are high [19]. Towards the top of the crypt, where Wnt levels are low, normal cells do not proliferate but differentiate into different types of cells, such as goblet cells. We model this behaviour by assuming that the proliferation rate of normal cells is a linear function of distance from the crypt base, the proliferation rate being maximal at the base (where Wnt levels are high) and minimal at the top of the crypt (where Wnt levels are low). When cells suffer a mutation in APC or β-catenin the dependence on Wnt is often lost [74]. We model this by assuming that mutant cells proliferate at a constant rate throughout the crypt.

We use our model to study two different situations. First, we model a situation where initially one cell population is placed above another in a crypt (§2.2). Model solutions are obtained using analytical techniques (§2.3) and numerical collocation (§2.4). Second, we model a distribution where initially the mutant cells are localised in a patch within the normal crypt epithelium (§2.5). This chapter concludes with a discussion of the key results (§2.6).

2.2 Model development

To begin, we consider the mass conservation equations for a mixture of two cell populations. We model cell proliferation with a spatially-varying source term and assume that diffusion is negligible. Following King and Franks [79], our mass conservation equations are given by

$$\frac{\partial \varrho_1}{\partial T} + \nabla \cdot \left(\varrho_1 \hat{\mathbf{V}}_1 \right) = K_1(\mathbf{X}) \varrho_1, \tag{2.1a}$$

$$\frac{\partial \varrho_2}{\partial T} + \nabla \cdot \left(\varrho_2 \hat{\mathbf{V}}_2 \right) = K_2(\mathbf{X}) \varrho_2, \tag{2.1b}$$

$$\varrho_1 + \varrho_2 = 1, \tag{2.1c}$$

where ϱ_1, ϱ_2 are the respective volume fractions of populations 1 (normal cells) and 2 (mutant cells),

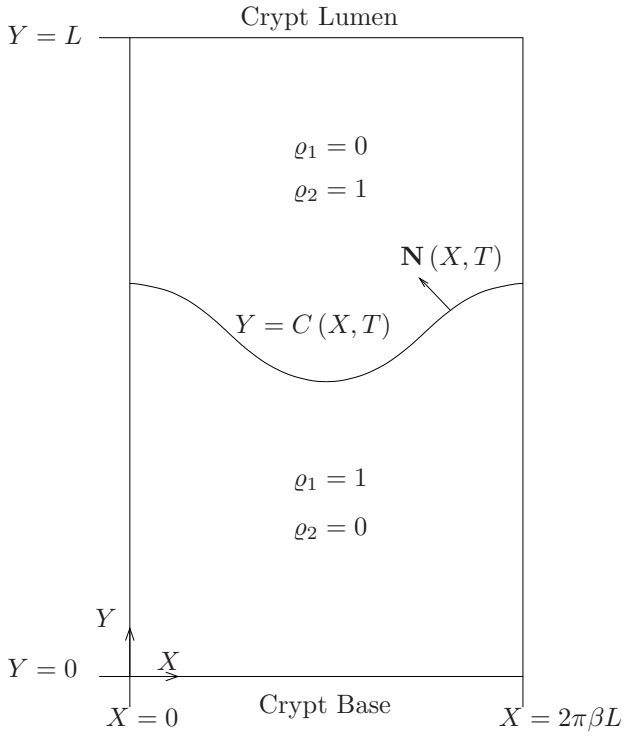

Figure 2.1: Sketch of the two-dimensional model for two epithelial cell populations, 1 (bottom) and 2 (top), growing on the surface of a cylindrical crypt, height L and radius βL. The volume fractions of each population are ϱ_1 and ϱ_2 respectively and they are separated by the boundary $Y = C(X,T)$, with normal $\mathbf{N}(X,T)$. Y represents the distance from the base of the crypt and X measures the distance around the crypt.

$\hat{\mathbf{V}}_1$, $\hat{\mathbf{V}}_2$ the cell velocities and $K_1(\mathbf{X})$, $K_2(\mathbf{X})$ their net proliferation rates. Spatial position is denoted by $\mathbf{X} = (X, Y)$ and T represents time.

We can now specialise the mass balance equations to a colorectal crypt. We view the crypt as being the 2D surface of a cylinder of length L ($\sim 300\mu$m) [7] and radius βL ($\sim 25\mu$m) [7], as shown in figure 2.1. We set X to be the azimuthal distance around the crypt and Y to be the distance from the base of the crypt. To capture the Wnt-dependent proliferation rate of cells in a colorectal crypt, we suppose that the source terms decrease with distance from the base of the crypt as follows:

$$K_i(\mathbf{X}) = k_i\left(1 - \lambda_i \frac{Y}{L}\right), \qquad i = 1, 2. \tag{2.2}$$

Here the positive constant k_i is the maximum rate at which the cells of type i proliferate and the positive constant λ_i describes how the proliferation rate reduces with distance from the crypt base.

We now assume that the two cell types are distinct such that $(\varrho_1,\ \varrho_2) = (1,\ 0)$ where cells of type

1 are present and $(\varrho_1,\ \varrho_2) = (0,\ 1)$ where cells of type 2 occur. Using this assumption along with (2.2), our mass balance equations (2.1a) and (2.1b), then reduce to

$$\nabla \cdot \hat{\mathbf{V}} = k_1\left(1 - \lambda_1 \frac{Y}{L}\right) \qquad \text{if } \varrho_1 = 1,\ \varrho_2 = 0, \tag{2.3a}$$

$$\nabla \cdot \hat{\mathbf{V}} = k_2\left(1 - \lambda_2 \frac{Y}{L}\right) \qquad \text{if } \varrho_1 = 0,\ \varrho_2 = 1. \tag{2.3b}$$

It is necessary only to define one cell velocity, $\hat{\mathbf{V}}$ $(= \hat{\mathbf{V}}_1 = \hat{\mathbf{V}}_2)$, as there is only one cell type present in each region.

The first scenario we consider is where the type-2 cells are placed higher up the crypt than the type-1 cells. The interface between the two cell populations is defined by $Y = C\,(X, T)$. We assume, in all cases, no part of the interface has reached the top or the bottom of the crypt, i.e. $0 < \min\{C(X,T)\}$ and $\max\{C(X,T)\} < L$.

As we have a two-dimensional problem it is necessary to supplement the mass balance law (2.3b) with a constitutive law. In our model, we use Darcy's law to describe how the cells move in response to a pressure gradient as follows,

$$\hat{\mathbf{V}} = \begin{cases} -D_1 \nabla \hat{P} & \text{if} \quad Y < C(X,T), \\ -D_2 \nabla \hat{P} & \text{if} \quad Y > C(X,T), \end{cases} \tag{2.4}$$

where $\hat{\mathbf{V}}$ is the velocity of the cells, $\hat{P}$ is the pressure of the cell layer and D_1, D_2 are Darcy constants describing the sensitivity of the cells' response to pressure gradients. Decreasing the Darcy constants is equivalent to increasing the viscosities of the cells as $D_i = \epsilon/\mu_i$, where ϵ represents the effective permeability of the medium and μ_i is the effective viscosity of the cell layer, for $i = 1, 2$.

Combining (2.4) and (2.3b), the model becomes

$$\nabla^2 \hat{P} = \begin{cases} -\dfrac{k_1}{D_1}\left(1 - \lambda_1 \dfrac{Y}{L}\right) & \text{if} \quad Y < C(X,T), \\ -\dfrac{k_2}{D_2}\left(1 - \lambda_2 \dfrac{Y}{L}\right) & \text{if} \quad Y > C(X,T). \end{cases} \tag{2.5}$$

2.2.1 Boundary and continuity conditions

To close the model, the following boundary conditions are imposed:

$$\frac{\partial \hat{P}}{\partial Y}(X, 0, T) = 0, \tag{2.6}$$

$$\hat{P}\,(X, L, T) = 0, \tag{2.7}$$

$$\hat{P}_X\,(0, Y, T) = \hat{P}_X\,(\pi\beta L, Y, T) = 0. \tag{2.8}$$

Condition (2.6) guarantees no flux of cells at the base of the crypt. We do not have any restrictions on the number of cells that are removed at the top of the crypt; instead we ensure that the cells there are at fixed pressure (taken as $\hat{P} = 0$) (2.7). We assume there are two lines of symmetry in the problem at $x = 0,\ \pi\beta$. This gives the boundary condition (2.8).

On $Y = C\,(X,T)$, the pressure and normal velocity are assumed to be continuous, so that

$$D_1 \frac{\partial \hat{P}}{\partial N}\bigg|^{-} = D_2 \frac{\partial \hat{P}}{\partial N}\bigg|^{+}, \qquad \left[\hat{P}\right]_{-}^{+} = 0, \tag{2.9}$$

where $\dfrac{\partial}{\partial N}$ is the derivative in the direction of the normal to C (shown as $\mathbf{N}\,(X,T)$ in figure 2.1). $|^{-}$ represents approaching the boundary from $Y < C(X,T)$, $|^{+}$ represents approaching the boundary from $Y > C(X,T)$ and $[.]_{-}^{+}$ is the difference in the values from each approach. The interface is assumed to move at the same speed as the normal component of cell velocity on the boundary such that

$$\frac{C_T}{(1+C_X^2)^{\frac{1}{2}}} = \hat{\mathbf{V}}.\mathbf{N}\,\big|_{\,Y=C}. \tag{2.10}$$

Finally, we prescribe the initial position of the moving boundary so that

$$C\,(X,0) = \bar{C}\,(X)\,. \tag{2.11}$$

The model is now complete and is defined by equations (2.4) - (2.11).

2.2.2 Nondimensional model

To reduce the number of parameters in the model, we nondimensionalise the governing equations using

$$\begin{aligned} Y &= Ly, & X &= Lx, & C &= L\chi, \\ \hat{P} &= \frac{k_1 L^2}{D_1}\hat{p}, & \hat{\mathbf{V}} &= k_1 L\hat{\mathbf{v}}, & T &= \frac{1}{k_1}t. \end{aligned} \tag{2.12}$$

This scaling leads us to introduce the following non-dimensional constants

$$k = \frac{k_2}{k_1}, \qquad D = \frac{D_2}{D_1}. \tag{2.13}$$

The parameter k is a ratio of the proliferation rates. For $k < 1$ the cells of type 1 proliferate more rapidly than those of type 2. The parameter D is a ratio of the Darcy constants of the cells. For $D < 1$ the cells of type 1 move faster in response to a given pressure gradient than those of type 2. This may arise if the cells of type 2 are more viscous than those of type 1.

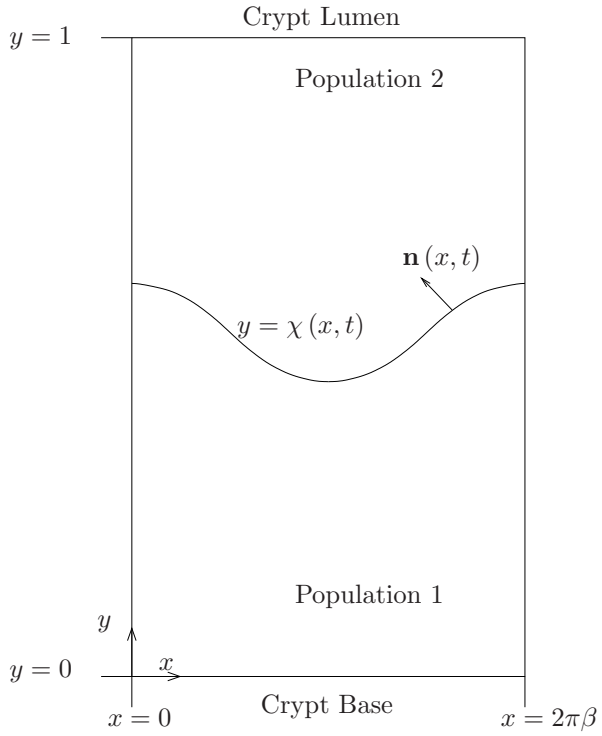

Figure 2.2: Sketch of the non-dimensional 2D model in which two epithelial cell populations [population 1 (bottom) and 2 (top)] grow on the surface of a cylinder. The two cell populations are separated by the boundary $y = \chi(x,t)$, with normal $\mathbf{n}(x,t)$. In Cartesian geometry, y represents the distance from the base of the crypt and x measures the distance around the crypt.

The structure of the nondimensional model is presented in figure 2.2. For $y < \chi(x,t)$ we have

$$\nabla^2 \hat{p} = -(1 - \lambda_1 y), \tag{2.14}$$

$$\hat{\mathbf{v}} = -\nabla \hat{p}, \tag{2.15}$$

and for $y > \chi(x,t)$

$$\nabla^2 \hat{p} = -\frac{k}{D}(1 - \lambda_2 y), \tag{2.16}$$

$$\hat{\mathbf{v}} = -D\nabla \hat{p}, \tag{2.17}$$

with boundary conditions

$$\hat{p}_y(x,0,t) = 0, \tag{2.18}$$

$$\hat{p}(x,1,t) = 0, \tag{2.19}$$

$$\hat{p}_x(0,y,t) = \hat{p}_x(\pi\beta,y,t) = 0. \tag{2.20}$$

The conditions for continuity of the normal velocity and pressure are now

$$\left.\frac{\partial \hat{p}}{\partial n}\right|^{-} = D\left.\frac{\partial \hat{p}}{\partial n}\right|^{+}, \qquad [\hat{p}]^{+}_{-} = 0, \tag{2.21}$$

where $\dfrac{\partial}{\partial n}$ represents the derivative in the direction of the unit normal $\mathbf{n}(x,t)$ to the interface, $y = \chi(x,t)$ (see figure 2.2). The interface between the cell populations, $y = \chi\,(x,t)$, moves according to

$$\frac{\chi_t}{(1+\chi_x^2)^{\frac{1}{2}}} = \hat{\mathbf{v}} \cdot \mathbf{n}\,\big|_{\,y=\chi} \tag{2.22}$$

and is initially given by

$$\chi\,(x,0) = \bar{\chi}(x). \tag{2.23}$$

The non-dimensional model is defined by (2.14) - (2.23). We develop solutions using asymptotic techniques in §2.3 and numerical methods in §2.4.

2.3 Planar interface: linear stability analysis

Our aim is to see how the two cell populations evolve as we vary the model parameters. We start by considering the case of a near-planar interface, for which it is possible to construct approximate analytical solutions. We assume that at leading order the solution depends only on the distance along the crypt axis, y. By contrast the correction terms depend on both x and y. We construct analytical solutions for the leading-order problem in §2.3.1 and then investigate the stability of the planar interface to small perturbations in §2.3.2.

We seek regular power series expansions for the dependent variables in terms of a small parameter, $\varepsilon \ll 1$, such that the moving boundary, pressure and velocity are given by

$$\chi\,(x,t) = \chi_0\,(t) + \varepsilon\chi_1\,(x,t) + \mathrm{O}\left(\varepsilon^2\right), \tag{2.24}$$

$$\hat{p}\,(x,y,t) = p_0\,(y,t) + \varepsilon p_1\,(x,y,t) + \mathrm{O}\left(\varepsilon^2\right), \tag{2.25}$$

$$\hat{\mathbf{v}}\,(x,y,t) = \mathbf{v}_0\,(y,t) + \varepsilon\mathbf{v}_1\,(x,y,t) + \mathrm{O}\left(\varepsilon^2\right). \tag{2.26}$$

We assume that the initial location of the interface between the two populations to be of the form

$$\bar{\chi}\,(x) = \chi_0(0) + \varepsilon\chi_1\,(x,0)\,, \tag{2.27}$$

where $\chi_0(0) = \bar{\chi}_0$ is a constant and $\chi_1(x,0)$ is an O(1) sinusoidal function of x. The amplitude of the initial perturbation 2.27 is ε.

Substituting (2.24) – (2.26), into (2.14) – (2.17) we find

$$\nabla^2\hat{p} = \frac{\partial^2 p_0}{\partial y^2} + \varepsilon\left(\frac{\partial^2 p_1}{\partial x^2} + \frac{\partial^2 p_1}{\partial y^2}\right) + \mathrm{O}\left(\varepsilon^2\right) = \begin{cases} -(1-\lambda_1 y) & \text{if} \quad y < \chi, \\ -\dfrac{k}{D}(1-\lambda_2 y) & \text{if} \quad y > \chi, \end{cases} \tag{2.28}$$

$$\hat{\mathbf{v}} = \begin{cases} -\begin{pmatrix} 0 \\ p_{0y} \end{pmatrix} - \varepsilon \begin{pmatrix} p_{1x} \\ p_{1y} \end{pmatrix} + \mathrm{O}\left(\varepsilon^2\right) & \text{if} \quad y < \chi, \\ -D\begin{pmatrix} 0 \\ p_{0y} \end{pmatrix} - \varepsilon D \begin{pmatrix} p_{1x} \\ p_{1y} \end{pmatrix} + \mathrm{O}\left(\varepsilon^2\right) & \text{if} \quad y > \chi. \end{cases} \tag{2.29}$$

To determine the continuity conditions we note that the unit normal to the boundary is given by

$$\mathbf{n} = \frac{1}{(1+\varepsilon^2\chi_{1x}^2)^{\frac{1}{2}}} \begin{pmatrix} -\varepsilon\chi_{1x} \\ 1 \end{pmatrix}. \tag{2.30}$$

On the interface, $y = \chi(x,t)$,

$$\hat{p}\,\big|_{y=\chi} = p_0\,\big|_{y=\chi_0+\varepsilon\chi_1} + \varepsilon p_1\,\big|_{y=\chi_0+\varepsilon\chi_1} + \cdots = p_0\,\big|_{y=\chi_0} + \varepsilon\chi_1 p_{0y}\,\big|_{y=\chi_0} + \varepsilon p_1\,\big|_{y=\chi_0} + \mathrm{O}\left(\varepsilon^2\right) \tag{2.31}$$

$$\hat{p}_y\,\big|_{y=\chi} = p_{0y}\,\big|_{y=\chi_0} + \varepsilon\chi_1 p_{0yy}\,\big|_{y=\chi_0} + \varepsilon p_{1y}\,\big|_{y=\chi_0} + \mathrm{O}\left(\varepsilon\right) \tag{2.32}$$

Using (2.29) - (2.32) the continuity conditions (2.21) become

$$\begin{aligned} p_{0y}^-(\chi_0,t) + \varepsilon\left(\chi_1 p_{0yy}^-(\chi_0,t) + p_{1y}^-(x,\chi_0,t)\right) &= Dp_{0y}^+(\chi_0,t) \\ &\quad +\varepsilon D\left(\chi_1 p_{0yy}^+(\chi_0,t) + p_{1y}^+(x,\chi_0,t)\right) + \mathrm{O}\left(\varepsilon^2\right), \end{aligned} \tag{2.33}$$

$$\begin{aligned} p_0^-(\chi_0,t) + \varepsilon\left(\chi_1 p_{0y}^-(\chi_0,t) + p_1^-(x,\chi_0,t)\right) &= p_0^+(\chi_0,t) \\ &\quad +\varepsilon\left(\chi_1 p_{0y}^+(\chi_0,t) + p_1^+(x,\chi_0,t)\right) + \mathrm{O}\left(\varepsilon^2\right). \end{aligned} \tag{2.34}$$

Equating coefficients of O(1) we have

$$p_{0y}^-(\chi_0,t) = Dp_{0y}^+(\chi_0,t), \tag{2.35}$$

$$p_0^-(\chi_0,t) = p_0^+(\chi_0,t), \tag{2.36}$$

while at O(ϵ)

$$\chi_1 p_{0yy}^-(\chi_0,t) + p_{1y}^-(x,\chi_0,t) = D\left(\chi_1 p_{0yy}^+(\chi_0,t) + p_{1y}^+(x,\chi_0,t)\right), \tag{2.37}$$

$$\chi_1 p_{0y}^-(\chi_0,t) + p_1^-(x,\chi_0,t) = \chi_1 p_{0y}^+(\chi_0,t) + p_1^+(x,\chi_0,t). \tag{2.38}$$

Combining (2.22), (2.29), (2.30) and (2.32) we deduce that the interface evolves as follows

$$\chi_t = \chi_{0t} + \varepsilon\chi_{1t} + \cdots = \begin{cases} -p^-_{0y}(\chi_0,t) - \varepsilon\left(\chi_1 p^-_{0yy}(\chi_0,t) + p^-_{1y}\big|_{y=\chi_0}\right) + \mathrm{O}\left(\varepsilon^2\right) & \text{if} \quad y=\chi^-, \\ -Dp^+_{0y}(\chi_0,t) - \varepsilon D\left(\chi_1 p^+_{0yy}(\chi_0,t) + p^+_{1y}\big|_{y=\chi_0}\right) + \mathrm{O}\left(\varepsilon^2\right) & \text{if} \quad y=\chi^+. \end{cases} \tag{2.39}$$

so that, consistent with (2.35),

$$\chi_{0t} = -p^-_{0y}(\chi_0,t) = -Dp^+_{0y}(\chi_0,t), \tag{2.40}$$

and, consistent with (2.37),

$$\chi_{1t} = -\left(\chi_1 p^-_{0yy}(\chi_0,t) + p^-_{1y}\big|_{y=\chi_0}\right) = -D\left(\chi_1 p^+_{0yy}(\chi_0,t) + p^+_{1y}\big|_{y=\chi_0}\right). \tag{2.41}$$

2.3.1 Planar solution

From (2.28) - (2.39) we deduce that, at leading order,

$$\frac{\partial^2 p_0}{\partial y^2} = \begin{cases} -(1-\lambda_1 y) & \text{if} \quad 0<y<\chi_0 \\ -\dfrac{k}{D}(1-\lambda_2 y) & \text{if} \quad \chi_0<y<1 \end{cases}, \tag{2.42}$$

with

$$p_{0y}(0,t) = 0, \tag{2.43}$$

$$p_0(1,t) = 0, \tag{2.44}$$

and continuity conditions

$$p_{0y}\big|^-_{y=\chi_0} = D\frac{\partial p_0}{\partial y}\Big|^+_{y=\chi_0}, \qquad [p_0]^+_- = 0, \tag{2.45}$$

where

$$\frac{\mathrm{d}\chi_0}{\mathrm{d}t} = -p_{0y}\big|^-_{y=\chi_0}, \tag{2.46}$$

$$\chi_0(0) = \bar{\chi}_0. \tag{2.47}$$

The solution to (2.42) - (2.47) is

$$p_0 = \begin{cases} \frac{1}{2}\left((\chi_0 + y) - \frac{\lambda_1}{6}\left(\chi_0^2 + \chi_0 y + y^2\right)\right)(\chi_0 - y) + \frac{k}{2D}\left(1 - \chi_0^2 - \frac{\lambda_2}{3}\left(1 - \chi_0^3\right)\right) \\ \qquad -\frac{(1-\chi_0)\chi_0}{D}\left(k - 1 + \frac{\chi_0}{2}(\lambda_2 - \lambda_1)\right) & \text{if} \quad y < \chi_0, \\ \\ \frac{k}{2D}\left(1 + y - \frac{\lambda_2}{3}\left(1 + y + y^2\right)\right)(1 - y) \\ \qquad -\frac{(1-y)\chi_0}{D}\left(k - 1 + \frac{\chi_0}{2}(\lambda_2 - \lambda_1)\right) & \text{if} \quad y > \chi_0, \end{cases} \tag{2.48}$$

where

$$\chi_0(t) = \frac{2\bar{\chi_0}e^t}{2 + \bar{\chi_0}\lambda_1(e^t - 1)}. \tag{2.49}$$

At leading order, height of the interface, $y = \chi_0(t)$, is independent of the k and D. This is because the cell proliferation rate has no dependence on pressure. Further, as there is no flux of cells at the bottom of the crypt ($y = 0$) new cells of type 1 simply push the interface $y = \chi_0(t)$, towards the top of the crypt. This is shown by substituting (2.42) into (2.47),

$$\frac{\mathrm{d}\chi_0}{\mathrm{d}t} = -\frac{\partial p_0}{\partial y}\bigg|^{-}_{y=\chi_0} = \int_0^{\chi_0}(1 - \lambda_1 y)dy = \chi_0(1 - \frac{\lambda_1}{2}\chi_0). \tag{2.50}$$

From equation (2.49) (or (2.50)), the position of the interface tends to a steady state value, $\chi_0(t) \to \frac{2}{\lambda_1}$ as $t \to \infty$, and we deduce that if $\lambda_1 > 2$ the cells of type 1 will never reach the top of the crypt.

Figure 2.3(a) confirms that increasing λ_1 from 0 to 2.5 changes the behaviour of χ_0 from predominantly exponential growth to a situation in which $\chi_0 \to 2/\lambda_1$ at long times. The biological interpretation of these results is that as λ_1 increases and the rate of cell death increases eventually there is net cell death for $y > 1/\lambda_1$, ($\nabla \cdot \mathbf{v} < 0$). This gives three cases: $\lambda_1 < 1$, where there is net cell birth throughout the crypt ($\nabla \cdot \mathbf{v} > 0$ everywhere) where the boundary always increases in speed as it moves up the crypt; $1 < \lambda_1 < 2$, where for, $1 > y > 1/\lambda_1$, there is net cell death and the boundary moves up the crypt, but not always increasing in speed; and $\lambda_1 > 2$ where in over half the crypt there is net cell death and the cells from population 1 never reach the top of the crypt. Figure 2.3(b) shows that the effect of increasing the initial position of the interface, $\bar{\chi}_0$, is similar to moving the starting point further along the $\chi_0(t)$ vs t graph.

2.3.2 O(ε) solution

To investigate the stability of the planar interface, we seek the O(ε) correction terms. From (2.14), (2.16), (2.24) and (2.48) we find that the correction to the cell pressure above and below the interface

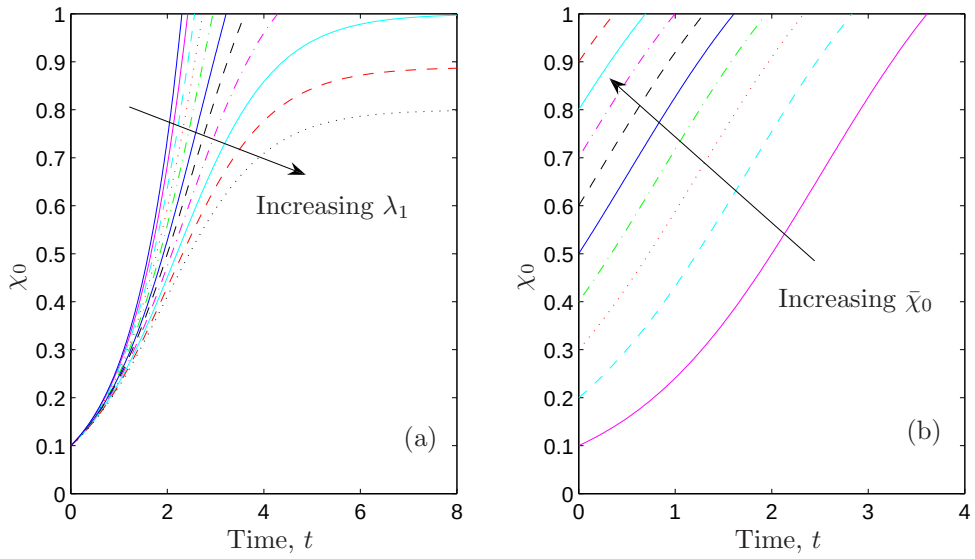

Figure 2.3: Series of plots showing how the time evolution of the leading order part of the boundary $y = \chi_0(t)$ changes as λ_1 varies from 0 to 2.5 (panel (a), $\bar{\chi}_0 = 0.1$) and $\bar{\chi}_0 = \chi_0(t = 0)$ varies from 0.1 to 1.5 (panel (b), $\lambda_1 = 1.5$).

satisfies

$$\frac{\partial^2 p_1}{\partial x^2} + \frac{\partial^2 p_1}{\partial y^2} = 0 \tag{2.51}$$

with

$$p_{1y}(x, 0, t) = 0, \tag{2.52}$$

$$p_1(x, 1, t) = 0, \tag{2.53}$$

$$p_{1x}(0, y, t) = p_{1x}(2\pi\beta, y, t) = 0. \tag{2.54}$$

The continuity equations, (2.21), give

$$[p_1]^+_- = \chi_1 [p_{0y}]^+_- = \frac{\chi_0 \chi_1}{D} \left(1 - \frac{\lambda_1}{2}\chi_0\right)(1 - D) \tag{2.55}$$

and

$$\begin{aligned} D p_{1y}\big|^+_{y=\chi_0} - p_{1y}\big|^-_{y=\chi_0} &= \chi_1 \left(p^-_{0yy}(\chi_0, t) - D p^+_{0yy}(\chi_0, t)\right) \\ &= -\chi_1 \left(1 - \lambda_1\chi_0 - k\left(1 - \lambda_2\chi_0\right)\right). \end{aligned} \tag{2.56}$$

In all equations in the section, all variables with superscript $-$ represent the value of the variable evaluated at $y = \chi_0(x, t)$ approaching the boundary from $y < \chi(x, t)$, and with superscript $+$ represents approaching the boundary from $y > \chi(x, t)$

Using (2.22), we find the evolution of $y = \chi_1(x,t)$ is given by

$$\chi_{1t} = \chi_1(1-\lambda_1\chi_0) - p_{1y}^{-}\big|_{y=\chi_0}. \tag{2.57}$$

Using separation of variables, we express the solutions of (2.51) which satisfy the boundary conditions in the form

$$p_1 = \begin{cases} \sum_{n=1}^{\infty} A_n(t)\,\cos(\omega_n x)\,\cosh(\omega_n y) & \text{if} \quad y < \chi(t), \\ \sum_{n=1}^{\infty} B_n(t)\,\cos(\omega_n x)\,\sinh(\omega_n(1-y)) & \text{if} \quad y > \chi(t), \end{cases} \tag{2.58}$$

$$\chi_1(x,t) = \sum_{n=1}^{\infty} \Upsilon_n(t)\,\cos(\omega_n x), \tag{2.59}$$

where the coefficients $A_n(t), B_n(t)$ are found by imposing (2.55) and (2.56). To guarantee periodicity on $x = 0, 2\pi\beta$, we require $\omega_n = n/\beta$, where n is an integer.

Imposing continuity conditions (2.55) and (2.56), we find

$$B_n = \frac{1}{\sinh(\omega_n(1-\chi_0))}\left[A_n\cosh(\omega_n\chi_0) + \Upsilon_n\chi_0\left(1-\frac{1}{D}\right)\left(1-\frac{\lambda_1}{2}\chi_0\right)\right], \tag{2.60}$$

$$A_n = \frac{\Upsilon_n\left[((1-\lambda_1\chi_0) - k(1-\lambda_2\chi_0))\,\tanh(\omega_n(1-\chi_0)) - \omega_n(1-D)\left(\chi_0 - \frac{\lambda_1}{2}\chi_0^2\right)\right]}{\omega_n\left[D\cosh(\omega_n\chi_0) + \tanh(\omega_n(1-\chi_0))\sinh(\omega_n\chi_0)\right]}. \tag{2.61}$$

Finally, substitution of A_n into (2.57), yields the following ODE for Υ_n:

$$\begin{aligned} \frac{1}{\Upsilon_n}\frac{\mathrm{d}\Upsilon_n}{\mathrm{d}t} = \quad & (1-\lambda_1\chi_0) - \\ & \frac{((1-\lambda_1\chi_0) - k(1-\lambda_2\chi_0))\,\tanh(\omega_n(1-\chi_0)) - \omega_n(1-D)\left(\chi_0 - \frac{\lambda_1}{2}\chi_0^2\right)}{D + \tanh(\omega_n(1-\chi_0))\tanh(\omega_n\chi_0)}\tanh(\omega_n\chi_0), \end{aligned} \tag{2.62}$$

where $\chi_0(t)$ is as defined in (2.49).

As $\beta \ll 1$, we would expect ω_n to be large. For large ω_n, $\tanh(\omega_n\chi_0) \approx 1$ and $\tanh(\omega_n(1-\chi_0)) \approx 1$ apart from when $\chi_0 \approx 0$ and $\chi_0 \approx 1$. So for $\omega_n \gg 1$, provided that $\epsilon < \chi_0 < 1-\epsilon$, for some ϵ satisfying $0 < \epsilon \ll 1$, (2.62) simplifies to give

$$\frac{1}{\Upsilon_n}\frac{\mathrm{d}\Upsilon_n}{\mathrm{d}t} = -\omega_n\frac{D-1}{D+1}\chi_0\left(1-\frac{\lambda_1}{2}\chi_0\right). \tag{2.63}$$

As $\omega_n \gg 1$, and assuming that $\lambda_1 < 2$, so that there is no O(1) steady state solution within the crypt, $\chi_0\left(1-\frac{\lambda_1}{2}\chi_0\right) > 0$, and the main determinant for whether Υ_n will increase or decrease in (2.63) is the value of D relative to unity. When $D > 1$ (cells of type 1 are less viscous than cells of type 2) any short wavelength ($\omega_n \gg 1$) disturbances remain small: the shorter the wavelength

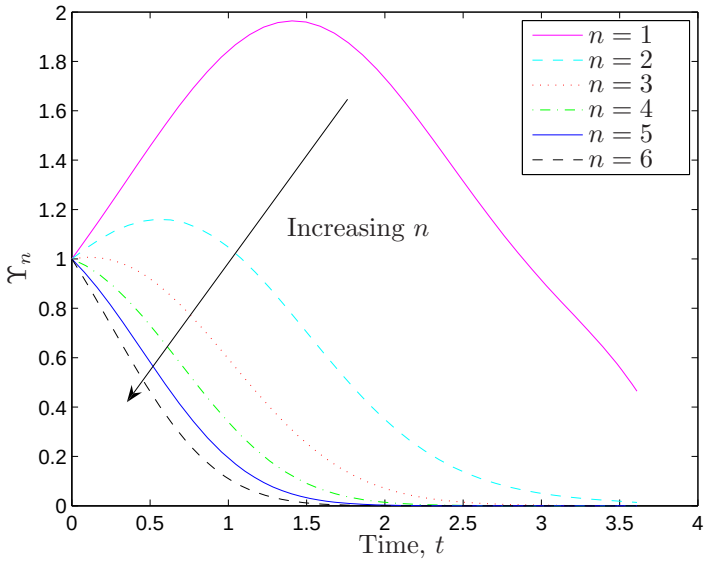

Figure 2.4: Series of plots showing the time evolution of Υ_n, the O(ε) corrections to the moving boundary for mode number, n. The amplitude remains small when $D = 2$ (the cells of population 1 are twice as viscous as cells from population 2) but still exhibits transient growth for $n = 1, 2$. Parameter values: $k = 2$, $\lambda_1 = 1.5$, $\lambda_2 = 0$, $\beta = 0.083$ with $\Upsilon_n(0) = 1$ and $\chi_0(0) = 0.1$.

the faster the disturbances decrease. However if the cells of type 2 (in the upper region) are more viscous (i.e. $D < 1$) then short wavelength disturbances become large very quickly: the shorter the wavelength, the faster the disturbances increase.

To illustrate this behaviour, we solve (2.62) numerically and use the solution for Υ_n together with (2.59), (2.23) and (2.49) to see how the boundary $y = \chi(x, t)$ evolves with time (see figures 2.4 - 2.7). In simulations, the cells at the bottom of the crypt (population 1) are normal cells with a depth-dependent proliferation rate with $\lambda_1 = 1.5$. The cells toward the top of the crypt, population 2, are mutant, with a proliferation rate independent of the Wnt gradient ($\lambda_2 = 0,\ k = 2$). The initial conditions are set to be $\chi_0(0) = 0.1, \Upsilon_n(0) = 1$ for each value of n, $n = 1, 2, ..6$, with $\beta = 1/12$ [7]. These initial conditions are chosen so that the behaviour can be studied before any part of the boundary passes over the top of the crypt. The behaviour is investigated for different values of D and n, and the results are presented in figure 2.4.

Our analytical results for large ω_n, (2.63), are consistent with the plots presented in figures 2.4 - 2.7. Figures 2.4 and 2.6 show that when cells of type 1 than cells of type 2 (towards the bottom of the crypt) are more viscous (i.e. $D = 2$) the amplitude of the disturbances remains small (and decays as

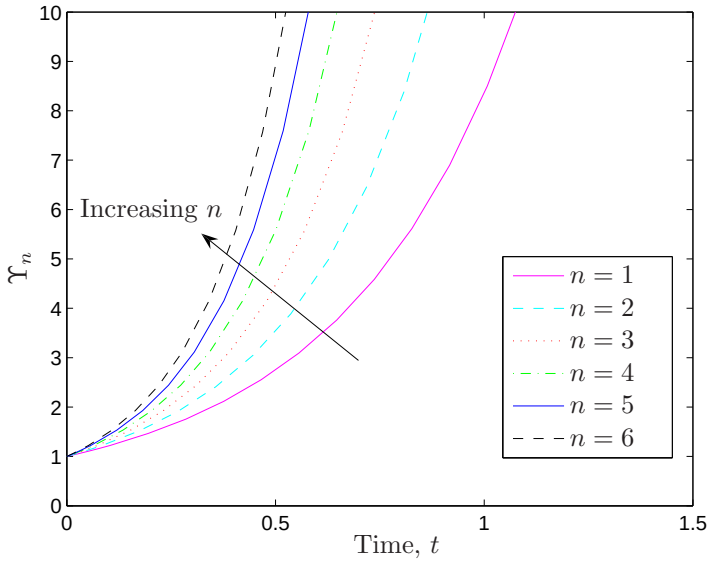

Figure 2.5: Series of plots showing how the time evolution of the amplitude, Υ_n, varies with mode number, n. The plots show that the amplitude increases rapidly when the type 2 cells are more viscous than those of type 1 ($D = 0.5$). Parameter values: $D = 0.5$, $k = 2$, $\lambda_1 = 1.5$, $\lambda_2 = 0$, $\beta = 0.083$ with initial conditions of $\Upsilon_n(0) = 1$ and $\chi_0(0) = 0.1$.

$t \to \infty$). As the mode number, n, increases, the perturbations decay more rapidly, although there is transient growth for small wavenumbers (figure 2.4). By contrast, when the cells of type 2 (toward the top of the crypt) are more viscous than cells of type 1 (i.e. $D = 0.5$) the $\mathrm{O}(\varepsilon)$ disturbances (see figures 2.5 and 2.7) increase in amplitude and the expansion rapidly breaks down (as the $\mathrm{O}(\varepsilon)$ disturbances can no longer be assumed to be small). Figures 2.5 and 2.7 also show that the growth rate of the modes is an increasing function of n, the mode number.

2.4 Planar interface: collocation

We have shown that the analytical approximation may cease to be valid at long times. In order to determine the system dynamics for this case we must construct numerical solutions. We use a collocation method to do this. Collocation methods for solving a PDE involve decomposing the solution into a sum of basis functions which, by construction, satisfy all but one of the boundary conditions [184]. At each timestep, the coefficients of the basis functions are determined such that the remaining boundary condition is met.

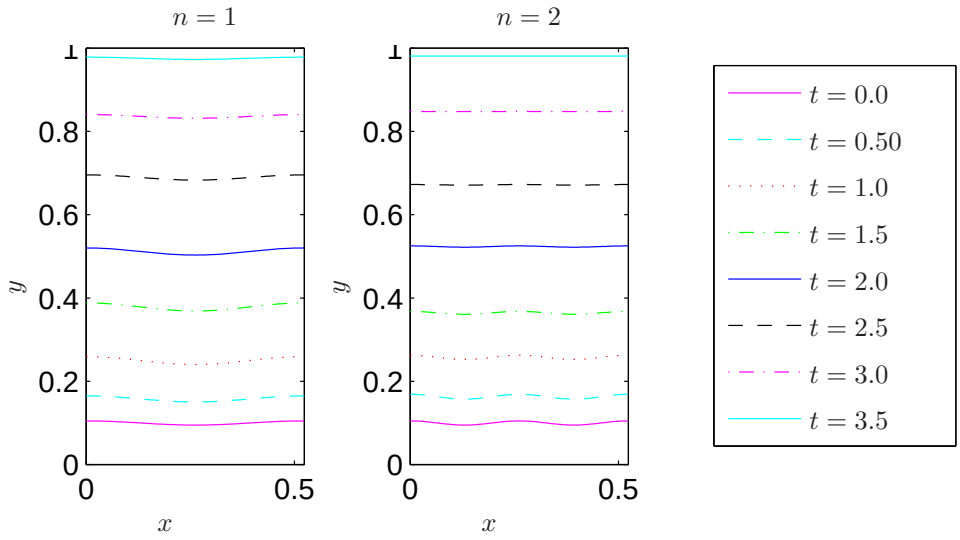

Figure 2.6: Series of plots showing how the boundary between the two populations evolves over time when the population 2 cells are less viscous than the population 1 cells ($D = 2$). As time increases, the interface $y = \chi(x,t)$ moves up the crypt and the amplitude of the $\mathrm{O}(\epsilon)$ perturbations to the $\mathrm{O}(1)$ planar solution decay. Parameter values: $k = 2$, $\lambda_1 = 1.5$, $\lambda_2 = 0$, $\beta = 0.083$ and an initial conditions of $\bar{\chi}_0 = 0.1$, $\Upsilon_n(0) = 1$ for the relevant value of n and $\Upsilon_n(0) = 0$ for all other values of n.

2.4.1 Numerical method

In this section, we describe the collocation method used to solve equations (2.15) - (2.23). First, it is convenient to decompose the pressure in each region in the following way

$$\hat{p}(x,y,t) = \bar{p}\,(y,t) + p\,(x,y,t) \tag{2.64}$$

where

$$\bar{p} = \begin{cases} \dfrac{1-y^2}{2} - \dfrac{\lambda_1}{6}\left(1-y^3\right) & \text{if} \quad 0 < y < \chi(t), \\ \dfrac{k}{2D}\left(1 - y^2 - \dfrac{\lambda_2}{3}\left(1-y^3\right)\right) & \text{if} \quad \chi(t) < y < 1. \end{cases} \tag{2.65}$$

In contrast to §2.3, the x-dependent part of the pressure, $p\,(x,y,t)$ is no longer assumed to be small. The new problem for $p(x,y,t)$ is

$$\nabla^2 p \quad = \quad 0, \tag{2.66}$$

$$p_x(0,y,t) = p_x(\pi\beta,y,t) \quad = \quad p_y(x,0,t) = p(x,1,t) = 0. \tag{2.67}$$

The appropriate continuity conditions at $y = \chi(x,t)$ are found by substituting (2.64) and (2.65) into

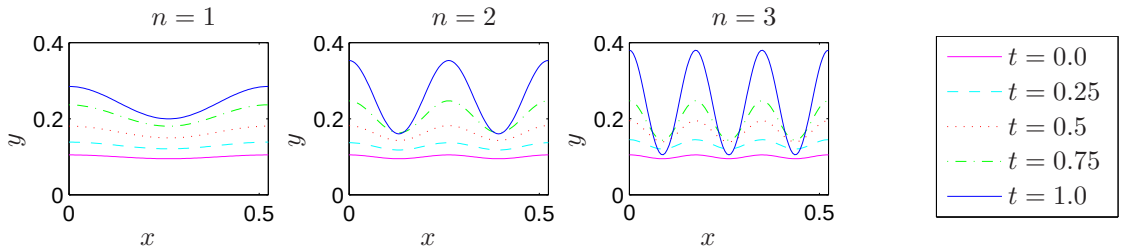

Figure 2.7: Series of plots showing how the boundary between the two populations evolves over time when the population 2 cells are more viscous than the population 1 cells ($D = 0.5$). As time increases, the interface $y = \chi(x,t)$ moves up the crypt and the amplitude of the O(ϵ) perturbations to the O(1) planar solution increase in size. Parameter values: $k = 2$, $\lambda_1 = 1.5$, $\lambda_2 = 0$, $\beta = 0.083$ and an initial conditions of $\bar{\chi}_0 = 0.1$, $\Upsilon_n(0) = 1$ for the relevant value of n and $\Upsilon_n(0) = 0$ for all other values of n.

(2.21):

$$0 = p^+\big|_{y=\chi^+} - p^-\big|_{y=\chi^-} = \left(1 - \frac{k}{D}\right)\frac{(1-\chi^2)}{2} - \left(\lambda_1 - \frac{k}{D}\lambda_2\right)\left(\frac{1-\chi^3}{6}\right), \quad (2.68)$$

$$0 = D\frac{\partial p^+}{\partial n}\bigg|_{y=\chi^+} - \frac{\partial p^-}{\partial n}\bigg|_{y=\chi^-} = \frac{1}{(1+\chi_x^2)^{\frac{1}{2}}}\left[(k-1)\,\chi - (k\lambda_2 - \lambda_1)\,\frac{\chi^2}{2}\right]. \quad (2.69)$$

The problem for p is defined by equations (2.66) - (2.69) and is valid while $0 < \min\{\chi\} \leq \max\{\chi\} < 1$.

To implement the collocation method, basis functions are needed that satisfy the boundary conditions, (2.67). For cells in population 1, in the lower part of the crypt, we demand that the boundary conditions (2.67) on $x = 0$, $x = 2\pi\beta$ and $y = 0$ are satisfied. For cells in population 2, in the upper part of the crypt, we require the boundary conditions on $x = 0$, $x = 2\pi\beta$ and $y = 1$ to be met. The separable solutions for p that satisfy these boundary conditions are of the form

$$p = \begin{cases} A_0(t) + \sum_{n=1}^{\infty} A_n(t)\cosh(\omega_n y)\cos(\omega_n x) & \text{if} \quad y < \chi, \\ B_0(t)\,(y-1) + \sum_{n=1}^{\infty} B_n(t)\,\sinh(\omega_n\,(1-y))\cos(\omega_n x) & \text{if} \quad y > \chi, \end{cases} \quad (2.70)$$

where $\omega_n = \dfrac{n}{\beta}$, $n = 1, 2, \cdots$. To determine the coefficients $A_i(t), B_i(t)$ $(i = 0, 1, 2, \cdots)$ at each time step, we implement (2.68) and (2.69) at collocation points located along the moving interface $y = \chi(x,t)$. The collocation points are spaced evenly in the x-direction between $x = 0$ and $x = \beta\pi$ (taking advantage of the symmetry). At each collocation point, j, with coordinates (x_j, χ_j), where $\chi_j = \chi(x_j, t)$, we demand

$$B_0(t)\left(\chi_j-1\right)+\sum_{n=1}^{N}B_n(t)\sinh\left(\omega_n\left(1-\chi_j\right)\right)\cos\left(\omega_n x_j\right)$$
$$-A_0(t)-\sum_{n=1}^{N}A_n(t)\cosh\left(\omega_n\chi_j\right)\cos\left(\omega_n x_j\right)=\left(1-\frac{k}{D}\right)\frac{\left(1-\chi_j^2\right)}{2}-\left(\lambda_1-\frac{k}{D}\lambda_2\right)\left(\frac{1-\chi_j^3}{6}\right) \tag{2.71}$$

and

$$\begin{aligned}DB_0(t)+D\sum_{n=1}^{N}B_n(t)\omega_n\Bigg[&\frac{\partial\chi_j}{\partial x}\sinh\left(\omega_n\left(1-\chi_j\right)\right)\sin\left(\omega_n x_j\right)\\&-\cosh\left(\omega_n\left(1-\chi_j\right)\right)\cos\left(\omega_n x_j\right)\Bigg]\\-\sum_{n=1}^{N}A_n(t)\Bigg(&\frac{\partial\chi_j}{\partial x}\cosh\left(\omega_n\chi_j\right)\sin\left(\omega_n x_j\right)+\sinh\left(\omega_n\chi_j\right)\cos\left(\omega_n x_j\right)\Bigg)\\&=\left(k-1\right)\chi_j-\left(k\lambda_2-\lambda_1\right)\frac{\chi_j^2}{2},\end{aligned} \tag{2.72}$$

where $\dfrac{\partial\chi_j}{\partial x}$ is evaluated by a central finite difference method.

For a well-defined problem, the total number of collocation points, J, must be such that $J\geq N+1$, where N is the number of modes.

Equations (2.71) and (2.72), constitute a linear problem of the form $\mathbf{QA}=\mathbf{b}$, where $\mathbf{A}$ is a vector of length $(2N+2)$ containing the unknowns $A_0(t),A_1(t),\cdots A_N(t)$, $B_0(t),B_1(t),\cdots B_N(t)$, $\mathbf{Q}$ is a matrix of size $2J\times(2N+2)$ containing the coefficients for the unknowns at the respective collocation points from the left-hand sides of (2.71) and (2.72) and $\mathbf{b}$ is a vector of length $2J$ containing the right-hand sides of (2.71) and (2.72) evaluated at the collocation points. In our simulations we set $J=N+1$, as this allows us to solve for $\mathbf{A}$ with $\mathbf{A}=\mathbf{Q}^{-1}\mathbf{b}$ [106], provided that $\mathbf{Q}^{-1}$ can be determined (i.e. $\mathbf{Q}$ is non-singular).

To ensure that the coefficients are similar in magnitude, for ease of computation, we scale them as follows:

$$A_n(t)=\frac{\bar{A_n}(t)}{\cosh(\omega_n\alpha(t))},\qquad B_n(t)=\frac{\bar{B_n}(t)}{\sinh\left(\omega_n\left(1-\alpha(t)\right)\right)}, \tag{2.73}$$

where $\alpha(t)=(\chi_{max}(t)+\chi_{min}(t))/2$.

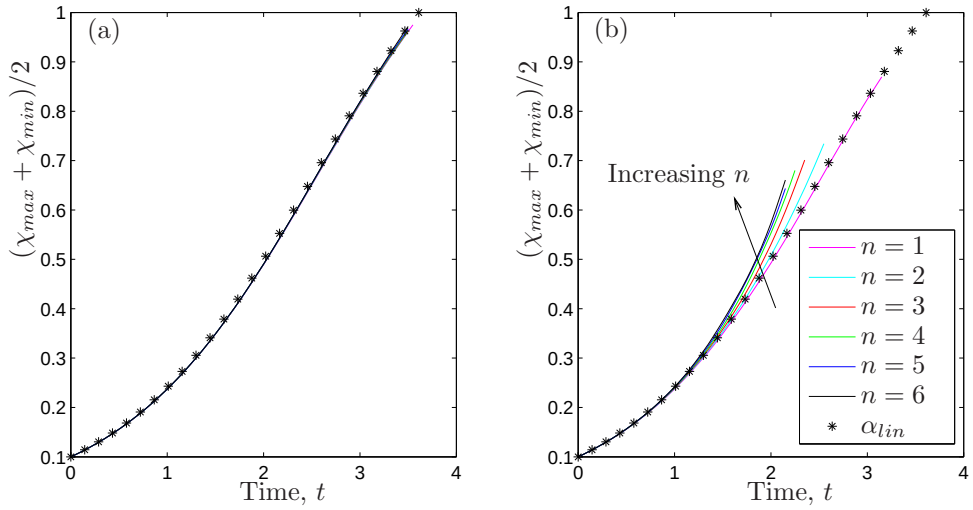

Figure 2.8: Series of plots comparing the collocation method (lines) and the analytic method (2.62)(* symbols) for the midpoint of the moving boundary between the populations of the cells, $(\chi_{max} + \chi_{min})/2$. χ_{max}, χ_{min} represent the maximum and minimum values at any x of $\chi(x,t)$ for each time value. The plots show how the behaviour varies for different mode numbers, n, of the initial conditions, $\chi_0 = 0.1 + 0.005\cos(nx/\beta)$. Parameter values: $k = 2$, $\lambda_1 = 1.5$, $\lambda_2 = 0$ and $\beta = 1$. In (a) $D = 2$ and in (b) $D = 0.5$.

2.4.2 Validation

When the collocation method was implemented, it soon became apparent that it is unsuitable when a realistic crypt geometry is used. In particular when $\beta = 1/12$, there are very large (order-of-magnitude) disparities in the entries in the matrix, $\mathbf{Q}$, making it computationally difficult to invert accurately.

Although our collocation method was not very accurate for $\beta = 1/12$, it was possible to generate results for wider crypts, with $\beta = 1$. Our results for this case agree well with the analytical results calculated in §2.3 (see figures 2.8 and 2.9).

We also verified that our collocation method was stable, by varying the number of collocation points used and checking there was no change in the results, see figure 2.10.

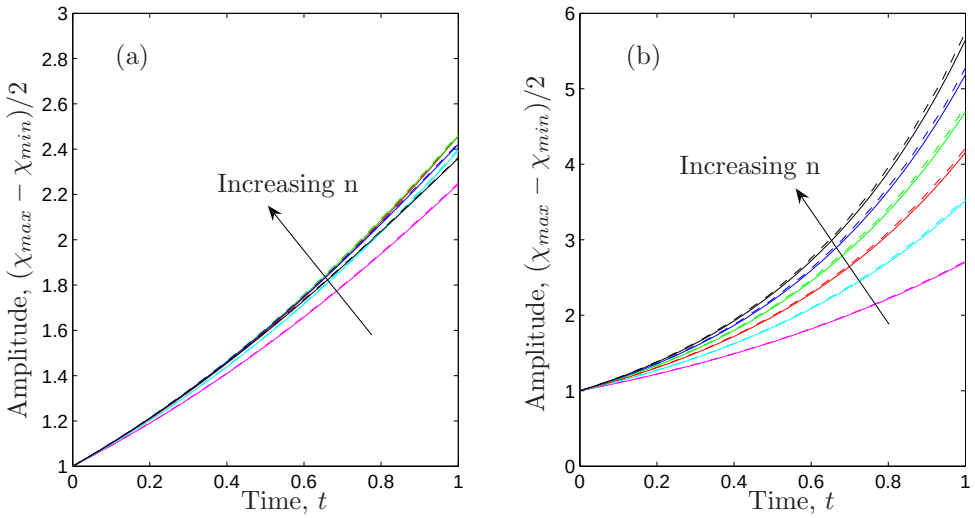

Figure 2.9: Further plots validating the collocation method, showing the evolution of the amplitude of the moving boundary that separates the two cell populations. For the collocation method $(\chi_{max} - \chi_{min})/2$ is plotted (solid lines) and for the asymptotic approximations, the O(ε) part of the boundary, $\Upsilon(t)$, (as calculated analytically in §2.3.2) is plotted (dashed lines). The plots show how the behaviour varies for different mode numbers, n, of the initial conditions, $\chi_0 = 0.1 + 0.005\cos(nx/\beta)$. Parameter values: $k = 2$, $\lambda_1 = 1.5$, $\lambda_2 = 0$ and $\beta = 1$. In (a) $D = 2$ and in (b) $D = 0.5$.

2.4.3 Results

Even though the crypt width, $\beta = 1$, is unphysiological, the 2D nonlinear collocation method yields useful insight into the dynamics of the interface separating the two populations of cells. Figure 2.11 shows that when the cells in the lower region are twice as viscous as cells in the upper region ($D = 2$) the results are qualitatively similar to the analytic results for a physiological crypt ($\beta = 1/12$) with the boundary between the two types of cells having little variation with azimuthal position. When $D = 0.5$, so that the cells in the upper region are twice as viscous as cells in the lower region, the interface loses its smooth sinusoidal form as it moves up the crypt (figure 2.12). The peaks of the boundary become much sharper than the troughs and the boundary appears to be U-shaped, showing signs of Hele-Shaw fingering [72, 78, 101, 150].

We also observe that if the viscosity of the cells in the upper region is sufficiently large, some of the type-2 cells move downward toward the base of the crypt (see figure 2.13). This could explain how top-down invasion may occur.

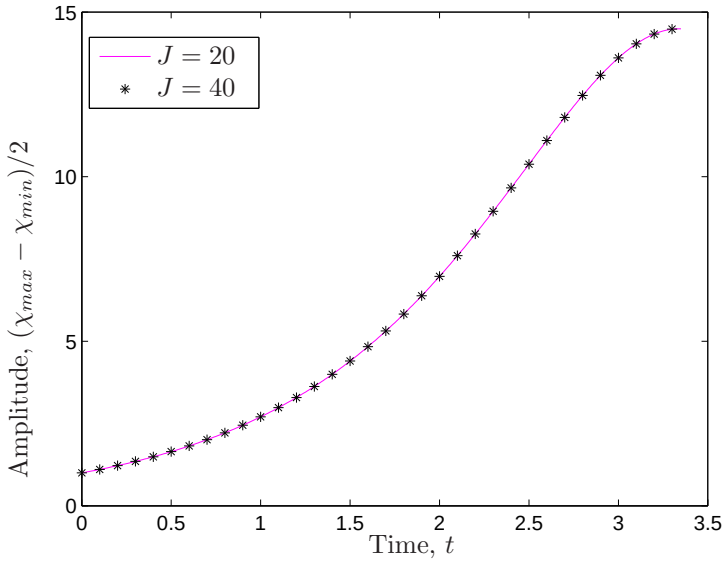

Figure 2.10: Plot of the amplitude of the moving boundary between the populations of the cells, $(\chi_{max} - \chi_{min})/2$, as the boundary moves up the crypt with time, t. The plots show how doubling the number of collocation points, J, from $J = 20$ to $J = 40$ produces the same results. Initial conditions, $\chi_0 = 0.1 + 0.005\cos(x/\beta)$. Parameter values: $k = 2$, $D = 0.5$, $\lambda_1 = 1.5$, $\lambda_2 = 0$ and $\beta = 1$. The collocation method is resolved up to the 10th mode in (2.67).

Using figure 2.14 we can explain the behaviour of the cells. When $D > 1$ (and the cells of type 2 are less viscous than those of type 1), cell movement is predominantly in the y-direction and the boundary $y = \chi(x,t)$ remains almost planar. However, when the cells in region 2 are more viscous than the normal cells, $D < 1$, the velocity is not always predominantly in the y-direction. At the base of the crypt (near $x = \pi\beta$), the pressure builds up due to the mutant cells offering more resistance to movement than when $D > 1$, see figure 2.15. This causes the normal cells to move azimuthally to places where there is less resistance to movement, i.e. regions where there are fewer mutant cells, $x = 0, 2\pi\beta$ (the peaks of $y = \chi(x,t)$). The boundary $y = \chi(x,t)$ develops large peaks or fingers at regions which offer less resistance to movement, i.e. where $\chi(x,t)$ is maximumal.

2.5 Patch of cells

To replicate the early stages of carcinogenesis, we now consider a mutant population initially in a circular patch on a wall, as shown in figure 2.16. This allows us to investigate how the behaviour of

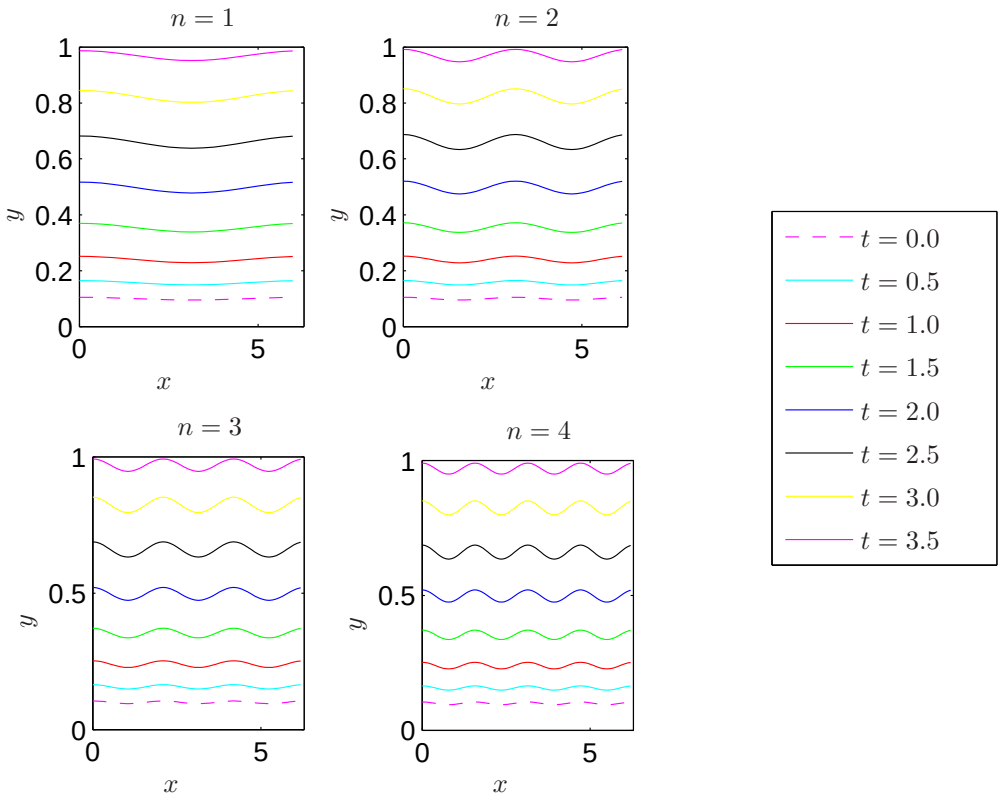

Figure 2.11: Series of plots showing how the evolution of the interface $y = \chi(x,t)$ depends on which spatially-periodic modes are excited. Each plot shows the perturbed interface between the normal cells (bottom) and the less viscous mutant cells (top) moving up the crypt in time, t, with the perturbations remaining small. Initial conditions, $\chi_0 = 0.1 + 0.005\cos(nx/\beta)$. Parameter values: $D = 2$, $k = 2$, $\lambda_1 = 1.5$, $\lambda_2 = 0$ and $\beta = 1$.

a mutant cell population can be affected by changing the initial position of the mutant cells.

2.5.1 Method

The model is constructed in the following way. The normal cells initially occupy most of the crypt surface, whereas the mutant cells are localised within the patch which occupies the region $x^2 + (y - a_0)^2 \leq b_0^2$, where $a_0,\ b_0$ are constants.

There are two lines of symmetry in the model, at $x = \pm\pi\beta$ and at $x = 0$. We ensure that solutions retain these symmetries by imposing the following boundary conditions

$$\hat{p}_x\left(0, y, t\right) = \hat{p}_x\left(\pi\beta, y, t\right) = 0, \tag{2.74}$$

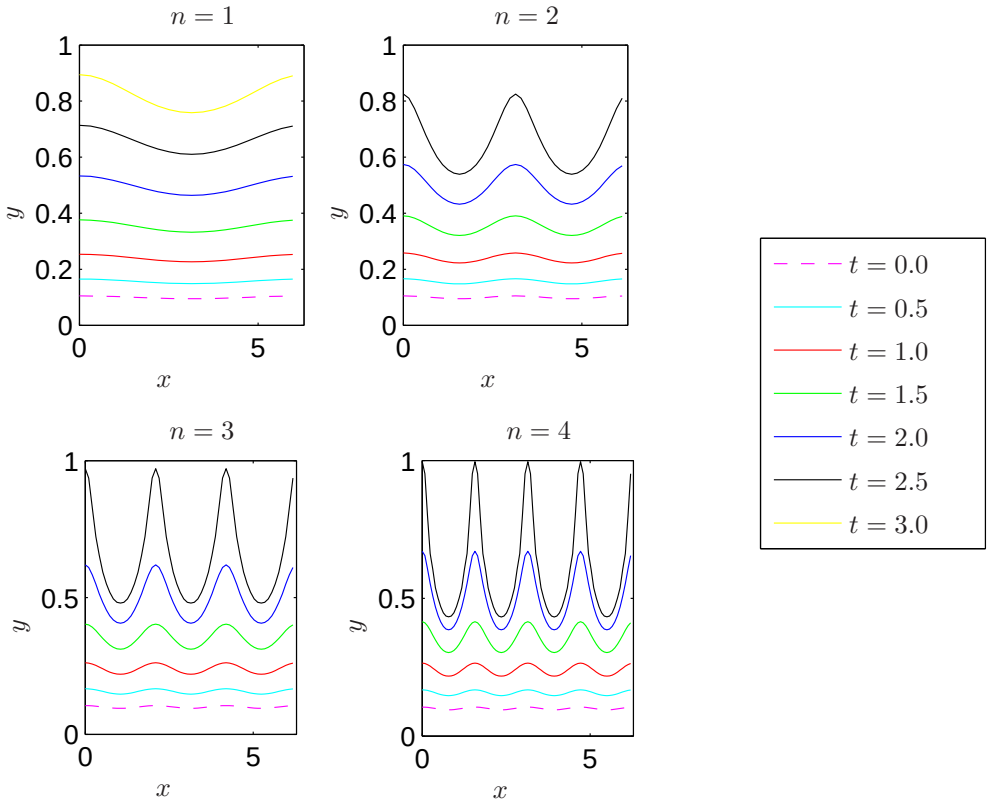

Figure 2.12: Series of plots showing how the evolution of the interface $y = \chi(x,t)$ changes depending on which spatially-periodic modes are excited. Each plot shows the perturbed interface between the normal cells (bottom) and the more viscous mutant cells (top) moving up the crypt in time, t, where the perturbations increase rapidly. Initial conditions, $\chi_0 = 0.1 + 0.005\cos(nx/\beta)$. Parameter values: $D = 0.5$, $k = 2$, $\lambda_1 = 1.5$, $\lambda_2 = 0$ and $\beta = 1$.

and solve only in half the domain, $0 \leq x \leq \pi\beta$.

We apply a transformation of coordinates to the type 2 cells based on a moving point in the centre of the patch, $y = a(t)$. The new coordinate system (r,θ) is given by

$$r(t) = (x^2 + (y - a(t))^2)^{1/2}, \tag{2.75}$$

$$\theta(t) = \tan^{-1}\left(\frac{x}{y - a(t)}\right), \qquad 0 \geq \theta < 2\pi. \tag{2.76}$$

We define the moving interface separating the two cell populations to be

$$\Gamma(r,\theta,t) = \gamma(\theta,t) - r(t) = 0 \tag{2.77}$$

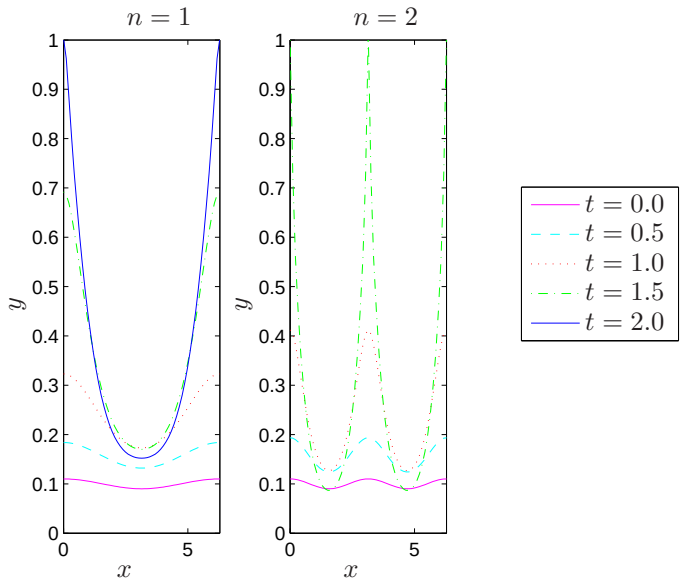

Figure 2.13: Series of plots showing showing how the boundary $y = \chi(x,t)$ changes over time and how this evolution depends on which spatial modes are being excited. The simulations suggest that if the type 2 cells are 10 times more viscous than the type 1 cells then at long times they may migrate downwards, towards the crypt base. The plots have initial conditions of $\chi_0 = 0.1 + 0.005\cos(nx/\beta)$, where $n = 1$ (left) and $n = 2$ (right). Parameter values: $D = 0.1$, $k = 3$, $\lambda_1 = 1.5$, $\lambda_2 = 0$ and $\beta = 1$.

where initially

$$\gamma(\theta, 0) = b. \tag{2.78}$$

The point, $y = a(t)$, moves up the crypt such that

$$\gamma(0,t) = \gamma(\pi,t). \tag{2.79}$$

Equivalently, the speed with which $y = a(t)$ moves vertically up the crypt is given by the average of the speeds of the points at the top and bottom of the patch,

$$\frac{da}{dt} = \frac{1}{2}\left(\mathbf{v}(\gamma(0,t),0,t) + \mathbf{v}(\gamma(\pi,t),\pi,t)\right)\cdot\hat{\mathbf{y}} \tag{2.80}$$

On the interface between the two cell populations (2.77) must hold for all time, so

$$\frac{D\Gamma}{Dt} = 0. \tag{2.81}$$

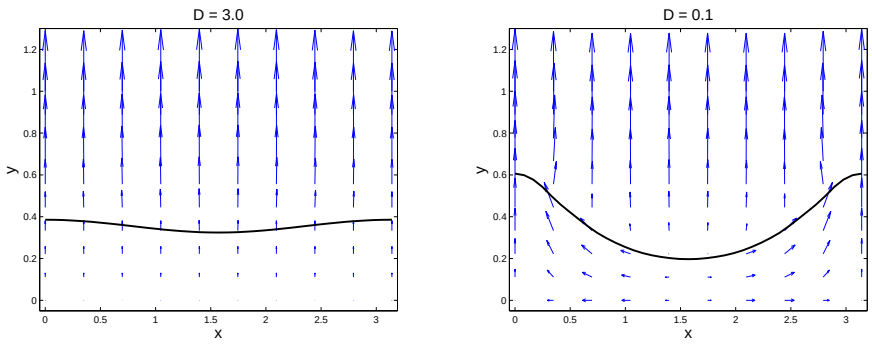

Figure 2.14: Quiver plots showing how the local velocity varies with position and for two different values of the relative viscosity, D. The results on the left correspond to a case for which $D = 3.0$, i.e. the cells of population 1 (bottom) are three times more viscous than cells of population 2 (top), allowing for predominantly vertical cell movement. The results on the right correspond to a case for which $D = 0.1$, i.e. the cells of population 2 (top) are ten times more viscous as cells of population 1 (bottom) leading to lateral and vertical movement of cells. The directions of the arrows represent the local movement of the cells and the size of the arrows represents their local speed. Parameter values: $k = 2.0$, $\chi(x,0) = 0.1 + 0.01\cos(x/2)$, $\lambda_1 = 1.5$, $\lambda_2 = 0$, $\beta = 1/2$.

Using (2.81) the boundary moves according to

$$\left(\frac{\partial}{\partial t} + \mathbf{u}\cdot\nabla\right)\left(r\left(t\right) - \gamma\left(\theta(t),t\right)\right) = 0 \tag{2.82}$$

$$\frac{\partial r}{\partial t} + \mathbf{u}\cdot\hat{\mathbf{r}} = \frac{\partial \gamma}{\partial t} + \frac{\partial \gamma}{\partial \theta}\frac{\partial \theta}{\partial t} + \frac{1}{\gamma}\frac{\partial \gamma}{\partial \theta}\mathbf{u}\cdot\hat{\boldsymbol{\theta}}, \tag{2.83}$$

where

$$\frac{\partial r}{\partial t} = \frac{y - a(t)}{r}\frac{da}{dt} = \cos\theta\frac{da}{dt}, \tag{2.84}$$

$$\frac{\partial \theta}{\partial t} = -\frac{x}{r^2}\frac{da}{dt} = -\frac{1}{r}\sin\theta\frac{da}{dt}. \tag{2.85}$$

As the reference point for the coordinate system, $y = a(t)$, is time-dependent, the boundary $r(t) = \gamma(\theta(t), t)$ evolves in the following way:

$$\frac{\partial \gamma}{\partial t} = \mathbf{u}\cdot\hat{\mathbf{r}} - \frac{1}{\gamma}\frac{\partial \gamma}{\partial \theta}\mathbf{u}\cdot\hat{\boldsymbol{\theta}} - \frac{\partial a}{\partial t}\left(\cos\theta - \frac{1}{\gamma}\frac{\partial \gamma}{\partial \theta}\sin\theta\right). \tag{2.86}$$

The new model consists of (2.14) and (2.15) for $\Gamma < 0$ and (2.16) and (2.17) for $\Gamma > 0$, boundary conditions (2.18), (2.19), and (2.74), initial condition (2.78) and continuity conditions (2.21) which

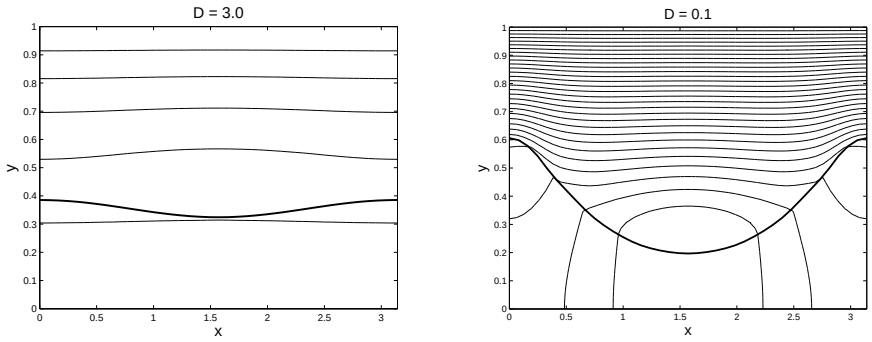

Figure 2.15: Plots showing contours of the pressure throughout the crypt, with high pressure at the crypt base and zero pressure at the top of the crypt for the same cases as the quiver plots in figure 2.14. The thick line represents $y = \chi(x,t)$, the boundary between the two cell populations. When cells of population 2 are less viscous than cells of population 1, ($D = 3.0$), pressure shows little variation with x. However, when cells of population 2 are more viscous than cells of population 1, ($D = 0.1$), pressure builds up where the viscous cells are furthest down the crypt, $y = \pi/2$, leading to cells in population 1 moving azimuthally (see figure 2.14). Parameter values as per figure 2.14. The contours are placed every 0.05 (left) and 0.20 (right) units of pressure, with $\hat{p} = 0$ at $y = 1$ and and reaching a maximum of $\hat{p} = 0.25$ at $(x,y) = (\pi/2, 0)$ in (left) and a maximum of $\hat{p} = 5.8$ at $(x,y) = (\pi/2, 0.25)$ in (right).

hold on $\Gamma(r,\theta,t) = 0$. We complete the model with equation (2.86) which describes the movement of the interface separating the two types of cells.

The unit normal, $\mathbf{n}$, that is used in the continuity conditions, (2.21), is given (in polar coordinates) by

$$\mathbf{n} = \left(1 + \frac{\gamma_\theta^2}{\gamma^2}\right)^{-1/2} \left(\hat{\mathbf{r}} - \frac{\gamma_\theta}{\gamma}\hat{\boldsymbol{\theta}}\right). \tag{2.87}$$

For simplicity we reduce (2.14) and (2.16) to homogeneous equations. We decompose the pressure into two parts: a solution that does not change with time, $\bar{p}$; and a solution to the homogeneous problem that changes with time, p. For cells in region 1, $\Gamma < 0$ (marked normal cells in figure 2.16),

$$\hat{p}\,(x,y,t) = \bar{p}\,(y) + p\,(x,y,t)\,, \tag{2.88}$$

$$\bar{p}\,(y) = \frac{1-y^2}{2} - \frac{\lambda_1}{6}\left(1-y^3\right). \tag{2.89}$$

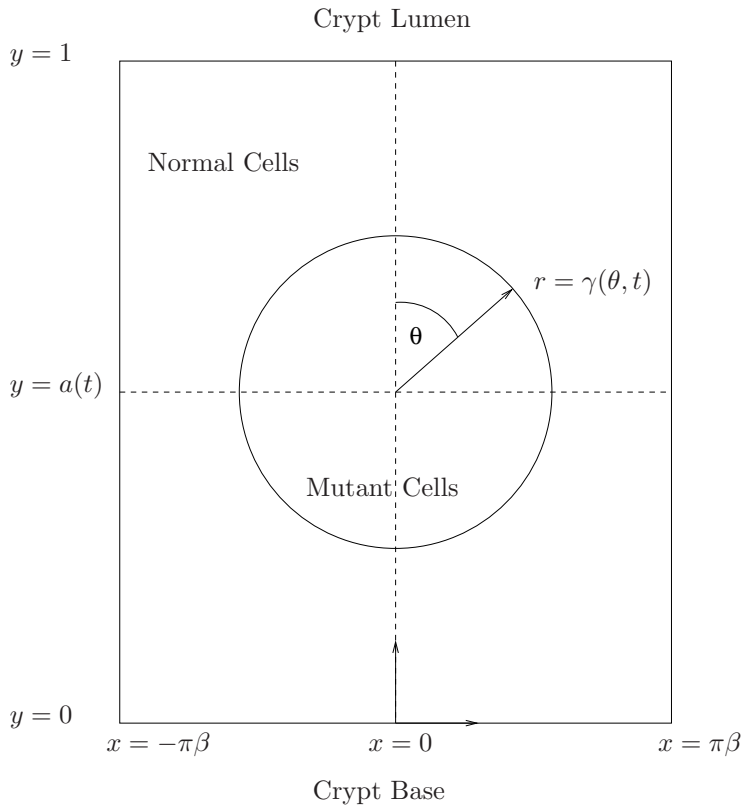

Figure 2.16: Sketch of the two dimensional model for two cell populations, population 1 - normal cells (initially covering the majority of the crypt), population 2 - mutant cells(initially in the circle $x^2 + (y - a_0)^2 \leq b^2$) growing on the surface of a crypt modelled as a cylinder.

For cells in region 2, $\Gamma > 0$ (marked mutant cells in figure 2.16),

$$\hat{p}\,(r, \theta, t) = \bar{p}\,(r, \theta) + p\,(r, \theta, t)\,, \tag{2.90}$$

$$\bar{p}\,(r, \theta) = -\frac{k}{2D}\,(a + r\cos\theta)^2 \left(1 - \frac{\lambda_2}{3}\,(a + r\cos\theta)\right). \tag{2.91}$$

Equations (2.14) and (2.16) can now be rewritten, for both $\Gamma < 0$ and $\Gamma > 0$, as

$$\nabla^2 p = 0. \tag{2.92}$$

In order to solve (2.92) we again use a collocation method. For cells in region 1, boundary conditions (2.18), (2.19) and (2.74) require that

$$p_y\,(x, 0, t) = p\,(x, 1, t) = p_x\,(\pi\beta, y, t) = 0. \tag{2.93}$$

Hence, for population 1, we choose basis functions of the form

$$p(x,y,t) = \sum_{n=1}^{N} A_n \cos\left(\omega_n y\right)\left(\cosh\left(\omega_n x\right) - \tanh\left(\omega_n \pi \beta\right)\sinh\left(\omega_n x\right)\right), \tag{2.94}$$

where $\omega_n = \left(n - \frac{1}{2}\right)\pi$. For population 2, boundary conditions (2.74) demand

$$p_\theta\left(r,0,t\right) = p_\theta\left(r,\pi,t\right) = 0. \tag{2.95}$$

We also assume that the pressure is continuous, so

$$p\left(r,0,t\right) = p\left(r,\pi,t\right), \quad \text{as } r \to 0. \tag{2.96}$$

Hence, for population 2, we assume the following decomposition for $p(r,\theta,t)$:

$$p(r,\theta,t) = B_0 + \sum_{m=1}^{N-1} B_m (B_f)^m r^m \cos\left(m\theta\right), \tag{2.97}$$

where $B_f = 1/\max\left\{\gamma\left(\theta,t\right)\right\}$. To find the coefficients, $A_1, A_2, \cdots A_N, B_0, B_1, \cdots B_{N-1}$, collocation points are distributed along the boundary in the following way: for $\Gamma \leq 0$ to satisfy the boundary condition $p_x(0,y,t) = 0$ we distribute points along $x = 0$; and to satisfy the continuity conditions, (2.21), we distribute points along $\Gamma = 0$. The boundary condition along $x = 0$ (points marked by (O) and ($\bigtriangleup$) in figure 2.17) is implemented in the following way,

$$\sum_{n=1}^{N} A_n \omega_n \cos\left(\omega_n y\right)\tanh\left(\omega_n \pi \beta\right) = 0. \tag{2.98}$$

On the interface $\Gamma = 0$ (points marked by ($\times$) in figure 2.17), continuity of pressure demands that

$$\begin{aligned}\sum_{n=1}^{N} A_n \cos\left(\omega_n\left(a + \gamma\cos\theta\right)\right)\Big(\cosh\left(\omega_n \gamma \sin\theta\right) - \tanh\left(\omega_n \pi \beta\right)\sinh\left(\omega_n \gamma \sin\theta\right)\Big) \\ - \left(B_0 + \sum_{m=1}^{N-1} B_m B_f^m \gamma^m \cos\left(m\theta\right)\right) = -\left(\frac{1 - \left(a + \gamma\cos\theta\right)^2}{2} - \frac{\lambda_1}{6}\left(1 - \left(a + \gamma\cos\theta\right)^3\right)\right) \\ - \frac{k}{2D}\left(a + \gamma\cos\theta\right)^2\left(1 - \frac{\lambda_2}{3}\left(a + \gamma\cos\theta\right)\right)\end{aligned} \tag{2.99}$$

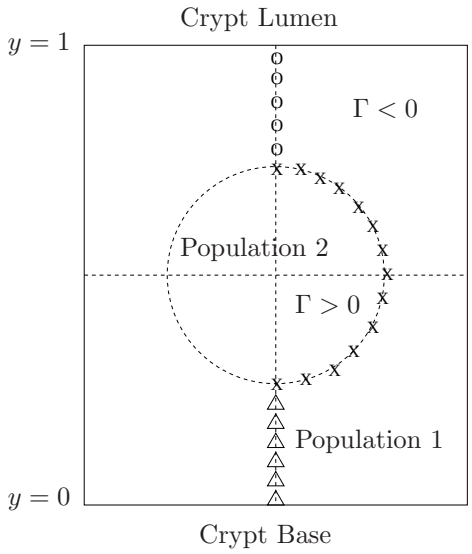

Figure 2.17: Sketch of the placements of the collocation points for two cell populations on the crypt wall. (X) marks collocation points where (2.99) and (2.100) need to be satisfied and at (O) and ($\bigtriangleup$) (2.98) needs to be satisfied.

and continuity of normal velocity leads to

$$\begin{aligned}\sum_{n=1}^{N} A_n\omega_n \Bigg[&\left(\sin\theta - \frac{\gamma_\theta}{\gamma}\cos\theta\right)\cos\left(\omega_n\left(a+\gamma\cos\theta\right)\right)\left(\sinh\left(\omega_n\gamma\sin\theta\right) - \tanh\left(\omega_n\pi\beta\right)\cosh\left(\omega_n\gamma\sin\theta\right)\right) \\ &- \left(\cos\theta + \frac{\gamma_\theta}{\gamma}\sin\theta\right)\sin\left(\omega_n\left(a+\gamma\cos\theta\right)\right)\left(\cosh\left(\omega_n\gamma\sin\theta\right) - \tanh\left(\omega_n\pi\beta\right)\sinh\left(\omega_n\gamma\sin\theta\right)\right)\Bigg] \\ &- D\sum_{m=1}^{N-1} B_m m B_f^m \gamma^{m-1}\left(\cos\left(m\theta\right) + \frac{\gamma_\theta}{\gamma}\sin\left(m\theta\right)\right) \\ &= \left(\left(a+\gamma\cos\theta\right)\left(1-k-\frac{\lambda_1 - k\lambda_2}{2}\left(a+\gamma\cos\theta\right)\right)\right)\left(\cos\theta + \frac{\gamma_\theta}{\gamma}\sin\theta\right).\end{aligned} \tag{2.100}$$

Equations (2.98), (2.99) and (2.100) define a system of J_{All} simultaneous equations which can be written in the form

$$\mathbf{QA} = \mathbf{b}, \text{ where } \mathbf{A} = (A_1, A_2, \cdots A_N, B_0, B_1, \cdots B_{N-1})^T \tag{2.101}$$

$$\begin{bmatrix} Q_{11} & Q_{12} & .. & .. & Q_{12N} \\ Q_{21} & Q_{22} & .. & .. & Q_{22N} \\ .. & .. & .. & .. & .. \\ .. & .. & .. & .. & .. \\ Q_{J_{All}1} & Q_{J_{All}2} & .. & .. & Q_{J_{All}2N} \end{bmatrix} \begin{bmatrix} A_1 \\ A_2 \\ .. \\ A_N \\ B_0 \\ B_1 \\ .. \\ B_{N-1} \end{bmatrix} = \begin{bmatrix} b_1 \\ b_2 \\ .. \\ .. \\ b_{J_{All}} \end{bmatrix} \tag{2.102}$$

where $\mathbf{b}$ is a vector of length $J_{All} = J_{Top} + 2J_{MI} + J_{Bottom}$ containing the right-hand sides of equations (2.98), (2.99) and (2.100), for the corresponding collocation points, and $\mathbf{Q}$ is a matrix of size $J_{All} \times 2N$ containing the coefficients of the unknowns at the respective collocation points found through the left-hand sides of equations (2.98), (2.99) and (2.100).

J_{Top} is the number of collocation points on $x = 0$ where $y \geq a(t) + \gamma(0, t)$ (points marked by (O) in figure 2.17), J_{Bottom} is the number of collocation points on $x = 0$ where $y \leq a(t) + \gamma(\pi, t)$ (points marked by ($\bigtriangleup$) in figure 2.17) and J_{MI} is the number of collocation points on the moving interface defined by $\Gamma = 0$ (points marked by (X) in figure 2.17).

If $\mathbf{Q}$ is a square matrix then the coefficients, $\mathbf{A}$, can be found by inverting $\mathbf{Q}$: $\mathbf{A} = \mathbf{Q^{-1}b}$. However, for a square matrix, if we have a large number of collocation points, it is necessary to solve for very short wavelengths, as $\omega_n \to 0$ when $n \gg 1$. However small wavelengths give rise to very small entries in the matrix $\mathbf{Q}$ making it computationally difficult to invert. To overcome this problem, we introduce additional collocation points, so our system, (2.101), is overspecified, $J_{All} > 2N$.

In order to solve (2.101), we initially used the method of least squares, minimising the sum of the squares of the residuals, $\| R \|^2 = \sum_1^{J_{All}} (\mathbf{b} - \mathbf{QA})^2$, in the L_2 norm. We found the optimum solution to be [106]

$$\mathbf{A}_{optimum} = \left(\mathbf{Q}^T\mathbf{Q}\right)^{-1}\mathbf{Q}^T\mathbf{b}. \tag{2.103}$$

Although easy to implement, the method of least squares is not an accurate method of interpolation as it is sensitive to wild points or outliers [179]. Instead we used the L_1 norm and minimised the absolute total of the residuals, $\| R \|_1 = \sum_1^{J_{All}} | \mathbf{b} - \mathbf{QA} |$, by implementing a minimum searcher [180]. At each time step we found $\mathbf{Q}$ and $\mathbf{b}$ and used (2.103) to calculate a starting value of $\mathbf{A}$, we then use MatLab's "norm" and "fminsearch" to minimise the L_1 norm. We used the resulting coefficients to advect the collocation points. If the distance from $y = 0$ to the moving interface,

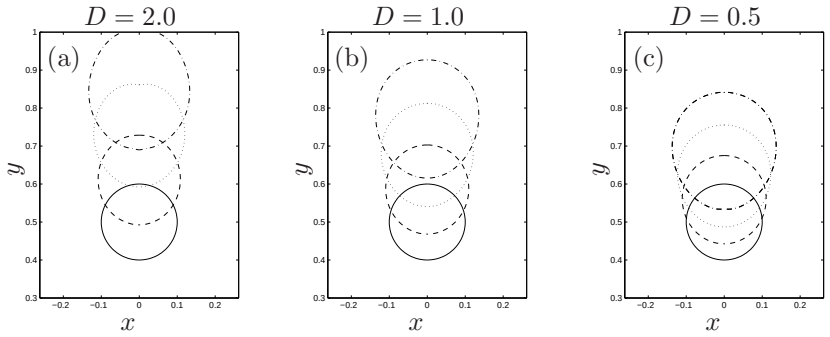

Figure 2.18: Series of plots showing how an initially circular patch of mutant cells spreads within a crypt and how the pattern of invasion varies as their relative viscosity changes. Lines plotted at times $t = 0$ (solid line), $t = 0.25$ (dashed line), $t = 0.50$ (dotted line), $t = 0.75$ (dot-dash line). Parameter values: $k = 1.0$, $a_0 = 0.5$, $b = 0.1$, $\lambda_1 = 1.5$, $\lambda_2 = 0$, $\beta = 0.083$.

the total length of the moving interface or the distance from the top of the mutant patch to $y = 1$ increased (or decreased) by more than certain tolerances we increased (or decreased) the number of collocation points in that region.

2.5.2 Validation

We checked the validity of our numerical method by simulating a simple test case for which the growth rates of both cell types is equal and independent of position with parameters $k = 1$, $\lambda_1 = \lambda_2 = 0$. For this case the growth is purely in the y-direction and is exponential. This means that the interface between the two sets of cells will be

$$\begin{pmatrix} x \\ y \end{pmatrix} = \begin{pmatrix} b_0 \sin\theta \\ (a_0 + b_0 \cos\theta) e^t \end{pmatrix}. \tag{2.104}$$

We also checked that the mass (proportional to area covered) of the cells in region 2 increased at the correct rate and that the maximum residual ($\max\{\mathbf{b} - \mathbf{QA}\}$) was always less than 0.001.

2.5.3 Results

We treat the cells in region 2 as being mutant, so they proliferate at a constant rate throughout the crypt ($\lambda_2 = 0$). Figure 2.18 shows that when the relative viscosity of the mutant cells is increased (so that D is reduced), the cells move up the crypt more slowly. This is because the viscous cells are more

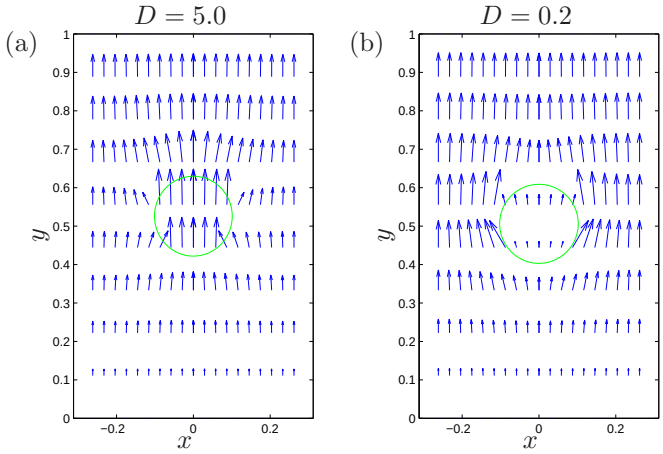

Figure 2.19: Plots showing how the local velocity varies with position for two different values of D. The directions of the arrows represent the local movement of the cells and the size of the arrows represents their local speed. For the plot on the left hand side, the cells in the patch are less viscous than the surrounding (normal) cells. The normal cells move towards the patch forcing it up the crypt. For the plot on the right hand side, the cells in the patch are more viscous than the surrounding (normal) cells. The normal cells move around the patch. Parameter values: $k = 1.0$, $a_0 = 0.5$, $b = 0.1$, $\lambda_1 = 1.5$, $\lambda_2 = 0$, $\beta = 0.083$, $t = 0.05$.

resistant to movement and less sensitive to the pressure gradient generated by cell proliferation. We illustrate this in more detail in figures 2.19 and 2.20, where the local velocities and pressure gradients are presented.

When the normal cells are more viscous than the mutant cells ($D = 5.0$), the latter move more rapidly than the surrounding normal cells (see figure 2.19(a)). As the mutant cells move down the pressure gradient, they relieve the pressure at the base of the mutant patch and cause pressure to build up in the cells above (see figure 2.20(a)). This has two effects: normal cells migrate preferentially to the lower pressure area below the patch and away from the area of higher pressure above the patch.

When the normal cells are much less viscous than the mutant cells ($D = 0.2$), the mutant cells move more slowly than the surrounding normal cells. In this case, the mutant patch can be viewed as an obstacle to the flow of normal cells (see figure 2.19(b)). The normal cells find it more difficult to displace the mutant cells, causing pressure to build at the base of the patch (see figure 2.20(b)). The pressure is lower at the top of the patch because the mutant cells move more slowly than the normal cells (similar to a slipstream effect behind a large object). As a result, the normal cells move around the patch.

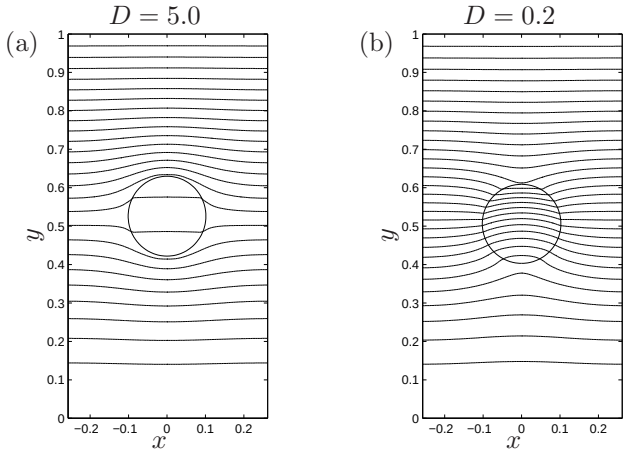

Figure 2.20: Plots showing contours of the pressure throughout the crypt, with high pressure at the crypt base and zero pressure at the top of the crypt for the same cases as the quiver plots in figure 2.19. With less viscous cells in the patch, (left), forces transfer more readily through the patch than through the other cells in the crypt leading to a lower pressure just below the patch. With more viscous cells in the patch, (right), forces transfer less easily through the patch than through the other cells in the crypt, leading to a higher pressure just below the patch. Parameter values as per figure 2.19. The contours are placed every 0.01 units of pressure, with $\hat{p} = 0$ at $y = 1$ and $\hat{p}$ in (left) and $\hat{p} = 0.3$ in (right) at $y = 0$.

If the relative viscosity of the mutant cells is sufficiently large, then cells at the bottom of the patch may move towards the crypt base (see figure 2.21). As the viscosity of the mutant cells in the patch is increased, their pressure also increases (as in figure 2.20). Mutant cells near the boundary of the patch require a larger pressure gradient to move away from the centre and make space for the new cells created due to proliferation. When the pressure exceeds that of the normal cells just below them, the mutant cells start to move towards the base of the crypt. An example of this is shown in figure 2.21. The simulation in figure 2.21 was terminated before the mutant cells could take over the crypt, as once the boundary separating the two populations reaches one of the boundaries, our numerical method breaks down.

Figure 2.22 shows how the starting position of the mutant patch affects its ability to spread downwards for a range of value of a_0, the initial centre of the patch in the vertical direction. We calculate the largest value of the relative viscosity (D^*) for which the mutant cells move downwards towards the base of the crypt. This is done by running the simulation until $t = 0.5$ for several values of D ($D = 1.1$ in steps of 0.001 until 0.001). The simulations were then checked to find the maximum

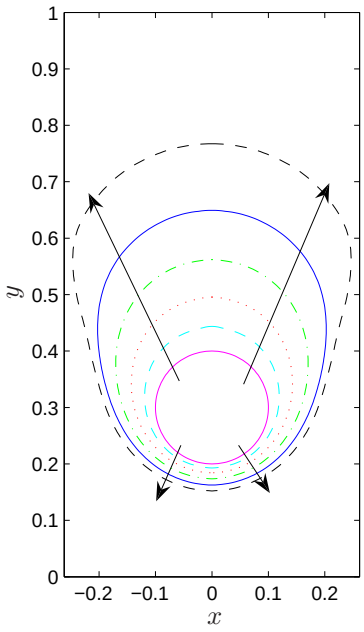

Figure 2.21: Plot showing how mutant cells, if sufficiently viscous, can invade downwards toward the crypt base. The arrows reveal how the boundary separating mutant cells (initially within a circle) and normal cells moves with time, with lines representing time increasing from $t = 0$ to $t = 1.0$ in steps of $t = 0.2$. Parameter values: $D = 0.1$, $k = 1.0$, $a_0 = 0.3$, $b = 0.1$, $\lambda_1 = 1.5$, $\lambda_2 = 0$, $\beta = 0.083$.

value of D, for which the bottom of the patch moved downwards. It was verified that for all $D < D^*$, the base of the mutant patch also moved downwards.

If the centre of the mutant patch is initially close to the bottom of the crypt ($a = 0.15$), then the mutant cells need only be four times more viscous than the normal cells ($D^* = 0.25$) to move downwards. However, when the patch is initially further up the crypt ($a = 0.6$), the mutant cells need to be at least ten times more viscous than the normal cells ($D^* < 0.10$) to move downwards.

Figure 2.22 shows that, more generally, the maximum value of D^* for which the mutant population could move downwards decreases as the starting height of the mutant patch increases. However once the bottom of the mutant patch passes the point where there is net cell death, $y = 1/\lambda_1$, the value of D necessary for downward movement increases with distance from the base of the crypt because the normal cells move more slowly (see figure 2.19). If $\lambda_1 < 1$, we find that the necessary value of D^* decreases monotically with a_0.

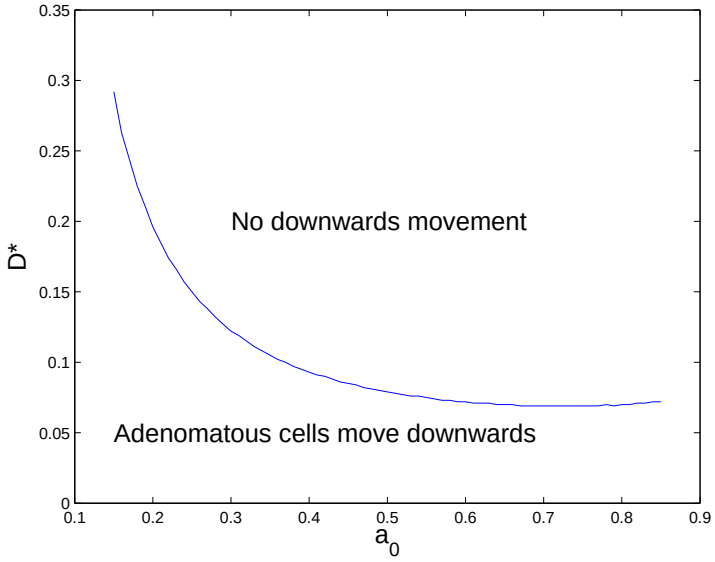

Figure 2.22: Plot of how D^* the minimum necessary value of D, the relative viscosities, needed for downwards movement of the cells at the base of the mutant patch varies with starting position of the centre of the mutant patch, a_0. It is shown if the patch is initially further up the crypt, the cells in the patch must be much more viscous to move downwards, than cells near the bottom of the crypt. Parameter values: $k = 1.0$, $b = 0.1$, $\lambda_1 = 1.5$, $\lambda_2 = 0$, $\beta = 0.083$.

2.6 Discussion

We have developed a continuum model that describes the proliferation and movement of cells in a crypt. We considered two cell populations which differ in their proliferation rates and viscosities. The model includes a spatially varying source term to account for Wnt-dependent growth; following Greenspan [64] and Franks [56], Darcy's law is used to model cell motion. Model solutions were constructed using a combination of asymptotic and numerical collocation methods. First, we studied cases for which the mutant cells were initially located toward the top of the crypt (and the normal cells at the bottom). Second, we studied cases for which a small circular mass of mutant cells was introduced into a healthy crypt. In both cases, mutant cells proliferated at a rate independent of the Wnt stimulus and had a different viscosity to normal cells.

Asymptotic solutions showed that when normal cells were placed below less viscous mutant cells, small disturbances to the interface between the cell populations remained small as the interface moved up the crypt. As a result of this, the mutant cells were flushed out of the crypt. However if the normal cells were less viscous than the mutant cells, as biological evidence suggests [141],

perturbations to the interface rapidly increased in magnitude as the interface moved up the crypt. In this case the asymptotic expansion broke down after a short period of time, due to the perturbations becoming large very rapidly.

It was not possible to simulate the case when the mutant cells were placed above the normal cells for crypts with a realistic geometry; the small aspect ratio makes it difficult to solve the model computationally. However when our method was implemented for a crypt with a larger aspect ratio, we found that some of the mutant cells invaded downwards toward the base of the crypt if their relative viscosity was sufficiently large. We must treat these results with caution as changing the crypt radius changed other variables, such as the coefficients in the collocation method.

Other results reveal that, when the mutant cells were less viscous than the normal cells, they moved out of the crypt faster than the normal cells (and conversely).

When used to simulate the dynamics of a circular patch of mutant cells introduced into a healthy crypt, the model predicted that mutant cells in a patch initially near the bottom of the crypt did not need to be as viscous to establish themselves within the crypt as cells initially further up the crypt.

Experimental results in [15, 115, 141] indicate that mutant cells, by losing their Wnt dependency, also have increased levels of cell adhesion [15] and a more rigid cytoskeleton [115]. They may also have lower levels of migration than normal cells due to a more rigid cytoskeleton and higher levels of adhesion [141]. Our model is consistent with these findings if the mutant cells have increased relative viscosity. Indeed, guided by our model simulations we predict that mutant cells that have increased levels of adhesion and a more rigid cytoskeleton, modelled by increased viscosity, could undergo top-down invasion and move more slowly than their normal counterparts.

We note that the above results are not incompatible with bottom-up morphogenesis. If a cell at the bottom of the crypt undergoes a mutation that renders it and its progeny insensitive to Wnt, then our model simulations suggest that the mutated cells would persist in the crypt and become the dominant population unless they had a lower viscosity (or lower levels of cell adhesion and a much more less rigid cytoskeleton) than normal cells.

One of the main strengths of our model is that we are able to describe biological phenomena with relatively few parameters. However there are some weaknesses. Our model makes no distinction between the rigidity of the cytoskeleton, cell-cell bonds (cadherins) and the cell-substrate bonds (integrins): these phenomena are combined in a single lumped parameter. It would be interesting to see, by modelling the effects separately, which of these has the greatest effect on whether mutant

cells can undergo top-down invasion. This could be addressed by developing a new continuum model (such as that by Armstrong *et al.* [11]) or by developing a cell-level model where each effect is modelled separately. Another weakness is that the proliferation rate term may not be accurate. We do not know whether there is net cell death at the top of the crypt or whether there is a sharp transition between where the cells proliferate and where they do not. This could be addressed by developing a cell-level model and embedding a protein-dependent cell-cycle model within each cell. This could then be compared to the continuum model to derive the correct source term. Also we have assumed that the crypt is symmetric about the crypt wall: this does not allow for a mutant patch to move as a whole azimuthally. Another weakness may be that there are not enough cells within the colorectal crypt for a continuum model to be a valid approximation. We could check this by comparing the model to a cell-level model. We aim to address some of the weaknesses in Chapters 3 and 4, where two cell-level models are developed.

In spite of its weaknesses, it may be of interest to extend our model to investigate the effects of other biological phenomena. Examples include: having a surface tension force around the mutant patch to model higher bonding between mutant cells; using a different constitutive law (for example Stokes' Law); and modelling the effects of cell removal at the top of the crypt more accurately. Including surface tension effects at the normal/ mutant interface would be straightforward to implement and has been done in similar models [44]. Using a different constitutive law has been done in similar continuum models before [79]. Implementing a more complex boundary condition for cell removal at the top of the crypt could greatly increase the complexity of the model and would not be simple to determine for a continuum model. It may also be interesting to model a crypt with flexible walls. The model could be combined with work done by Edwards and Chapman [52], who investigated buckling of the colorectal crypt, in order to investigate investigate crypt fission.

In summary, the main conclusions of this chapter are that for cells to perform top-down invasion they would need a more rigid cytoskeleton and higher levels of cell-cell and cell-substrate adhesion. The further up the crypt a cell suffers a mutation, the more rigid the cytoskeleton and the stronger the levels of cell adhesion the cell would need to be for top-down invasion to occur.

Chapter 3

Cell-centre model of the colorectal crypt

3.1 Introduction

In the previous chapter we described how a continuum model may be used to study the proliferation and migration of cells within a colorectal crypt. The model is useful for describing certain aspects of the physiology of the crypt but there are weaknesses that need to be addressed. One of the main problems with the continuum model is that we cannot easily include information about how individual cells behave [123], such as details of the cell-cycle. In our continuum model all normal cells were of the same type, even though it is known that cells change type as they move up the crypt, from transit to differentiated cells [103]. It is also unclear whether there are enough cells within the crypt to justify modelling it as a continuum. Further, the suitability of applying a Darcy constitutive law to epithelial cells has not been established.

Possible resolutions of these problems include using a model with a different constitutive law, such as Stokes Law [79, 97], using a multi-phase model framework [89] or developing a solid-mechanics model using linear [77, 138] or non-linear elasticity [136]. While such approaches may address problems associated with using Darcy's law, they do not address the other difficulties.

As an alternative to developing another continuum model, in this chapter we use a cell-based model, and in particular, a cell-centre model, based on the work of Meineke *et al.* [109]. Cell-centre models are dynamic lattice-free models in which each cell is represented by a point at its centre and a Voronoi tessellation is used to define the cell's shape [29]. By distinguishing between individual cells we can ascribe specific properties to each cell (eg. proliferation rates and adhesion properties) and incorporate sub-cellular features, such as cell-cycle models. This allows us to study colorectal cancer on several scales, for example protein-level and cell-level, and forms the basis of a multiscale model of colorectal cancer. Another advantage of the cell-centre model is that cell birth can be modelled in

greater detail than in continuum models, as we can track individual cells and their lineages. Being able to view individual cells, we hope, will be more informative to biologists, since with a cell-centre model, one is able to track a specific cell and its progeny.

A benefit of using a lattice-free cell-centre model is that, unlike lattice-based models of the crypt such as that presented in [94], cells can be represented as realistic polygonal shapes that change smoothly rather than remaining as rectangles [29]. Also cell division only affects local connections. By contrast, in [94], a lattice-based model, the cells are represented by rectangles that move in vertical columns, no lateral movement, such that proliferation results in numerous bonds being broken and reformed to accommodate new daughter cells.

3.1.1 Outline

In this chapter we adapt a cell-centre model which describes the proliferation and movement of epithelial cells within a colorectal crypt. This forms the basis of our multiscale model of colorectal cancer. The chapter is structured in the following way. In §3.2, Meineke's original cell-centre model is introduced. In §3.3, the changes we have made to the model are described. In §3.4 we discuss the programming styles used to solve the governing equations numerically. Results from the simulations are presented in §3.5 and their implications are discussed in §3.6 together with suggestions for further work.

3.2 The cell-centre model

In this section we introduce Meineke *et al.*'s cell-centre model [109]. Each cell is characterised by the position and velocity of its centre (see figure 3.1). A Delaunay triangulation [176] is performed to determine each cell's neighbours. Connections between neighbouring cells are modelled by linear springs, which simulate cell-cell adhesion forces (by pulling cells together) and intracellular forces designed to preserve a cell's shape (by forcing tightly-packed cells apart). The forces from the springs are assumed to be balanced by a viscous drag term, proportional to the cell's velocity, representing cell-stroma adhesion and the reforming of a cell's cytoskeleton.

3.2.1 Delaunay triangulation and Voronoi tessellation

To find the nearest neighbours of a given cell a Delaunay triangulation is performed (figure 3.1 (top-right)). A Delaunay triangulation, for a set of points in a plane, connects all the points in

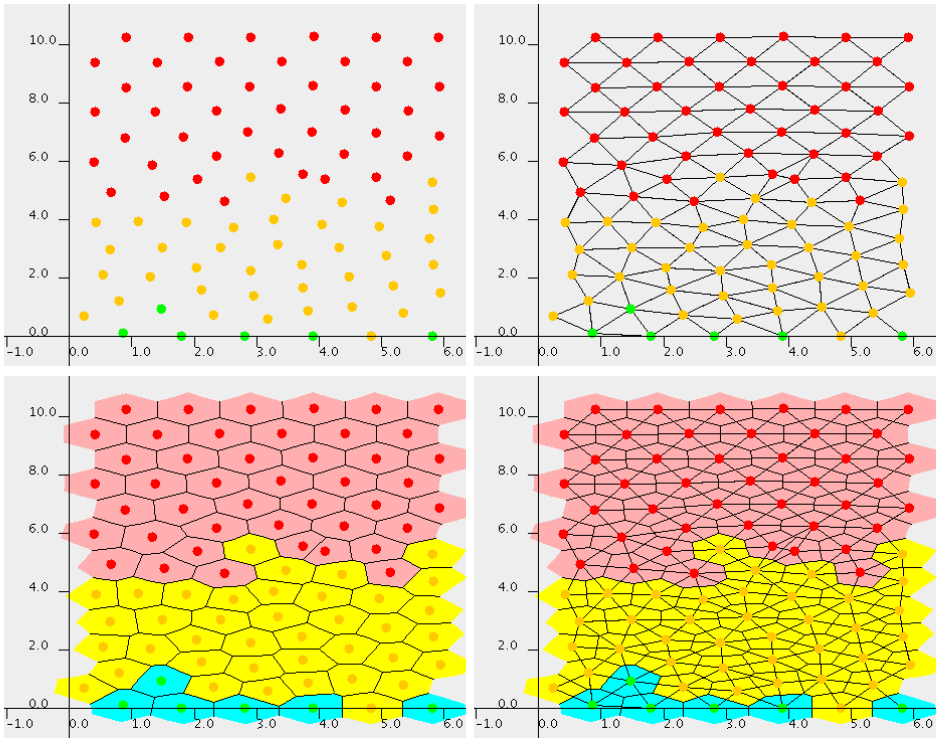

Figure 3.1: Series of schematic diagrams showing the Delaunay triangulation and Voronoi diagram used to model the epithelial cells. The vertical axis (y) represents the distance from the base of the crypt. The horizontal axis (x) represents the azimuthal distance, with periodic boundary conditions imposed on $x = 0$, $x = W_C$ (in this case $W_C = 6$). (Top left) Positions of the cell centres, different colours represent different cell types: green - stem cells, yellow - transit cells, red - differentiated cells. (Top right) Plot of cell centres and corresponding Delaunay triangulation that is used to determine spring connections. Lines between cells represent neighbouring cells connected by springs (note cells on the periodic boundaries are connected but, for clarity, this is not shown). (Bottom left) Cell centres and associated Voronoi diagram, used to calculate actual cell shapes. Colours represent different cell types: turquoise - stem cells, yellow - transit cells, pink - differentiated cells. (Bottom right) Cell centres along with Delaunay triangulation and Voronoi diagram [12].

triangles (elements) such that for each triangle, no other point is inside its circumcircle [120]. The points in this case are the cell centres and the triangulation is such that nearest neighbouring cells are connected and no connections between the cells cross over each other.

To find the cell shapes, a Voronoi tessellation is performed (figure 3.1 (bottom-left)). For each cell, the circumcentres of each triangle for which the cell is apart of are connected to produce a polygonal shape [120]. This polygon represents the cell. The Voronoi tessellation is not necessary

to calculate the cell movement and, hence, is not normally performed at each time step, but is used for visualisation purposes.

3.2.2 Forces due to cell-cell interactions

Cell-cell interactions are modelled by linear springs that lie along the edges of the triangles connecting neighbouring cells (see figure 3.1 (top-right)). Each spring connecting cells i and j has a natural length, $s_{ij}(t)$, and spring constant, k_{ij}. The natural spring length, $s_{ij}(t)$, is the same for all connections, apart from those between cells that have just given birth (see below). The force, $\mathbf{F}_{ij}$, exerted on cell i by a neighbouring cell j is calculated through Hooke's Law, giving

$$\mathbf{F}_{ij} = k_{ij}\left(|\mathbf{r}_i - \mathbf{r}_j| - s_{ij}(t)\right)\frac{(\mathbf{r}_j - \mathbf{r}_i)}{|\mathbf{r}_j - \mathbf{r}_i|} \tag{3.1}$$

where $\mathbf{r}_i$ and $\mathbf{r}_j$ are the positions of cells i and j respectively. In Meineke's implementation, k_{ij} is independent of the length of the interface between cells i and j: we relax this assumption later (see §3.3.4).

The natural spring length, $s_{ij}(t)$, of a mature cell is used as the non-dimensional unit of length for all calculations within our model. Further details are provided in Appendix A.1.

The total spring force acting on cell i is obtained by summing over its neighbours j,

$$\mathbf{F}_i = \sum_{j=1}^{j=N_i} \mathbf{F}_{ij} \tag{3.2}$$

where N_i is the number of cells that are adjacent to cell i.

3.2.3 Cell drag

The cell-cell forces (3.2) are balanced by a drag force which is assumed to be proportional to the velocity of the cell, $d\mathbf{r}_i/dt$. The drag force represents the breaking and reforming of bonds, such as integrins and the reforming of the cell's cytoskeleton. Balancing the drag and spring forces that act on cell i we set

$$\eta_i \frac{d\mathbf{r}_i}{dt} = \mathbf{F}_i \tag{3.3}$$

where η_i is the drag coefficient of cell i. We have assumed in (3.3) that inertial effects can be ignored. In Meineke's implementation, η_i is independent of cell size: we relax this assumption below (see §3.3.5).

3.2.4 Cell birth

In [109], cells are given either a fixed cell-cycle time or a stochastically varying one (see §A.1). Stem cells are fixed in position at the base of the crypt and can divide indefinitely. When they proliferate they divide into a stem cell and transit cell. Transit cells undergo three divisions; they divide into two transit cells on the first two occasions and two differentiated cells on the third cell division. Differentiated cells cannot proliferate.

When a cell is about to proliferate an angle is chosen at random in the range $(0, 2\pi]$ and a new cell centre is placed a distance 0.1 mature natural spring lengths away from the centre of the parent cell. The spring connecting these cells is given an initial natural spring length of 0.1 mature natural spring lengths that increases at a constant rate to a fully mature spring length over the first hour following proliferation.

3.2.5 Boundary conditions

In order to simulate cell shedding into the lumen, any cells that migrate beyond the top of the crypt, $y = H_C$, are removed from the simulation. Stem cells are fixed in place at the base of the crypt, $y = 0$, and no cells can move below the stem cells. Periodic boundary conditions are imposed by placing a copy of the cell centres (ghost cells) on the opposing side of the crypt before performing the Delaunay triangulation (see figure 3.2). The algorithm used for the Delaunay triangulation, Triangle [151], needs to have a convex hull. To ensure no cells are connected over large, unrealistic distances, we place ghost cells at the top and bottom of the crypt (see figure 3.3).

3.2.6 Algorithm for constructing numerical simulations

The model described above is solved numerically in the following way.

- Initially, a population of cells is placed on a hexagonal mesh. Each cell is given a cell-cycle time randomly chosen from a normal distribution and birth time randomly chosen from a uniform distribution.
- On each time step:
  - any cells that have moved further than the top of the crypt (a designated distance from the base of the crypt) are removed;
  - the remaining cells are checked to see if any are ready to proliferate; the relevant cell

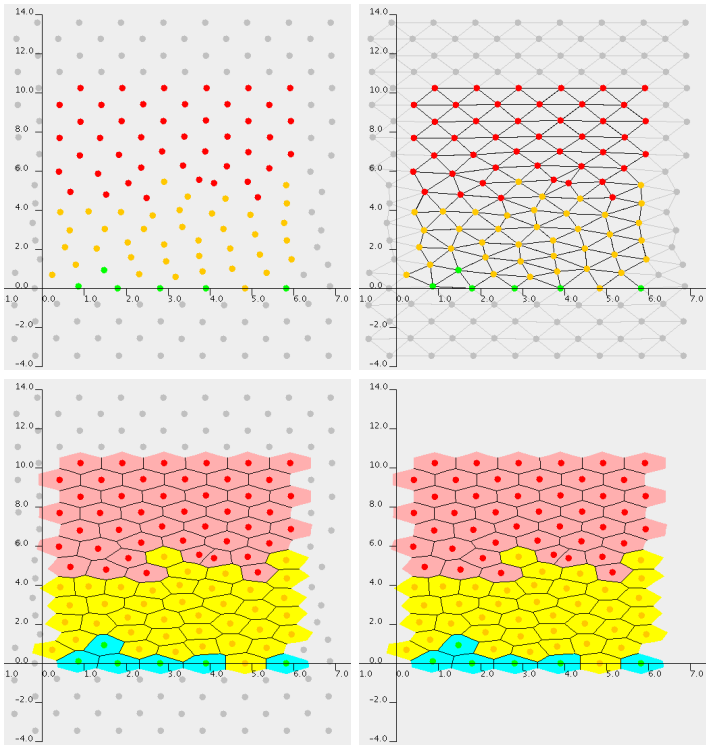

Figure 3.2: Implementation of ghost nodes. Plots showing the how Delaunay triangulation and Voronoi diagram are performed on a cylindrical crypt. (Top left) Copies of the cell centres near the crypt boundaries are placed on the opposite side of the crypt. Further ghost cells are placed on the top and bottom of the crypt to ensure a convex hull (needed for Delaunay triangulation). (Top right) Delaunay triangulation performed on cell centres and ghost cells. (Bottom left) Now a Voronoi diagram can be made on the cells to find each cell's shape. (Bottom right) Finally ghost cells are removed.

divisions then take place;

- a Delaunay triangulation is performed to determine the connections between the cells;
- using these connections, the spring forces F_{ij} connecting neighbouring cells are calculated (see equation (3.1));
- the total force on each cell is calculated from equation (3.2);
- cell positions are updated by using a forward Euler method to integrate (3.3) with time.

- This process is repeated until the simulation time ends.

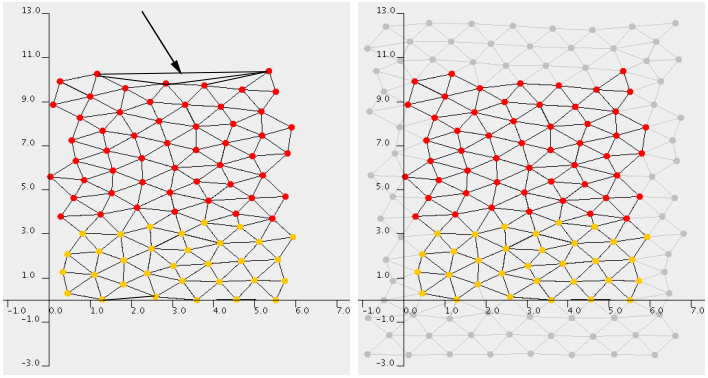

Figure 3.3: Plots showing why ghost nodes are needed at the top and bottom of the crypt. (Left) When there are no ghost cells, the Delaunay triangulation connects cells large distances away from each other, to achieve a convex hull. (Right) When there are ghost cells, large unrealistic connections are avoided.

3.3 Adaptations to the Meineke *et al.* model [109]

Even though Meineke *et al.*'s model [109] produced some useful results, such as being able to follow cell lineages in the crypt, we wish to extend it to incorporate additional biological information. These changes include unpinning the stem cells (§3.5.1), more detailed cell-cycle models (§3.3.1), different models of the effects of the protein Wnt (§3.3.2), new cell dynamics models (§3.3.4 and §3.3.5) and inclusion of mutant cells (3.3.6).

3.3.1 Cell cycle

The cell-cycle is a series of events through which a cell passes before undergoing mitosis [2]. It consists of four phases: G_1-phase, where the cell grows and produces certain proteins; S-phase, the DNA synthesis phase, G_2-phase, a growth phase where further proteins are produced so that the cell can undergo mitosis in M-phase. At the end of M-phase two daughter cells are produced. They start again at the beginning of the cell cycle. If, before the cell enters S-phase, there are insufficient transcription proteins within the cell, it exits the cell cycle [102] (and is placed in G_0-phase) and does not resume cycling unless further transcription proteins are produced.

To reflect the dependence of proliferative behaviour on protein levels within our model, we embed a cell-cycle model within each cell. We use several types of models ranging from ODE models due to Tyson and Novak [167] and Swat *et al.* [159] to simpler models in which each phase of the cell cycle is given a fixed duration. At each time step, the cell-cycle model in each cell is checked to see

if it has reached the end of its current phase. This can be defined by the levels of proteins within the cell (for ODE models) or by the cell's age (simpler models). If the cell has reached the end of M-phase it produces two new daughter cells, as discussed in §3.2.4.

Differentiated cells are assumed to remain indefinitely in G_0-phase and do not proliferate.

3.3.2 Wnt dependence

It is believed that the proliferation rate of epithelial cells within the crypt depends on the extracellular protein Wnt [126, 134, 171], with cells able to proliferate in high levels of Wnt (found at the base of the crypt) and unable to do so in low levels of Wnt (found at the top of the crypt). To mimic this dependence, a fixed linear Wnt gradient, with the highest value at the base of the crypt, is imposed along the crypt axis and the ability of a cell to proliferate is assumed to depend on the local levels of Wnt.

When simple (non-ODE-based) cell-cycle models are used, if the Wnt stimulation is lower than a threshold value, the cells are termed differentiated and cannot proliferate. Cells with more detailed, ODE-based cell-cycle models are combined with Wnt-signalling models, such as [172] and [88]. For these cell-cycle models, the levels of proteins such as APC and β-catenin depend on the Wnt stimulus which, in turn, the level of β-catenin is used to determine the length of different phases of the cell cycle. An illustrative example showing how van Leewen *et al.*'s Wnt-signalling model [172] can be implemented in the cell-centre model is given in Appendix A.2. Details of how other models are implemented are presented in [110] and [170].

3.3.3 Unpinned stem cells

In [109], the stem cells are pinned at the bottom of the crypt. Consequently no cell lineage can ever populate the entire crypt as the other stem cells always remain at the base of the crypt. However there is experimental data which suggests that a single lineage may populate the crypt [63, 108, 161]. For these reasons we decided to unpin the stem cells at the bottom of the crypt. The modification we make is to no longer term cells on the crypt base stem cells. We define all proliferating cells transit cells, where the restriction of a fixed number of cell-divisions is removed, and assume that they move according to (3.3).

At the base of the crypt we impose a no-flux condition such that any net spring force that would cause a cell to move below the crypt base ($y = 0$) is balanced by an opposing force that keeps the

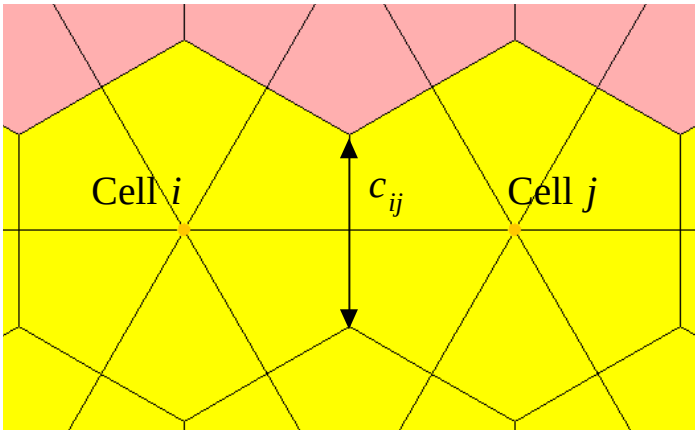

Figure 3.4: Schematic showing the edge-length c_{ij} between cells i and j used in (3.4), below. The lines between the cell-centres represent the spring connections.

cell on $y = 0$. The cells can move laterally along the crypt base and off the crypt base. The effects of unpinning the stem cells are shown in §3.5.1.

3.3.4 Edge-dependent springs

When two cells come into contact they form bonds mediated by cadherins and other molecules. The number of bonds formed is thought to depend on the contact area, the adhesion strength depending on the number of bonds formed [24, 67]. In order to incorporate these phenomena in our model, we relax the assumption that the spring constant k_{ij} connecting cells i and j is constant. Instead we assume that k_{ij} is linearly proportional to the edge-length c_{ij} (the two dimensional representation of contact area, see figure 3.4), so that in (3.1) we have

$$k_{ij} = \bar{k}_{ij}\frac{c_{ij}}{c_N}, \tag{3.4}$$

where $\bar{k}_{ij}$ is a constant determining the spring strength and c_N is the edge-length between cells in the equilibrium packing state. In all cases we set, $c_N = \frac{1}{\sqrt{3}}$ natural cell-length (see §A.1). This corresponds to the edge-length when cells are packed hexagonally 1 cell-length apart.

Implementation of (3.4) in (3.1) causes cells that are very close to each other (with a large contact area) to be more quickly forced away from each other (provided other surrounding cells are not very close) than if the cells did not have edge-dependent springs. The effects of implementing (3.4) are presented in §3.5.1, below.

3.3.5 Area-dependent drag

As with to cell-cell adhesion, the strength of the integrin bonds between the epithelial cells and the underlying stroma is believed to depend on the area of contact. The integrin bonds [2, 24, 67] work in a similar way to the cadherin bonds, with the total adhesion force dependent on the number of bonds formed, which is assumed to be dependent on the area of contact with the underlying stroma.

To take account for this effect, we assume that the drag term (which represents the breaking and reforming of integrin bonds) depends on A_i, the area of contact between cell i and the underlying stroma. More specifically the drag term, η_i, in (3.3) is now assumed to be

$$\eta_i = \bar{\eta}_i \left(0.1 + 0.9\frac{A_i}{A_N}\right), \tag{3.5}$$

where $\bar{\eta}_i$ is a constant depending on the cell type of cell i and A_N is the area of a cell at its equilibrium packing size, ($= \frac{\sqrt{3}}{2}$ for hexagonally-packed cells, see §A.1). This modification causes smaller cells to move faster than larger ones.

Adjusting the spring length (§3.3.4) and making the drag area-dependent require us to monitor cell shapes, not just their positions and hence we must produce a Voronoi diagram and a Delaunay triangulation at every time step (see figure 3.1). The Voronoi diagram is not required in Meineke *et al.*'s model (unless for visualisation purposes) and can be time-consuming to compute. The effects of making the drag coefficients area-dependent are presented in §3.5.1, below.

3.3.6 Mutant cells

In the crypt, two common mutations found in the early stages of colorectal cancer are in the proteins APC and β-catenin. These proteins are involved in the Wnt signalling pathway and when mutated can lead to cell proliferation no longer being dependent on the presence of Wnt [19, 74]. We will investigate how such mutant cells develop within a crypt by introducing them as a separate cell type which proliferate at a constant rate regardless of the local level of Wnt.

APC and β-catenin are both multi-functional proteins and, in addition to affecting proliferation, mutations in these proteins can affect the cell's cytoskeleton [115], cell-stroma adhesion [141] and cell-cell adhesion [18]. To model changes to the cytoskeleton we allow the drag on a cell, η_i or $\bar{\eta}_i$ (depending on whether the drag is area-dependent) to depend on a cell's mutation state. For clarity, the drag on a normal cell is denoted by η_n or $\bar{\eta}_n$ and the drag on a mutant cell by η_m or $\bar{\eta}_m$. As

mutant cells are found to move slower, we assume $\eta_m \geq \eta_n, \bar{\eta}_m \geq \bar{\eta}_n$.

Regarding cell-cell adhesion, the spring strength between two cells, k_{ij} or $\bar{k}_{ij}$ (depending on whether the cells have edge-length-dependent springs), depends on whether the two cells in contact are mutant or not. The spring strength between two normal cells is denoted by k_{nn} or $\bar{k}_{nn}$, between two mutant cells, k_{mm} or $\bar{k}_{mm}$ and between a normal and a mutant cell (or a mutant and a normal cell) k_{nm} or $\bar{k}_{nm}$. The behaviour of mutant cells within the crypt is presented in §3.5.2, below.

3.4 Programming style

The programming environment of CHASTE (**C**ancer, **H**eart **A**nd **S**oft **T**issue **E**nvironment) was developed and used to run numerical simulations of the model. CHASTE is a large group project whose objective is to establish a new and long-lasting programming framework for cancer and heart modelling, since, as we now explain, traditional methods are not well suited to simulating large-scale biomedical models [125].

When using traditional methods of programming, code is often reproduced each time a new model is created, even though much of the code could have been reused from a previous model [125]. Additionally, code written by a single developer is often poorly commented and uses the developer's idiosyncratic naming conventions and programming style. As a result the code can be hard for other users to follow and is therefore often abandoned [125]. A further problem is that code is often poorly tested, leading to problems of unreliability that may not be discovered until much later on, when adaptations are made to the model [125].

To overcome these problems we use an agile method known as eXtreme programming. This involves working in iterations (see §3.4.1), programming in pairs (see §3.4.2), having collective code ownership (see §3.4.3), using object-orientated code (see §3.4.4) and test-driven development (see §3.4.5).

3.4.1 Iterations

With CHASTE being a group project involving several members, each with their own particular aims, it was necessary to keep the project focused. To do this the code development was split into periods, or iterations, of around a month. In each iteration, short term goals were defined that would be completed within the iteration. This kept the code development well-directed and helped ensure tasks were completed more quickly [16].

Using iterations with well-defined goals can lead to developers working on parts of the code in which they have no direct interest, but this leads to a better understanding of the code as a whole.

3.4.2 Pair programming

At the start of each iteration the group met for three to four days and worked on the code in pairs. Pair programming involves two developers working on a task together on one computer [16]. The pairs usually consist of a "guru", an experienced programmer, and a "layman" or less experienced programmer who may be from a mathematical background. One person types or "is in the driving seat" whilst the other gives advice or "directs". After half an hour the "driver" and "director" swap places. After four hours of working together a pair rotation occurs, where one member of the pair moves onto another task and is replaced by someone from a pair who has been working on a different task. No member of a pair remains on a task for more than two pair rotations.

Although this may seem extravagant in its use of resources, it is effective, as the "director" can spot mistakes made by the "driver" that would not be spotted as quickly by one person working alone [43]. Also when planning a task it is often better to have two people working together as they are less likely to implement a bad idea [43]. The rapid pair rotation means that each member of the team gets to see many different areas of the code, leading to a greater understanding of the code as a whole [173].

3.4.3 Collective code ownership

Another feature of eXtreme programming is that no one user is wholly responsible for any part of the code: the group is responsible for the code. This means that any developer can change the code or add functionality and prevents any particular developer becoming a bottleneck for the project [173].

3.4.4 Object orientated programming

The CHASTE project is written primarily in C++, an object-orientated programming (OOP) language. The advantage of using OOP is that parts of the code can be easily decomposed into simpler tasks, allowing several pairs to work simultaneously on similar areas of the code. Another advantage is that the code can be easily adapted and new functionality added, without disrupting existing functionality [35].

3.4.5 Test-driven development

One of the most important aspects of agile programming is the implementation of test-driven development. As CHASTE is a large project involving many people, it is impossible for any one person to know all of the code. This means that it is possible inadvertently to break a piece of code that another user relies upon. Test-driven development aims to minimise this in the following way. Before any new piece of code is written, a test is created for it and, before being committed to the main repository, any new code must not only pass the new test but also not cause any other tests to fail [173]. This ensures that no committed code breaks any previous functionality. An example of a simple test may be, for an ODE solver: define an ODE where the solution is known (eg $y'(t) = y(t),\ y(0) = 1$) and solve up to a point ($t = 1$) and check the solution is correct to within a given tolerance.

To ensure that no untested code is incorporated, a daily coverage test is run to check every line of the code is checked at least once by one of the tests. This should ensure that if any code is incorrectly changed the problem will be flagged in another test.

Test-driven development is useful in several ways; not only does it encourage developers to think carefully about the aim of a piece of code but also it checks that progress does not break the code [16].

Other features of the eXtreme programming method, including the more offbeat concepts such as stand-up meetings and project velocity, are detailed on the eXtreme programming website[1]. Further details of how eXtreme programming was used in CHASTE can be found in [125].

3.4.6 Validation of the model

The model was validated in three ways: by writing tests and by checking against previous models and experimental results. As mentioned in §3.4.5, each individual part of the code is checked to ensure that it works in the correct way. We reproduced the results of the Meineke model (see figure 3.5 and 3.6, discussed below) and checked that the results compared to biological experiments, such as Sunter *et al.*'s study of cells movement in the crypt [158] (see §3.5.1).

[1] `http://www.extremeprogramming.org/index.htm`

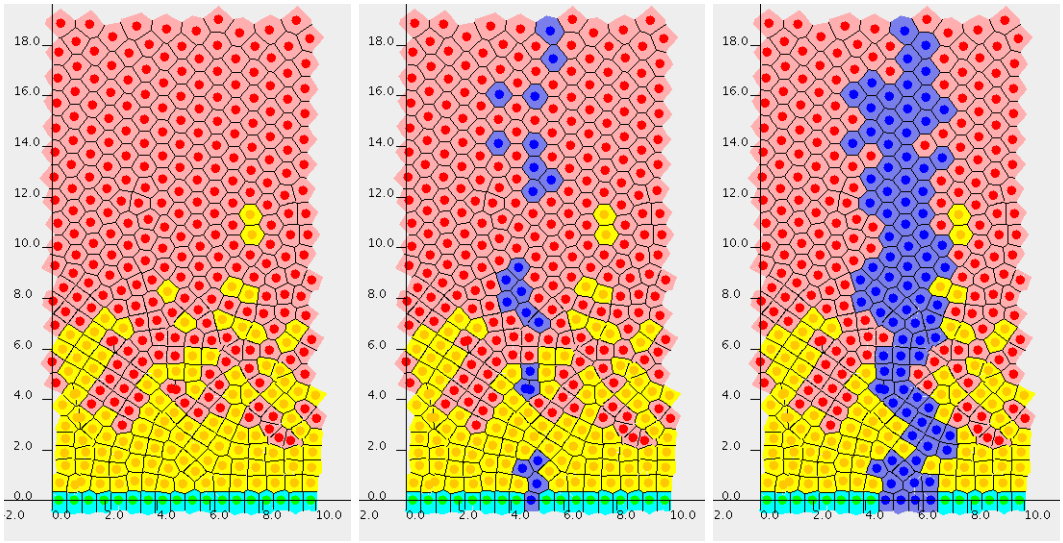

Figure 3.5: Three snapshots of a simulation of the Meineke crypt, all at time $t = 500$: (left) a simulation with no lineages marked within the crypt; (middle) the same crypt with one stem cell lineage marked (in blue); (right) a crypt with the lineages from 4 stem cells marked (in blue). Stem cells (turquoise) are pinned in position and proliferate to produce transit cells (yellow), which can undergo 3 cell divisions until they become differentiated cells (pink). The proliferation by cells toward the bottom of the crypt forces cells up the crypt. When the cells reach the top of the crypt they are removed. See §A.1 for parameter values.

3.4.7 Personal contribution

The CHASTE project was a group collaboration involving many researchers. Everyone worked on the code, but could specialise and devote extra time to parts of the code of particular interest to them. My own work focused on adjusting the mechanical properties of the cells such as cell-cell adhesion and cell drag. I also focused on incorporating mutant cells and adjusting their properties. Most of the associated code was written by me, although others could adapt it.

The core members of the CHASTE development team were Jonathan Cooper, Alex Fletcher, Lee Momtahan, Gary Mirams, Phillip Murray, James Osborne, Joe Pitt-Francis, Pras Pathmanathan and myself. Others who contributed to the code development in the CHASTE project included: Miguel Bernabeu, Sarah Young, Susheel Varma, Ingeborg van Leeuwen, Jonathan Whiteley, David Gavaghan, Helen Byrne, Sarah Waters, Eleanor Boston, Carina Edwards and Matthew Johnston.

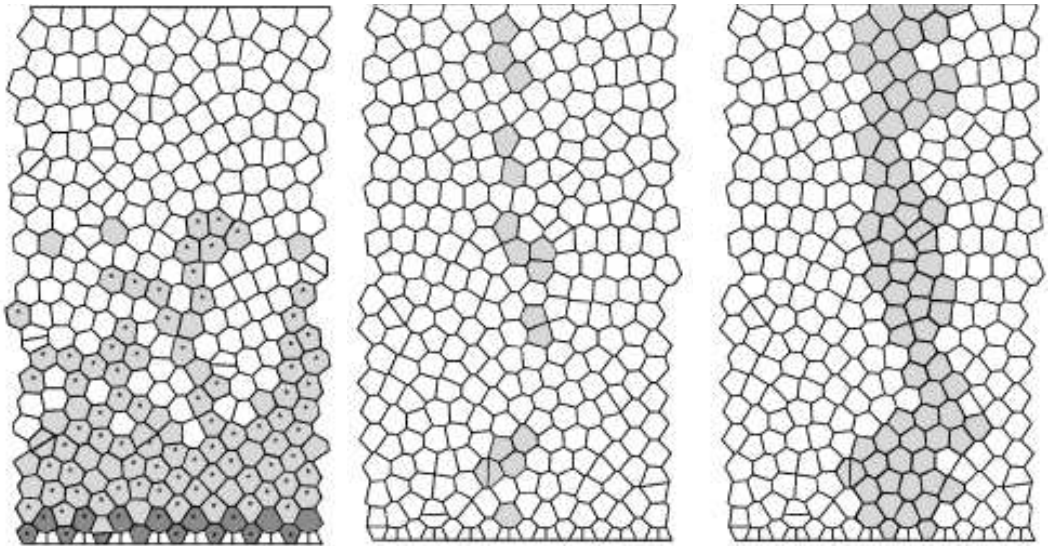

Figure 3.6: Results taken from Meineke *et al.* [109] for comparison with figure 3.5. Left: a quasi-steady-state crypt, where stem cells are marked dark grey, transit cells light grey, and differentiated cells white. Middle: a quasi-steady-state crypt with the lineage from a single stem cell marked in grey, all other cells in white. Right: the lineage from four stem cells at the base of the crypt.

3.5 Results

Simulations of Meineke *et al.*'s basic model to provide a a comparison for the results of §3.5.1, where the effects of the various modifications are discussed, and §3.5.2, where the effect of introducing mutant cells is studied.

3.5.1 The normal crypt

Meineke *et al.*'s model [109]

Initially, we use the same parameter values as Meineke *et al.* to reproduce the results in [109]. In figure 3.5 (left) we reproduce qualitatively a quasi-steady-state crypt and the labelling of lineages from stem cells as in [109] (shown in figure 3.6). A quasi-steady-state crypt is one for which the number of cells born balances the number removed at the top of the crypt. In figure 3.5 (left), the stem cells at the base of the crypt (marked turquoise) give birth to transit cells (marked yellow) which move up the crypt (whilst proliferating) and differentiate after they have proliferated three times. The differentiated cells carry on moving up the crypt and are eventually removed when they pass over the top of the crypt.

In figure 3.5 (middle), we labelled a single stem cell and track it and its progeny. The cells move up the crypt with small levels of lateral movement. The cells descended from the stem cell mix with other transit and differentiated cells and do not form a continuous trail up the crypt. This is in good qualitative agreement with the findings of Meineke *et al.* [109] (see figure 3.6 (middle)).

The lineage from four neighbouring stem cells that are next to each other is shown in figure 3.5 (right). The progeny form a continuous band stretching from the base of the crypt to the top. Again these results are qualitatively similar to findings in [109] (see figure 3.6 (right)).

Unpinned stem cells

The first modification to Meineke *et al.*'s model that we considered was to unpin the stem cells at the base of the crypt. To investigate this behaviour, the crypt was simulated with the parameters described in §A.1, with $k_{ij} = k_{nn}$ and $\eta_i = \eta_n$. The only mechanical difference between the two simulations presented in figure 3.7 is that the stem cells in the Meineke model (top) are fixed in place.

In addition to unpinning the stem cells, we also changed the proliferation rates of the cells. In Meineke *et al.*'s model, Wnt-dependent proliferation is not modelled directly. Instead, transit cells undergo three cell divisions and stem cells can divide an unlimited number of times. In our model, no stem cells were defined and Wnt-dependend proliferation was modelled directly. Cells were termed transit if they had position $y < H_W$ and could proliferate, otherwise they were termed differentiated and could not (for further details, see §A.1).

Unpinning the stem cells had a major effect on the simulations. With the Meineke *et al.* model [109] (figure 3.7 top) even after six thousand hours (262 days), the crypt still comprises lineages from all the stem cells, whereas in the adapted Meineke model (figure 3.7 bottom), after the same length of time, the crypt is monoclonal (all cells are generated from the same progenitor cell). These new results are consistent with independent experimental results which suggest that crypts are monoclonal [63, 108, 161].

Further details on the unpinning of the stem cells can be found in [170].

Mechanical properties

In §3.3 we described how we adapted the Meineke model such that the springs connecting neighbouring cells could be edge-length dependent (§3.3.4) and that cells could have area-dependent drag

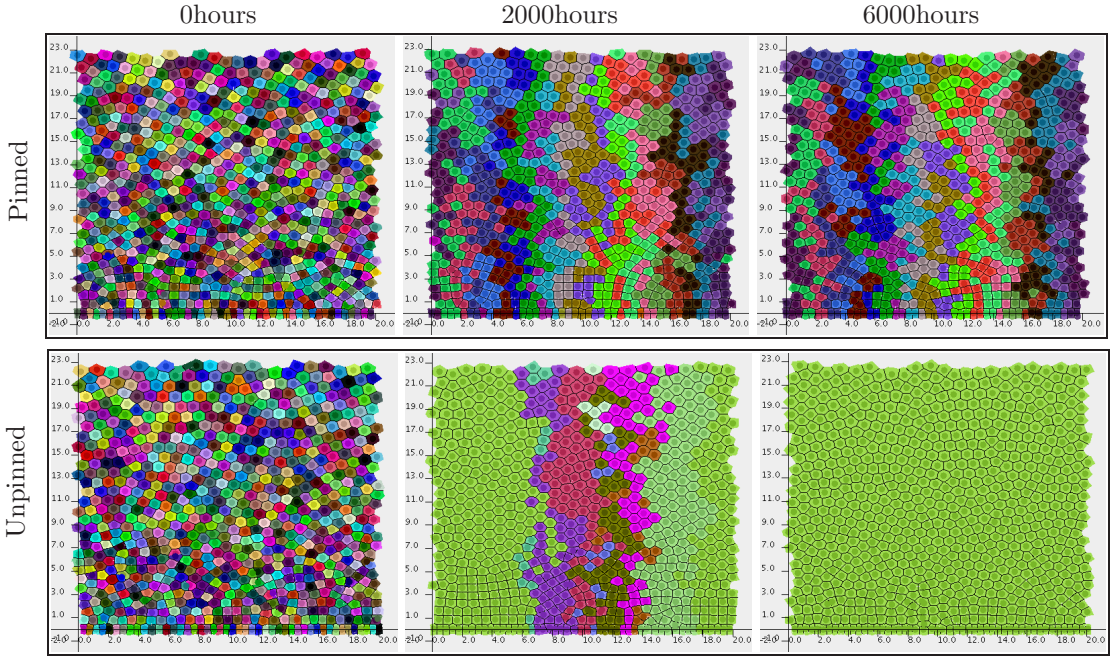

Figure 3.7: Snapshots showing how unpinning the stem cells (bottom three plots) can lead to a monoclonal crypt; this is not possible in Meineke *et al.*'s original model (top three plots). In the left two snapshots, initially all the cells are marked with a different colour. When a cell divides, both daughter cells retain the same colour as the parent cell. When the stem cells are pinned (top), no one lineage dominates the crypt, and the crypt's composition is similar after two thousand hours (middle top) and six thousand hours (right top), with 23 lineages in each. When the stem cells are unpinned (bottom), eventually one lineage dominates the crypt (middle bottom) and after six thousand hours the crypt becomes monoclonal (right bottom). See §A.1 for parameter values.

(§3.3.5). We now discuss how these changes affected the crypt dynamics.

In figure 3.8, we compare the cell distributions at $t = 500$ for different choices of k_{ij} and η_i. We allowed the spring strength, k_{ij}, in (3.1) to depend on edge-length, $k_{ij} = k_{ij}(c_{ij})$, as in (3.4) (figure 3.8 B & D) or to be constant, $k_{ij} = k_{nn}$ (figure 3.8 A & C). Similarly we allowed the drag, η_i, in (3.3) to depend on cell area, $\eta_i = \eta_i(A_i)$, (figure 3.8 C & D) or remain a constant, $\eta_i = \eta_n$ (figure 3.8 A & B).

The results presented in figure 3.8 show that when the cells have area-dependent drag (figure 3.8 C & D), there are fewer cells in the lower part of the crypt, in particular at its base (~ 30 when drag is area-dependent compared to ~ 50 otherwise). This is because tightly-packed cells at the base of the crypt experience less drag (due to having a smaller area) and can move away from areas of high

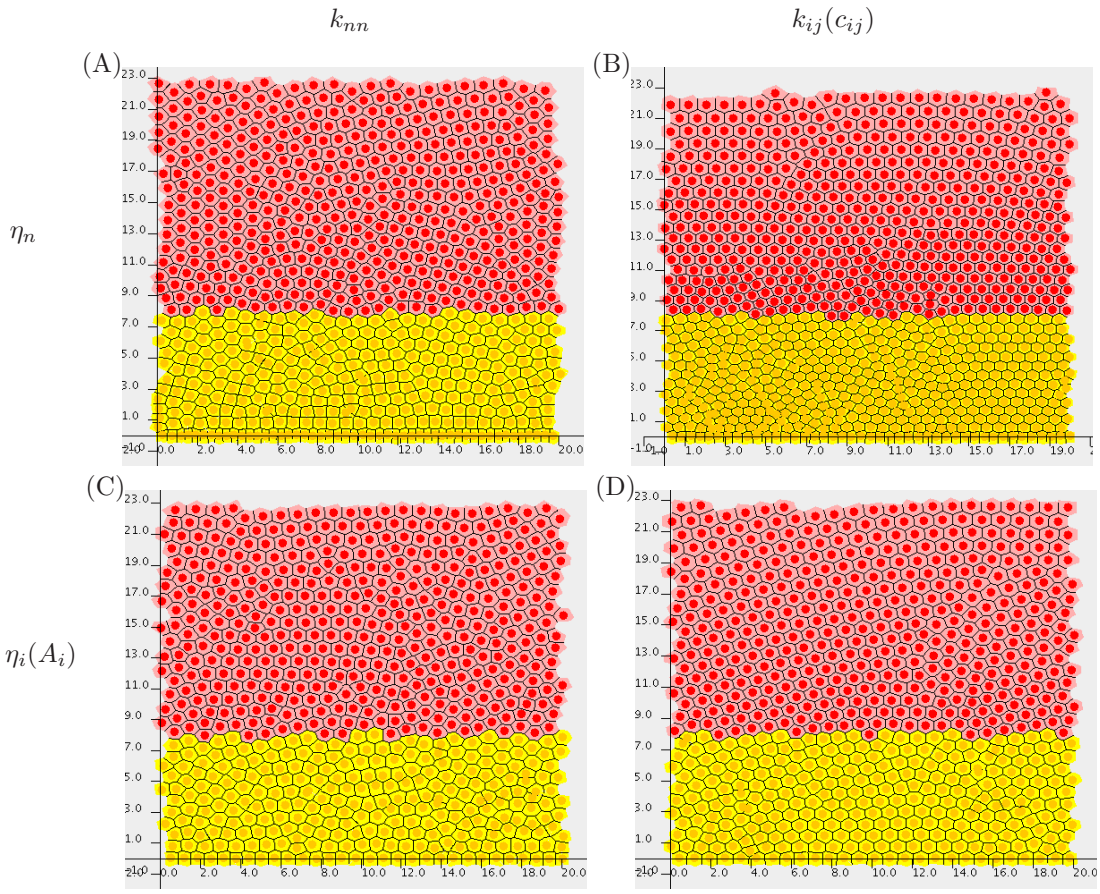

Figure 3.8: The effect of making the spring constant depend on length of contact-edge between cells, ($k_{ij} = k_{ij}(c_{ij})$) (B and D, cells packed more hexagonally) and having drag dependent on cell area, ($\eta_i = \eta_i(A_i)$) (C and D, fewer cells at the bottom of the crypt) for cells in the crypt. Series of simulation snapshots for cells in the colorectal crypt after 500 hours with (A) (η_n, k_{nn}) constant drag and linear springs, (B) $(\eta_n, k_{ij}(c_{ij}))$ constant drag and edge-length dependent springs, (C) $(\eta_i(A_i), k_{nn})$ area-dependent drag and linear springs and (D) $(\eta_i(A_i), k_{ij}(c_{ij}))$ area-dependent drag and edge-length dependent springs. Transit cells are marked yellow and differentiated cells marked pink. See §A.1 for parameter values.

packing (where the springs will be highly compressed) more easily.

When the spring constant depends on the length of the contact-edge between cells, the cells organise into a regular hexagonal structure (figure 3.8 B & D). This effect is less pronounced when the spring constants are fixed (figure 3.8 A & C).

When the spring constant is contact-edge-length dependent but the drag coefficient is constant (figure

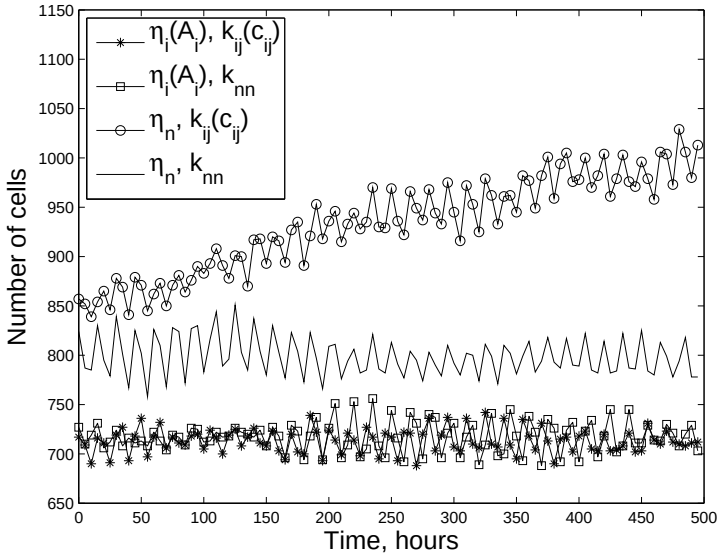

Figure 3.9: Plot of how the number cells within in the crypt varies over time and with the mechanical properties. All crypts initially in a quasi-steady-state at $t = 0$. For three mechanical cases (η_n, k_{nn}, $\eta_i(A_i), k_{nn}$ and $\eta_i(A_i), k_{ij}(c_{ij})$) the number of cells crypt remains approximately constant (with small changes due to cell proliferation), however for $\eta_n, k_{ij}(c_{ij})$, the number of cells in the crypt increases. Each line represents different mechanical scenarios for the cells with (η_n, k_{nn}) constant drag and linear springs, $(\eta_n, k_{ij}(c_{ij}))$ constant drag and edge-length dependent springs, $(\eta_i(A_i), k_{nn})$ area-dependent drag and linear springs and $(\eta_i(A_i), k_{ij}(c_{ij}))$ area-dependent drag and edge-length dependent springs. See §A.1 for parameter values.

3.8B), cells accumulate in the lower half of the crypt (see figure 3.9). The accumulation happens to such an extent that the code breaks down. This is because when there is a slight increase in cell number, the cells become more closely packed with smaller contact edges on all sides. If the spring constant is fixed then the force due to the springs is high and the cells are quickly forced away from one another. However when the spring constant is dependent on edge-length, the force is smaller. As a result, the force pushing the cells apart is weaker, increasing cell packing, creating smaller cell edges and weaker springs. This causes an increase in cell number and destabilises the quasi-steady-state crypt dynamics: the number of cells born outnumbers the number being removed at the top of the crypt, causing the number of cells within the crypt to reach biologically unrealistic large numbers.

No such problem arises if the spring coefficient is edge-length-dependent and the drag coefficient is area-dependent (see figure 3.8D). In this case, cells can easily move away from the region of high

packing as they will be smaller in size and, hence, have a lower drag. As a result, the crypt attains a quasi-steady state.

Cell position and movement

To understand how the cells move, a series of virtual labelling experiments were performed. At a fixed time point, all cells in S-phase (defined by their time until mitosis) were labelled. These cells and their offspring were labelled. After forty minutes the crypt was sectioned into horizontal bands of unit width and the percentage of labelled cells in each band calculated. A similar calculation was made nine hours after the simulation started. To reduce the dependence on the simulation's stochasticity, the process was repeated for one hundred simulations and the average results plotted (see figure 3.10).

We notice from figure 3.10 that the average percentage of marked cells is similar for each case (with/without contact area-dependent springs and with/without area-dependent drag). The percentage of marked cells after forty minutes (red) is about 35% in the Wnt stimulated region and 0% in the unstimulated region. After nine hours (blue), all marked cells have undergone cell division and so there are more marked cells, some of which have migrated up the crypt.

Virtual dissection

For comparison with experimental results, virtual dissections were performed. Here, the cells are labelled as in figure 3.10 and readings of the cell locations are taken after forty minutes and nine hours. However unlike in figure 3.10 where averages were taken across the crypt, here virtual cuts are made in the crypt by connecting two points, randomly placed on the top of the crypt and the bottom of the crypt. The cells are then numbered along the cut (with cell 1 at the bottom, see figure 3.11) and it is noted whether each cell is labelled or not. This process is repeated for one hundred simulations and the average results, showing the percentage of marked cells in each position, are plotted in figure 3.12.

Figure 3.12 shows that all cases produce similar results except when the spring constant is dependent on edge-length and drag is constant. In the other three scenarios (figure 3.12 A, C & D) we observe that after forty minutes, marked cells appear up to position 20 and after nine hours cells they appear up to position 30. These results compare well with the experimental results presented in [109]. By contrast, for cells that have contact area-dependent spring coefficients and constant drag coefficients (figure 3.12B), the results are quite different: after forty minutes, marked cells appear up to position

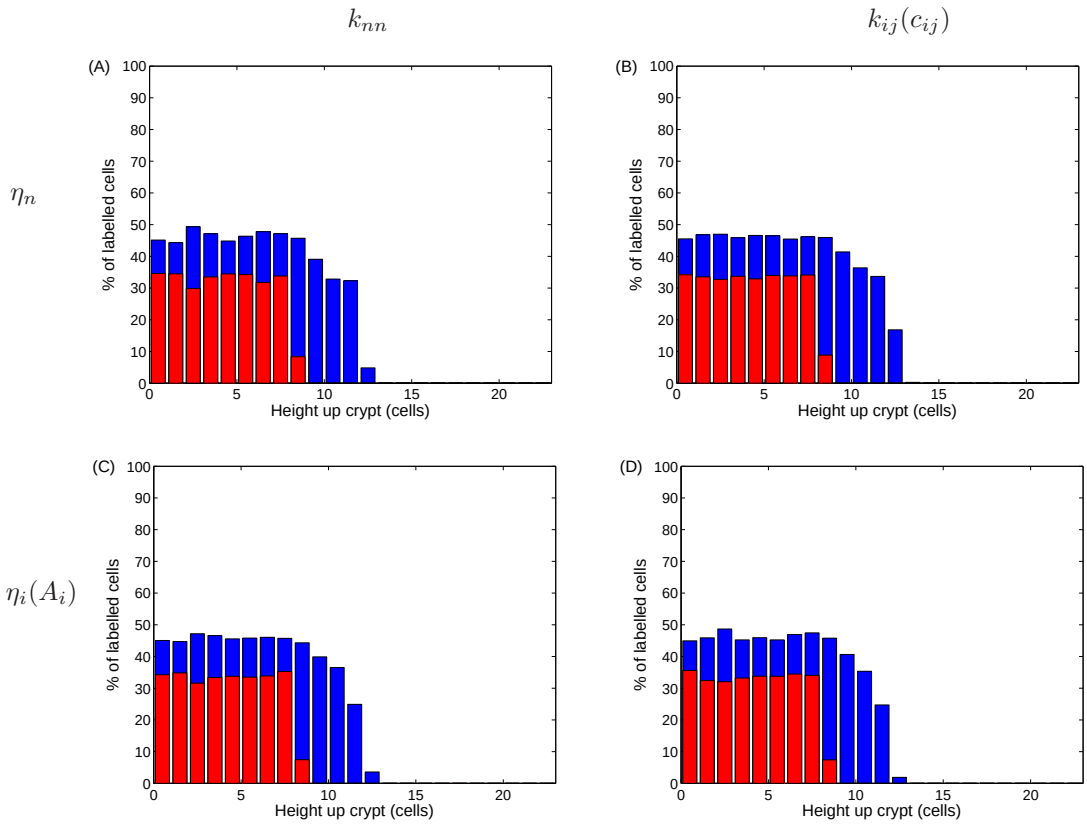

Figure 3.10: Series of plots showing how the number of labelled cells varies with distance up the crypt. At $t = 0$, cells in S-phase are labelled. These cells and their progeny retain the label. At $t = 40$min (red) and $t = 9$hrs (blue) the crypt is split into horizontal bands of unit width and calculate the proportion of labelled cells in each band, averaging these results over 100 simulations. The four plots are for cells with (A) constant drag and linear springs, (B) constant drag and edge-length dependent springs, (C) area-dependent drag and linear springs and (D) area-dependent drag and edge-length dependent springs. See §A.1 for parameter values.

30 and after nine hours, they appear up to position 40. This does not compare favourably with experimental results in [109] and is due to the build-up of cells in the lower part of the crypt (figure 3.8 B). From this we conclude that assuming the cells have edge-dependent springs and constant drag is unrealistic.

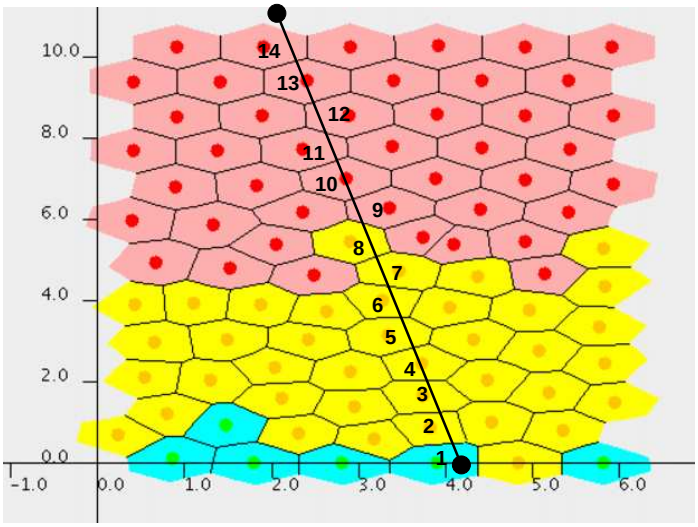

Figure 3.11: Schematic of a virtual dissection. Two points are randomly placed at the top and the bottom of the crypt (black circles) and connected by a virtual dissection line. Any cells the line passes through are numbered, starting at the bottom, and it is noted whether they are marked or not.

Average cell area and shape

Even though our results compare well with experiments (see figure 3.12), we do not yet know which of the alternative models describes the crypt most accurately. We now present results that help us to discriminate between the different cases.

The three measurements taken are average cell size, a measure of cell deformation (area difference) and a measure of cell shape. The crypt is split into horizontal sections of unit width and the average measurements for the cells in each band are calculated. This process is repeated for one hundred simulation readings at different times and the averages are plotted for each case (with/without edge-length-dependent springs, $k_{nn}/k_{ij}(cij)$, with/without area-dependent drag, $\eta_i(A_i)/\eta_n$) in figures 3.13, 3.14 and 3.15 respectively.

Cell Area

Figure 3.13 shows clearly that in all cases, cell area increases approximately linearly with distance from the base of the crypt. There are, however, noticeable differences. Throughout the crypt, cells that have spring constants which depend on edge length and constant drag ($\eta_n, k_{ij}(cij)$) are on average much smaller than in any of the other cases (when $\eta_i(A_i), k_{ij}(cij)$ or when k_{nn}). This is consistent with our findings in figure 3.8B, where cells build up within the crypt.

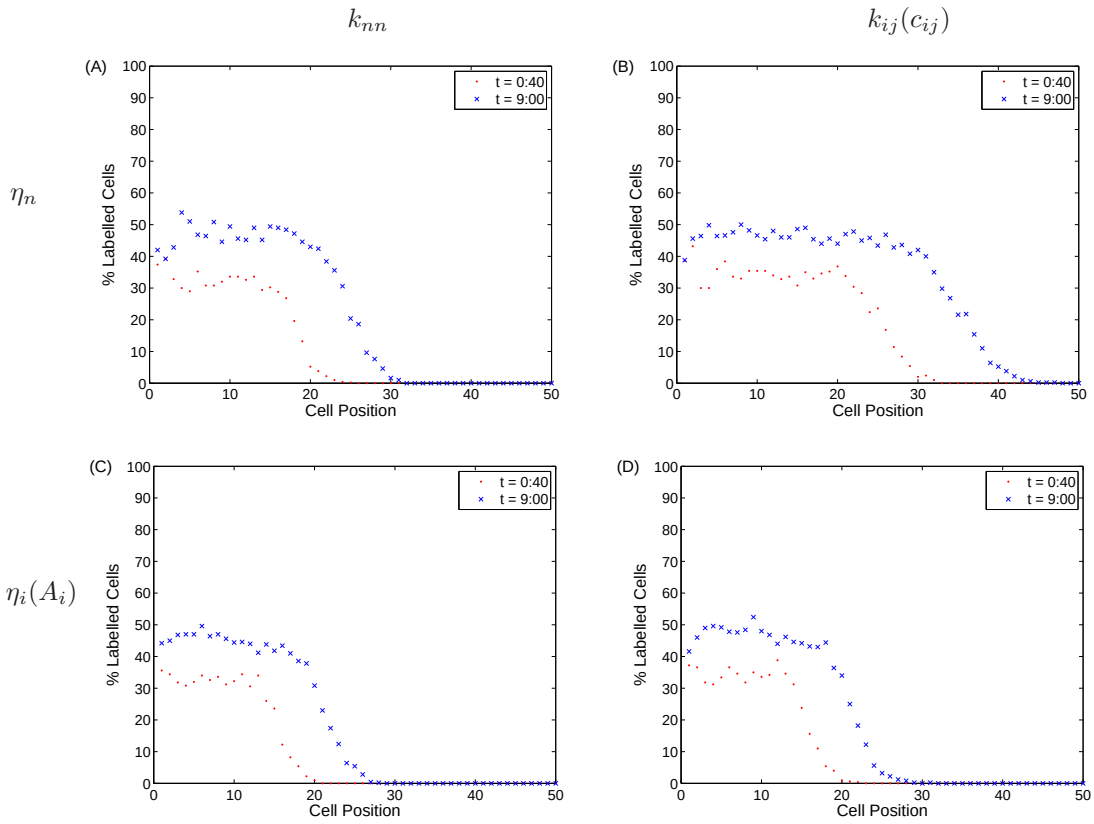

Figure 3.12: Virtual dissection of the crypt. Cells are marked as in figure 3.10 at time $t = 0$ and readings are taken after $t = 40$ min (red $\cdot$) and $t = 9$hrs (blue $\times$). 100 simulations were run and for each reading, the crypt was sliced at a random angle and the cells are numbered going up the crypt, as in figure 3.11. Whether the cell in each position is a marked was noted. The percentage of marked cells for all readings in each position is plotted. The four plots are for cells with (A) constant drag and linear springs, (B) constant drag and edge-length dependent springs, (C) area-dependent drag and linear springs and (D) area-dependent drag and edge-length dependent springs. See §A.1 for parameter values.

Area difference

The results presented in figure 3.14 provides a simple measure of how compressed the cells are within the crypt. We plot $P_i = A_N - A_i$ the difference between a cell's natural area, A_N, and its actual area, A_i. The average value of P_i is calculated in a similar way to the cell area (figure 3.13) by averaging in bands across the crypt and over time. We observe that all cells are compressed, $P_i > 0$, with the most compressed cells at the bottom of the crypt.

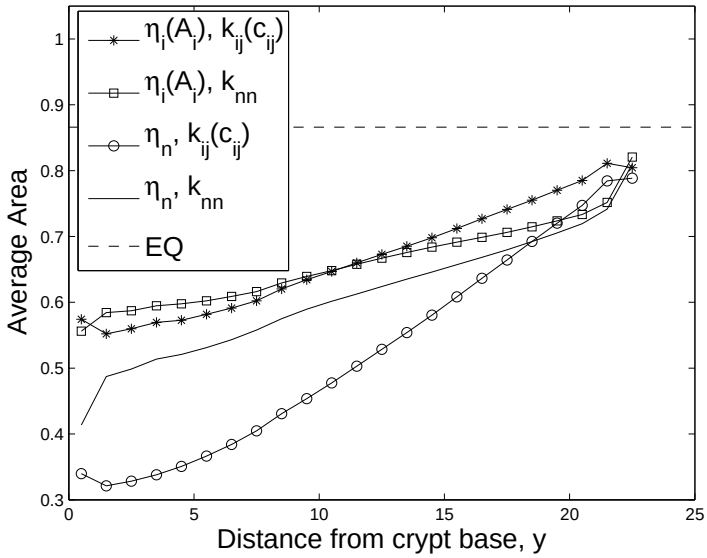

Figure 3.13: Plot showing how average cell area, (A_i), varies with distance from the base of the crypt and the mechanical properties of the cell. Each line represents different mechanical scenarios for the cells with (η_n, k_{nn}) constant drag and linear springs, $(\eta_n, k_{ij}(c_{ij}))$ constant drag and edge-length dependent springs, $(\eta_i(A_i), k_{nn})$ area-dependent drag and linear springs and $(\eta_i(A_i), k_{ij}(c_{ij}))$ area-dependent drag and edge-length dependent springs. Also plotted is the natural area for cells, in all cases, when the system is at rest (EQ). See §A.1 for parameter values.

Cell Shape

To understand how cell shape varies with position in the crypt, following [182] each cell is assigned a dimensionless shape measurement, S_i (= perimeter^2 / area). The values are then averaged as before and the results plotted in figure 3.15. Low values of S_i correspond to rounder cells ($S_i = 8\sqrt{3}$ for hexagonal cells and $S_i = 4\pi$ for circular cells) and high values to elongated cells.

The plots in figure 3.15 reinforce the results presented in figure 3.8, that cells with edge-length dependent spring constants $(k_{ij}(c_{ij}))$ are more hexagonal than cells with constant spring constants (k_{nn}). We notice two distinct plateaux in figure 3.15 for the cells with edge-length-dependent spring strength: cells in the non-proliferating zone (the top part of the crypt) are on average rounder (with lower values of S_i) than cells in the proliferating zone (the bottom part of the crypt). This can be explained by the geometrical rearrangement that occurs when a cell divides. For example, a cell that is a regular hexagon will divide into two irregular pentagons (see figure 3.16), each with a higher value of S_i. Consequently where there are proliferating cells (as in the lower part of the crypt) the

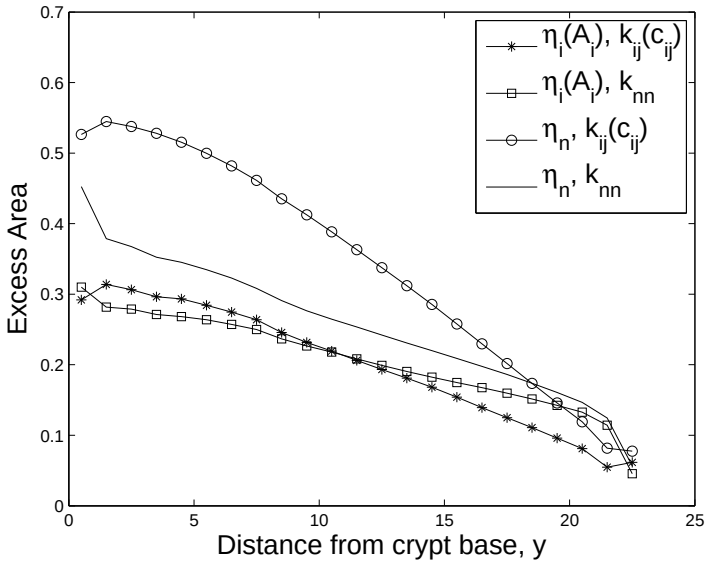

Figure 3.14: Series of plots showing how a simple measure of the compression experienced by the cells P_i ($= A_N - A_i$, the difference between actual area and target area), varies within the crypt and how it depends on the mechanical properties of the cells. Each line represents different mechanical scenarios for the cells with (η_n, k_{nn}) constant drag and linear springs, $(\eta_n, k_{ij}(c_{ij}))$ constant drag and edge-length dependent springs, $(\eta_i(A_i), k_{nn})$ area-dependent drag and linear springs and $(\eta_i(A_i), k_{ij}(c_{ij}))$ area-dependent drag and edge-length dependent springs. In all cases, the compression decreases with distance up the crypt. See §A.1 for parameter values.

average value of S_i will be larger.

The plots for S_i for cells with area-dependent drag and fixed spring constants $(\eta_i(A_i),\ k_{nn})$ also show two plateaux, one associated with the proliferating region and one with the non-proliferating region. However, on average, the cells are more elongated (higher values of S_i) than those with edge-dependent springs. Cells with fixed drag and spring constants $(\eta_n,\ k_{nn})$ do not seem to generate the same obvious plateaux but the cells are on average rounder at the top of the crypt than toward the bottom of the crypt.

3.5.2 Mutant cells

A weakness of Meineke *et al.*'s model [109] is that as stem cells are pinned, a mutant cell could never populate the entire crypt (see figure 3.7). This is biologically unrealistic as crypts populated only by mutant cells have been found [131]. Unless all the stem cells suffer a mutation, the stem cells need

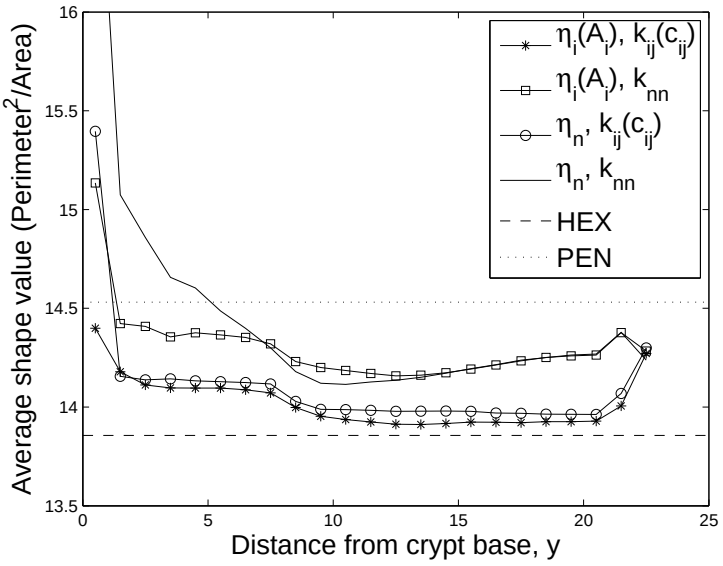

Figure 3.15: Plot of how cell shape varies with distance from the base of the crypt and the mechanical properties of the cell. The dimensionless shape parameter S_i is calculated by squaring the perimeter of the cell, C_i, and dividing by the cell area, $S_i = C_i^2/A_i$. Large values of S_i represent highly elongated cells, low values represent rounder cells. Each line represents different mechanical scenarios for the cells with (η_n, k_{nn}) constant drag and linear springs, $(\eta_n, k_{ij}(c_{ij}))$ constant drag and edge-length dependent springs, $(\eta_i(A_i), k_{nn})$ area-dependent drag and linear springs and $(\eta_i(A_i), k_{ij}(c_{ij}))$ area-dependent drag and edge-length dependent springs. Also plotted are lines representing values for regular hexagonal cells (HEX) and regular pentagonal cells (PEN). See §A.1 for parameter values.

to be unpinned to allow other cells to take their position at the bottom of the crypt (see monoclonal crypt in figure 3.7).

Using the adapted Meineke model (with unpinned stem cells), we now introduce a mutation into a transit cell and see how the mutant cell population varies as its properties are changed. The properties of interest include the drag on the mutant cells, the spring strength between mutant cells and the distance from the crypt base at which the mutation initially occurs.

Throughout this section all cells have fixed spring constants (not edge-dependent) and a constant drag, regardless of their size. Cells without mutations proliferate in the lower part of the crypt where there is sufficient Wnt stimulation. Further details of the parameter values used are presented in §A.1.

We assume that mutant cells proliferate at a constant rate thoughout the crypt, even where there

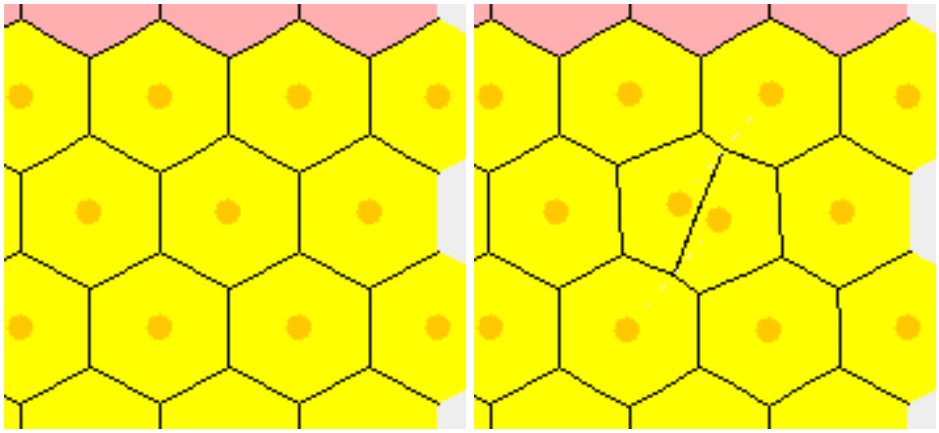

Figure 3.16: Schematic of how cell birth leads to two new cells having elongated shapes. Regular hexagonal cell (left) undergoes cell division, leading to two elongated pentagonal cells and the reshaping of the surrounding cells (right).

are low levels of Wnt and 'normal' cells would not proliferate. We also allow the drag coefficient and spring constant of the mutant cells to differ from those of 'normal' cells. In the rest of this section, we present results which can be used to predict conditions under which such a mutant cell can colonise a crypt.

No Wnt-dependence

We start by supposing that a single mutant cell appears at the crypt base. The mutant cells are identical to the normal ones except that they proliferate at a constant rate throughout he crypt.

Figure 3.17 shows how for a typical simulation. The mutant cell proliferates and moves off the base of the crypt (top, right). Its progeny continue to proliferate where normal cells would not be able to (bottom, left) but are eventually flushed out of the crypt (bottom, right).

Results from repeated simulations (not shown) reveal that mutations that simply render cell proliferation independent of Wnt will not usually dominate the crypt. As with the earlier simulations showing the eventual monoclonal conversion of a crypt (see figure 3.7) there is a (small) probability that the mutant cells may become the dominant population within the crypt. However running several other simulations, where the cell with the initial mutation was changed, showed the mutant cell population was flushed out of the crypt in each case. We conclude from these simulations that a mutation in a cell that does not change its mechanical properties is unlikely to result in the mutant population taking over the crypt.

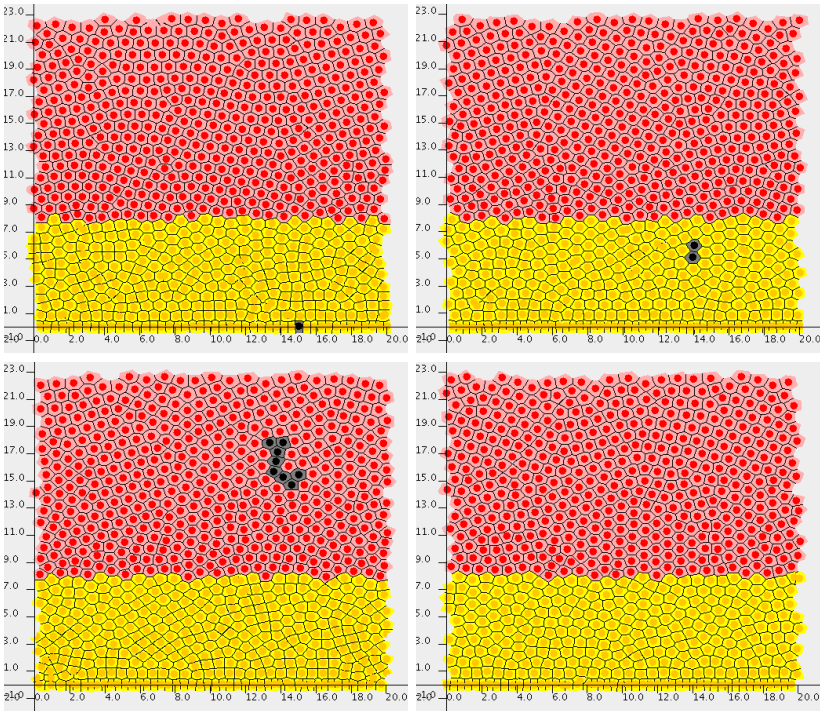

Figure 3.17: Results from a simulation showing how a mutant cell and its offspring are flushed out of a crypt. Mutant cells are marked as grey, transit cells as yellow and differentiated cells as pink. The snapshots show (top, left) the crypt when a mutation is initiated ($t = 0$), progression of the simulation after (top, right) 25 hours, (bottom, left) 50 hours and (bottom, right) 75 hours. The only difference between mutant cells and normal cells is that mutant cells have less dependence on Wnt; all mechanical properties are the same ($\eta_m = \eta_n,\ k_{mm} = k_{nm} = k_{nn}$). See §A.1 for parameter values.

No Wnt-dependence and stronger drag

As mentioned in §3.3.6, mutations in APC and β-catenin can affect cell movement by altering cell-adhesion and the stiffness of a cell's cytoskeleton in addition to changing a cell's proliferation rate. We model this this effect by increasing the drag on a mutant cell, and show below how this changes the mutant cells' behaviour.

Figure 3.18 shows that by doubling the drag on mutant cells, $\eta_m = 2\eta_n$, a mutant population is able to become the dominant population with in the crypt. The initial mutant cell is the same one chosen as in figure 3.17. This increase in drag means the mutant population is not forced off the base of the crypt. The mutant population persists and eventually becomes dominant within the crypt.

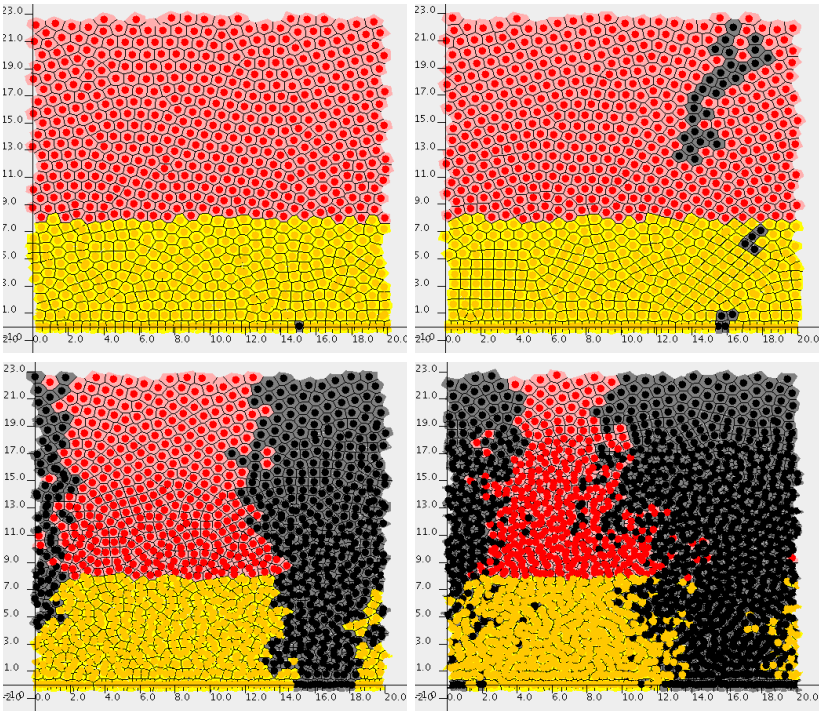

Figure 3.18: Results from a simulation showing how a mutant cell and its offspring become the dominant population within a crypt. Mutant cells are marked as grey, transit cells as yellow and differentiated cells as pink. The snapshots show (top, left) the crypt when a mutation is initiated ($t = 0$), progression of the simulation after (top, right) 100 hours, (bottom, left) 300 hours and (bottom, right) 400 hours. The mutant cells proliferate at a constant rate independent of Wnt, their drag coefficients are twice that of normal cells ($\eta_m = 2\eta_n$), but their spring constants are the same as for normal cells ($k_{mm} = k_{nm} = k_{nn}$). See §A.1 for parameter values.

Unfortunately increasing the drag coefficient leads to a large build-up of cells in the crypt, causing the simulation to break down. When there is a large number of mutant cells with high drag in the crypt, the net proliferation rate is higher, as mutant cells can proliferate throughout the crypt and they move slowly. When these two effects combine we find that more cells are born than are removed from the crypt, meaning the crypt is no longer in a quasi-steady-state. Eventually the simulation breaks down when number of cells in the crypt is about 10 times that in a normal crypt. Even though aberrant crypts may contain more cells than normal ones (as evidence in [141] reports), in practice it is unlikely that there would be the same build-up shown in the bottom-right snapshot in figure 3.18. If cells became too small (smaller than a threshold value) then it is likely that cells would arrest, undergo apoptosis or the crypt wall would buckle [131]. None of these phenomena are considered in our model; their implementation is the subject of future work.

Mutation further up the crypt

We now investigate how the position at which the mutant cells appear affects their ability to establish themselves within the crypt. This is of interest as there is great debate as to whether the initial mutation occurs in a cell at the bottom and its offspring move up the crypt ("bottom-up morphogenesis" as suggested by Preston *et al.* [131]) or whether the mutation occurs further up the crypt and move downwards ("top-down morphogenesis" as suggested by Shih *et al.* [153]).

In this case, the proliferating cells beneath the mutant cells exert a stronger mitotic force on the mutant cells, pushing them up and out of the crypt. As a result the mutant cells require a much stronger drag force to prevent them from being eliminated from the crypt. Figure 3.19 shows that, even when the drag coefficient of the mutant cells is ten times that of the normal cells, the mutant cells are flushed out of the crypt. However, when the drag is greatly increased (to thirty times that of normal cells) the mutant population is able to establish in the crypt, (see figure 3.20).

Figure 3.20 shows that the mutant population is initially pushed up the crypt (top, right). However as the mutant cells have a stronger drag than in those in figure 3.19, they move more slowly and establish a larger patch (figure 3.20, bottom, left). The force required to move the large patch is much greater than that needed to displace a single cell. This means that it is easier for mutant cells at the bottom of the patch to displace and compress the normal cells below them than to force the mutant patch upwards. This allows the mutant patch to expand downwards in the crypt.

The time sequence presented in figure 3.20 illustrates the potential for misinterpretting experimental data. In particular given only the data at late times $t = 150$ and $t = 300$ hours, it would appear as though a mutation had occurred at the top of the crypt (even though it actually occurred in a cell near the base of the crypt).

Change in mutant spring strength

As well as varying the drag coefficient, we also vary the spring constant for mutant-mutant and mutant-normal interactions. We consider these changes as experimental evidence suggests that mutations in APC and β-catenin change the cells' adhesion properties [18]. In figure 3.21, we present results for a case in which the spring constants between normal and mutant cells and between mutant cells are larger than those between normal cells ($k_{nm} = 1.5k_{nn}$, $k_{mm} = 2.0k_{nn}$). In this case, the mutant cells eventually colonise the crypt. This happens because when $k_{mm} > k_{nn}$, the mutant cells are less deformable than their normal counterparts. This prevents regions of high cell density from building up (contrast this with figures 3.18 and 3.20) and enables the mutant cells to eliminate the

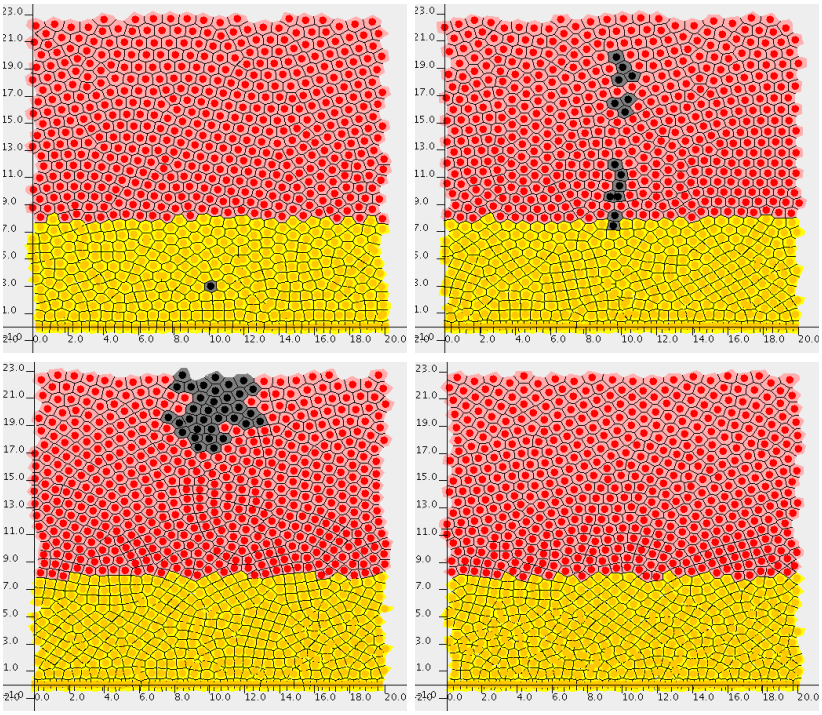

Figure 3.19: Results from a simulation showing how a mutant cell and its offspring are flushed out of a crypt. Mutant cells are marked as grey, transit cells as yellow and differentiated cells as pink. The snapshots show (top, left) the crypt when a mutation is initiated ($t = 0$), progression of the simulation after (top, right) 50 hours, (bottom, left) 100 hours and (bottom, right) 125 hours. The mutant cells proliferate at a constant rate independent of Wnt, their drag coefficients are ten times that of normal cells ($\eta_m = 10\eta_n$), but their spring constants are the same as for normal cells ($k_{mm} = k_{nm} = k_{nn}$). See §A.1 for parameter values.

normal ones from the crypt.

We remark that the fully mutant crypt is in quasi-steady-state with a cell density that is higher than that of a normal crypt. This is agreement with experimental evidence by Sansom *et al.* [141], who report higher levels of cell packing in mutant crypts.

When a crypt contains a homogeneous population of cells, the equations of motion can be characterised by a single parameter, $\xi_T = \dfrac{k_{TT}}{\eta_T}$, where $T = M, N$ depending on cell type. We show this by combining (3.1), (3.2) and (3.3):

$$\frac{d\mathbf{r}_i}{dt} = \frac{k_{TT}}{\eta_T} \sum_{j=1}^{j=N_i} \left(|\mathbf{r}_i - \mathbf{r}_j| - s_{ij}(t)\right) \frac{(\mathbf{r}_j - \mathbf{r}_i)}{|\mathbf{r}_j - \mathbf{r}_i|}, \tag{3.6}$$

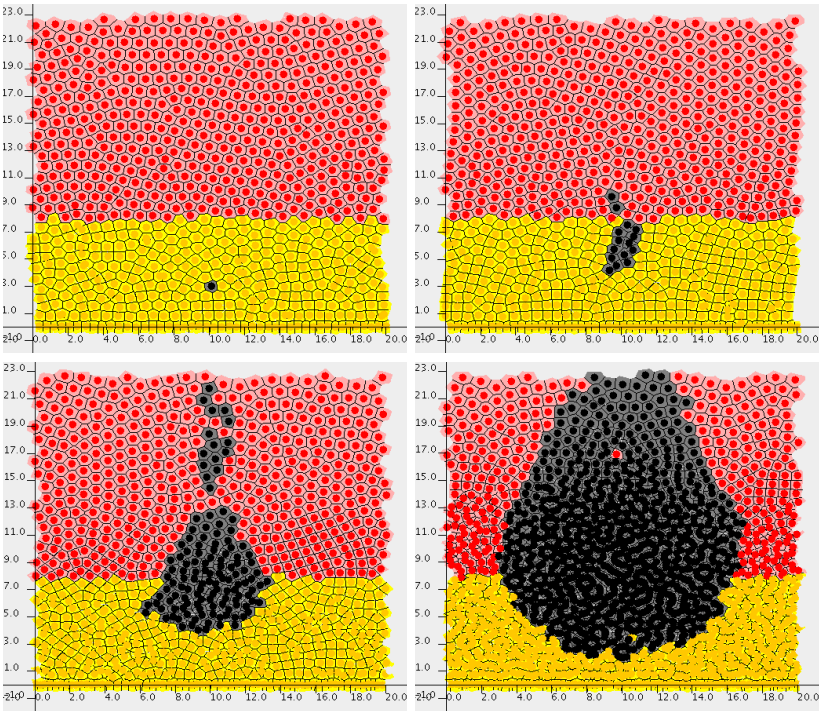

Figure 3.20: Results from a simulation showing how a mutant cell and its offspring establish themselves within a crypt. Mutant cells are marked as grey, transit cells as yellow and differentiated cells as pink. The snapshots show (top, left) the crypt when a mutation is initiated ($t = 0$), progression of the simulation after (top, right) 50 hours, (bottom, left) 100 hours and (bottom, right) 150 hours. The mutant cells proliferate at a constant rate independent of Wnt, their drag coefficients are thirty times that of normal cells ($\eta_m = 30\eta_n$), but their spring constants are the same as for normal cells ($k_{mm} = k_{nm} = k_{nn}$). See §A.1 for parameter values.

where $\mathbf{r}_i$ is the position of cell i, $\mathbf{r}_j$ the position of cell j and N_i the number of cells adjacent to cell i.

If we consider a crypt containing only mutant cells for which $\eta_m = 2\eta_n$ and $k_{mm} = 2k_{nn}$ (see figure 3.21 bottom, right) then the equations of motion are the identical to a crypt containing only normal cells. This explains how it is possible that the quasi-steady-state mutant crypt in figure 3.21(bottom, right) arises. In contrast to figure 3.18, in figure 3.21 the number of mutant cells does not build up as the increased drag on the mutant cells in balanced by the increased spring strength between mutant cells.

In addition to considering the effect of increasing the spring constant between mutant cells, we also investigate what happens if we decrease the spring constants between mutant cells (see figure 3.22).

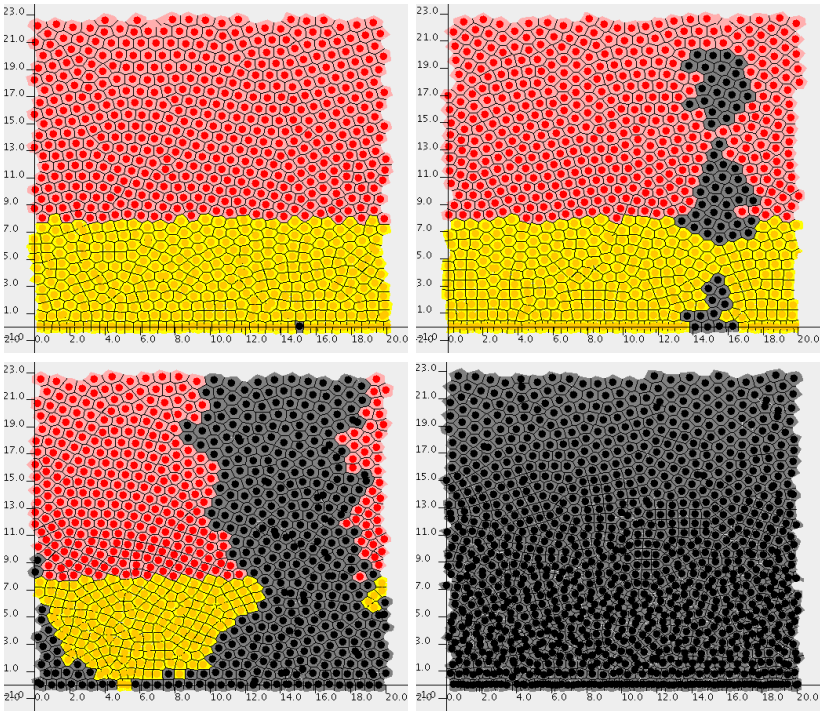

Figure 3.21: Results from a simulation showing how a mutant cell and its offspring populate a crypt. Mutant cells are marked as grey, transit cells as yellow and differentiated cells as pink. The snapshots show (top, left) the crypt when a mutation is initiated ($t = 0$), progression of the simulation after (top, right) 100 hours, (bottom, left) 200 hours and (bottom, right) 275 hours. The mutant cells proliferate at a constant rate independent of Wnt, their drag coefficients are twice that of normal cells ($\eta_m = 2\eta_n$). The spring constants between two mutant cells is $k_{mm} = 2k_{nn}$ and between mutant and normal cells is $k_{nm} = 1.5k_{nn}$. See §A.1 for parameter values.

In this case $k_{mm} = k_{nn}/4$ and $k_{nm} = k_{nn}/2$ (all other parameters are as in figure 3.18). These changes cause the mutant cells to be flushed out of the crypt. The mutant cells are forced together and offer less resistance to the mitotic pressure exerted by the normal cells, which have stronger springs.

3.6 Discussion

In this chapter we have adapted a cell-centre model [109] that describes the proliferation, migration and differentiation of cells within a colorectal crypt. The model includes cell-level mechanics and the ability to include details of subcellular signalling that influence the cell cycle (see Appendix A.2).

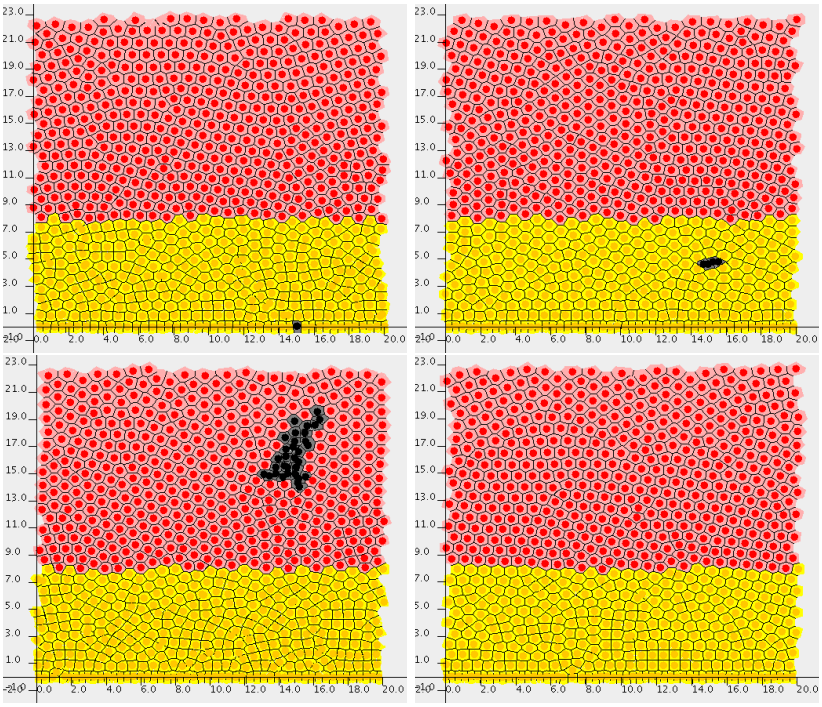

Figure 3.22: Results from a simulation showing how a mutant cell and its offspring are flushed out of a crypt. Mutant cells are marked as grey, transit cells as yellow and differentiated cells as pink. The snapshots show (top, left) the crypt when a mutation is initiated ($t = 0$), progression of the simulation after (top, right) 40 hours, (bottom, left) 80 hours and (bottom, right) 120 hours. The mutant cells proliferate at a constant rate independent of Wnt, their drag coefficients are twice that of normal cells ($\eta_m = 2\eta_n$). The spring constants between two mutant cells is $k_{mm} = 0.25k_{nn}$ and between mutant and normal cells is $k_{nm} = 0.5k_{nn}$. See §A.1 for parameter values.

By using agile computational methods to include these features, we have developed a framework for a multiscale model of colorectal cancer. The adaptations made to the model take into account biological features such as Wnt-dependent proliferation, free movement of cells at the base of the crypt, drag coefficients proportional to cell size, cell-cell adhesion coefficients proportional to the area of contact between the cells, and the inclusion of mutant cells.

We showed that unpinning the stem cells at the base of the crypt, enabled it to become monoclonal. When the drag-coefficients depended on cell area, we found that fewer cells built up on the base of the crypt. Having the cell-cell interaction forces between cells dependent on the amount of contact between them resulted in the cells having a more hexagonal shape.

When mutant cells were introduced into the crypt, the ability of those with a higher drag, $\eta_m > \eta_n$

(representing a more rigid cytoskeleton and stronger bonds to the underlying stroma), to colonise the crypt was higher than those of mutant cells for which $\eta_m = \eta_n$. This effect became more pronounced as the position at which the initial mutation occurred was further up the crypt. In this case, the mutant cells required a much stronger drag coefficient than normal cells in order to establish themselves within the crypt. This is consistent with the finding in our continuum model, detailed in §2, that the drag on the mutant cells needed to be higher if the initial mutant cell was further up the crypt.

We uncovered a case that showed how experimental results could potentially be misinterpreted. In some cases mutant cells need to establish a large population before they start to invade downwards into a crypt. Before the larger population is established, the mutant cell may have been moved up the crypt. If this was viewed at a late stage, it may appear that the first mutant cell occurred near the top of the crypt, when in fact it occurred near the bottom.

Further results showed that it was possible to get a crypt filled entirely with mutant cells when both the cell-cell interaction fores and drag of mutant cells was increased.

There is biological evidence to suggest that the most common mutations in colorectal cancer are in APC and β-catenin. Further evidence suggests these mutations lead to cells no longer having Wnt-dependent proliferation [19, 74], having increased levels of cell adhesion [15], a more rigid cytoskeleton [115] and lower levels of cell migration [141]. When mutant cells have these properties, we were able produce a crypt filled only by mutant cells, descended from a single mutant cell. This "fully adenomatous crypt" has been reported as being one of the earliest stages of colorectal cancer [131]. Further, the "fully adenomatous crypt" had a higher level of cell packing as reported in [141].

The models developed show good correlation to experiments for the staining and dissection of the crypt. However we were unable to distinguish which of the mechanical models (constant or edge-length-dependent springs, constant or area-dependent drag) best reflect the biology, as several of the models produced qualitatively similar results. We have produced some readings from our simulations of measureable quantities, such as how cell size and cell shape vary with position in the crypt. We hope biologists will find these measurements useful and will be able to help us distinguish which models best reflect the crypt physiology.

When modelling the crypt, we have assumed that the combined effect of cell-cell adhesion (attractive) and forces conserving cell size (repulsive) could be modelled by linear springs. This assumption was not ideal as it is difficult to implement stronger or weaker adhesion bonds between cells. For example, if the spring strength is increased to model stronger bonds between cells, it will pull cells together faster if they are further than the natural spring length apart. However, when cells are closer than

the natural spring length apart, it will force them apart faster. This problem could be solved by using a different constitutive law for cell movement that models cell-cell adhesion and forces restoring cell size separately. Examples of how this could be done include assuming cells to be deformable spheres as in other cell-cell centre models such as [48, 145]. However the cost to modelling in this way is that it requires estimation of more parameters. Having a separate term for cell-cell adhesion would also allow the inclusion of adhesion dependent on the level of membrane-bound β-catenin. This has been achieved by authors such as Conde-Ramis *et al.* [133] for a model of tumour invasion, and would allow us to have more coupling in our model between protein levels and the mechanical properties of the cells within our multiscale model of the colorectal crypt.

Another modelling assumption is that the crypt can be viewed as a cylinder. This causes too many cells to accumulate at the base of the crypt. This has been addressed, in part, by other developers in the CHASTE project (Alex Fletcher, see [125]) with the development of a "crypt-projection" model. This model projects a three-dimensional, test-tube shaped crypt onto a two dimensional sheet. This addresses the problem of cell build-up at the base as cells can transfer forces under the crypt base. Ideally a full three dimensional model should be developed, but this is beyond the scope of this thesis.

If a fully three dimensional model of the crypt were to be developed it would be interesting to incorporate the work of Drasdo *et al.* [48] to study how crypt buckling can occur due to the build up of mutated cells. We could then use the model to study how protein-level mutations can lead to changes in crypt morphology.

Further numerical simulations are needed to confirm the findings in §3.5.2. Here we found that mutant cells initially near the base of the crypt with a higher drag were more likely to become the dominant population within the crypt. However, to ascertain how the probability of a mutant population becoming dominant change as its properties vary, many more simulations are needed - approximately 100 simulations (each one taking approximately eight hours) for each set of parameter values. Unfortunately due to time restrictions we were unable to perform the required number of simulations and therefore leave this as further work.

In summary in this chapter we have developed a multiscale cell-centre model of the crypt. Numerical simulations reveal that mutant cells which do not have Wnt-dependent proliferation can establish themselves within the crypt if they have higher levels of cell-substrate adhesion and a more rigid cytoskeleton. The level cell-substrate adhesion and cytoskeleton rigidity required depends on the position of the initial mutant cell.

Chapter 4

Cell-vertex model of the colorectal crypt

4.1 Introduction

In the previous chapter we explained how we adapted a cell-centre model [109] of the colorectal crypt to reproduce several biological phenomena, such as crypt monoclonality. However the model has several weaknesses. The main weakness arises because the forces related to cell-cell adhesion are indistinguishable from those designed to conserve cell size. This is because all cell-cell interactions are modelled by springs connecting neighbouring cells. As a result it is difficult to model increased (or decreased) cell-cell adhesion. For example, if you were to model increased cell-cell adhesion by increasing the spring constant, then cells further than the natural spring length apart would be pulled together faster, but cells closer than the natural spring length would be pushed away from each other faster.

To address this issue we could adapt the cell-centred model and follow the approach of Schaller and Meyer-Hermann [145, 146, 147, 148] or Drasdo *et al.* [48, 49, 57, 68]. These authors treat cells as deformable spheres and and include terms for volume conservation and contact-area-dependent cell-cell adhesion. However the shapes the cells can take are limited [29] and often require the time-consuming Delaunay tessellation to be performed and a Voronoi diagram must be constructed at each time step [145].

As an alternative to adapting the cell-centre model we use a cell-vertex model. Cell vertex models are similar to cell-centre models in that both are dynamic lattice-free cell-level models [112]. However they differ in how the cells are defined. In cell-centre models, cells are defined by a point at their centre, whereas in cell-vertex models, the polygonal cells are characterised by the location of their vertices [181] (see figure 4.1).

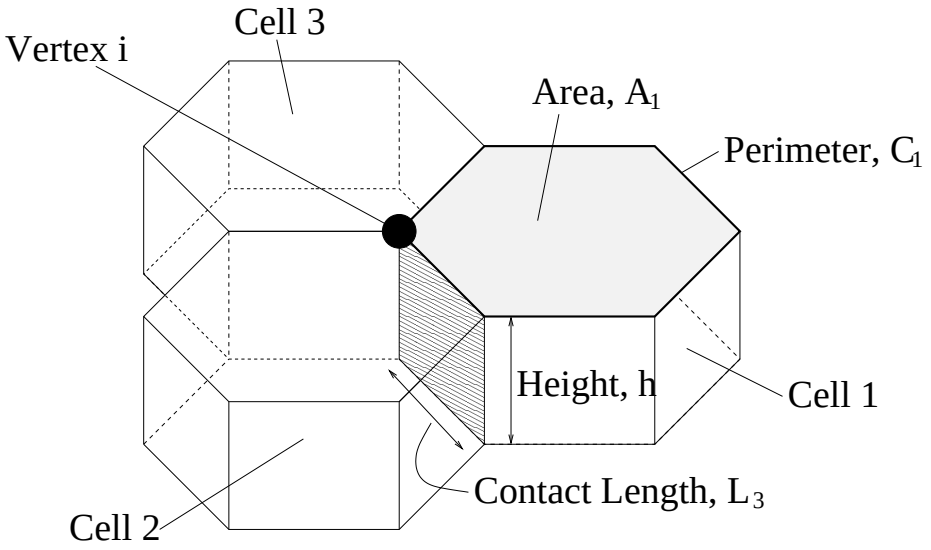

Figure 4.1: Schematic showing three prism-shaped cells (1,2,3) that form part of an epithelium. Each of the cells are of the same height, h, such that the cells can be described by a 2D sheet, with vertices such as vertex i defined where three cell edges meet. The movement of the vertex i is dependent on the properties of the surrounding cells such as their size, $h \times A$, perimeter, C, and the cell-cell contact area, $h \times L$.

The main advantage of cell-vertex models is that they lend themselves to the study of cell-cell adhesion [27]. This is because connecting vertices define the contact area between two cells and, in contrast to cell-centre models, no time-consuming Delaunay tessellation or Voronoi diagram is needed [29]. Cell-vertex models have also been shown to accurately model patterns of cell shapes found in monolayers [69, 71], whereas cell-centre models are restricted to shapes permitted by Voronoi tessellation [27].

4.1.1 Outline

In this chapter we develop a cell-vertex model to describe the proliferation and movement of epithelial cells in a colorectal crypt, paying particular attention to the role of cell-cell adhesion. The chapter is structured in the following way. In §4.2 we describe the features of the cell-vertex model in more detail, the results from simulations of the model are presented in §4.3 and finally our findings and the relative merits of using such a model are discussed in §4.4.

4.2 The cell-vertex model

In this section we introduce and develop a cell vertex model for a colorectal crypt. In §4.2.1 we introduce the basic features of a cell-vertex model. In §4.2.2 we explain how the basic model has been refined to describe a colonic crypt. The boundary conditions and initial conditions required to complete the model are presented in §4.2.3.

4.2.1 Basic model

The model described in this sub-section is similar to that used by Nagai and Honda [112] to investigate the formation of epithelial tissues. The basis of the model is that each cell has a free energy associated with it and vertices move in order to reduce the total free energy of the population of cells. The model is described below in stages. We start by stating the underlying assumptions. We then describe how the vertices move, present the equations of motion and finish by describing the other processes needed for a cell-vertex model.

Assumptions

In order to model the epithelial cells within a 2D cylindrical crypt, we must first make some assumptions:

- Cells are all of the same height. This allows us to treat the cells as a two dimensional monolayer and thereby greatly reduces the complexity of the problem. This assumption has often been made in cell-vertex models of epithelium [71, 112, 181, 182, 183] and has often been used when modelling a colorectal crypt [109, 155].
- Cells can be of only a limited number of types: transit (T), differentiated (D) or mutant (M). Specific types of differentiated cells, such as Goblet cells, are ignored.
- All mature cells have the same target size. This may be overly simplistic as some mutant cells are found to be smaller than normal cells [9, 91]. However this assumption is made by most other models of the colorectal crypt [57, 109].
- When cells undergo mitosis they split into two equal areas, again a common assumption in many cell-level models [31, 48, 147].
- Cells are assumed to move in response to passive mechanical effects, such as cell-cell adhesion and volume conservation; active effects such as chemotaxis are ignored. The main driver of

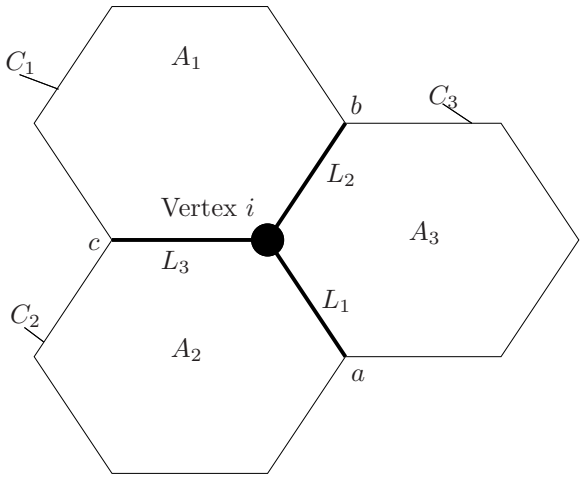

Figure 4.2: Figure showing the three cells (1,2,3) which are affected by movement of vertex i. The surrounding cells have areas, A_1, A_2, A_3 and perimeters C_1, C_2, C_3. Lengths L_1, L_2, L_3 represent the distances from vertex i to vertices a, b, c respectively.

cell movement in the colorectal crypt is thought to be mitotic pressure [171], although there is some evidence of active migration especially in the mouse intestinal villi [116]. However the significance of these phenomena are in the colorectal crypt is unclear [65].

Equations of motion

We consider a population of n epithelial cells each of height h, where each of the polygonal cells is defined as an ordered list of vertices. Associated with each cell is a free energy and the total free energy, U, of the population of cells is determined by a summation over all the cells. For each vertex, the gradient of free energy evaluated at the vertex is assumed to exert a force on the vertex. This force is balanced by a viscous drag term proportional to the vertex's velocity. As with the cell-centre model in Chapter 3, the viscous force represents the breaking and reforming of integrin bonds with the substrate and rearrangement of the cytoskeleton in the cells surrounding the vertex. It is that assumed inertial effects are negligible and by balancing the forces on the vertex, we find each vertex i, at position $\mathbf{r}_i$, moves according to the following equation of motion,

$$\eta_i \frac{d\mathbf{r}_i}{dt} = -\nabla_i U, \tag{4.1}$$

where t is time, η_i is the drag on vertex i and ∇_i is the gradient with respect to vertex i.

Free energy

The free energy, U, is comprised of three parts, a deformation energy, U_D, a membrane surface tension energy, U_S, and a cell-cell adhesion energy, U_A, as follows:

$$U = U_D + U_S + U_A = \sum_{j=1}^{n} \left(U_D^j + U_S^j + U_A^j \right). \tag{4.2}$$

The terms U_D^j, U_S^j, U_A^j represent, respectively, the deformation energy, membrane surface tension energy and cell-cell adhesion energy for each cell j and n is the total number of cells.

The volume deformation term aims to ensure that cells attain a target volume [71, 112, 183]. The deformation energy, U_D^j, for cell j, is given by

$$U_D^j = \kappa(V_j - V_{N,j})^2 = \kappa h^2 (A_j - A_{N,j})^2, \tag{4.3}$$

where the volume of cell j is $V_j = hA_j$, with A_j the two-dimensional area and h the cell height. Similarly the natural volume is $V_{N,j} = hA_{N,j}$, where $A_{N,j}$ is a target area. κ is a positive constant analogous to an elastic constant per unit volume [71].

The membrane surface tension term is included to conserve membrane length and acts to drive cells to a circular shape. This concept is often used in cellular Potts models [122] and other vertex models [142]. The membrane surface energy, U_S^j, for cell j, is given by

$$U_S^j = \tau h^2 \left(C_j - C_{N,j} \right)^2, \tag{4.4}$$

where C_j is the cell's perimeter (in two dimensions), $C_{N,j}$ is the natural perimeter and τ is a positive constant. The natural perimeter is the circumference of a circular cell of area $A_{N,j}$, $C_{N,j} = 2(A_{N,j}\pi)^{\frac{1}{2}}$. This functional form is chosen as cells in free suspension generally will tend to a circular shape [147].

The cell-cell adhesion energy term represents the free energy associated with cadherin and other bonds on the cell's membrane. It is proportional to the contact area between the two cells involved and dependends on the cell types involved. Different cell types can have selective cell-cell adhesion due to the different types of cadherin junctions in contact [160]. This concept features in most cell-vertex models [27, 71, 112, 181, 182, 183]. The cell-cell adhesion energy, U_A^j, for cell j is given by

$$U_A^j = \sum_{m=1}^{M_j} \alpha \left(T_j, T_m \right) h L_{j,m}, \tag{4.5}$$

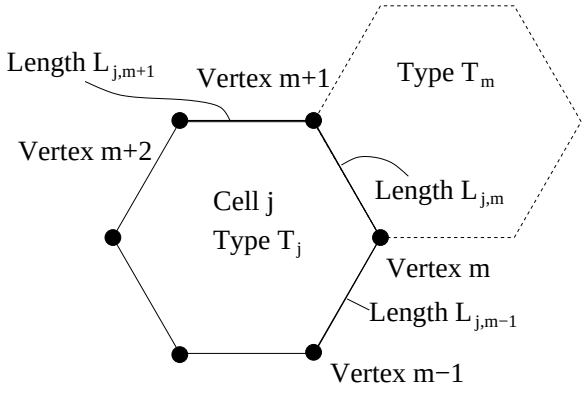

Figure 4.3: Figure showing the lengths used when calculating cell-cell adhesion energy, U_A^j, for a cell j.

where M_j is the total number of vertices in cell j, $L_{j,m}$ is the length of the edge m, the line connecting the mth vertex and vertex $m+1$, the next vertex in an anticlockwise direction in cell j (see figure 4.3), T_m is the cell type of the other cell containing edge m, T_j is the type of cell j and $\alpha\left(T_j, T_m\right) \equiv \alpha\left(T_m, T_j\right)$ is a positive constant dependent on the cell types in contact. The cell-cell adhesion energy associated with cells j and m is proportional to the contact area $hL_{j,m}$ between the two cells involved.

High values of α represent cells which do not want to be in contact, low values of α correspond to cells that prefer to be in contact. The length $L_{j,m}$ is counted twice, once by cell j and once by cell m. The only lengths that are not counted twice are those on an external boundary.

Combining (4.1) - (4.5), the equation of motion for vertex i can be written as

$$\eta_i \frac{d\mathbf{r}_i}{dt} = -\nabla_i U = -\nabla_i \sum_{j=1}^{n} \left[\lambda (A_j - A_{N,j})^2 + \beta \left(C_j - C_{N,j}\right)^2 + \sum_{m=1}^{M_j} \gamma \left(T_j, T_m\right) L_{j,m} \right], \tag{4.6}$$

where $\lambda = \kappa h^2$, $\beta = \tau h^2$, $\gamma\left(T_j, T_m\right) = \alpha\left(T_j, T_m\right) h$ and η_i is the average of the drag of the three surrounding cells.

As the movement of vertex i affects only the free energy of the three surrounding cells [112], the gradient of free energy, $\nabla_i U$, can be written explicitly in terms of these cells as

$$\begin{aligned} \nabla_i U = \sum_{k=1}^{3} \Big[& 2\lambda (A_k - A_{N,k}) \nabla_i A_k \quad + \quad 2\beta \left(C_k - C_{N,k}\right) \left(\nabla_i L_{k-1} + \nabla_i L_{k+1}\right) \\ & + \quad \gamma\left(T_k, T_{k-1}\right) \nabla_i L_{k+1} + \gamma\left(T_k, T_{k+1}\right) \nabla_i L_{k-1} \Big] \end{aligned} \tag{4.7}$$

where k represents the corresponding cell around the vertex, and A_k, C_k are the cell's area and

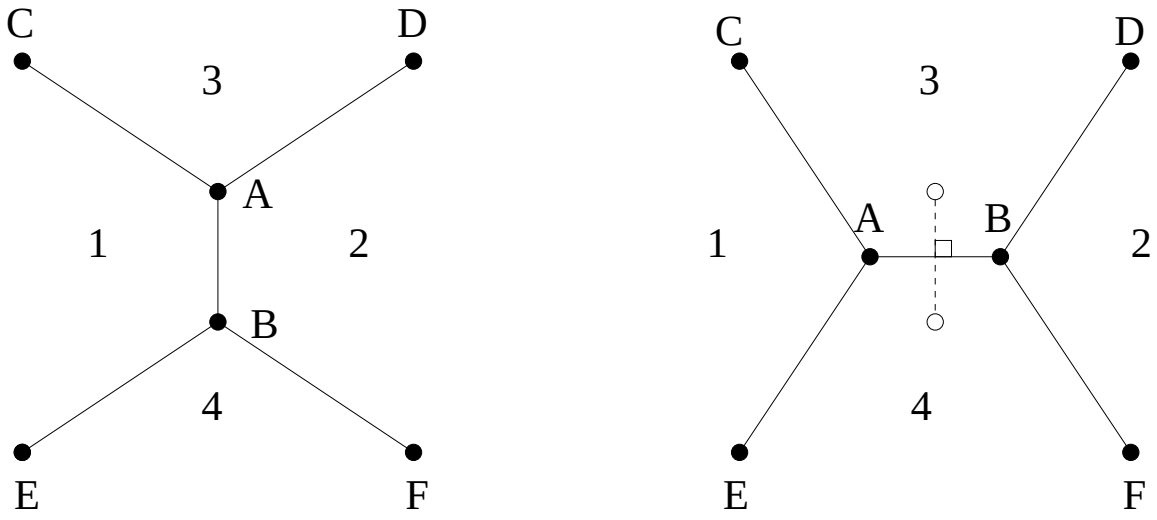

Figure 4.4: Topological rearrangement of cells via a T1 swap. Before the rearrangement (left), cells 1 and 2 are in contact. Following the rearrangement (right), cells 3 and 4 are in contact. Cells are represented by numbers $1-4$ and vertices are represented by letters A–B

perimeter, respectively, (see figure 4.2). L_k represents the length of the connection from vertex i to the vertex it is connected to that is not part of cell k. For example L_1 in figure 4.2 represents the distance from vertex i to vertex a.

By combining (4.6) and (4.7) and by using the identities in Appendix B.1, the equations of motion for the vertices can be simplified to a non-linear expression in terms of vertex positions (not shown).

T1 swap

Along with equations of motion we must also allow cells to come into contact and to lose contact with one another. This is achieved by a topological change known as the T1 swap [50]. It is widely used in cell-vertex models [50, 71, 112, 181, 182, 183] and can be described with the aid of figure 4.4.

The T1 swap happens in the following way: when the connecting length between cells 1 and 2 (AB in figure 4.4) is sufficiently small (0.05 natural cell-lengths in our simulations), we move the vertices (A & B) to positions the same distance away from each other but perpendicular to where they previously were. The vertices of each cell are updated so cells 1 and 2 lose a vertex and cells 3 and 4 gain a vertex. The edges between vertices are also updated (so A is now connected to B, C, E; B is now connected to A, D, F; D is now connected to B instead of A; and E is now connected to A

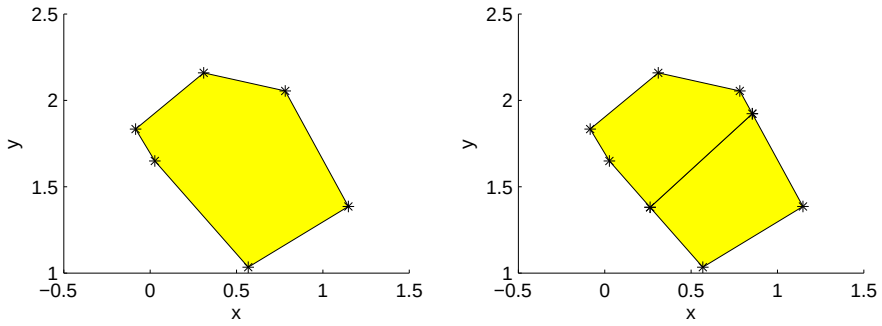

Figure 4.5: Plot showing how a cell (left) giving birth splits into two (right) along its shortest axis that passes through the centroid.

instead of B). The result of the T1 swap is that cells 3 and 4 are now in contact with each other as opposed to cells 1 and 2.

4.2.2 Specialisation for the crypt

As well as the features described in §4.2.1, modifications are made so that the model reflects the biology of the colorectal crypt. These specialisations are the inclusion of cell birth, cell-cycle models, the effect of Wnt and accounting for the behaviour of mutant cells.

Cell birth

When a cell reaches the end of the cell cycle, its moments are calculated (Appendix B.2) in order to determine how to it divides [31]. The cell is split into two equal parts along the shortest axis (perpendicular to its long axis) through the centroid (see figure 4.5) (If the cell is perfectly symmetric, for example a hexagon, the cell chooses, at random, an axis to split along). Two new vertices are placed at the intersection between the dividing line that passes through the centroid and the cell perimeter, thereby creating two daughter cells from a single parent cell.

It has been suggested that the cleavage plane of a cell during mitosis can be defined by its long axis or by a tissue-orientated system [143]. As we are unsure of whether mitosis in the colorectal crypt is tissue-oriented, unless stated, we assume it is based on long-axis orientation.

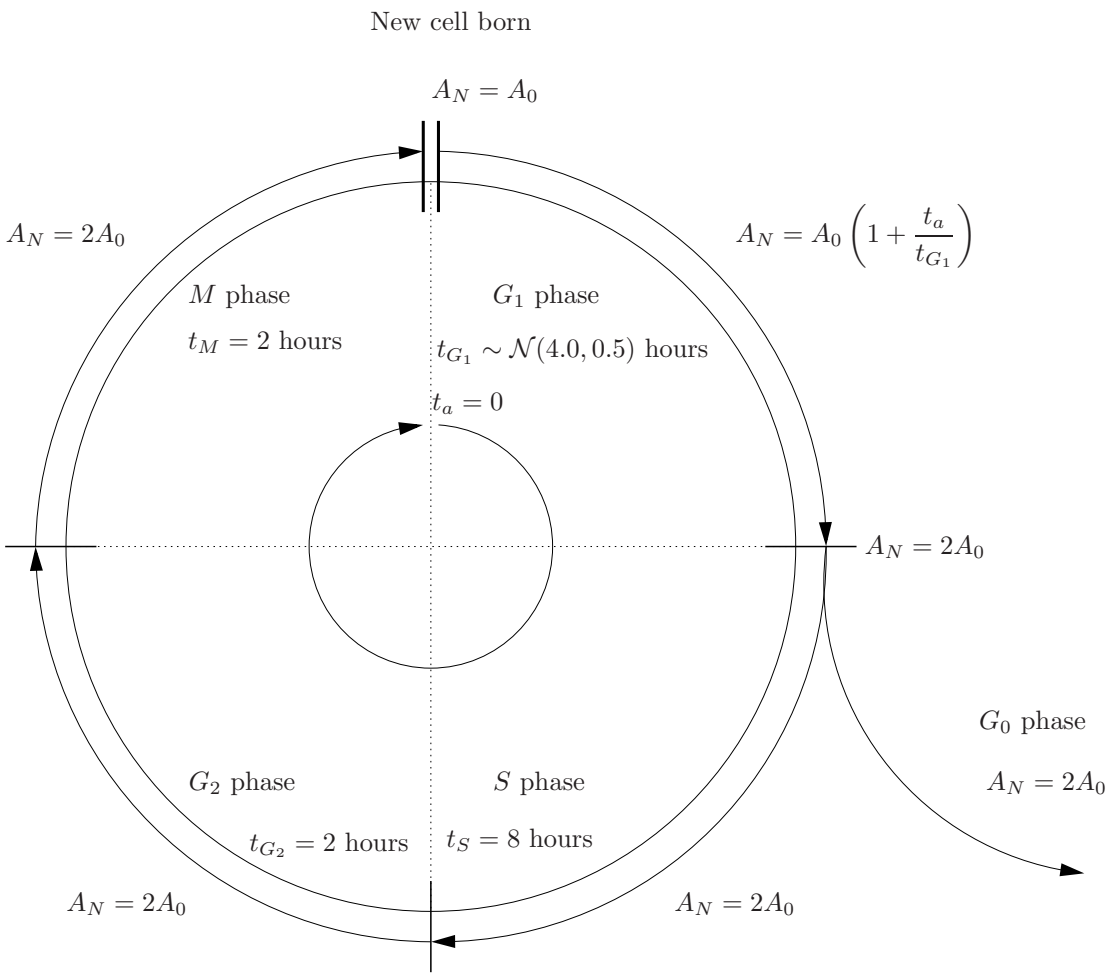

Figure 4.6: The cell-cycle model for epithelial cells within a colorectal crypt. Cells are born (top ||), grow in size through G_1 phase, by changing their target area A_N, and either become quiescent and enter G_0 phase or carry on through the cell cycle passing through S, G_2 and M phase.

Cell-cycle model

As detailed in the previous chapter (see §3.3), the cell cycle is a series of phases (regulated by protein levels) through which a cell passes before proliferation [2]. To reflect this within our model, we embed a cell-cycle model within each cell in the simulation. When a cell is born, its age, t_a, is set to zero and it starts at the beginning of G_1-phase with target area half that of a mature cell, $A_N = A_0$ (see figure 4.6). The cell is assigned a G_1-phase time, t_{G_1}, and hence a cell-cycle time of $t_{CC} = t_{G_1} + t_S + t_{G_2} + t_M$. The duration of the G_1 is chosen randomly to ensure that a cell's offspring are not synchronised. The values of t_S, t_{G_2} and t_M are fixed for all cells. Throughout G_1-phase,

Age of cell	Phase	Cell Target Area
$0 < t_a \leq t_{G_1}$	G_1	$A_0\left(1+\frac{t_a}{t_{G_1}}\right)$
$t_{G_1} < t_a \leq t_{G_1}+t_S$	S	$2A_0$
$t_{G_1}+t_S < t_a \leq t_{G_1}+t_S+t_{G_2}$	G_2	$2A_0$
$t_{G_1}+t_S+t_{G_2} < t_a \leq t_{CC}$	M	$2A_0$
$t_a \geq t_{G_1}$	G_0	$2A_0$

Table 4.1: How a cell's phase and area depend on its age, t_a.

$0 < t_a \leq t_{G_1}$, the target area of the cell grows linearly until it reaches the natural size it will maintain throughout the rest of the cell cycle, $A_N = 2A_0$. If the cell is terminally differentiated it exits the cell cycle and enters G_0-phase, with $A_N = 2A_0$, and remains in that phase for the rest of its life, $t_{CC} \to \infty$. If the cell is a transit cell it passes through the following phases: for $t_{G_1} < t_a \leq t_{G_1}+t_S$, the cell enters S-phase; it enters G_2-phase for $t_{G_1}+t_S < t_a \leq t_{G_1}+t_S+t_{G_2}$; and finally it enters M-phase for $t_{G_1}+t_S+t_{G_2} < t_a \leq t_{CC}$. At the end of M-phase the cell splits in two giving birth to another cell and the cell cycle is restarted for each cell. The details are summarised in Table 4.1.

Wnt-dependent proliferation

To mimic the proliferative architecture of a crypt within our model, cells that are within a threshold distance of the bottom of the crypt, $y = H_W$, are deemed to be stimulated by Wnt and are termed transit cells (Type T); cells above the threshold distance from the base of the crypt are deemed to have insufficient levels of Wnt and are termed differentiated cells (Type D). Transit cells progress through the cell cycle and can proliferate, whereas differentiated cells always move from G_1 to G_0.

Mutations

To account for mutations in APC and β-catenin, we define a new cell type, mutant cells (Type M), in our model. Mutant cells never enter G_0 phase or become differentiated, regardless of their position; as such these cells can proliferate throughout the crypt.

Since APC and β-catenin are multi-functional proteins, when mutated they alter (i) the behaviour of a cell's cytoskeleton [115], (ii) cell-stroma adhesion [141] and (iii) cell-cell adhesion [18]. To account for (i) and (ii), we assign normal (both transit and differentiated) and mutant cells different drag terms, η_N and η_M, respectively, and assume that the drag on a vertex, η_i, is the average of the drags of the three cells that surround it. Consequently for a vertex surrounded by mutant cells the drag

is $\eta_i = \eta_M$, a vertex surrounded by two mutant cells and one normal cell has $\eta_i = 2\eta_M/3 + \eta_N/3$, while a vertex with one mutant cell and two normal cells has $\eta_i = \eta_M/3 + 2\eta_N/3$ and one involving three normal cells has $\eta_i = \eta_N$.

To account for (iii), we allow mutant cells to have different surface contact energies. So, for example, mutant cells can be made more adhesive to each other than to transit or differentiated cells, $(\gamma(M,M) < \gamma(T,M), \gamma(M,M) < \gamma(D,M))$, or more adhesive to transit cells than differentiated cells, $(\gamma(M,T) < \gamma(M,D))$.

4.2.3 Boundary and initial conditions

The geometry of the crypt is simplified to a two dimensional cylindrical sheet of height, H_C, and circumference, W_C. At no point can cells pass into the stroma (surrounding material); cells can only be removed by being shed into the lumen at the top of the crypt.

At the top of the crypt, if the mean position of a cell's vertices is more than a distance of H_C from the base, the cell is deemed to be dead and vertices that are not part of any living cell are removed. This simplification neglects the behaviour of cells on the luminal surface.

If any vertices on the base of the cylinder attempt to move below $y = 0$, as for the modified cell-centre model in Chapter 3, they experience a reaction force perpendicular to the base of the crypt such that they remain on $y = 0$. Vertices on $y = 0$ can only move off $y = 0$ through a T1 swap, (§4.2.1), with one of the vertices being placed on $y = 0$ and the other being placed directly above it. This rule ensures that there is no flux of cells through the base of the crypt and that there are no gaps in the epithelium.

To account for the periodicity of the cylindrical crypt, any vertices with an azimuthal distance $x > W_C$ have their azimuthal position changed to $x \mapsto x - W_C$, where W_C is the crypt width. Similarly any vertices that have an azimuthal distance of $x < 0$ have their azimuthal position changed to $x \mapsto x + W_C$. Any cells with edges that lie across the $x = 0, W_C$ boundary, have the positions of their vertices temporarily moved when calculating cell areas, edge-lengths and perimeters.

Initially all cells are assumed to be regular hexagons, (apart from those at the top and bottom, defined to be pentagons) of area $\sqrt{3}/2$. There are no gaps between the cells, which are packed in rows up the crypt. Cells with a mean vertex position further than H_W from the base of the crypt are assumed to be differentiated, while those closer than H_W from the base of the crypt are assumed to be transit cells. Each transit cell is assigned a stochastically varying cell-cycle time, chosen from a normal distribution, and the time since the transit cells are born is set to be the cell-cycle time

multiplied by random number chosen from the uniform distribution $(0, 1)$.

4.2.4 Numerical method and validation

The model is solved numerically in the following way: at the beginning of each time loop, the area, equation (B.1), and perimeter of each cell is calculated and used to calculate the gradient of free energy, (4.7), for each vertex. The displacement of each vertex, (4.1), is then calculated using a forward-Euler method. All vertices are checked to see if any neighbouring vertices are close enough for a T1 swap; if necessary these swaps are performed. The age of each cell, j, is checked to see if $t_a(j) > t_{CC}(j)$; if so, the cell divides into two daughter cells. The coordinates of all transit cells are checked: if any transit cells have moved out of the Wnt stimulated zone, $y = H_W$, their type is changed to be differentiated. Finally, if the mean position of the vertices of any cell has passed the top of the crypt, $y = H_C$, the cell is removed.

Other explicit solvers such as second-order Runge-Kutta and fourth-order Runge-Kutta were used to calculate the movement of the vertices. However they did not increase stability of the model significantly and made the code two or four times slower, respectively, than an Euler solver.

To validate our model we reproduced results from a cell-sorting model [28]. A mixed population of two types of cells was considered and by varying the cell-cell adhesion constants, $\gamma(I, J)$, $I, J = 1, 2, E$, different types of behaviour were observed (the indices $1, 2, E$ refer to the two cell types and the region exterior to the cells). The behaviour included: the sorting of one population from the other, mixing of the two populations to produce a checkerboard pattern and the engulfment of one population by another.

4.2.5 Notation

The cell-cell adhesion energy is the same for cells of the same type but may depend on the types of cells in contact. For ease of notation we represent the parameters relating to cell-cell contact as follows

$$\gamma(I, J) = \gamma_{IJ}, \text{ where } I, J \in \{T, D, M, E\} \tag{4.8}$$

where T, D, M represent transit, differentiated and mutant cells and E represents the external boundary.

The drag parameter for transit and differentiated (normal) cells is represented by η_N and for mutant

cells by η_M. The values of these parameters are discussed in Appendix B.3.

4.3 Numerical results

4.3.1 Normal crypt

The model described in §4.2 was solved for a crypt containing only transit and differentiated cells. We were able to replicate behaviour that has been observed experimentally, including the movement of cells from the base to the top of the crypt. We are also able to follow the offspring of a cell within the crypt.

In all the simulations in this sub-section, the mechanical parameters of all the cells are assumed identical (unless stated otherwise): the drag parameter (η_i) and parameters relating to cell size (λ) and shape (β), are given in §B.3. The cell-cell adhesion energy is identical for all cells ($\gamma_{TT} = \gamma_{TD} = \gamma_{DD} = \gamma_{TE}/2 = \gamma_{DE}/2$). The values of γ_{TE} and γ_{DE} are twice that of γ_{TT}, as external edges (at the top and bottom of the crypt) are only counted once (all other edges are counted twice).

Cell lineages and monoclonality

To investigate how a cell and its offspring evolve within a crypt, we label a single transit cell on the base of the crypt at time $t = 0$. The marker is retained by the cell and all its offspring as they move through the crypt. The positions of the marked cells at times $t = 0,\ 50$ and 100 hours are shown in figure 4.7. As well as cell movement up the crypt due to mitotic pressure, there is also some lateral movement, due to local changes in forces. These local changes are due to stochastically variation in the cell-cycle durations. This leads to cells dividing at different times and growing at different rates, which in turn, creates local areas where gradients of free energy are high. We also note, over long times, that the number of cells born is the almost same as the number of cells removed at the top of the crypt. This quasi-steady-state is thought to occur *in vivo* [126].

In figure 4.8, each cell initially on the base of the crypt is individually marked and their offspring retain that label. The offspring of the progenitor cells form approximately linear columns parallel to the crypt axis. The fragmentations in the columns and lateral movement are due to stochastic variation in the cell-cycle times. Figure 4.8 also reveals that some lineages produce more progeny than others. This can not be due to the cells having different mechanical properties, as all cells are mechanically identical. The effects are due to the stochastic variations in birth times and cell-cycle

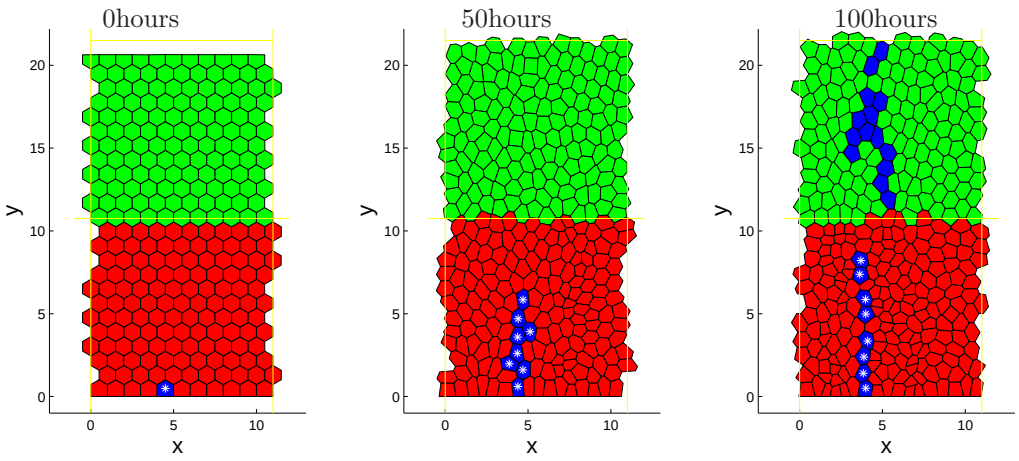

Figure 4.7: Figure showing how a progenitor cell and its offspring move within a crypt with (left) $t = 0$ hours, (centre) $t = 50$ hours, (right) $t = 100$ hours. The blue cells arise from the same lineage, the red cells are transit cells and green cells are differentiated cells not from that lineage. Blue cells marked with a $(*)$ are also transit cells; those without a $(*)$ are differentiated. The vertical lines at $x = 0$ and $x = W_C$ represent the periodic boundary conditions and the horizontal line at $y = H_W$ represents the Wnt-stimulated region. The units for x and y are given in cell-lengths. The parameters are as listed in §B.3 except $H_W = 11$.

times.

Eventually, however, one lineage dominates the crypt. This is demonstrated in figure 4.10 where the lineages of three cells initially on the base of the crypt (figure 4.9) and their progeny are followed. Figure 4.10 shows the positions of the cells in each lineage after 100 hours (column 1), 1000 hours (column 2), 1600 hours (column 3) and 2700 hours (column 4).

Initially each lineage contains only one cell (see figure 4.9). However, at $t = 100$ hours (column 1 in figure 4.7) that cells from the lineage in the third row greatly outnumber those from in the first two rows. This pattern persists until $t = 1000$ hours (column 2), at which time the lineage in the first row no longer has any progeny on the base of the crypt. The lineage represented in the second row of plots has a similar number of cells to the case when $t = 100$, whereas the number of cells in the lineage represented in the third row of plots has greatly increased. At $t = 1600$ hours (column 3), the lineage in the first row of plots has been washed out of the crypt, and it is dominated by cells from the lineage represented in the third row. At $t = 2700$ hours (column 4), the lineage in the third row accounts for all the cells from the crypt, i.e. the crypt is monoclonal. The time it takes for the crypt to become monoclonal in this model is comparable to that found for the simulations

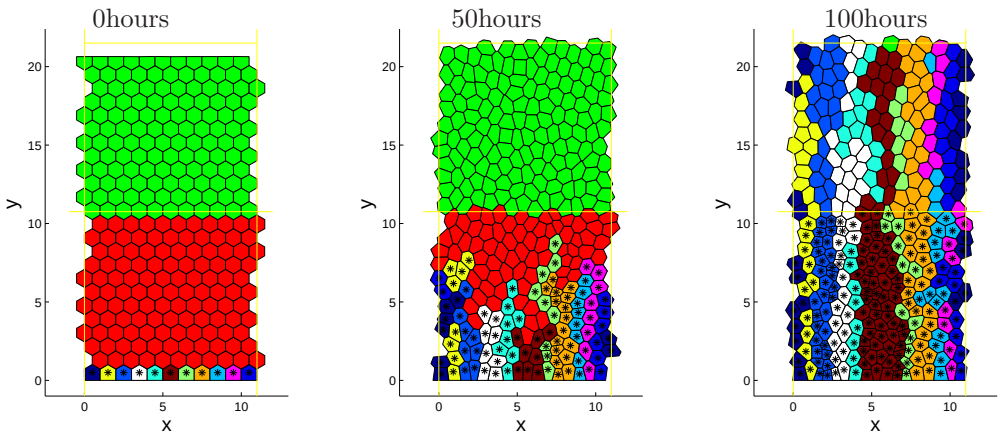

Figure 4.8: Figure showing how the offspring of each progenitor cell, initially on the base of the crypt, move within a crypt with (left) $t = 0$ hours, (centre) $t = 50$ hours, (right) $t = 100$ hours. The cells coloured the same are all generated from the same progenitor cell, apart from the red (transit) and green (differentiated) cells, which are not form any lineage initially on the base of the crypt. The cells marked with a $*$ are transit cells, all other cells are differentiated cells. The parameters are the same as figure 4.7.

for the cell-centre model (more details are provided in Chapter 3 and in [110]).

Figure 4.10 also reveals the degree of lateral movement of cells at the base of the crypt. The lineages in rows 1 and 2 move leftwards whilst those from the lineage in the third row expand leftwards.

From figure 4.11 we can see how the number of cells within each lineage varies with time. The rapid fluctuations are due to the proliferation of cells. The plot also shows the times at which a lineage is washed out of the crypt. The time that each lineage remains in the crypt can vary greatly. Some lineages remain for only a short period of time, whereas others can persist with a relatively low number of cells in the crypt such as those that are sloughed out of the crypt after 2700 hours. As mentioned previously, there are no intrinsic differences in the cell lineages that survive, apart from stochastic variation in the cell-cycle times.

Average cell deformation, velocity and shape

Our numerical simulations reveal that the size and shape of the cells, and the speed with which they move, depend on their distance from the base of the crypt. Figure 4.12 shows how the average cell deformation, p, and average velocity up the crypt, v_y, vary with distance from the base of the crypt,

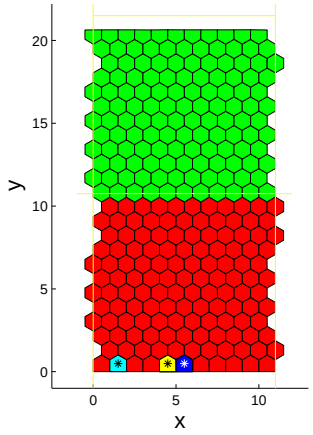

Figure 4.9: Figure showing the initial positions of the progenitor cells later shown with their lineages in figure 4.10. The left-most marked cell on the bottom row (cyan) is the cell whose lineage represents the top row of plots in figure 4.10, the yellow cell leads to the second row of plots in figure 4.10 and the dark-blue cell leads to the third row of plots in figure 4.10.

y. The deformation of a cell, p, is related to the natural area of a cell, A_N and its actual area, A, via $p = A_N - A$. The velocity of a cell is calculated by finding the mean positions of the vertices of the cell and comparing them to the mean positions of the vertices of the cell one hundred timesteps (12min) before. We cannot simply measure the velocity of a cell by calculating the movement of its vertices, as cells can lose and gain vertices from T1 swaps and birth of surrounding cells. To construct the plots in figures 4.12 and 4.13, the crypt is split into horizontal bands of unit width (figure 4.12, right) and the averages cell velocity and deformation within each band are calculated. This process is repeated for 1000 different time readings and the cell deformation and velocity are averaged over all time readings for each band.

Figure 4.12 (left) shows how the average vertical velocity, v_y, varies with y, the distance from the crypt base. Two distinct regions are apparent: one in which cells are proliferating and one in which they are not. Where cells are proliferating, $y \leq H_W$, there is a sharp linear increase in v_y. Where cells are not proliferating, $y > H_W$, there is a linear increase in v_y but the increase is less pronounced than in the proliferating region.

As there are no gaps within the epithelium, cells can only grow during G_1 phase if they displace surrounding cells. Since no cells can escape through the bottom of the crypt, cells are forced up the crypt, leading to a positive value for v_y. Cells further up the crypt within the proliferative region have a higher upward speed as there are, on average, more cells proliferating below them. Cells in the non-proliferating region also have a high v_y value due to the large number of cells proliferating

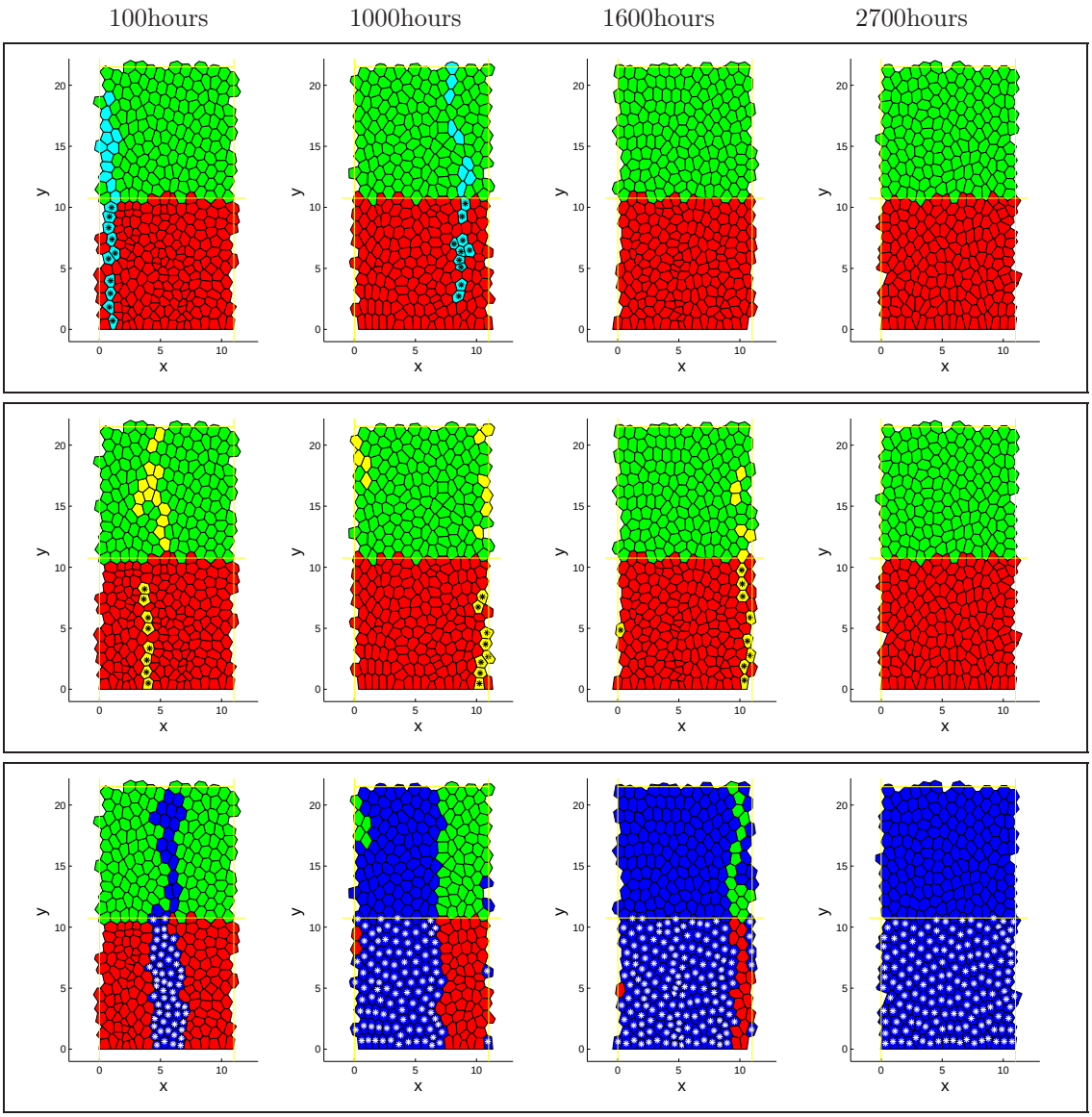

Figure 4.10: Figure shows the progression to a monoclonal crypt. All plots are from the same simulation and each column represents a different time in the simulation, column 1 - 100 hours, column 2 - 1000 hours, column 3 - 1600 hours, column 4 - 2700 hours. Each row corresponds to a different cell lineage within the same crypt, with the initial cell shown in figure 4.9 (top - cyan, middle - yellow, bottom - blue). All cells in the crypt after 2700 hours have the same progenitor cell; the cell marked blue in 4.9. All other lineages (for example the lineages marked in rows 1 & 2) are washed out of the crypt. The progenitor cell that ends up populating the crypt has properties which are identical to all the other progenitor cells. The parameters are the same as figure 4.7.

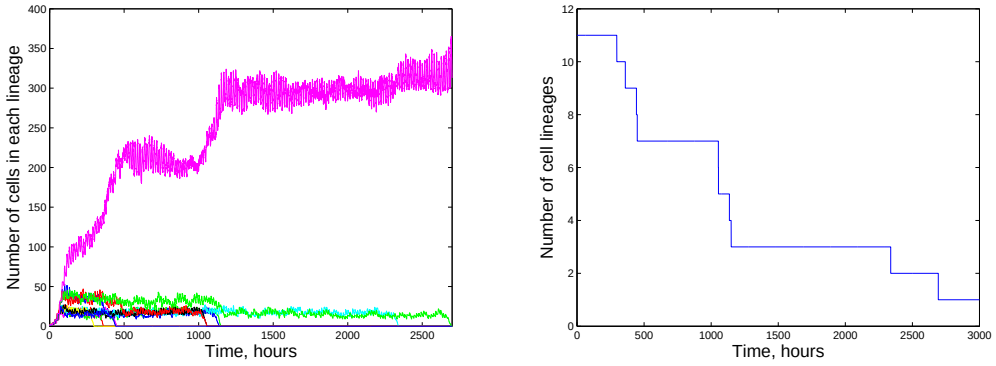

Figure 4.11: Plots showing the cell lineages making up the crypt over time. These plots are for the same data as shown in figure 4.10. The plot on the left shows how the number of cells of each lineage within the crypt varies with time, with one lineage of cells (in pink) coming to dominate the crypt. The plot on the right shows how the number of cell lineage surviving with in the crypt varies with time. Initially there are 11 cell lineages marked, however over time the crypt is filled by cells of only one lineage.

below them. The increase in v_y is smaller as there are no additional cells proliferating. However there is a small amount of relaxation of the cells, as shown in the cell deformation plot (figure 4.12 (centre)), causing a small increase in cell velocity.

The cell deformation, p, in figure 4.12 (centre), which primarily measure cell compression, does not exhibit the same change in behaviour in the proliferating and non-proliferating regions; there appears to be a linear decrease in cell deformation along the length of the crypt, with the exception of a boundary layer at its bottom. The decrease in cell deformation with distance up the crypt is due to the free boundary at the top of the crypt. Cells near the top of the crypt can relax to their natural area more easily, needing to displace a few cells which would be forced out of the crypt, in order to create extra space. However cells near the bottom of the crypt would need to force many cells (encountering a large drag force) to force a cell out of a crypt.

In figure 4.13 (left), we plot the average velocity of the cells in the azimuthal direction, v_x, calculating it in a similar way to the average for v_y. The resulting values of v_x are negligible ($\mathrm{O}(10^{-3})$) compared to those of v_y ($\mathrm{O}(10^{-1})$) and vary more in the proliferating region than in the non-proliferating region. The variation in the proliferating region is due to cells pushing each other apart when they divide to produce two daughter cells.

A measure of the shape of the cells is plotted in figure 4.13 (right). For each cell, j, a dimensionless

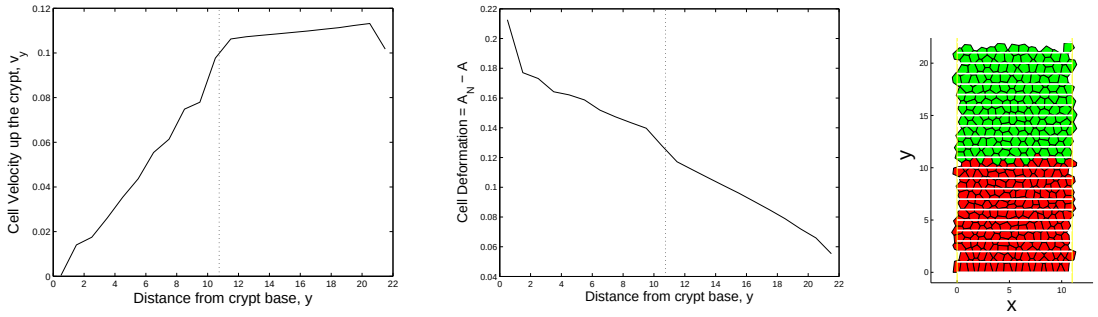

Figure 4.12: Plot (left) showing how velocity in the direction of up the crypt, $v_y = (y(t) - y(t - 100dt))/(100 * dt)$, and (middle) cell deformation, $p\ (= A_N - A)$ varies with distance from the base of the crypt, y. To calculate the values of p and v_y, average values are calculated for cells in each band across the crypt (right), these values are then averaged for 1000 different readings of t. The vertical line at $y = H_W$ represents the point at which Wnt is "turned off" and transit cells become differentiated cells. The parameters are the same as figure 4.7.

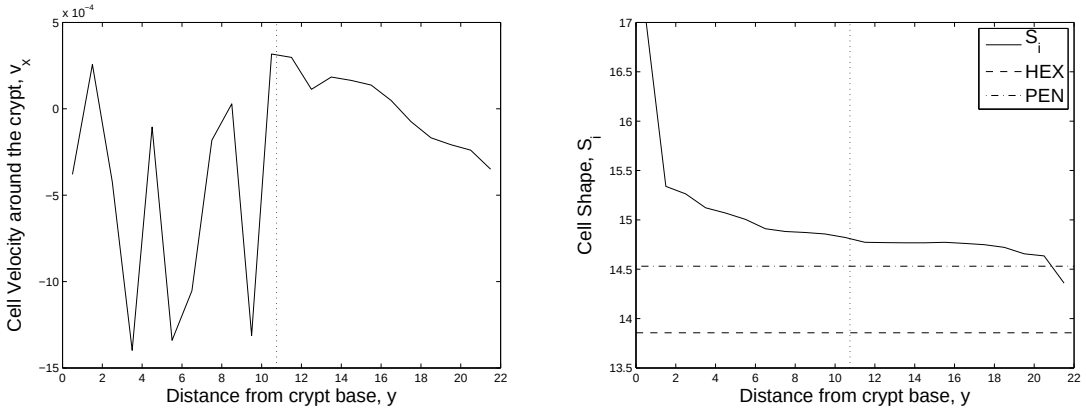

Figure 4.13: Plots showing how (left) azimuthal velocity, v_x, and (right) cell shape, $S = C^2/A$, vary with distance along the crypt axis, y. High values of S represent elongated cells and low values such as marked by HEX (for regular hexagons) and PEN (for regular pentagons) represent more symmetric cells. The vertical line at $y = H_W$ represents the point at which Wnt is "turned off" and transit cells become differentiated cells. The values of v_x and S are averaged in a similar manner to figure 4.12. Parameter values are the same as in figure 4.7.

shape parameter $S_j = C_j^2/A_j$ is calculated, where C_j is cell j's perimeter, and A_j is its area. The lower the value of S_j, the rounder the cell is, high values indicate highly elongated cells [182]. Perfectly circular cells would have $S_j = 4\pi$ and regular hexagons $S_j = 8\sqrt{3}$. The values are then

averaged across each horizontal band of unit width and over 1000 time readings.

Figure 4.13 (right) shows that the cells at the top of the crypt are the least elongated and cells at the base are the most elongated. This is because when cells proliferate, the two daughter cells will typically be more elongated than the parent cell. For example, a regular hexagon would split into two elongated pentagons. These more elongated cells will become less elongated over time. Cells at the very base of the crypt are much more elongated than all other cells in the crypt due to the forcing boundary condition on $y = 0$. This condition only allows vertices to move off $y = 0$ through T1 swaps.

The shape of the cells is not on average the ideal packing of regular hexagons. Even cells at the top of the crypt only have the average value of S_j for regular pentagons. This is because viscous drag acting on the cells means that the cells do not have time to relax to their preferred shape before they are removed from the top of the crypt.

Tracking of a single cell

To understand how a cell's properties vary throughout its lifetime we investigated how the area, shape and position of a single cell vary with time (see figures 4.14 and 4.15). The cell of interest is initially on the base of the crypt in a quasi-steady-state crypt. It then proliferates at $t \approx 1$. One daughter cell remains on the bottom of the crypt and the other cell (the one that is followed) moves away. The cell then grows (figure 4.15(a)) and becomes less elongated (figure 4.15(b)). The cell proliferates twice more, becoming much more elongated each time (figure 4.15(b)). As the cell moves through the proliferative region, the number of cells forcing it up the crypt increases. Once the cell moves out of the proliferative region ($t \sim 50$), it no longer proliferates but continues to move up the crypt. As the cell approaches the top of the crypt, it becomes less elongated and closer to its target area. When the cell reaches the top of the crypt at $t \sim 90$ it is sloughed off into the lumen.

The vertical velocity of the cell increases as it moves up the crypt, with the cell taking 45 hours to move from $y = 0.5$ to $y = 5$ and a further 45 to move a much greater distance, $y = 5$ to $y = 21$. This is due to more cells forcing the cell up the crypt as it moves up through the proliferating region. The cell does not move up the crypt with a constant velocity; the cell moves in surges (see figure 4.15(d)). These surges are due to a number of cells proliferating below the cell at a similar time.

Lateral movement of the cells is much less than vertical movement. This is because the component of the energy gradient is much smaller than that in the vertical direction. In turn this is due to there being a large change in average cell deformation from the base to the top of the crypt (see

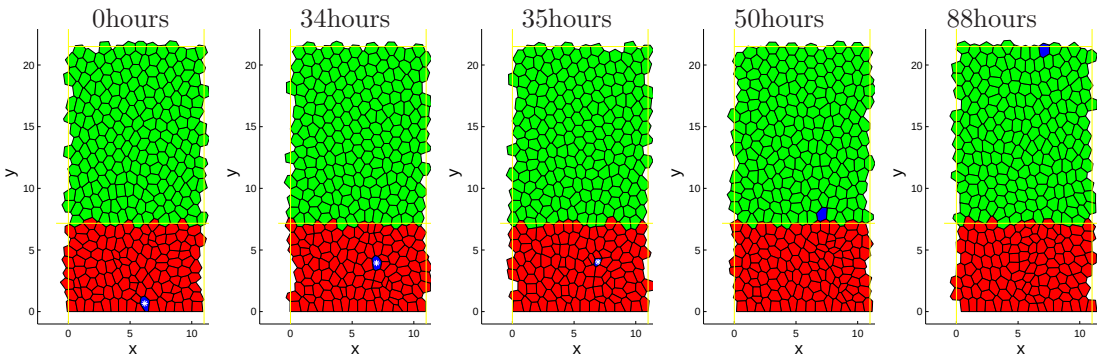

Figure 4.14: Series of plots showing a single cell (marked in blue) move throughout the crypt. Plotted for (left to right) initial position ($t = 0$), shortly before a cell division ($t = 34$), shortly after a cell division ($t = 35$), shortly after the cell has moved out of the proliferative region ($t = 50$), shortly before the cell is to be removed from the top of the crypt ($t = 88$). Transit cells are coloured red or blue marked with a $*$, differentiated cells are coloured green or blue without a $*$. The parameter values are as stated in §B.3.

figure 4.12), but little change azimuthally. From figure 4.15(c), we that note the largest change in azimuthal distance occurs just after mitosis. This is due to the two daughter cells being forced apart from each other as they grow.

The small sharp changes in area in figure 4.15(a) are due to T1 swaps. These occur more often in the proliferative zone, $y < H_W$, where there is a large amount of vertex rearrangement due to the cell proliferation and growth occurring. This effect also explains the sharp changes in cell shape seen in figure 4.15(b).

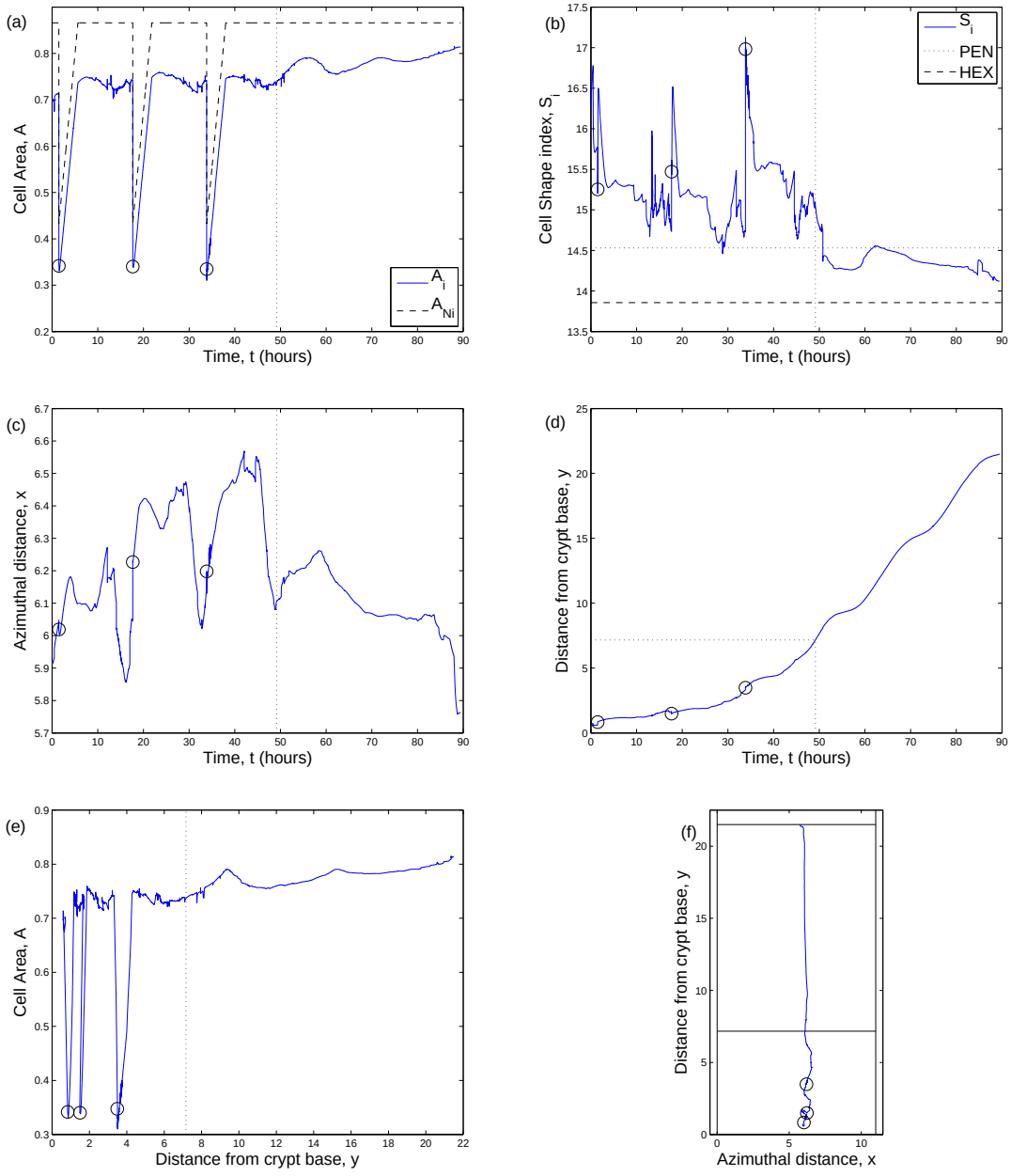

Figure 4.15: Series of plots showing how (a) the area, A_i (and natural area, A_{N_i}- dashed line), (b) shape, (c) mean azimuthal position of the vertices, (d) mean distance from the base of the vertices evolve over time. We also show (e) how the area of the individual cell varies with distance from the base of the crypt and (f) the path taken by the cell as it moves up the crypt. The circles show when the cell divides and the vertical dotted lines ($t = 49.1,\ y = 7.2$) represent when the cell passes into the non-proliferating region. In (b) shape values for regular pentagons (PEN) and regular hexagons (HEX) are shown. The parameter values are as stated in §B.3.

Effects of differential cell-cell adhesion

Experimental evidence suggests that variation in levels of membrane-bound β-catenin within a cell can lead to cell sorting [169]. By implementing a Wnt signalling model in the cell-centre model described in the previous chapter (see Appendix A.2), we found that the level of membrane-bound β-catenin changed with distance from the base of the crypt.

Guided by other authors who have studied cell sorting [27, 30], we assumed that the cell-cell contact energy depended on the cell types in contact. The contact energy between cells of different types (γ_{TD}, T - transit, D - differentiated) was not equal to that of like cells (γ_{TT}, γ_{DD}).

Figure 4.16 reveals that changing γ_{TD} does not strongly influence the behaviour of the cells. In all cases (when cells of a different type have a preference to be next to each other, figure 4.16 (a), or cells of a different type do not wish to be next to each other, figure 4.16 (c, d)) the cells behave in a similar way: they move primarily parallel to the crypt axis with minimal lateral movement.

However, there are noticeable differences at the boundary between transit cells and differentiated cells. When $\gamma_{TD} > \gamma_{TT} = \gamma_{DD}$ (figure 4.16 (c, d)), the boundary is noticeably smoother than when $\gamma_{TD} \leq \gamma_{TT} = \gamma_{DD}$ (figure 4.16 (a, b)), as shown in the lower plots in figure 4.16.

To investigate this behaviour further, we plot the average cell deformation, velocity (azimuthal and up the crypt) and cell shape versus distance from the crypt base (see figure 4.17). The components of average velocities of the cells v_y and v_x, are similar irrespective of the bonding energies between cells of a different type. The vertical velocity increases sharply in an approximately linear fashion in the proliferating zone and less rapidly in the non-proliferative zone. In all cases $|v_x| \ll |v_y|$ and v_x has less variation in the non-proliferating zone than in the proliferating zone.

The plots of cell deformation and cell shape, however, change significantly when the cell-adhesion energy between cells of different type, γ_{TD}, is varied. When there is a high penalty for cells of different types being in contact ($\gamma_{TD} = 5\gamma_{TT} = 5\gamma_{DD} = 0.05$, see figures 4.16(d) & 4.17(d)), the cell deformation increases on the boundary between transit and differentiated cells and the cells are highly elongated. This is to be expected as the cells are continuously moving in order to shorten the length of the interface between the transit and differentiated cells.

Also of interest is the average shape and size of the cells in the non-proliferating region of the crypt. When $\gamma_{TD} \neq \gamma_{TT}$, ($\gamma_{TD} \neq \gamma_{DD}$), the cells are less elongated and less deformed than when $\gamma_{TD} = \gamma_{TT} = \gamma_{DD}$. A possible explanation for this behaviour is that if the cells do not sort at the interface, the differentiated cells adopt a distribution in which they are at a local energy minimum. However, when there is a large amount of sorting at the interface, the differentiated cells move away

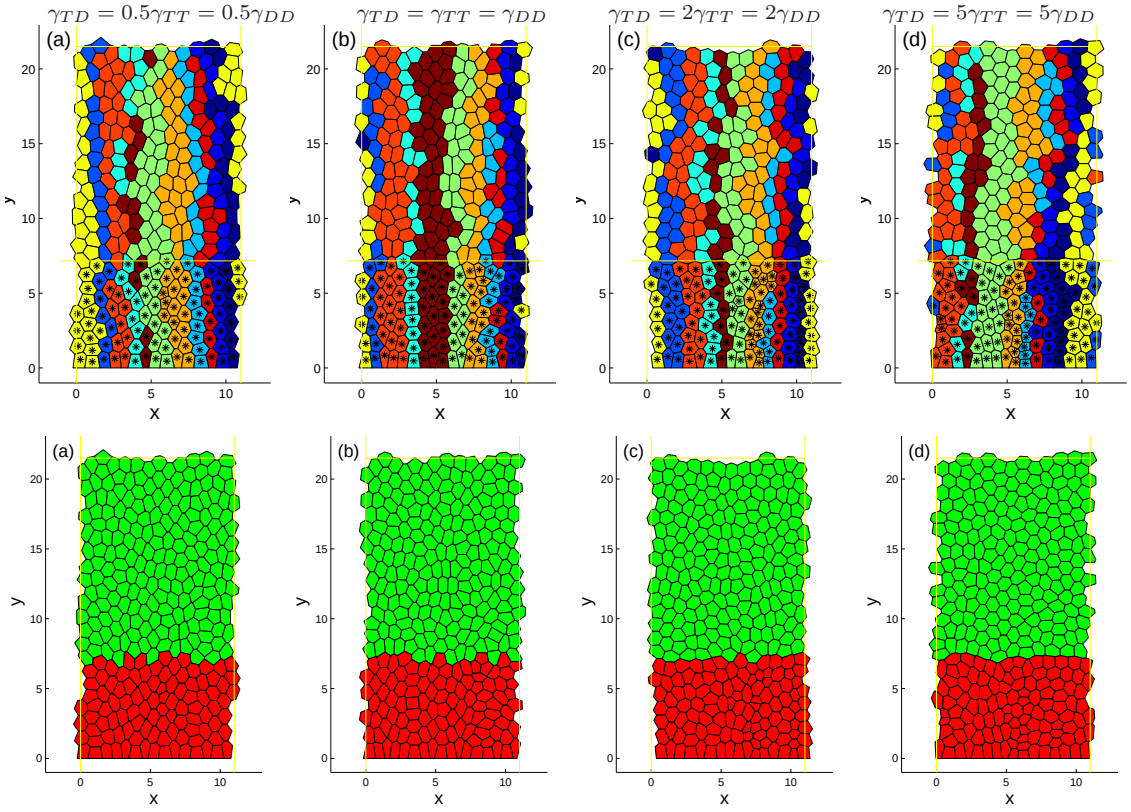

Figure 4.16: Series of plots ($t = 400$) showing how changes in cell-cell adhesion influence the movements of stem cell lineages (top) within a crypt. (a) ($\gamma_{TD} = 0.5\gamma_{TT} = 0.5\gamma_{DD} = 0.005$) (b) ($\gamma_{TD} = \gamma_{TT} = \gamma_{DD} = 0.01$) (c) ($\gamma_{TD} = 2\gamma_{TT} = 2\gamma_{DD} = 0.02$) and (d) ($\gamma_{TD} = 5\gamma_{TT} = 5\gamma_{DD} = 0.05$). The lower plots show how the shape of the interface between the transit (red) and differentiated cells (green) changes as γ_{TD} varies. Unless otherwise stated, parameters are as in §B.3.

from the local minimum and organise themselves into a pattern with a lower energy state.

Tissue-oriented mitosis

A different rule for cell mitosis was investigated by Brodland and Veldhuis [31]. In this case of tissue-oriented birth, the plane of cleavage when a cell divides is parallel to the base of the crypt, whereas previously we have assume cell-oriented birth, where the cell splits along its short axis.

The effect implementing tissue-oriented birth is shown in figure 4.18. As before, the cells move primarily up the crypt, however there are noticeable differences. With tissue-oriented mitosis, there are fewer cells on the base of the crypt: 11 cells in figure 4.18(b) as opposed to 15 cells in 4.18(a).

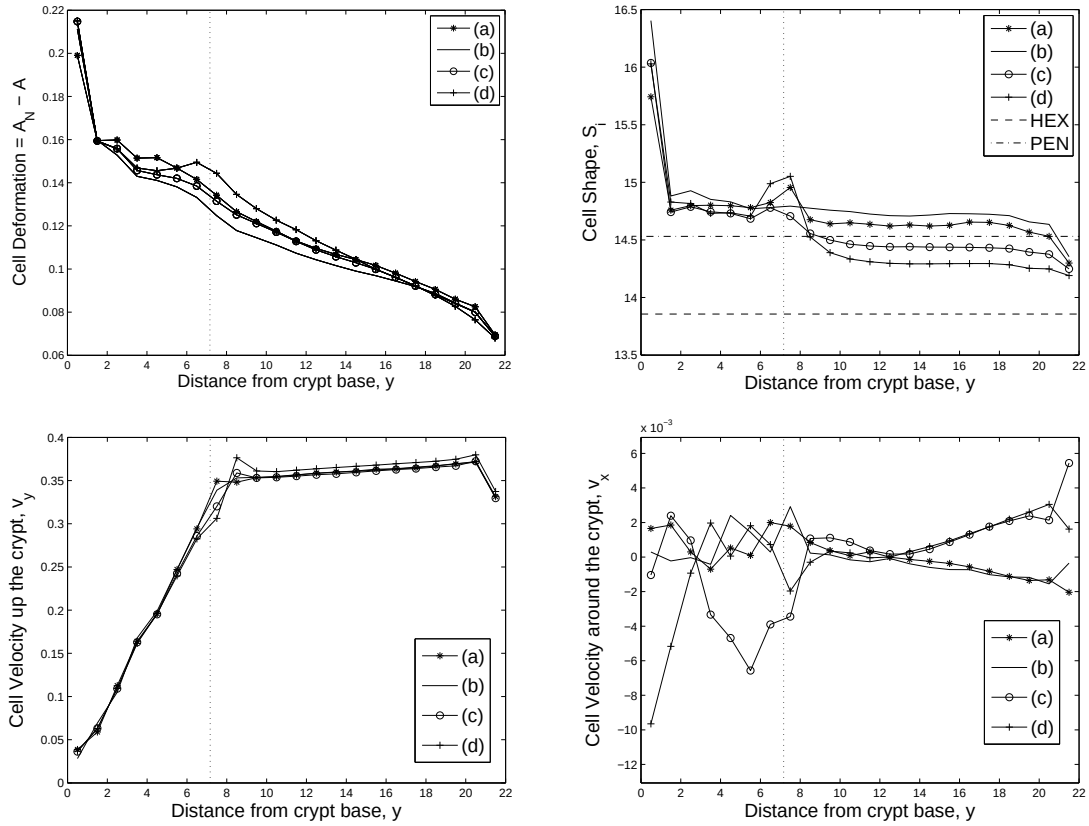

Figure 4.17: Series of plots showing how the average cell deformation (top-left), cell shape (= Perimeter × Perimeter / area) (top-right), vertical velocity (bottom-left), and azimuthal velocity (bottom-right) vary with distance from the crypt base for the different cell adhesion cases (a, b, c, d) described in figure 4.16. The crypt is split into unit bands from crypt base, and averages taken from all the cells within a given band. This is repeated for 100 different time readings. For comparison, lines are also plotted for regular hexagons (HEX) and pentagons (PEN) in the shape cell plot (top-left). The parameter values are as stated in figure 4.16.

With tissue-oriented birth transit cells in the crypt appear to be squashed vertically whereas in cell-oriented birth they are more regular with no obvious direction of deformation.

This behaviour is investigated further by calculating the average cell deformation, shape parameter and velocity (see figure 4.19). In tissue-oriented birth, the cells in the non-proliferative region are less deformed and less elongated than the cells with cell-oriented mitosis. The average values of v_x and v_y both are less affected, with v_y increasing rapidly in the proliferating region and increasing slowly in the non-proliferating region and $|v_x| \ll |v_y|$.

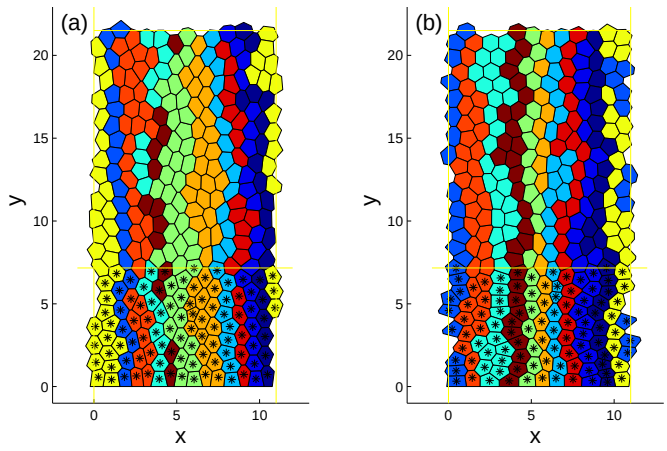

Figure 4.18: Plots ($t = 400$) showing how changing the plane of mitosis from cell-oriented (a) to tissue-oriented (b) affects the behaviour of the cells. When cells have tissue-oriented birth, lineages from the same cell form clear unbroken lines and there are fewer cells at the base of the crypt. Parameter values for (a) and (b) are as stated for (a) in figure 4.16.

4.3.2 Numerical results for crypts containing mutant cells

In order to investigate the early stages of colorectal cancer we now introduce mutant cells into the crypt. Mutant cells never enter G_0 phase and can proliferate throughout the crypt (§4.2.2).

When following the evolution of a mutant cell and its progeny, we simulate a normal crypt (where the cell adhesion parameters are all equal, $\gamma_{TT} = \gamma_{TD} = \gamma_{DD}$) until $t = 100$ hrs and use the resulting quasi-steady-state as our starting point for all other simulations. We transform a single transit cell to mutant. This cell and its progeny are labelled and remain mutant throughout their lifespan.

The drag on vertices that are part of mutant cells is changed by varying η_M and the cell-cell adhesion for mutant cells varied by changing γ_{MM} (adhesion between mutant cells), γ_{MT} (adhesion between mutant and transit cells) and γ_{MD} (adhesion between mutant and differentiated cells). The parameter values we use are summarised in Table 4.2.

In this section, we follow a similar procedure to Chapter 3, by initially investigating cells where there is only a change in proliferation, followed by investigating changing the mutant cells' drag, initial position and cell-cell adhesion.

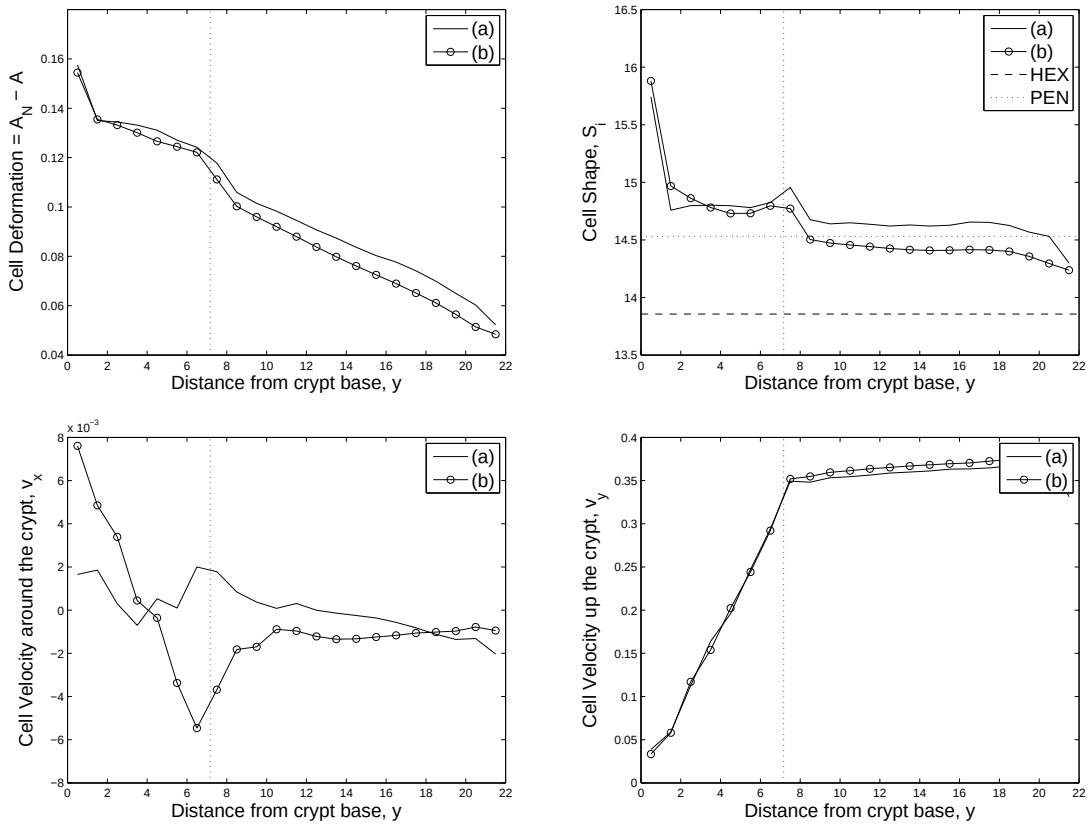

Figure 4.19: Series of plots showing how the average cell deformation (top-left), cell shape (= Perimeter × Perimeter / area) (top-right), azimuthal velocity (bottom-left), and velocity up the crypt (bottom-right) vary with distance from the crypt base for cells with cell-oriented, (a), and tissue-oriented mitosis, (b). For comparison, results for regular hexagons (HEX) and pentagons (PEN) are included in the shape cell plot (top-left). Parameter values for (a) and (b) are as stated for figure 4.16(a).

Mutants with only a change in proliferation

Initially we assume that the only difference between the mutant and normal cells is that mutant cells can proliferate throughout the crypt. All parameters relating to cell drag and cell-cell adhesion are the same as normal cells (case 1 in table 4.2). The results presented in the top row in figure 4.20 show the mutant cells increasing in number as they move up the crypt, as they can proliferate throughout all the crypt.

In this case, the mutant cells do not dominate the crypt, although, due to the monoclonal nature of crypt (see figure 4.10), there is a (small) probability that such cells may become the dominant

Case	Figure	η_M	γ_{MM}	γ_{TM}	γ_{DM}
1	4.20 (top row)	η_N	γ_{TT}	γ_{TT}	γ_{TT}
2	4.20 (bottom row)	$10\eta_N$	γ_{TT}	γ_{TT}	γ_{TT}
3	4.21 (top row)	$20\eta_N$	γ_{TT}	γ_{TT}	γ_{TT}
4	4.21 (bottom row)	$30\eta_N$	γ_{TT}	γ_{TT}	γ_{TT}
5	4.22 (top row)	$4\eta_N$	$2\gamma_{TT}$	$0.5\gamma_{TT}$	γ_{TT}
6	4.22 (bottom row)	$4\eta_N$	$0.5\gamma_{TT}$	$2\gamma_{TT}$	γ_{TT}

Table 4.2: Summary of mutant parameters for each figure in §4.3.2. Values of η_N and γ_{TT} are given in Appendix B.3

population within the crypt. Several other simulations (not shown) in which a different cell at the base of the crypt was labelled mutant but the cell properties were the same as in figure 4.20 (top) were performed. The mutant population remained small and did not become the dominant population. We conclude that a mutation in a cell that does not change its mechanical properties is unlikely to result in the mutant population taking over the crypt. However to check this properly, many more simulations would need to be run for long times (until $t = 2700$hrs as in figure 4.10), varying the initial mutant cell and also the random seed input in the random number generator. Unfortunately time constraints did not allow us to do this.

Mutants with a larger drag and a change in proliferation

We now investigate the behaviour of mutant cells which not only proliferate throughout the crypt but also have an increased drag (case 2 in table 4.2). When the mutant cells have a higher drag than the normal cells, $\eta_M = 10\eta_N$, they typically dominate the crypt (see figure 4.20(bottom)). We choose the same initial mutant cell as in figure 4.20 (top): the only difference between figure 4.20 (top) and (bottom), is that the drag of the mutant cells is higher in figure 4.20 (bottom).

Higher drag means the mutant cells offer more resistance to movement and a larger force is required to move them up the crypt. As such, it is easier for mutant cells to move around the crypt, displacing normal cells laterally, than to move up the crypt (and displace other mutant cells). Eventually the mutant cells force the normal cells out of the crypt and become the dominant population. We notice that the cells are more tightly packed when the mutant population dominates the crypt. This is consistent with experimental results by Sansom *et al.* [141]: they report higher levels of cell packing in mutant crypts. Unfortunately the simulation breaks down at $t = 200$ hours because the cells become too small, the movement of the vertices becomes unstable and vertices pass through the

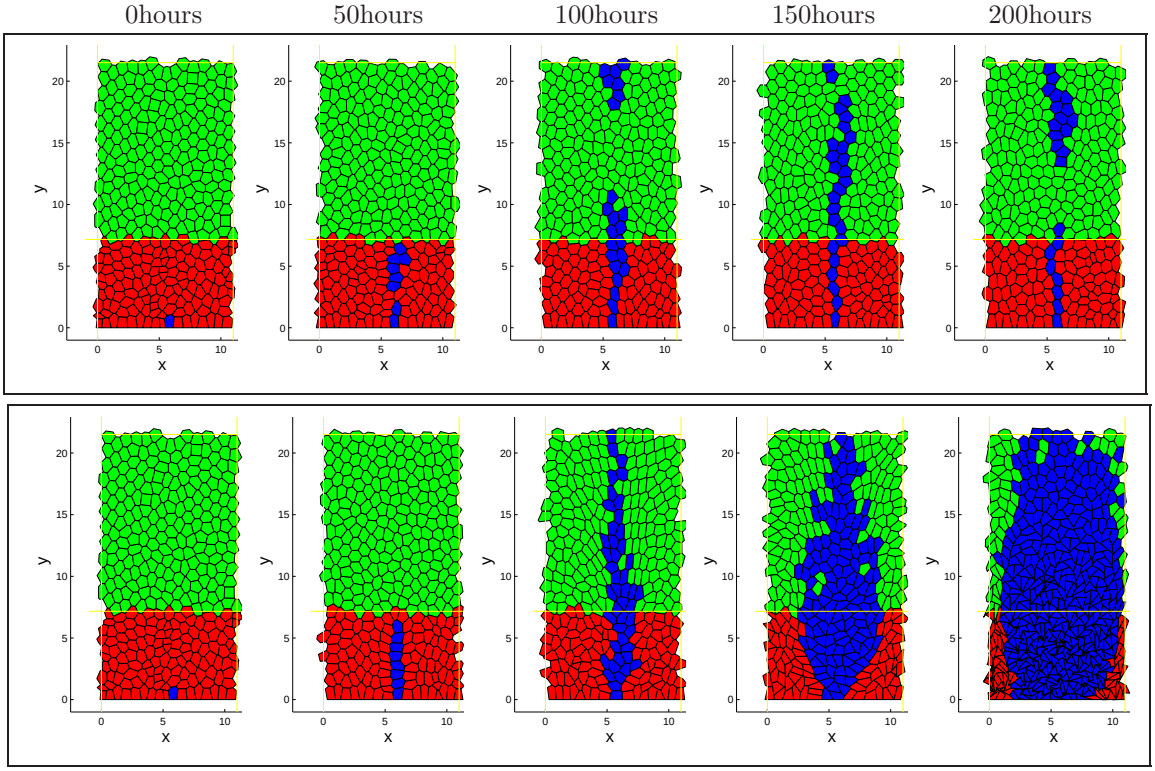

Figure 4.20: Series of plots show how changing the drag on the mutant cells (blue) from being the same as normal cells, $\eta_M = \eta_N$, (top) to being ten times that of normal cells, $\eta_M = 10\eta_N$, (bottom) affects whether the mutant population establishes within the crypt. Plots are shown (from left to right) the initial crypt and the crypt after 50, 100, 150, 200 hours. Transit cells are coloured red and differentiated cells coloured green. The parameters unless otherwise stated are as in §B.3.

edges of other cells.

Our simulations suggest that increasing the drag on mutant cells increases the likelihood of a mutant population establishing itself within the crypt. However we must treat any such inferences with caution, since it is possible for a single normal cell lineage to dominate the crypt (see figure 4.10). In order to validate our findings, many more simulations should be performed, and the position of the initial mutant cell varied. Due to limited resources (it took 18 hours to simulate a crypt for 200 hours), we were unable to perform the necessary simulations.

Cell mutations occurring further up the crypt

We now investigate how the position at which the first mutation appears in the crypt affects its ability to establish itself within the crypt. This is of interest as there is great debate as to whether the initial mutation occurs in a cell at the bottom and its offspring move up the crypt ("bottom-up morphogenesis" as suggested by Preston *et al.* [131]) or whether the mutation occurs further up the crypt and move downwards ("top-down morphogenesis" as suggested by Shih *et al.* [153]).

In figure 4.21, we introduce a mutation into a cell above the base of the crypt. The top row of plots in figure 4.21, show that when the mutant cells have a drag twenty times that of the normal cells, $\eta_M = 20\eta_N$ (case 4 in table 4.2), the mutant cells are washed out of the crypt: the drag is not strong enough to balance the mitotic pressure from cells further down the crypt. We also notice that the normal cells just below the mutant patch are the most deformed (for example in figure 4.21, after 150 hours). This is due to the normal cells moving around the mutant patch and reflects the pressure distributions and cell movement described in the continuum model (§2.5.3, figures 2.19 and 2.20).

The lower plots in figure 4.21, show that if the drag on the mutant cells is thirty times that of normal cells, $\eta_M = 30\eta_N$ (case 4 in table 4.2), then it is possible for the mutant population to establish themselves within the crypt. In this case the drag forces are strong enough to resist the mitotic force from cells further down the crypt. This allows the mutant cells to form a patch in the crypt.

Similarly to our findings in Chapters 2 and 3, these simulations suggest that mutant cells which originate away from the base of the crypt must have a much higher drag coefficient if they are to establish themselves within the crypt. The results in figure 4.21 also show that it would be possible for top-down morphogenesis to occur, although it is much more difficult for it to occur than bottom-up morphogenesis (as was shown in figure 4.20).

Mutant cells with differing cell-cell adhesion

In addition to varying the drag coefficient of the mutant cells, we also investigated the effect of varying the cell-cell adhesion constants. Figure 4.22 shows that changing the adhesion energy between mutant and transit cells, γ_{MT}, and between mutant cells, γ_{MM}, greatly changes the behaviour of the mutant cells.

Firstly, we simulate the case where $\gamma_{MT} = 0.5\gamma_{TT}$ and $\gamma_{MM} = 2\gamma_{TT}$, so that mutant cells in contact with each other have a higher free energy than mutant cells in contact with transit cells (case 5 in

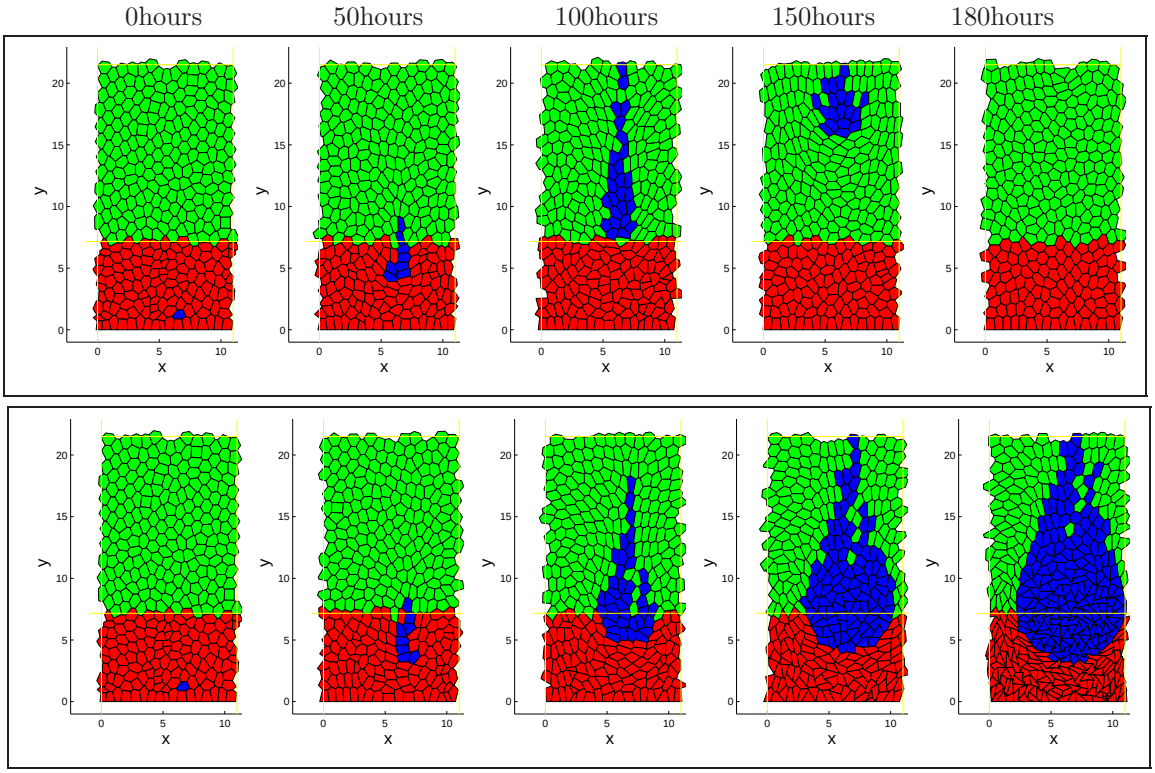

Figure 4.21: Series of plots show how changing the drag on the mutant cells (blue) from being twenty times that of normal cells, $\eta_M = 20\eta_N$, (top) to being thirty times that of normal cells, $\eta_M = 30\eta_N$, (bottom) affects whether the mutant population establishes within the crypt. Plots are shown (from left to right) the initial crypt and the crypt after 50, 100, 150, 180 hours. Transit cells are coloured red and differentiated cells coloured green. The parameters unless otherwise stated are as in §B.3.

table 4.2). In this case, the mutant cells move away from each other when moving up the crypt and there is a large amount of mixing between the mutant and transit cells (see figure 4.22(top)). The mutant cells remain mixed with the normal cells when the transit cells differentiate. The mutant cells then move up the crypt more quickly and are flushed out of the crypt with the normal cells.

By contrast, when $\gamma_{MT} = 2\gamma_{TT}$ and $\gamma_{MM} = 0.5\gamma_{TT}$, so that mutant cells in contact with each other have a lower free energy than mutant cells in contact with transit cells (case 6 in table 4.2), the mutant cells remain together in a patch (see figure 4.22 (bottom)). When the mutant cells form a patch, they move more slowly up the crypt and can produce more offspring while they remain in the crypt. As a result the mutant cells quickly become the dominant population.

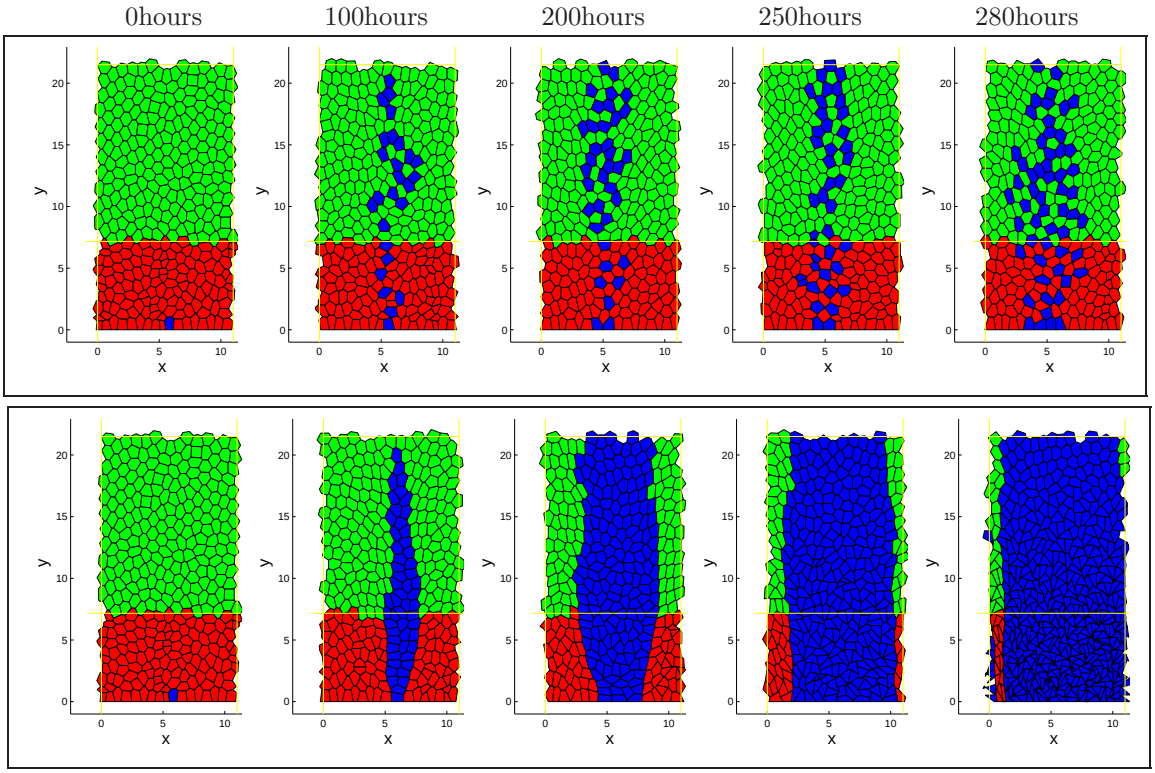

Figure 4.22: Series of plots show how changing the cell-cell adhesion parameters changes the behaviour of mutant cells (blue). The top row of plots show the case when mutant cells are penalised for being in contact with other mutant cells but have an affinity to be in contact with transit cells, $\gamma_{MM} = 2\gamma_{TT} = 4\gamma_{MT}$. The bottom row of plots shows the case when mutant cells have an affinity to be in contact with other mutant cells and are penalised for being in contact with transit cells, $4\gamma_{MM} = 2\gamma_{TT} = \gamma_{MT}$. The drag on the mutant cells is four times that of normal cells $\eta_M = 4\eta_N$ and all other parameters are as mentioned in B.3. Plots are shown (from left to right) the initial crypt and the crypt after 100, 200, 250, 280 hours. Transit cells are coloured red and differentiated cells coloured green.

4.4 Discussion

In this chapter we have developed a cell-vertex model to describe the proliferation and migration of cells in a colorectal crypt. Using a cell-vertex model we could easily distinguish between cell-cell adhesion forces and cell deformation forces, unlike in our cell-centre model where both effects are coupled together. The cell-vertex model also lends itself to modelling cell-cell adhesion, as the contact area can easily be found by calculating the length between neighbouring vertices, dispensing

with the need to calculate a Voronoi tessellation as for many cell-centre models. The cell-vertex model also allows us to model cell growth more easily, with the cells' target area increasing linearly over the G_1 phase.

Similarly to Chapter 3, to model Wnt-dependent proliferation, in the lower part of the crypt, where Wnt levels are assumed to be high, cells were termed transit cells and could proliferate. Cells in the upper part of the crypt, where Wnt levels are assumed to be low, were termed differentiated and could not proliferate.

Using the cell-vertex model, we were able to reproduce results found in the cell-centre model in the previous chapter. Cells proliferate in the lower part of the crypt and move in response to mitotic forces parallel to the crypt axis, but with some azimuthal movement. When tracking cells generated from the same progenitor cell, we were able to see that the crypt became monoclonal.

We also investigated how cell properties varied with distance from the base of the crypt, by averaging cell behaviour in horizontal bands across the crypt and over time. Analysis of the simulations revealed that if cell-cell adhesion was the same for all cells, there was an approximately linear decrease in cell deformation from the bottom to the top of the crypt. The vertical component of average velocity up the crypt, v_y, exhibited a clear pattern of behaviour. In the proliferating region (the bottom part of the crypt), there was a steep linear increase in v_y with distance from the base of the crypt. In the upper part of the crypt, where cells do not proliferate, the increase in v_y is less marked. Although cells move around the crypt, we found that on average $|v_x| \ll |v_y|$. Additionally, cells became less elongated as they moved further away from the crypt base.

When the cell-cell adhesion parameters were such that it was less (or more) favourable for cells of a different type to be in contact than cells of the same type, the cells were more elongated and more deformed at the interface between transit and differentiated cells. However when the cells moved into the non-proliferating zone, cells with unequal adhesion parameters were less deformed (and less elongated) than cells in crypts where the cell adhesion energy was identical for all cells. A possible explanation for this behaviour could be that if cell-cell adhesion is identical for all cells, then they adopt a local-minimum-packing formation. However, when there is a large amount of cell movement to increase (or decrease) the contact between transit and differentiated cells, the cells reorganise themselves into a lower minimum of free energy as they move up the crypt.

When mutant cells were introduced into the crypt, increasing their drag (representing higher cell-stroma adhesion and a more rigid cytoskeleton) enabled dominate the crypt. However when the mutant cells had the same drag as the normal cells, they remained in the crypt but did not become the dominant population. As the distance from the crypt base at which the initial mutation occurred

was increased, our simulations revealed that the drag on the mutant cells needed to be increased markedly in order for the mutant cells to establish themselves in the crypt.

When the cell-cell adhesion parameters were changed such that the mutant cells bonded preferentially to transit cells, the mutant cells mixed with the normal cells but did not greatly increase in number. However when the mutant cells bonded preferentially to themselves, they remained in a patch and typically became the dominant population in the crypt.

These results imply that drag (modelling cell-stroma adhesion and cytoskeleton rigidity), cell-cell adhesion and the position of the initial mutant cell are important factors in whether a mutant population of cells can colonise a crypt. These findings concur with experimental results that suggest that the most common mutations found in the early stages of colorectal cancer are in β-catenin and APC [60]. Due to their role in Wnt-signalling, mutations in these proteins not only influence cell proliferation but also affect cell-cell adhesion [15], lead to a more rigid cytoskeleton [115] and reduce cell migration [141].

Even though we have obtained some interesting results with the cell-vertex model, it has some limitations. To verify our findings, many more simulations are needed. At present, the computational code is written in MatLab and runs relatively slowly, it taking 18 CPU hours for 200 hours of cellular crypt dynamics. An obvious improvement would be to re-write the code in a faster compiled programming language, such as C++; this could be done by embedding the model within CHASTE (see Chapter 3).

Currently the model only has a simple cell-cycle model embedded within it. However we do know how changes in proteins, such as Wnt, affect the behaviour of cells within the colorectal crypt and several mathematical models have been developed to describe these phenomena. By embedding the model in CHASTE, we could include these more-detailed cell-cycle models within our cell-vertex model. We would then be able to relate the cell-cell adhesion coefficients to the level of membrane-bound protein β-catenin (which is involved in cell-cell adhesion, as shown in §A.2), and develop a multiscale cell-vertex model of the colorectal crypt.

In this chapter we have modelled the crypt as the two-dimensional surface of a solid cylinder. This is reasonable approximation for the main part of a crypt, however it does not model its bowl-shaped base or the cell migration onto the luminal surface. This problem could be addressed by either projecting the three dimensional surface of the crypt and lumen onto a two-dimensional sheet or by extending the model into three dimensions. A longer-term aim is to account for the biomechanical properties of the underlying stroma which is currently treated as a rigid solid although in practice it is deformable. Such modifications would enable us to model biological phenomena such as crypt

buckling and crypt fission due to the over-proliferation of mutant cells.

In summary, in this chapter we have developed a simple cell-vertex model for the colorectal crypt. As far as we are aware, this approach has not previously been used to model a colorectal crypt. It has the benefit of enabling us to study differential cell-cell adhesion without producing a Voronoi diagram at each time step. In addition to modelling the dynamics of normal cells, we also studied the behaviour of mutant cells. These simulations revealed that cell-substrate adhesion, cell-cell adhesion and the position of the initial mutant cell play important roles in dictating whether mutant cells spread within the crypt. We hope that the approach described in this chapter will serve as the foundation for further models of the colorectal crypt.

Chapter 5

Comparison of the continuum, cell-centre and cell-vertex models

5.1 Introduction

In this thesis we have used three different approaches to model the cellular dynamics within a colorectal crypt: a continuum model (Chapter 2), a cell-centre model (Chapter 3) and a cell-vertex model (Chapter 4). In this chapter we assess the relative merits of each modelling framework and discuss their suitability for the colorectal crypt. To do this, we consider a crypt of fixed size and run a test problem using each approach. We also discuss the insight gained from each model and consider how well they agree with experimental findings.

The chapter is structured in the following way: summaries of each model is presented in §5.2; the models are adapted to facilitate their comparison in §5.3; the behaviour of cells in a normal crypt is assessed in §5.4; each model is then used to simulate a test problem, where a circular patch of mutant cells is introduced into a normal crypt in §5.5; a general discussion is presented in §5.6; before further work and our conclusions are discussed in §5.7.

5.2 Summary of the models

Each model exhibits features that are observed in the crypt. These include its proliferative structure and how mutations cause changes in cell behaviour. Experimental results [126] suggest that normal crypts have a proliferative structure, determined by a spatial gradient in Wnt [126], such that cells toward the bottom of the crypt proliferate but cells toward the top do not [134]. Further experimental evidence suggests that the most common early mutations in colorectal cancer are in APC and β-

catenin [60], key proteins in the Wnt-signalling pathway. Mutations in these proteins enable cells to proliferate independently of Wnt [74]. Such mutant cells have also been shown to have (i) a more rigid cytoskeleton [115], (ii) higher levels of cell-stroma [141] and (iii) stronger cell-cell adhesion [18].

5.2.1 Continuum model

In Chapter 2, we developed a continuum model to describe the proliferation and movement of cells in a colorectal crypt. Cell proliferation was modelled by a source term that decreases linearly with distance along the crypt axis (to reflect its dependence on Wnt). Following Greenspan [64] and Franks [56], we used Darcy's law to model cell motion. Two distinct cell populations were considered: normal and mutant cells. The mutant cells were assumed to proliferate at a constant rate throughout the crypt and to have a higher viscosity to capture, within a single parameter, effects (i)-(iii) mentioned above. Model solutions were constructed using a combination of asymptotic analysis and numerical collocation methods.

Our main findings of the model was that the ability of the mutant cells to remain in the crypt depended on their viscosity relative to normal cells and the position at which they first appeared. In general, the mutant cells needed to have a higher viscosity than the normal cells in order to remain in the crypt. Mutant cells that first appeared near the top of the crypt required a much higher viscosity to remain in the crypt (or to invade downwards) than those that were initiated near the base.

5.2.2 Cell-centre model

The continuum model did not allow us to follow lineages generated from a single cell or to have mutations in single cells. Thus, in Chapter 3 we focussed on an existing cell-centre model [109] for the proliferation, migration and differentiation of cells within a colorectal crypt. We used agile computational methods to develop a computational framework, CHASTE, for a multiscale model of colorectal cancer. This allowed us to include subcellular models of cell behaviour.

In the model, the cells are treated as discrete entities and the mechanical effects are accounted for by connecting neighbouring cells with linear springs. The neighbouring cells are determined by a Delaunay tessellation and the cell shapes determined by a Voronoi diagram. Inertial effects are neglected and cell-cell interaction forces associated with the compression and extension of the springs are balanced by viscous drag terms to determine cell velocities. The drag on the cells represents the combined effects of cell-stroma adhesion and cytoskeleton rigidity and is independent of cell-

cell adhesion. Running simulations of the model, yielded a quasi-steady-state crypt for which the number of cells born balances the number of cells removed from the top of the crypt, as is the case *in vivo*.

The modifications made to the original cell-centre model by Meineke *et al.* [109] account for biological features such as Wnt-dependent proliferation, unpinning of cells at the base of the crypt, dependence of drag on cell size, dependence of cell-cell adhesion on the area of contact between the cells and the inclusion of mutant cells. Mutant cells proliferate at rates which are independent of Wnt and may have different cell-cell interaction forces and drag properties to normal cells.

Model simulations yielded behaviour similar to that seen in the continuum model. Cells proliferated in the lower part of the crypt and were forced upwards by mitotic pressure. The ability of mutant cells to remain in the crypt depended on their initial position and the magnitude of their drag.

The cell-centre model generates results not evident in the continuum model. For example, the size of the cells in a fully mutant crypt: when both the cell-cell interaction forces and the cell drag of mutant cells were increased, a fully mutant crypt, in a quasi-steady state, could be achieved. This fully mutant crypt had more (smaller) cells than a normal quasi-steady-state crypt, in good qualitative agreement with experimental findings of Sansom *et al.* [141]. This could not be seen in the continuum model, which assumed uniform cell-density in both the normal and the mutant cell regions.

We investigated the effects of several other changes to Meineke's original model [109]. By unpinning the stem cells at the base of the crypt, our simulations revealed that, over long times, the crypt would be occupied by cells all descended from the same transit cell, i.e. the crypt was monoclonal. When cell drag was assumed to depend on cell area, we found that fewer cells accumulated on the base of the crypt. Having the force between cells dependent on the area of contact resulted in the cells having a rounder shape.

5.2.3 Cell-vertex model

The cell-centre model, from Chapter 3, has some problems in how cell-cell adhesion is modelled: adhesion is indistinguishable from other cell-cell interaction forces, such as forces concerned with retaining cell size. The cell-centre model also requires time-consuming Delaunay tessellations and Voronoi diagrams to be produced at each time step. In order to overcome these problems, in Chapter 4 we developed a cell-vertex model to describe cell proliferation and migration in a colorectal crypt.

The model defines the shape and movement of polygonal cells by their vertices. The cells are

assumed to have a free energy that comprises terms for cell-cell adhesion and cell deformation. The gradient of the free energy is assumed to exert a force on the cell vertices, which is balanced by a drag term proportional to the velocity of the vertices. The vertex model lends itself to modelling cell-cell adhesion as the contact area between cells can easily be found by calculating the length between neighbouring vertices (and assuming cells to be of the same height). This dispenses with the need to create a time-consuming Delaunay tessellation and Voronoi diagram at every timestep (as is required by many cell-centre models). The cell-vertex model also provides greater control over cell growth, with cells having a target area which increases linearly over their G_1 phase.

Wnt-dependent proliferation is modelled as for the cell-centre model, with cells in the lower part of the crypt (termed transit cells) able to proliferate and cells in the upper part of the crypt (termed differentiated cells) not able to proliferate. As before, mutant cells are assumed to proliferate throughout the crypt due to the breakdown in the Wnt-signalling pathway.

Using the cell-vertex model, we were able to generate results similar to those found using the cell-centre model. This included crypt monoclonality for long times and the ability of mutant cells to remain in the crypt depending on their initial position and their drag (representing cell-stroma adhesion and cytoskeleton rigidity).

We also used the model to monitor the speed and size of the cells as they moved up the crypt. We found that cells moved slowly when they were close to the crypt base. However as they moved through the proliferative region, their speed increased due to the increase in the number of proliferating cells below them. When the cells moved into the non-proliferating region, they increased in size, tended to their natural area and became more hexagonal in shape.

The cell-vertex model allowed us to easily change the cell-cell adhesion properties of mutant cells. This enabled us to demonstrate that cell-cell adhesion has an effect that is independent of cell-stroma adhesion and cytoskeleton rigidity. If mutant cells have an affinity to bond with other mutant cells, their chances of dominating the crypt increased.

5.3 Parameter values

In §5.4 and §5.5, we present a qualitative comparison of the three models. Before doing this we must ensure that the models are as similar as possible. As the basis for comparison, we use the cell-vertex model as it is the most detailed and involves the largest number of parameters. The changes made to the cell-centre and continuum models are discussed in §5.3.1 and §5.3.2 and a summary of the

parameters is given in Table 5.1.

The standard model we use represents a cylindrical crypt of height 21.5 cell lengths and circumference 11 cell lengths (where a cell length is taken as $8\mu m$, the mean of the range of cell diameters $(6-10\mu m)$ suggested in [49]). To mimic the Wnt-stimulus, normal cells are assumed proliferate in the lower third of the crypt while mutant cells proliferate throughout the crypt. The cell-cycle time of the proliferating cells varies stochastically from cell to cell with mean 16 hours and standard deviation 0.5 hours. We assume that the mechanical parameters associated with the normal cells are the same throughout the crypt, with all normal cells having the same drag and the same values in the free energy function. Detailed explanations of how the parameter values were chosen are presented in Appendix B.

5.3.1 Adaptations to the cell-centre model

To adjust the cell-centre model so that it is comparable with the cell-vertex model, we fix the same crypt size and cell-cycle times. However the drag coefficient and the spring constant used in the cell-centre model are not directly comparable to the cell-vertex model. To estimate these parameters, we compare simulations for the cell-centre and cell-vertex models.

In the cell-centre model, when a crypt contains only normal cells, the combined drag, $\mu_i = \mu_n$, and the strength of the springs between neighbouring cells, $k_{ij} = k_{nn}$, can appear as a single lumped parameter, $\xi = k_{nn}/\mu_n$. This parameter was estimated by comparing the average vertical component of the cell velocity along the crypt axis from the cell-centre and cell-vertex model.

Firstly we take a crypt, of the size and with cell-cycle times of that described above. We simulate the cell-centre model until it reaches a quasi-steady-state and then for a further 100 hours to determine how the average cell velocity in the direction of up the crypt, v_y varies with distance up the crypt. This process was repeated for several values of ξ. and then compared with the values of v_y for the cell-vertex model described in Chapter 4 (not shown). The value of ξ that generated velocities v_y that compare best with those from the cell-vertex model is $\xi = 85\texttt{hours}^{-1}$, as illustrated in figure 5.2, below.

As ξ represents two parameters, k_{nn} and μ_n, we set without loss of generality $\mu_n = 1.0$ Kg hours^{-1} and $k_{nn} = 85$ Kg hours^{-2}.

Ideally we would create many more tests to estimate ξ, for example, placing a population of cells under compression and tension for both the cell-vertex and cell-centre models. Unfortunately time-constraints prevented us from carrying out these tests.

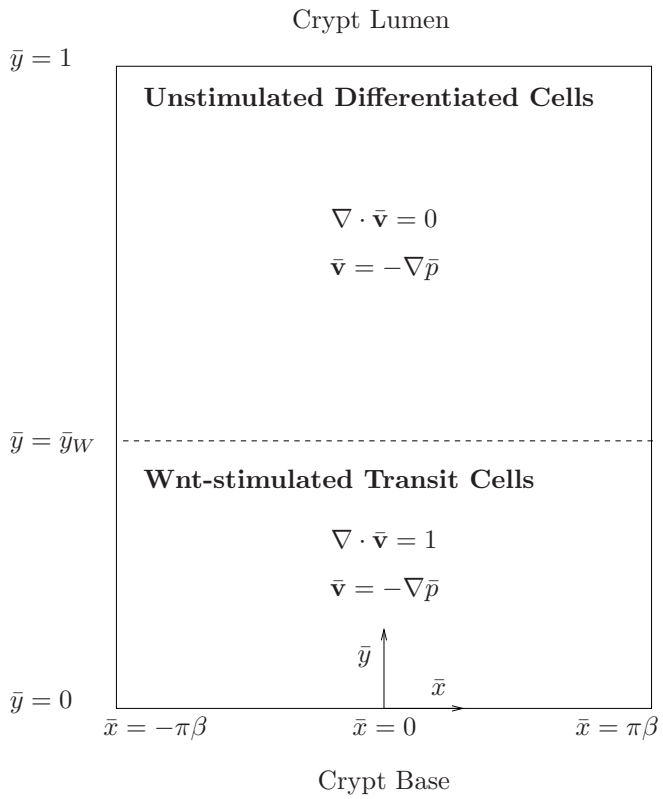

Figure 5.1: Sketch of the continuum model of the crypt, when no mutant cells are present. Cells proliferate in the lower part of the crypt, $\bar{y} \leq \bar{y}_W$, where they are subject to the Wnt stimulus.

5.3.2 Adaptations to the continuum model

To ensure consistency of the three models, we needed to change the functional form used to describe cell proliferation rate for normal cells. In the original continuum model (Chapter 2), it decreased linearly with (non-dimensional) distance up the crypt, $\bar{y}$. However, in the cell-level models, cells only proliferate in the lower third of the crypt. To facilitate comparison, the source term in the continuum model was changed to a step function. We allowed proliferation for $\bar{y} \leq \bar{y}_W$, where cells are Wnt-stimulated, and assume there was no proliferation for $\bar{y} > \bar{y}_W$, where cells are unstimulated (see figure 5.1). The value of $\bar{y}_W$ is set to be $\bar{y}_W = 1/3$, for consistency with the cell-level models.

The balance of mass for the normal cells gives

$$\nabla \cdot \bar{\mathbf{v}} = H(\bar{y}_W - \bar{y}) \tag{5.1}$$

where $\bar{\mathbf{v}}$ is the cell velocity and H is the Heaviside step function. For the cell velocity, a Darcy constitutive law is used, so for normal cells, $\bar{\mathbf{v}} = -\nabla \bar{p}$, where $\bar{p}$ is the pressure of the cells.

Parameter	Model	Value	Units	Description
H_C	All models	21.5	cell lengths	Crypt height
W_C	All models	11	cell lengths	Crypt width
H_W	All models	7.17	cell lengths	Proliferative region
t_{cc}	Cell-level	$\mathcal{N}(16.0, 0.5)$	hours	Cell-cycle time
k_1	Continuum	1/16.0	hours^{-1}	Proliferation rate
φ_1	Continuum	1.0	Kg^{-1}hours [cell lengths]^3	Darcy parameter
k_{ij}	Cell-centre	85	Kg hours^{-2}	Spring strength
μ_N	Cell-centre	1.0	Kg hours^{-1}	Cell drag (normal cells)
γ_{ij}	Cell-vertex	0.01	Kg hours^{-2} [cell lengths]	Cell-cell adhesion
γ_{iE}	Cell-vertex	0.02	Kg hours^{-2} [cell lengths]	Cell-boundary adhesion
λ	Cell-vertex	1.0	Kg hours^{-2} [cell lengths]$^{-2}$	Cell-size constraint
β	Cell-vertex	0.1	Kg hours^{-2}	Cell-perimeter constraint
η_N	Cell-vertex	100	Kg hours^{-1}	Cell drag (normal cells)

Table 5.1: Table summarising the parameters used in Chapter 5.

Using mass balance and Darcy's law, discussed in Chapter 2, and new proliferation terms, we change the terms in the collocation method accordingly. The ratio, β, of crypt radius to crypt height is calculated from the cell-vertex model as $\beta = \dfrac{11}{21.5 \times 2\pi}$.

For comparison with the cell-level models we transform the non-dimensional results from the model described in §5.3.2 and cast them into dimensional form using the scalings from Chapter 2,

$$y = H_C\bar{y},\ x = H_C\bar{x},\ p = \frac{k_1 H_C^2}{\varphi_1}\bar{p},\ \mathbf{v} = k_1 H_C \bar{\mathbf{v}},\ t = \frac{1}{k_1}\bar{t}. \tag{5.2}$$

In (5.2) H_C is the length of the crypt, which we take to be 21.5 cell lengths ($= 21.5 \times 8\mu m$). The proliferation rate of normal cells, k_1, is taken as the reciprocal of the average cell-cycle time in the cell-vertex model, so that $k_1 = 1/16$ hours^{-1}. In the absence of any data to estimate φ_1, the Darcy constant for the normal cells, we set $D_1 = 1.0$ Kg hours^{-1} [cell lengths]^3.

5.4 Normal crypts

In this section we use the three models to study the dynamics of a healthy crypt containing only normal cells and compare the results obtained for each approach.

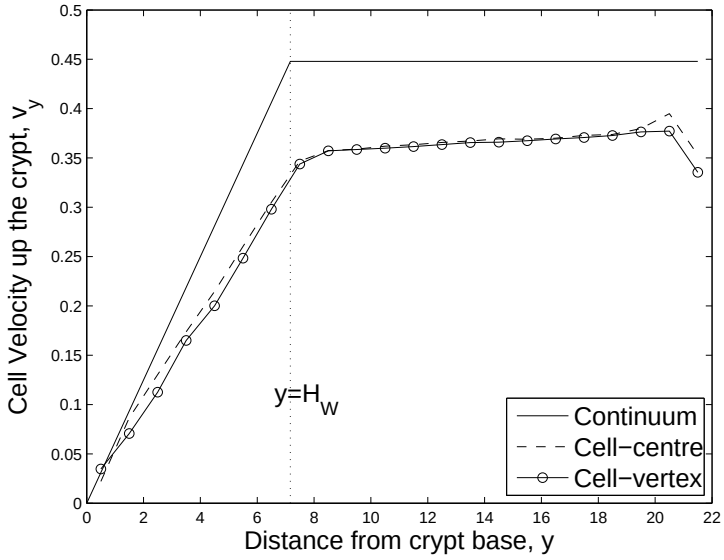

Figure 5.2: Plots showing how the averaged vertical component of the cell velocity varies with distance from the base of the crypt for the continuum, the cell-centre and the cell-vertex models. The dotted vertical line, $y = H_W$, delineates the upper boundary of the Wnt-stimulated region: cells proliferate for $y \leq H_W$ and for $y > H_W$ they do not.

5.4.1 Velocity

In Chapter 4, we showed v_y, the averaged vertical component of the cell velocity, varied with distance along the crypt axis for the cell-vertex model. The average was computed by splitting the crypt into horizontal bands of unit width and computing the average velocity for cells in each band. To compare the cell velocities predicted for each model, we calculate the average cell velocity for the cell-level models and the cell velocity for the continuum model. The results are summarised in figure 5.2.

In each case, there is a marked change in the velocity profile as we pass from the proliferating region ($0 < y < H_W$) to the differentiated region. In the proliferating region all three models exhibit a linear increase in v_y, from zero at the crypt base. There are however differences in the value of v_y on H_W, the boundary between the proliferative and non-proliferative region. The value of $v_y(H_W)$ is larger for the continuum model than for the cell-level models. This is not due to the choice of parameter values but to differences in the models. In the continuum model, cells move parallel to the y-axis so at $y = H_W$, $v_y = k_1 H_W$. Both H_W and $k_1 (= 1/t_{CC})$ are fixed across all models. The difference in values of $v_y(H_W)$ is due to cellular signals prematurely halting the cell-cycles in the

cell-level models. In the cell-level models, if a cell moves past $y = H_W$, it is termed differentiated and can no longer proliferate, even if it is near the end of its cell cycle. This results in many transit cells failing to proliferate and means that the overall proliferation rate is lower than the constant rate assumed in the continuum model. In addition, the continuum model assumes fixed cell density, so that individual cells are incompressible, whereas the cell-level models allow for some degree of cell compression. Proliferative expansion in the continuum model is entirely accommodated by cell displacement, whereas in the cell-level models, it is accommodated to some extent by cell compression leading to lower cell velocities.

There are also differences in the profiles of $y > H_W$. In the cell-level models, v_y increases slightly with y, whereas in the continuum model it remains constant. Again, in the continuum model, the cells are incompressible, whereas in the cell-level models they can be compressed below their natural size. In the non-proliferating region, cells in the cell-level models relax, forcing those above them to move faster. However in the continuum model, the cells are incompressible and there is no relaxation and the cells reach their maximum velocity at $y = H_W$.

5.4.2 Cell compression

In Chapters 3 and 4 we found that the cells are more compressed toward the bottom of the crypt than near the top of the crypt. In order to see whether this behaviour is common to all models, in figure 5.3 we consider how cell compression varies with distance from the crypt base. For the cell-level models, we plot an average of $A_N - A$, the difference between the cell's natural area and its actual area. The average is calculated in a similar way to v_y in §5.4.1. For the continuum model, since the cells are incompressible, we show how pressure varies with distance from the crypt base.

In all three models, cell compression is highest at the base of the crypt and decreases with increasing distance. For both cell-level models, the decrease in area difference is approximately linear in the non-proliferative zone, which compares well with the linear decrease in the continuum model.

However there are differences between the models. In the continuum model, we have assumed the pressure decreases to zero at the top of the crypt. This does not happen in the cell-level models, as the cells still have not fully relaxed to their natural size by the time they reach the top of the crypt. This is due, in part, to the cells having insufficient time to relax to their natural area before they are removed from the crypt. It is also due to the restoring forces being small when the cells are very close to their natural size.

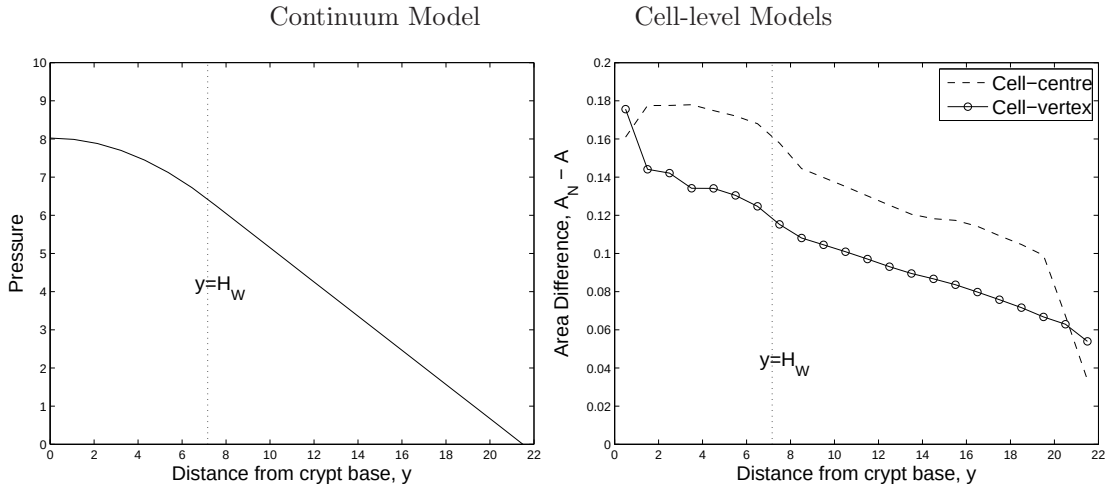

Figure 5.3: Plots showing how the compression of the cells varies with distance from the base of the crypt for (left) the continuum model, (right) the cell-centre model and the cell-vertex model. For the continuum model, the pressure, p, is plotted; for the cell-centre and cell-vertex models the difference between actual cell area, A, and natural cell area A_N, is plotted. The dotted horizontal line, $y = H_W$, shows the edge of the Wnt-stimulated region, where for $y \leq H_W$ cells can proliferate and for $y > H_W$ cells cannot.

5.5 Test problem

For further comparison, we ran another test problem on all three models. This involved inserting a circular patch of mutant cells into a normal crypt (see figure 5.4). We investigated the effect of varying the drag on the mutant cells and their initial position on the behaviour of the mutant cells and, in particular, their ability to colonise the crypt.

Results presented earlier (see Chapters 2-4) suggest that relative changes in the drag coefficient of the mutant cells and their initial position can influence their ability to establish within the crypt. By choosing this test problem, which is straightforward to implement in all three models, we can see how the behaviour of the mutant cells changes between the different models. In Chapters 3 and 4, we introduced a single mutant cell at $t = 0$. Here, by considering a larger group of mutant cells, we reduce the dependence of our results on the intrinsic stochasticity of the cell-level models.

When simulating the test problem, normal cells proliferate for $y \leq H_W$, whereas mutant cells proliferate throughout the crypt. To model changes in drag, we vary the model parameters in the following way: in the cell-level models, the mutant cells have drag coefficients μ_M (for the cell-

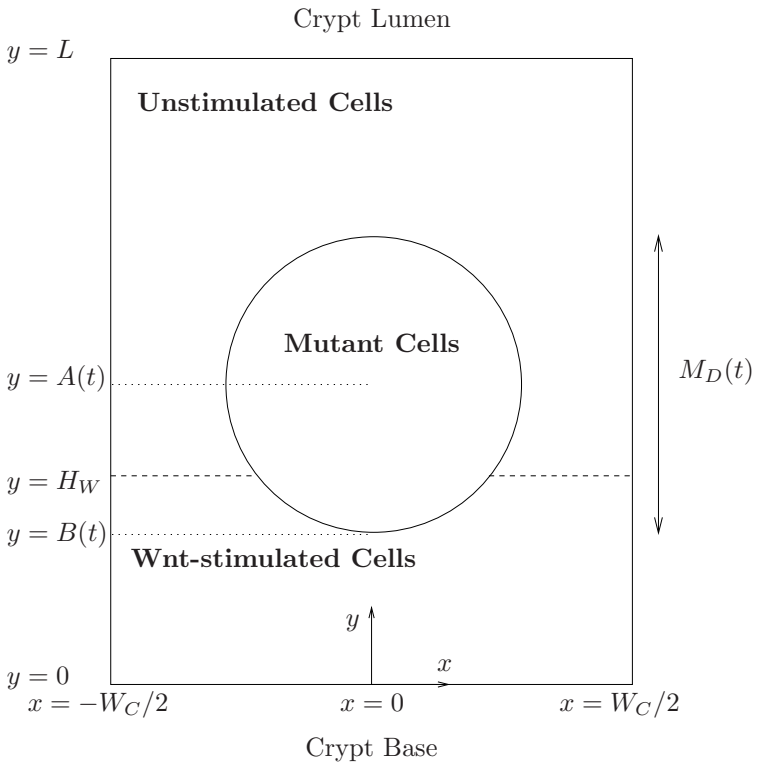

Figure 5.4: Sketch of the model for two cell populations, normal cells (initially covering the majority of the crypt), and mutant cells (initially in the circle $x^2 + (y - A_0)^2 \leq (M_D(0)/2)^2$) growing on the surface of a cylindrical crypt. $A(t)$ is the centre of the patch in the vertical direction, initially $A(0) = A_0$, $B(t)$ is the position of the mutant cell closest to the crypt base and $M_D(t)$ is the span of the mutant patch in the y-direction, where $M_D(0) = 4$ cell-lengths.

centre model) and η_M (for the cell-vertex model) which we vary in the ranges $\mu_N \leq \mu_M \leq 20\mu_N$, $\eta_N \leq \eta_M \leq 20\eta_N$, where μ_N and η_N are the drag coefficients of the normal cells for the cell-centre and cell-vertex models respectively. In the cell-centre model, the drag acts at the cell centre, whereas in the cell-vertex model, it acts at each vertex and is the average of the drag on the cells that surround the vertex. In the continuum model we alter the drag on the mutant cells by changing $D = \varphi_N/\varphi_M$ (the ratio of φ_N, the viscosity of normal cells, φ_M to mutant cells) so that $\frac{1}{20} < D < 1$. We recognise however, there is limited direct equivalence between the three drag coefficients.

For each model, a patch of mutant cells of diameter $M_D(0) = 4$ cell lengths, centred at $(x, y) = (0, A_0)$, is introduced at $t = 0$ and simulations performed for different values of the (relevant) drag coefficient and at different values of A_0 ($A_0 = 3, 7, 11, 15$ cell lengths). The position, $B(t)$, of the lowest point of the patch is recorded every 10 hours (see figures 5.5, 5.6 and 5.7).

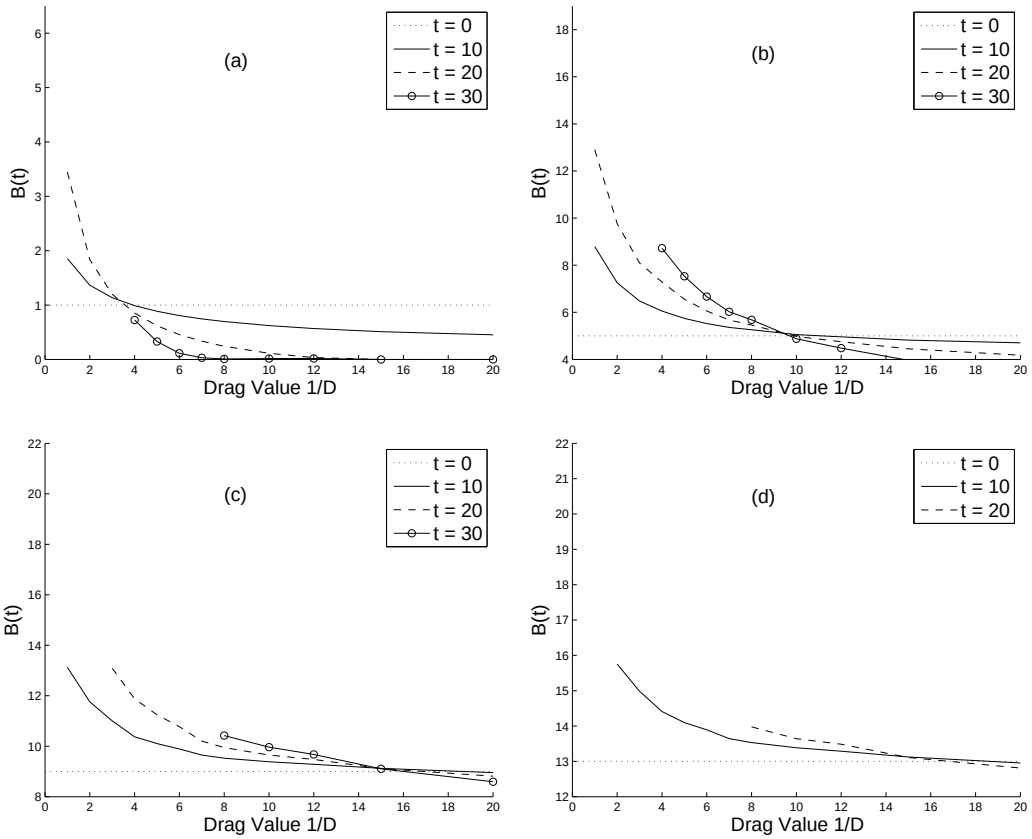

Figure 5.5: Series of plots showing how $B(t)$, the base of the mutant patch, in the continuum model varies with the drag ratio, D, with position plotted after $t = 0,\ 10,\ 20,\ 30$ hours. Plots are for different initial positions of the circular mutant patch of initial radius 2 and azimuthal position $x = 0$ and $y = A_0$, with (a) $A_0 = 3$, (b) $A_0 = 7$, (c) $A_0 = 11$, (d) $A_0 = 15$.

5.5.1 Test problem results

A common feature of all three models, for all starting positions of the mutant cells, is that the higher the drag coefficient on the mutant cells, the slower they move and the more likely they are to invade downwards. This can be explained by the greater resistance offerred by the mutant cells to the mitotic force exerted on them by the normal cells beneath them (see figures 5.5, 5.6 and 5.7 for the continuum, cell-centre and cell-vertex models respectively).

Another common feature that of all three models is that the cells' behaviour is dictated by the initial position of the mutant cells and, in particular, the velocity of normal cells at $y = B(0)$. This is exemplified by the fact that cases for which $A_0 = 15,\ B(0) = 13$ (see figures 5.5(d), 5.6(d), 5.7(d))

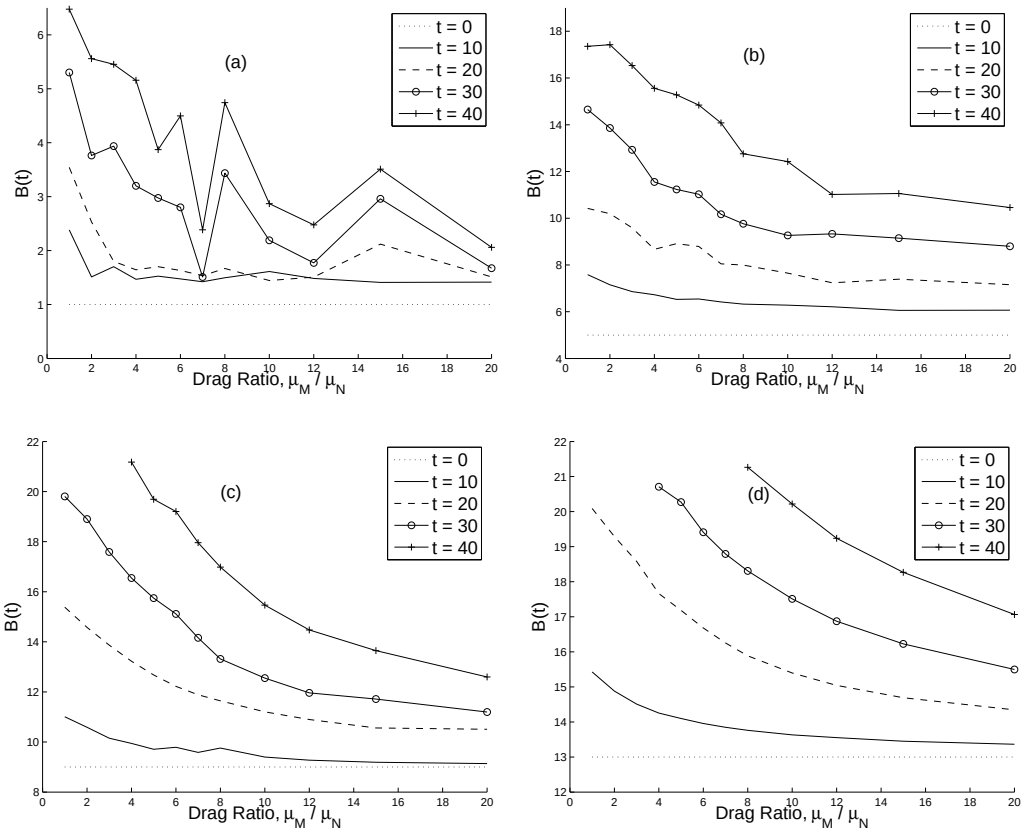

Figure 5.6: Series of plots showing how $B(t)$, the position of the lowest cell in the mutant patch in the cell-centre model varies with the drag ratio, μ_M/μ_N, with position plotted after $t = 0,\ 10,\ 20,\ 30,\ 40$ hours. Plots are for different initial positions of the circular mutant patch of initial radius 2 and azimuthal position $x = 0$ and $y = A_0$, with (a) $A_0 = 3$, (b) $A_0 = 7$, (c) $A_0 = 11$, (d) $A_0 = 15$.

exhibit similar behaviour to that when $A_0 = 11,\ B(0) = 9$ (see figures 5.5(c), 5.6(c), 5.7(c)). This is is because the velocity of the normal cells is very similar for both $y = 9$ and $y = 13$ (see figure 5.2). This finding (the dependence on $v_y(B(0))$) is further supported, by the fact that there are more cases of top-down invasion when the mutant cells are initially near the base of the crypt, $A_0 = 3,\ B(0) = 1$ (see figures 5.5(a), 5.6(a), 5.7(a)), where the velocity is lower (see figure 5.2).

Some behaviour is model specific. Consider, for example, cases for which the mutant cells initially move up the crypt ($B(t_1) > B(0),\ t_1 > 0$) but move back down the crypt at later times, $B(t_2) < B(t_1),\ t_2 > t_1$. This occurs in the cell-vertex model (when $\mu_M = 15\mu_N$ in figure 5.7(a)) but not in the continuum or cell-centre models (although it can occur for certain parameter regimes for the cell-centre model, see figure 3.20). An explanation for this phenomenon is that mutant cells

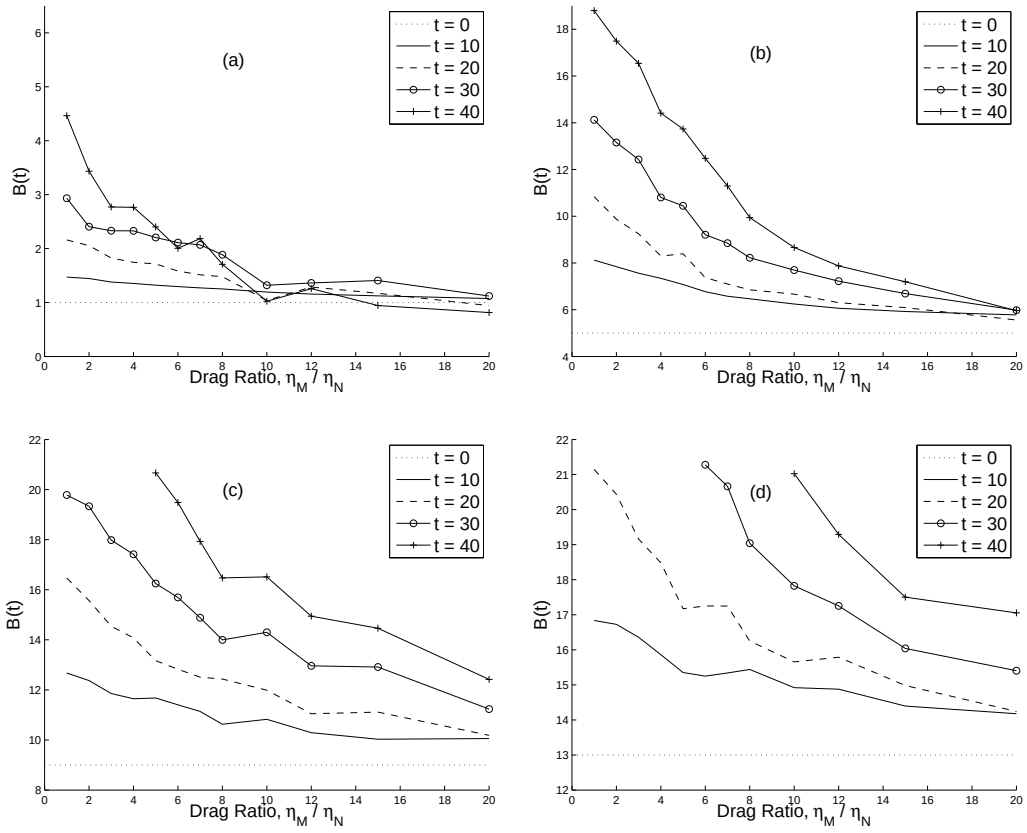

Figure 5.7: Series of plots showing how $B(t)$, the position of the lowest cell in the mutant patch in the cell-vertex model varies with the drag ratio, η_M/η_N, with position plotted after $t = 0,\ 10,\ 20,\ 30,\ 40$ hours. Plots are for different initial positions of the circular mutant patch of initial radius 2 and azimuthal position $x = 0$ and $y = A_0$, with (a) $A_0 = 3$, (b) $A_0 = 7$, (c) $A_0 = 11$, (d) $A_0 = 15$.

need time to establish a critical mass in the cell level models. Once this mass has been established, the mutant cells displace the normal cells beneath them in preference to displacing the normal and mutant cells above.

Other differences between the models concern the ratios of the drag coefficients (of mutant cells to normal cells) needed for the mutant cells to invade downwards. For example, when $A_0 = 3,\ B(0) = 1$, the continuum model predicts downward invasion when $1/D = 4$ for downward invasion, whereas a ratio of $\eta_M/\eta_N = 10$ is needed to achieve the same effect in the cell-vertex model. This discrepancy can be explained by the fact that drag in the continuum model represents more effects (cell-cell adhesion in addition to cell-stroma adhesion and cytoskeleton rigidity) than in the cell-level models (where it does not represent cell-cell adhesion). Hence changing the drag ratio in the continuum

model has more effect than in the cell-level models.

5.6 Discussion

In the following section we review the three models and discuss their relative merits. We assess the computational speed of the models in §5.6.1, their biological realism and the insight they give in §5.6.2 and explain how they could be extended in §5.6.3.

5.6.1 Computation

Since speed of computation is often a limiting factor, we now compare the time it takes to compute solutions for the three models.

The continuum model is the simplest and fastest. The maximum timestep (60 seconds) needed to ensure stability (such that it passes the validation tests in §2.5.2) is the largest of the three models (comparing with values of 10 seconds and 7 seconds for the cell-centre and cell-vertex models respectively) and fewer calculations are needed at each timestep. The main bearing on the model run-time is the length of time required to determine the coefficients (~ 60 for a test problem such as that in §5.5) that minimise the residual in a system of equations (size ~ 120). This may be done quickly by inverting a matrix and finding the least squares error, or more accurately and less rapidly, by using an iterative minimum finder to minimise the L_1. It takes 90 minutes to produce one of the graphs in figure 5.5 on a desktop machine (Intel Pentium 4, 2.80 GHz, 1GB memory, 512KB Cache) using Matlab to solve the continuum model.

An additional advantage of the continuum model over the cell-level models is that the computation time does not depend on the domain size. The model is solved in dimensionless form so that computation time is independent of the number of cells in the domain (see figure 5.8).

While the cell-centre model requires many more calculations than the continuum model, it still runs relatively quickly. This is because the associated code was written efficiently in C++, with large amounts of re-factoring to reduce run-time. It takes 8 hours on a desktop machine to produce a graph in figure 5.6. Another benefit of using C++ is that it is possible to exploit multi-processor facilities to run simulations twice as fast as a desktop machine, with up to 8 simulations running concurrently.

A disadvantage of the cell-centre model is that the computation time greatly increases with the

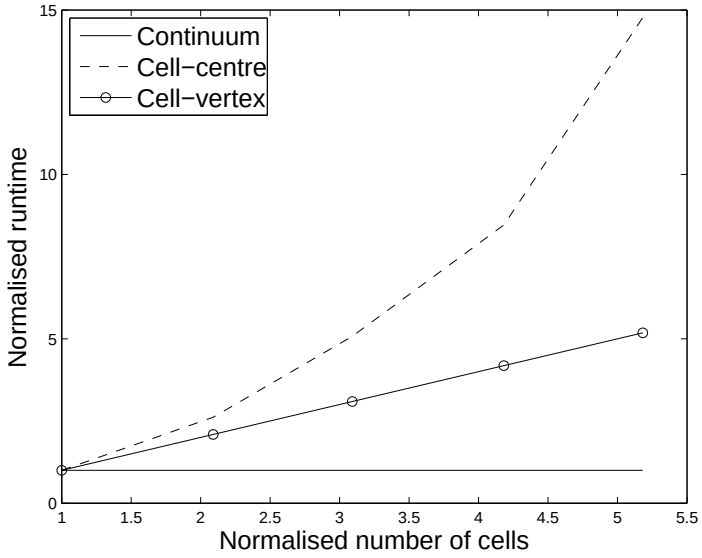

Figure 5.8: Plot showing how the runtime changes with the number of cells in the simulation. Runtime and number of cells normalised for each model for the results mentioned in §5.6.1. Plots show runtime is constant with cell number for the continuum model, linear for the cell-vertex model and increases at a greater than linear rate for the cell-centre model. Runtime was calculated by running, for 200 hours of simulation time, a simulation for a crypt where the width, W_C, was varied and all other parameters are as in table 5.1.

number of cells (see figure 5.8). The model requires a Delaunay triangulation to be performed at each time-step. The time for the Delaunay triangulation scales like $\sim n\log(n)$, where n is the number of cells [152]. This means the model may be unsuitable for very large numbers of cells, as would be the case if more than one crypt were modelled.

The cell-vertex model is the slowest of the three but this may be because the code is written in Matlab which is much slower than a compiled language such as C++. However the algorithm for solving the model may be as fast (or faster) than the cell-centre model. Although the cell-vertex model has more objects to loop over than the cell-centre model (number of vertices $\sim 2\times$ number of cells), the cell-vertex model does not require a Delaunay triangulation to be performed at each timestep (this takes approximately half of the runtime of the cell-centre model). On the other hand, the timestep needed for stability in the cell-vertex model is smaller than that needed in the cell-centre model. To compare the computational speeds of the two models rather than the code, the cell-vertex model should be written in the CHASTE framework; a longer term aim of ours. Currently, when the model is run in Matlab on a desktop machine, it is three times slower than the cell-centre model

(it takes 24 hours to produce a graph in figure 5.7).

The runtime of the cell-vertex model scales linearly with the number of cells (as shown in figure 5.8). This means that despite being more detailed than the cell-centre model, the cell-vertex model would outperform the cell-centre model for large number of cells.

5.6.2 Biological realism and insight

Major tests of a mathematical model are how well it reproduces experimental observations and whether it generates any new insight. In this section, we assess how well each of the models performs in these regards.

Comparison with experiments

All three models reproduce the basic features of a normal colorectal crypt. Cells proliferate in the lower region of the crypt and move up the crypt. However the cell-level models could reproduce more detailed experimental features, such as crypt monoclonality and realistic snapshots of cell lineages.

Taylor *et al.* [161] used mitochondrial-DNA staining methods to label lineages generated from a single cell within a crypt. The lineages resembled wave-like ribbons extending from the base to the top of the crypt. The cell-level models are able to reproduce similar results (see figure 5.9), however the continuum model can not. In the continuum model, for a normal crypt, all movement is parallel to the crypt axis and cells from the same lineage form a vertical band parallel to the crypt axis.

Other data from McDonald *et al.* [108] reveal that over long times crypts become monoclonal, with all epithelial cells generated from the same progenitor cell. The cell-level models reproduce this phenomenon (as shown in §3.5.1 and §4.3.1), whereas the continuum model does not as there is no azimuthal movement of cells (for a normal crypt).

Sansom *et al.* [141] reported high levels of cell packing in fully mutant crypts. The cell-level models were able to reproduce this phenomena but the continuum model could not, as individual cells are not distinguished in the continuum model. However the cells were under higher pressure in a fully mutant crypt than in a normal crypt.

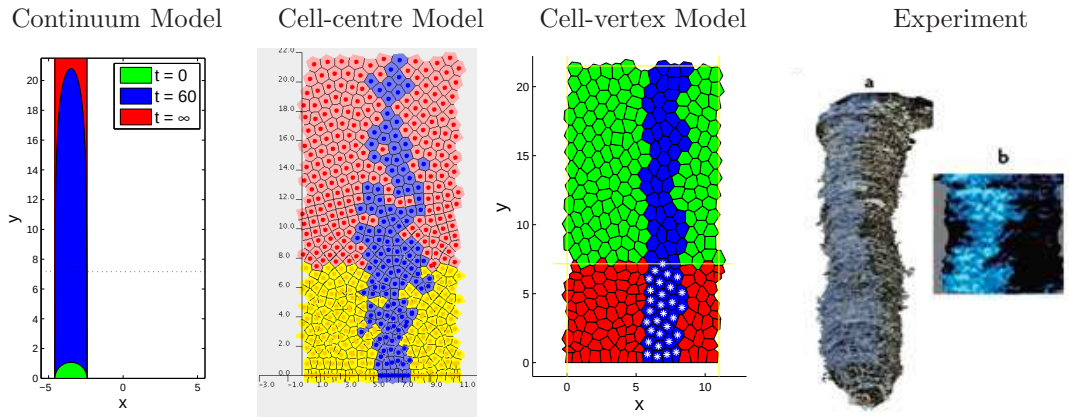

Figure 5.9: Snapshots of a cell lineage from (left) the continuum model, (centre-left) the cell-centre model, (centre-right) the cell-vertex model and from experiment (right) taken from [73] and [161]. For the continuum, model all movement is parallel to the crypt axis. The dotted horizontal line, $y = H_W$, shows the edge of the Wnt-stimulated region, where for $y \leq H_W$ cells can proliferate and for $y > H_W$ cells cannot. The two cell-level models show marked cells moving as a waved ribbon as in the experiments. For the cell-centre model, cells from the lineage are blue, transit cells are marked yellow and differentiated cells marked pink. For the cell-vertex model, cells from the lineage are blue, transit cells are marked red (or blue with a white $*$) and differentiated cells marked green. For the experiment cells from the lineage are marked in blue, other cells are in black.

New Insight

All models showed that mutant cells introduced closer to the base were more likely they were to remain in the crypt (see §5.5). We also observed that the likelihood of a mutant population remaining in the crypt depended on how the mutant population was modelled. For example, experimental evidence suggests that loss in Wnt-dependence leads not only to changes in proliferation but also to (i) a more rigid cytoskeleton [115], (ii) higher levels of cell-stroma adhesion [141] and (iii) higher levels of cell-cell adhesion [18]. How easily these three effects can be discriminated depends on the choice of the model.

In the continuum model we showed that the combined effects of (i)-(iii) influenced whether the mutant cells remained in the crypt. However we were unable to discriminate between changes in each process as all three effects were modelled with a single lumped parameter.

In the cell-centre model effects (i) and (ii) were modelled separately from (iii). This enabled us to show that increased cell-stroma adhesion and a more rigid cytoskeleton can increase the likelihood

of mutant cells persisting in the crypt.

The cell-vertex model generated results which were similar to those of the cell-centre model for changes in (i) and (ii). Additionally, the model also gave insight into how changes in cell-cell adhesion affected the mutant cells. For example, we found that if mutant cells had an affinity to bind to other mutant cells, their chances of fixating in the crypt was increased (see §4.3.2).

5.6.3 Extensions

Although we have generated some interesting results, there are many model extensions we could consider. These include simulating the models in a more realistic geometry, applying the model to multiple crypts, including more subcellular effects and incorporating cell death. In this section, we discuss the challenges that introducing these features represent.

Geometry

An obvious limitation of all the models we have described is that the crypts are assumed to be cylindrical, whereas in practice they are test-tube-shaped. By simplifying the bottom of crypt, we neglect effects such as cells to passing from one side of the crypt to the other via the base of the crypt. By ignoring the flat surface at the top of the crypt, we neglect features such as cell movement onto the luminal surface.

Each of the models could be adapted with relative ease by projecting the test-tube shaped crypt onto a two-dimensional surface. We have previously developed a crypt-projection model for the continuum model when the crypt is filled entirely of normal cells (not shown) and this could be fairly easily adapted to include mutant cells. The cell-centre model has been adapted by another member of the CHASTE group (Alex Fletcher) [125] to project a test-tube-shaped crypt onto a surface and the cell-vertex method could be similarly adapted.

It would also be interesting to create a fully three-dimensional model for the crypt with cells modelled as three-dimensional shapes. With a three-dimensional model, we would be able to model cell-cell adhesion more accurately as we could calculate the contact-area between cells, rather than assuming all the cells are of the same height. We could also include deformation of the underlying stroma and model phenomenon such as crypt buckling due to overproliferation of mutant cells. The results could be compared with those from a continuum model of crypt buckling such as that presented in [52].

However there are practical limitations to 3D modelling of crypts. The extra spatial dimension means, the models would require more memory and hence would run more slowly. For example in a 2D cell-vertex model, a cell is represented by a single polygonal shape. However in a 3D model, each cell would have several polygonal faces, increasing the number of vertices. There would also be difficulties extending the cell-centre model to 3D, particularly when using the Delaunay triangulation to find neighbouring cells. Attention would need to be paid to placing 'ghost cells' (non-existent cells used when creating a Delaunay triangulation) to prevent cells connecting to cells on the other side of the crypt.

Multiple crypts

It would also be interesting to investigate further stages of colorectal cancer, such as invasion of mutant cells into neighbouring crypts and polyp formation. To do this multiple crypts (and large numbers of cells) would need to be simulated. As mentioned in §5.6.1, this would cause the cell-centre model to run much more slowly. However the reduction computational speed would be less pronounced in the cell-vertex and continuum model.

Extensions to include subcellular models

Other model extensions could include further development of the subcellular models within the cells. For example, β-catenin levels could be coupled to model cell adhesion in greater detail in a similar way to Ramis-Conde *et al.* [133]. They assumed that β-catenin membrane proteins were spread equally over all surfaces and made cell-cell adhesion proportional to the number of proteins in contact. To do this we could use the membrane-bound β-catenin levels found by incorporating Van Leeuwen *et al.*'s Wnt-signalling model [172], as detailed in Appendix A.2. It would also be interesting to include additional signalling pathways, rather than just canonical-Wnt signalling, to see how different mutations affect the cells' behaviour. These may reveal why mutations in either APC and β-catenin are commonly found in the early stages of colorectal cancer, but very rarely together. These subcellular effects would be simple to include in the cell-centre and cell-vertex models but difficult to include in the continuum model.

Cell death

Another factor we have not considered in any great detail is the death of cells when they reach the top of the crypt. Experimental evidence shows that mutations in APC and β-catenin can alter the

levels of proteins related to apoptosis [171]. These changes may affect how mutant cells are shed into the lumen, possibly causing the cells to undergo apoptosis further down in the crypt.

In the continuum model, this can be addressed by modifying the source term so that it is negative at the top of the crypt. However, in the cell-level models we have to model how the space left by a dead cell is filled by surrounding cells. In the cell-vertex model we can shrink the size of the cell smoothly by decreasing the size of the boundary surrounding the empty space. Then, by using T1 and T2 swaps [50, 113], the empty space can be deleted. In the cell-centre model, cell-death is less easy to include. When the Voronoi diagram is drawn at the next timestep after a cell is deleted, any empty space is immediately taken up by the surrounding cells, rather than in the cell-vertex model, where the empty space shrinks over several time-steps. This means cell-death is easiest to include in the cell-vertex and continuum model, but less easy to include in the cell-centre model.

5.7 Further work and conclusions

Although we have been able to compare some of the features of the models, further work is needed to gain a fuller understanding. One such aim would be to investigate the relationship between the cell-level models. To understand the relationship between the two models, mechanical loading tests such as those described in [124] could be performed on the models to determine the sensitivity of the response to the choice of parameters values assessed.

To quantify how cell-cell and cell-stroma adhesion affect the chances of mutant cells remaining in the crypt, more cell-level model simulations are needed. This could be achieved, by running many simulations where different initial mutant cells are chosen and the seed in our random number generator is changed. This would remove the dependence of any results on stochastic effects.

Continuum models are faster to simulate and easier to apply to large scale systems (see §5.6.1) than discrete cell-level models. As such, one of the further aims of the research would be to develop an appropriate continuum-model of the crypt that could used to model large sections of the colon. In the opening chapter of this thesis (§1.3), we introduced several constitutive laws that have be used to model the epithelium. These include using Darcy's Law [64] and Stokes' Law [79], linear elasticity [77], non-linear elasticity [136] and viscoelasticity [99]. Deciding which constitutive law to use could be achieved by mechanical testing of the cell-level models, as in [124], and by using homogenisation techniques [21, 22, 55, 82], to derive a constitutive law from the cell-level models.

Other future aims include developing a 3D version of the model and modelling cell death (see §5.6.3).

Mathematical models play an increasingly important role in the life sciences [107]. They serve two main purposes: to simulate experiments and to test hypotheses [149]. When used to simulate experiments, a model can reveal behaviour that is difficult to view experimentally. For example, when viewing the epithelial cells in the colorectal crypt, a common approach taken by experimentalists [131, 153] is to remove sections of the colon from the body. These sections are then fixed using formalin and paraffin. This means there is no movement of epithelial cells, as happens in the body. With a mathematical model, we can create *in silico* experiments where cell movement is shown.

One of the main difficulties in mathematical modelling is choosing how much detail to include in the model [107, 149]. This has a bearing on the choice of model framework. By developing a model on a larger scale, the model may provide answers to biological questions but may omit crucial details. Conversely, a highly detailed model may include details that are irrelevant to the main biological questions.

Within this thesis, we have demonstrated the benefits of different theoretical frameworks for studying the proliferation and movement of epithelial cells within a colorectal crypt. We have shown how cell-level and continuum models can replicate experimental findings and give new insight into the study of the colorectal crypt.

Appendix A

Cell-centre model appendices

The following appendix contains additional material for the cell-centre model described in chapter 3. It includes the parameter values used (§A.1) and also an example of how a Wnt-signalling model could be implemented within the cell-centre model (§A.2).

A.1 Cell-centre model parameters

To simplify the model we scale cell lengths on the natural spring length of a mature cell ($\sim 6-10\mu m$) [49]. The natural spring length of a fully mature cell $s_{ij}(t) = 1$ for $t > 1$ hour.

If all of the cells in the crypt are mature and not proliferating, there is a stable steady state where there are no spring forces between the cells. This is when they are packed hexagonally, separated by a distance of 1 cell length. In this case, all the cells are at rest and the springs between them are unstretched. We use this state to determine the natural cell area, A_N, and edge-length, c_N. Accordingly, $A_N = \sqrt{3}/2$ cell lengths^2 and $c_N = \sqrt{3}/3$ cell lengths.

In the model simulations, unless otherwise stated, the cell-cycle time parameters used were taken from experimental results reported by Sunter *et al.* for the large bowel of mice [158]. We used the data for the crypts found in descending colon marked (i) in [158]. The times given for each phase of the cell cycle were: M-phase, $t_M = 0.5$ hours; S-phase, $t_S = 6.2$ hours; G_2-phase, $t_{G_2} = 1.8$ hours. To allow for some stochasticity, such that cell-cycle times were not in phase, we assumed that the duration of the G_1-phase time was normally distributed ($t_{G_1} \sim \mathcal{N}(7.0, 1.0)$ hours), with the mean value taken from [158]. The simulations were given a random seed such that the stochastically varying results could be reproduced.

The size of the crypt was also taken from [158] and given to be 20 cell lengths in circumference and

26 cell lengths in height.

In Meineke *et al.*'s original model [109] (on which the model described in Chapter 3 is based), the cell drag and spring strength are homogeneous for all cells. The movement of the cells is then described by a single parameter representing the ratio between the spring strength between cells and the drag on the cell. In our model, the forces between cells and the drag on the cells depend on factors such as cell type, cell area and contact area between cells. This means cell drag η_i (on cell i), and spring strength k_{ij} (between cells i and j), need to be treated separately. Initially to estimate a parameter for the spring strength, we run a crypt where all cells are normal (Type n) and the parameters are homogeneous. As such, the cell movement depends on the ratio k_{nn}/η_n. Without loss of generality, we set $\eta_n = 1.0$ kg hours^{-1}.

To estimate a value for k_{nn}, the spring constant between normal cells, we use the experimental evidence that, when filled with normal cells, the crypt is in a quasi-steady state (homoeostasis) [127] with the number of cells born is equal to the number of cells pushed out of the top of the crypt. To model this a crypt is filled with normal cells and then simulated with the parameters mentioned previously. By trial and error, a value for the spring strength is found such that the crypt is in a quasi-steady state and the movement of the cells was sufficiently damped that the cells move smoothly. A spring constant between normal cells that fits the required criteria is $k_{nn} = 30$ kg hours^{-2} and this is used in all simulations unless otherwise stated.

For cells with edge-dependent spring strength, k_{ij} in (3.1) is represented by $k_{ij} = \bar{k}_{ij}\frac{c_{ij}}{c_N}$, where c_{ij} is the contact length between cells i and j. The parameter $\bar{k}_{ij}$ for two normal cells is set to be $\bar{k}_{ij} = \bar{k}_{nn} = 30$ Kghours^{-2} and the natural edge-length set to be $c_N = \sqrt{3}/3$ cell lengths (discussed above). Similarly when the drag is set to be dependent on cell area, the drag is represented by $\eta_i = \bar{\eta}_i\frac{A_i}{A_N}$, where A_i is the area of cell i, the natural area set to be $A_N = \sqrt{3}/2$ cell lengths^2 (discussed above). For normal cells, $\bar{\eta}_i = \bar{\eta}_n = 1.0$ kg hours^{-1}. Parameter values for mutant cells are as mentioned for the relevant figures in §3.5.2.

To model the dependency of a cell's proliferation on the level of the protein Wnt, a Wnt gradient is implemented within the crypt. The Wnt concentration decreases linearly from 1.0 Wnt units (an arbitrary scale) at the base of the crypt to zero at the top of the crypt. Any normal cells, for which the Wnt level is above 0.65 units are marked as transit cells and can proliferate; the remainder are marked as differentiated cells. As the Wnt gradient and the crypt height do not vary with time, the effect is that any cell less than $H_W = 9.1$ cell lengths from the crypt base can proliferate. Mutant cells do not have this restriction and can proliferate throughout the crypt. The value of the Wnt threshold (0.65) was chosen such that the overall proliferation rate in the crypt was the same as for

Parameter	Value	units	Description
t_M	0.5	hours	Mitosis-phase
t_S	6.2	hours	Synthesis-phase
t_{G_2}	1.8	hours	G_2-phase
t_{G_1}	$\sim \mathcal{N}(7.0, 1.0)$	hours	G_1-phase

Table A.1: Cell cycle parameters

Parameter	Value	units	Description
η_n	1.0	kg hours^{-1}	Drag on normal cells
k_{nn}	30	kg hours^{-2}	Spring strength between normal cells

Table A.2: Parameters for a standard crypt

Meineke *et al.*'s model [109] (where transit cells divide three times).

For any simulation, the starting point is a quasi-steady state crypt. To create a quasi-steady state crypt, initially a population of cells are placed in the crypt arranged hexagonally. Each cell is then given a cell cycle time, t_{CC} and an initial birth time, $t_B = -Ut_{CC}$, where U is a uniform random number. The simulation is then run until $t = 300$ hours, to a quasi-steady state and this is then taken as the starting point for any simulation. This is to reflect the starting point of any experiments.

All parameters are summarised in tables A.1-A.5.

Parameter	Value	units	Description
H_C	26	cell lengths	Crypt height
H_W	9.1	cell lengths	Crypt proliferation region height
W_C	20	cell lengths	Crypt width

Table A.3: Crypt size parameters

Parameter	Value	units	Description
c_N	$\frac{\sqrt{3}}{3}$	cell lengths	Natural edge-length
$\bar{k}_{nn}$	30	kg hours^{-2}	Spring strength between normal cells

Table A.4: Parameters for a crypt with edge-dependent springs used in §3.5.1

Parameter	Value	units	Description
A_N	$\frac{\sqrt{3}}{2}$	cell lengths^2	Natural Area
$\bar{\eta}_n$	1.0	kg hours^{-1}	Drag on normal cells

Table A.5: Parameters for a crypt with area-dependent drag used in §3.5.1

A.2 Incorporation of a Wnt-signalling model

In this section we show how a Wnt-signalling model [172] can be incorporated into the cell-centre model and how the protein levels can be visualised. A common experimental technique for viewing the subcellular protein levels is to use GFP (Green Fluorescent Protein) staining [164]. Here, GFPs attach to the protein of interest and localise where levels of the protein are high. When viewed under a UV light, the GFPs emit high levels of light [36] from areas where levels of the protein of interest are high. Using the model developed in Chapter 3, we are able to run *in silico* GFP staining experiments and produce results for different mathematical models.

In figure A.1, an *in silico* GFP staining experiment for the protein β-catenin is performed for two different hypotheses suggested in Van Leeuwen *et al.*'s Wnt-signalling model [172]. As mentioned in Chapter 1, β-catenin is a multi-functional protein and plays a role in proliferation [19], cell-cell adhesion [40] and cell migration [15]. To perform these functions, the proteins are required to be in different regions of the cell. For example, to perform cell-cell adhesion tasks the β-catenin proteins need to be near the membrane; to perform proliferation duties, the β-catenin proteins need to be in the nucleus. The model by Van Leeuwen *et al.* uses a system of ODEs to predict the levels of β-catenin proteins in three different parts of the cell: bound to the membrane, in the nucleus and in the cytoplasm. The level of β-catenin is determined in part by the level of the protein Wnt within the cell.

Two hypotheses are modelled by Van Leeuwen *et al.*: hypothesis 1, where there is a purely competitive scenario in how β-catenin is apportioned between membrane, nucleus and cytoplasm; hypothesis 2, where in the presence of Wnt, β-catenin has a morphological change such that it is less likely to be membrane-bound. For further details on the model, see [172].

Using the cell-centre model described in Chapter 3, we run simulations where each cell has an associated Wnt-signalling model, as described in [172]. The Wnt-signalling model is used to describe the level of β-catenin in each part of the cell (membrane, nucleus and cytoplasm). The level of nuclear β-catenin is used as an input into a cell-cycle model for each cell, that described by Swat *et al.* [159]. This cell-cycle model uses a system of ODEs to calculate levels of proteins used to determine when the cell proliferates.

In figure A.1, we show how the levels of β-catenin (in the membrane, the nucleus and the cytoplasm) change with the position of the cell. The snapshots are for two different simulations; (left) where hypothesis 1 was assumed and (right) where hypothesis 2 was assumed in Van Leeuwen *et al.*'s Wnt-signalling model [172].

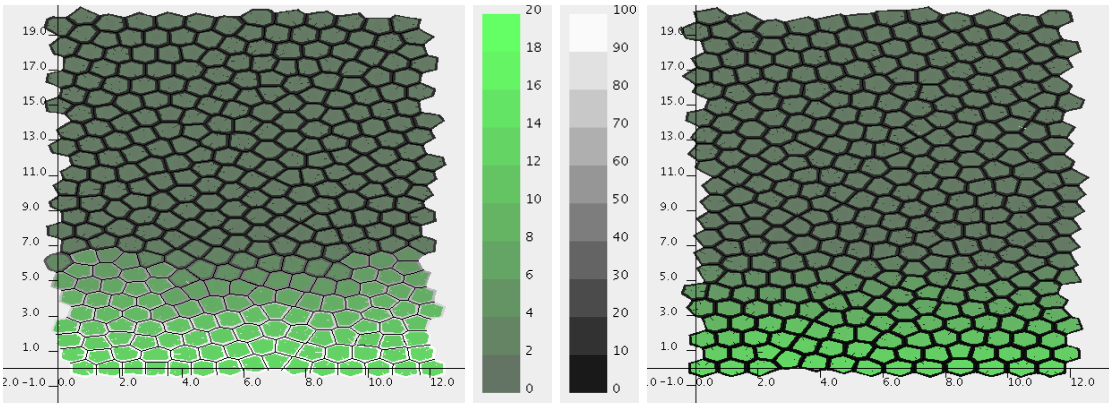

Figure A.1: Snapshots ($t = 500$) showing how the levels of β-catenin change with position within the crypt for when two different hypotheses are assumed in the Wnt signalling model in [172]. (Left) Hypothesis 1, a purely competitive scenario in how β-catenin is distributed between the membrane, the nucleus and the cytoplasm; (Right) Hypothesis 2, where in the presence of Wnt, β-catenin changes such that it is less likely to be membrane bound. Light colours (white on the membrane, light green for the cytoplasm and nucleus) represent high levels of β-catenin and dark colours (black on the membrane, dark green for the cytoplasm and nucleus) represent low levels of β-catenin. Plots show in both cases that cytoplasmic and nuclear β-catenin are high at the base of the crypt and low at the top. However membrane-bound β-catenin varies much more under Hypothesis 1 (higher levels at the base, low levels at the top of the crypt), than under hypothesis 2, (levels vary little within the crypt).

Figure A.1 shows that, for both hypotheses, nuclear levels of β-catenin (involved in proliferation) is high toward the bottom of the crypt (where Wnt levels are high) and low at the top of the crypt (where Wnt levels are low). Our results are consistent with experimental evidence that shows cells proliferating only in the lower half of the crypt [103].

There is a difference in the levels of membrane-bound β-catenin for the two hypotheses, with levels varying greatly with position in hypothesis 2 and less so in hypothesis 1 (see figure A.2). For hypothesis 1, the level of membrane-bound β-catenin is high in the presence of Wnt (in the lower part of the crypt) (around 100 units of β-catenin) and low toward the top of the crypt (around 20 units of β-catenin), where Wnt levels are low. Under hypothesis 2, the cells at the top of the crypt have similar levels of membrane-bound β-catenin as under hypothesis 1 (around 20 units of β-catenin). However when the cells are stimulated by Wnt, in the lower part of the crypt, the β-catenin changes morphologically such that it does not bind as easily to the membrane. The result is that the level of membrane-bound β-catenin is much lower in cells stimulated by Wnt near the

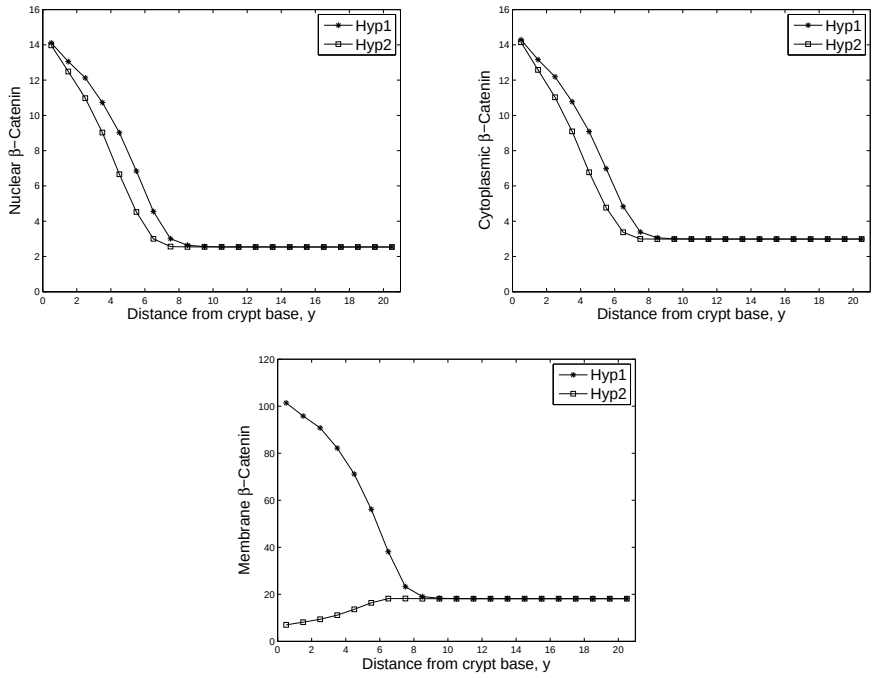

Figure A.2: Plots showing how the average β-catenin values within each cell vary with position in the crypt. The two lines in each plot represent crypts filled with cells where different hypotheses (hypothesis 1 (Hyp1) and hypothesis 2 (Hyp2))in Van Leeuwen *et al.*'s Wnt-signalling model [172]. Plots show the average levels of nuclear (top-left), cytoplasmic (top-right) and membrane-bound (bottom) β-catenin in each cell. To calculate the values in the plots above, the crypt was split into horizontal bands of width 1, and the average value for cells with centres in that band was calculated. This process was repeated for 100 different time readings over 500 simulation hours and the average was taken and is plotted above.

base of the crypt (around 6 units for hypothesis 2 compared to around 100 units in hypothesis 1).

In summary, under both hypothesis, cytoplasmic and nuclear β-catenin levels range from high at the bottom of the crypt to low at the top of the crypt. Under hypothesis 1, levels of membrane-bound β-catenin range from high at the bottom to low at the top of the crypt and under hypothesis 2 the levels of membrane-bound β-catenin remain low throughout the crypt. It would be of interest to compare these results with experimental GFP staining experiments to see which hypothesis best fits the data.

Appendix B

Cell-vertex model appendix

The following appendix contains additional material for the cell-vertex model described in chapter 4. It includes formulae used for calculating the area and lengths of the polygonal cells (§B.1) and their moments (§B.2). We also include the parameter values and how they are derived in (§B.3).

B.1 Area and length formulae

By ordering the vertices of each cell in an anti-clockwise manner, we can use a special case of Green's theorem [112] to calculate the area of a cell, j, which has M vertices

$$A_j = \frac{1}{2}\sum_{m=1}^{M}\left(x_m^j y_{m+1}^j - x_{m+1}^j y_m^j\right). \tag{B.1}$$

In (B.1) $(x_m^j,\ y_m^j)$ are the x and y coordinates of the mth vertex of cell j. Note that cell j is a fully enclosed polygon so when $m = M$, $x_{m+1}^j = x_1^j$ and $y_{m+1}^j = y_1^j$.

Movement of a vertex m will affect two terms in the summation (B.1), the $(m-1)$th and the mth terms. Using this information we can calculate $\nabla_m A_j$, the gradient of A_j associated with moving the mth vertex:

$$\nabla_m A_j = \frac{1}{2}\begin{pmatrix} y_{m+1}^j - y_{m-1}^j \\ x_{m-1}^j - x_{m+1}^j \end{pmatrix}. \tag{B.2}$$

For example in figure B.1, the gradient of area for cell 1 associated with the movement of vertex i would be

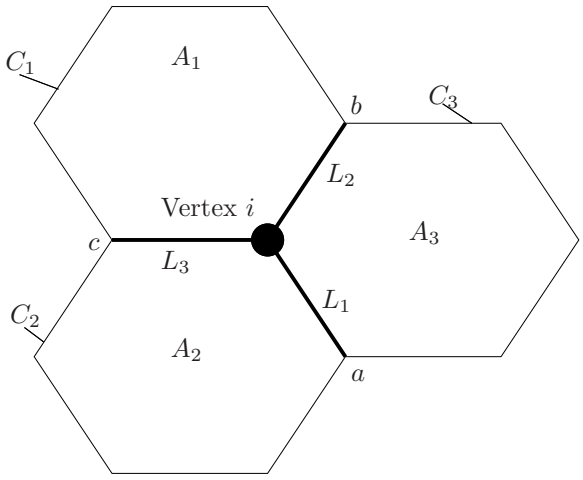

Figure B.1: Figure showing the three cells (1,2,3) which are affected by movement of vertex i. The surrounding cells have areas, A_1, A_2, A_3 and perimeters C_1, C_2, C_3. Lengths L_1, L_2, L_3 represent the distances from vertex i to vertices a, b, c respectively.

$$\nabla_i A_1 = \frac{1}{2} \begin{pmatrix} y_b - y_c \\ x_c - x_b \end{pmatrix}, \tag{B.3}$$

where (x_b, y_b) and (x_c, y_c) are the coordinates of vertices b and c, respectively.

For the energy constraints on cell-cell adhesion, U_C^j, and membrane shape, U_S^j, in (4.2), it is necessary to calculate $\nabla_i L$, the gradient of length L associated with moving vertex i:

$$\nabla_i L = \frac{1}{L} \begin{pmatrix} x_i - X \\ y_i - Y \end{pmatrix}, \tag{B.4}$$

where L is the length of the connection of interest, (x_i, y_i) and (X, Y) are the coordinates at the endpoints. For example, in figure B.1, for the line segment L_1 connecting vertices i and a, the gradient is found to be

$$\nabla_i L_1 = \frac{1}{L_1} \begin{pmatrix} x_i - x_a \\ y_i - y_a \end{pmatrix}. \tag{B.5}$$

B.2 Moments

As mentioned in §4.2.2, when a cell undergoes mitosis it is split in two along its shortest axis through the centroid. To calculate the shortest axis, the moments of the cell are calculated. This is done in

the following way [189]:

$$I_{xx} = -\frac{1}{12}\sum_{m=1}^{m=M}(x_{m+1}-x_m)\left(y_m^3+y_m^2y_{m+1}+y_my_{m+1}^2+y_{m+1}^3\right), \tag{B.6}$$

$$I_{yy} = \frac{1}{12}\sum_{m=1}^{m=M}(y_{m+1}-y_m)\left(x_m^3+x_m^2x_{m+1}+x_mx_{m+1}^2+x_{m+1}^3\right), \tag{B.7}$$

$$\begin{aligned} I_{xy} = \frac{1}{24}\sum_{m=1}^{m=M}\Big(x_m^2y_{m+1}\left(2y_m+y_{m+1}\right) &- x_{m+1}^2y_m\left(y_m+2y_{m+1}\right) \\ &+ 2x_mx_{m+1}\left(-y_m^2+y_{m+1}^2\right)\Big), \end{aligned} \tag{B.8}$$

where M is the total number of vertices a cell has, (x_m, y_m) are the coordinates of the mth vertex in the cell and (x_{m+1}, y_{m+1}) are the coordinates of the vertex one position further anti-clockwise than the mth vertex of the cell.

The angle of the shortest axis is determined by calculating the eigenvector corresponding to the smaller eigenvalue of the 2×2 matrix $\begin{bmatrix} I_{xx} & I_{xy} \\ I_{xy} & I_{yy} \end{bmatrix}$ [189].

B.3 Parameter values

In this section, we list the parameter values of the cell-vertex model described in §4 and, where possible, explain how they were obtained.

For simplicity, all lengthscales are scaled by the width of a fully mature cell, taken as $\sim 6-10\mu m$ [49]. We assumed, as in Chapter 3, that the cells will be in a stable steady-state if arranged in a regular hexagonal pattern of distance 1 cell length apart. Thus the natural area of a fully mature cell is $A_{N,j} = \sqrt{3}/2$ cell lengths^2 and the natural size of a newly born cell is $A_0 = \sqrt{3}/4$ cell lengths^2.

For the natural perimeter length, we set the natural cell area to be that of a circle, $C_{N,j} = 2(A_{N,j}\pi)^{0.5}$ cell lengths.

We take the crypt size to be similar to that Meineke *et al.* [109] used for mouse intestinal crypt, so that the crypt is 21.5 cell lengths long and 11 cell lengths in circumference. Unfortunately due to the time the simulation took to run we could not run the simulation for a human colorectal crypt (typical length $40-60$ cell lengths and ~ 25 cell lengths in circumference [7, 137]). This would have required simulations for a larger crypt with many more cells, and hence taken much longer to run the simulations.

We took the proliferating region, where the cells are stimulated by Wnt, to be the same size as in the previous chapter for the cell-centre model, $H_W = H_C/3$.

The duration of each of the different phases of the cell cycle were taken from [95] and are detailed in table B.1, with stochasticity added to ensure that not all cells are synchronised.

The parameters related to free energy, λ, β and γ_{TT}, and the drag coefficient were estimated such that the cell movement fitted two criteria: the crypt was in a quasi-steady state (the number of cells born is equal to the number removed at the top of the crypt) and the movement of the vertices was stable, such that they moved smoothly and no vertices passed through edges of other cells. If the drag is too high, the cells build up in the crypt, making it no longer in a quasi-steady state. If the cell deformation parameter, λ, is too low, cells are too easily deformed and vertices can pass through other cell edges. If the cell perimeter constraint is too low, the cells end up too elongated. A parameter regime that fitted these constraints was $\eta_N = 100$, $\lambda = 1.0$, $\gamma_{TT} = \gamma_{TD} = \gamma_{DD} = 0.01, \gamma_{TE} = \gamma_{DE} = 0.02$, $\beta = 0.1$. Note that γ_{TE} and γ_{DE} are twice the value of all other cell-adhesion parameters as external edges are counted once when all other edges are counted twice.

When mutant cells were introduced into the crypt, the parameters were set to be the same as that for normal cells unless otherwise stated, $\eta_M = \eta_N = 100$, $\gamma_{MM} = \gamma_{MT} = \gamma_{MD} = 0.01$, $\gamma_{ME} = 0.02$.

The values of the parameters are summarised in the tables B.1-B.4.

Parameter	**Value**	**units**	**Description**
t_M	2.0	hours	Mitosis-phase
t_S	8.0	hours	Synthesis-phase
t_{G_2}	2.0	hours	G_2-phase
t_{G_1}	$\sim \mathcal{N}(4.0, 0.5)$	hours	G_1-phase

Table B.1: Cell cycle parameters for the cell-vertex model

Parameter	Value	units	Description
γ_{TT}	0.01	kg cell lengths hours^{-2}	Transit and Transit
γ_{TD}	0.01	kg cell lengths hours^{-2}	Transit and Differentiated
γ_{DD}	0.01	kg cell lengths hours^{-2}	Differentiated and Differentiated
γ_{TE}	0.02	kg cell lengths hours^{-2}	Transit and External Boundary
γ_{DE}	0.02	kg cell lengths hours^{-2}	Differentiated and External Boundary
γ_{TM}	0.01	kg cell lengths hours^{-2}	Transit and Mutant
γ_{DM}	0.01	kg cell lengths hours^{-2}	Differentiated and Mutant
γ_{MM}	0.01	kg cell lengths hours^{-2}	Mutant and Mutant
γ_{ME}	0.02	kg cell lengths hours^{-2}	Mutant and External Boundary

Table B.2: Cell-cell adhesion parameters for the cell-vertex model

Parameter	Value	units	Description
λ	1.0	kg cell lengths^{-2}hours^{-2}	Cell-size constraint
β	0.1	kg hours^{-2}	Cell-perimeter constraint

Table B.3: Cell deformation parameters for the cell-vertex model

Parameter	Value	units	Description
η_N	100	kg hours^{-1}	Drag on normal cells
η_M	100	kg hours^{-1}	Drag on mutant cells

Table B.4: Drag parameters for the cell-vertex model

References

[1] M. Alber, N. Chen, T. Glimm, and P.M. Lushnikov. Multiscale dynamics of biological cells with chemotactic interactions: From a discrete stochastic model to a continuous description. *Phys. Rev. E*, 73(5):51901, 2006.

[2] B. Alberts, D. Bray, J. Lewis, M. Raff, K. Roberts, and J. Watson. The Molecular Biology of the Cell (ed.). *New York: Garland Science*, 2002.

[3] D. Ambrosi and F. Guana. Stress–modulated growth. *Math. Mech. Solids*, 12(3):319–342, 2005.

[4] D. Ambrosi and F. Mollica. On the mechanics of a growing tumor. *Int. J. Eng. Sci.*, 40(12):1297–1316, 2002.

[5] D. Ambrosi and F. Mollica. The role of stress in the growth of a multicell spheroid. *J. Math. Biol.*, 48(5):477–499, 2004.

[6] S. Anwar, I.M. Frayling, N.A. Scott, and G.L. Carlson. Systematic review of genetic influences on the prognosis of colorectal cancer. *Brit. J. Surg.*, 91(10):1275–1291, 2004.

[7] K. Araki, T. Ogata, M. Kobayashi, and R. Yatani. A morphological study on the histogenesis of human colorectal hyperplastic polyps. *Gastroenterology*, 109(5):1468–74, 1995.

[8] R.P. Araujo and D.L. McElwain. New insights into vascular collapse and growth dynamics in solid tumors. *J. Theor. Biol.*, 228(3):335–46, 2004.

[9] N. Arber, H. Hibshoosh, S.F. Moss, T. Sutter, Y. Zhang, M. Begg, S. Wang, I.B. Weinstein, and P.R. Holt. Increased expression of cyclin D1 is an early event in multistage colorectal carcinogenesis. *Gastroenterology*, 110(3):669–674, 1996.

[10] P. Armitage and R. Doll. The age distribution of cancer and a multi-stage theory of carcinogenesis. *Br J Cancer*, 8(1):1–12, 1954.

[11] N.J. Armstrong, K.J. Painter, and J.A. Sherratt. A continuum approach to modelling cell–cell adhesion. *J. Theor. Biol.*, 243(1):98–113, 2006.

[12] F. Aurenhammer. Voronoi diagrams: a survey of a fundamental geometric data structure. *ACM Comput. Surv.*, 23(3):345–405, 1991.

[13] S.P. Bach, A.G. Renehan, and C.S. Potten. Stem cells: the intestinal stem cell as a paradigm. *Carcinogenesis*, 21(3):469–476, 2000.

[14] E. Batlle, J. Bacani, H. Begthel, S. Jonkeer, A. Gregorieff, M. van de Born, N. Malats, E. Sancho, E. Boon, T. Pawson, S. Gallinger, S. Pals, and H. Clevers. EphB receptor activity suppresses colorectal cancer progression. *Nature*, 435(7045):1126–1130, 2005.

[15] E. Batlle, J.T. Henderson, H. Beghtel, M.M.W. van den Born, E. Sancho, G. Huls, J. Meeldijk, J. Robertson, M. van de Wetering, T. Pawson, and H. Clevers. β-Catenin and TCF Mediate Cell Positioning in the Intestinal Epithelium by Controlling the Expression of EphB/EphrinB. *Cell*, 111(2):251–263, 2002.

[16] K. Beck. *Extreme programming explained: embrace change, Second Edition*. Addison-Wesley Longman Publishing Co., Inc. Boston, MA, USA, 2004.

[17] A. Bertuzzi and A. Gandolfi. Cell kinetics in a tumour cord. *J. Theor. Biol.*, 204(4):587–99, 2000.

[18] M. Bienz. β-Catenin: A Pivot between Cell Adhesion and Wnt Signalling. *Curr. Biol.*, 15(2):64–67, 2005.

[19] M. Bienz and H. Clevers. Linking Colorectal Cancer to Wnt Signaling. *Cell*, 103(2):311–320, 2000.

[20] M. Bienz and F. Hamada. Adenomatous polyposis coli proteins and cell adhesion. *Curr. Opin. Cell. Biol.*, 16(5):528–35, 2004.

[21] M. Bodnar and JJL Velazquez. Derivation of macroscopic equations for individual cell-based models: a formal approach. *Math. Methods Appl. Sci.*, 28(15):1757, 2005.

[22] M. Bodnar and JJL Velazquez. An integro-differential equation arising as a limit of individual cell-based models. *J. Differ. Equations*, 222(2):341–380, 2006.

[23] B.M. Boman, R. Walters, J.Z. Fields, A.J. Kovatich, T. Zhang, G.A. Isenberg, S.D. Goldstein, and J.P. Palazzo. Colonic Crypt Changes during Adenoma Development in Familial Adenomatous Polyposis Immunohistochemical Evidence for Expansion of the Crypt Base Cell Population. *American Journal of Pathology*, 165(5):1489–1498, 2004.

[24] P. Bongrand. Ligand-receptor interactions. *Rep. Prog. Phys*, 62:921–968, 1999.

[25] J.L. Bos. ras Oncogenes in Human Cancer: A Review. *Cancer Res*, 49(17):4682–9, 1989.

[26] C.J.W. Breward, H.M. Byrne, and C.E. Lewis. The role of cell-cell interactions in a two-phase model for avascular tumour growth. *J. Math. Biol.*, 45(2):125–152, 2002.

[27] G. W. Brodland and H. H. Chen. The mechanics of cell sorting and envelopment. *J. Biomech.*, 33(7):845–51, 2000.

[28] G.W. Brodland. The Differential Interfacial Tension Hypothesis (DITH): A Comprehensive Theory for the Self-Rearrangement of Embryonic Cells and Tissues. *J. Biomech. Eng.*, 124:188, 2002.

[29] G.W. Brodland. Computational modeling of cell sorting, tissue engulfment, and related phenomena: A review. *Applied Mechanics Reviews*, 57:47, 2004.

[30] G.W. Brodland and H.H. Chen. The Mechanics of Heterotypic Cell Aggregates: Insights From Computer Simulations. *J. Biomech. Eng.*, 122:402, 2000.

[31] G.W. Brodland and J.H. Veldhuis. Computer simulations of mitosis and interdependencies between mitosis orientation, cell shape and epithelia reshaping. *J. Biomech.*, 35(5):673–681, 2002.

[32] H. Byrne and L. Preziosi. Modelling solid tumour growth using the theory of mixtures. *Math. Med. Biol.*, 20(4):341, 2003.

[33] H.M. Byrne, J. King, D. McElwain, and L. Preziosi. A two-phase model of tumour growth. *Appl. Math. Lett*, 16:567–573, 2003.

[34] J. Cairns. Somatic stem cells and the kinetics of mutagenesis and carcinogenesis. *Proc. Nat. Acad. Sci. U.S.A.*, 99(16):10567–10570, 2002.

[35] J.R. Cary, S.G. Shasharina, J.C. Cummings, J.V.W. Reynders, and P.J. Hinker. Comparison of C++ and Fortran 90 for object-oriented scientific programming. *Computer Physics Communications*, 105(1):20–36, 1997.

[36] M. Chalfie, Y. Tu, G. Euskirchen, W.W. Ward, and D.C. Prasher. Green fluorescent protein as a marker for gene expression. *Science*, 263(5148):802–805, 1994.

[37] W. W. Chang and C. J. Whitener. Histogenesis of tubular adenomas in hereditary colonic adenomatous polyposis. *Arch. Pathol. Lab. Med.*, 113(9):1042–9, 1989.

[38] R. Chaturvedi, C. Huang, B. Kazmierczak, T. Schneider, J.A. Izaguirre, T. Glimm, H.G.E. Hentschel, J.A. Glazier, S.A. Newman, and M.S. Alber. On multiscale approaches to three-dimensional modelling of morphogenesis. *J. R. Soc. Interface*, 2(3):237–253, 2005.

[39] C.Y. Chen, H.M. Byrne, and J.R. King. The influence of growth-induced stress from the surrounding medium on the development of multicell spheroids. *J. Math. Biol.*, 43(3):191–220, 2001.

[40] H. Chen, N.E Paradies, M. Fedor-Chaiken, and R. Brackenbury. E-cadherin mediates adhesion and suppresses cell motility via distinct mechanisms. *J. Cell Sci.*, 110(3):345–356, 1997.

[41] H. Clevers. Wnt/β-Catenin Signaling in Development and Disease. *Cell*, 127(3):469–480, 2006.

[42] H. Clevers and E. Batlle. EphB/EphrinB Receptors and Wnt Signaling in Colorectal Cancer. *Cancer Res.*, 66(1):2–5, 2006.

[43] A. Cockburn and L. Williams. The Costs and Benefits of Pair Programming. *Extreme Programming Examined*, pages 223–248, 2001.

[44] V. Cristini, J. Lowengrub, and Q. Nie. Nonlinear simulation of tumor growth. *J. Math. Biol.*, 46(3):191–224, 2003.

[45] J. J. Decosse. *Large Bowel Cancer*. Churchill Livingstone, 1981.

[46] M. Deheragoda and N. Wright. An update on the pathophysiology of the intestinal crypt. *Current Diagnostic Pathology*, 12(4):268–278, 2006.

[47] A. d'Onofrio and IP Tomlinson. A nonlinear mathematical model of cell turnover, differentiation and tumorigenesis in the intestinal crypt. *J. Theor. Biol.*, 2006.

[48] D. Drasdo. Buckling Instabilities of One-Layered Growing Tissues. *Phys. Rev. Lett.*, 84(18):4244–4247, 2000.

[49] D. Drasdo and M. Loeffler. Individual-based models to growth and folding in one-layered tissues: intestinal crypts and early development. *Nonlinear Anal.*, 47(1):245–256, 2001.

[50] B. Dubertret and N. Rivier. The renewal of the epidermis: a topological mechanism. *Biophys. J.*, 73(1):38–44, 1997.

[51] P. S. Edelstein. *Colon and Rectal Cancer*. Wiley-Liss, 2000.

[52] C.M. Edwards and S.J. Chapman. Biomechanical Modelling of Colorectal Crypt Budding and Fission. *B. Math. Biol.*, 69(6):1927–1942, 2007.

[53] E. R. Fearon and B. Vogelstein. A genetic model for colorectal tumorigenesis. *Cell*, 61(5):759–67, 1990.

[54] S. File. P53 abnormalities and outcomes in colorectal cancer: a systematic review. *Brit. J. Cancer*, 92:434–444, 2005.

[55] J.A. Fozard, O. E. Jensen, H. M. Byrne, and J. R. King. Continuum approximations of individual-based models for multicellular systems. *Math. Med. Biol.*, 2008. Submitted.

[56] S. J. Franks. *Mathematical Modelling Of Tumour Growth and Stability.* PhD thesis, University of Nottingham, 2001.

[57] J. Galle, M. Loeffler, and D. Drasdo. Modeling the Effect of Deregulated Prolif.eration and Apoptosis on the Growth Dynamics of Epithelial Cell Populations In Vitro. *Biophys. J.*, 88(1):62–75, 2005.

[58] A.L. Gartel and K. Shchors. Mechanisms of c-myc-mediated transcriptional repression of growth arrest genes. *Exp. Cell Res.*, 283(1):17–21, 2003.

[59] M. Ghaemi and A. Shahrokhi. Combination of the Cellular Potts Model and Lattice Gas Cellular Automata for Simulating the Avascular Cancer Growth. *Lect. Notes Comput. Sci.*, 4173:297, 2006.

[60] R.H. Giles, J.H. van Es, and H. Clevers. Caught up in a Wnt storm: Wnt signaling in cancer. *Biochim. Biophys. Acta*, 1653(1):1–24, 2003.

[61] J. A. Glazier and F. Graner. Simulation of the differential adhesion driven rearrangement of biological cells. *Phys. Rev. E*, 47(3):2128–2154, Mar 1993.

[62] F. Graner and J. A. Glazier. Simulation of biological cell sorting using a two-dimensional extended potts model. *Phys. Rev. Lett.*, 69(13):2013–2016, Sep 1992.

[63] L. C. Greaves, S. L. Preston, P. J. Tadrous, R. W. Taylor, M. J. Barron, D. Oukrif, S. J. Leedham, M. Deheragoda, P. Sasieni, M. R. Novelli, J. A. Z. Jankowski, D. M. Turnbull, N. A. Wright, and S. A. C. McDonald. Mitochondrial DNA mutations are established in human colonic stem cells, and mutated clones expand by crypt fission. *Proc. Nat. Acad. Sci. U.S.A.*, 103(3):714–719, 2006.

[64] H. P. Greenspan. On the growth and stability of cell cultures and solid tumors. *J. Theor. Biol*, 56(229):2, 1976.

[65] J.P. Heath. Epithelial Cell Migration in the Intestine. *Cell Biol. Int.*, 20(2):139–146, 1996.

[66] L. Hinck, W.J. Nelson, and J. PapKoff. Wnt-1 modulates cell-cell adhesion in mammalian cells by stabilizing beta-catenin binding to the cell adhesion protein cadherin. *J. Cell Biol.*, 124(5):729–741, 1994.

[67] S. Hirohashi and Y. Kanai. Cell adhesion system and human cancer morphogenesis. *Cancer Sci.*, 94(7):575–581, 2003.

[68] S. Höhme, J.G. Hengstler, M. Brulport, M. Schäfer, A. Bauer, R. Gebhardt, and D. Drasdo. Mathematical modelling of liver regeneration after intoxication with CCl4. *Chem. Biol. Interact.*, 168(1):74–93, 2007.

[69] H. Honda, Y. Ogita, S. Higuchi, and K. Kani. Cell movements in a living mammalian tissue: Long-term observation of individual cells in wounded corneal endothelia of cats. *J. Morphol.*, 174(1):25–39, 1982.

[70] H. Honda, M. Tanemura, and T. Nagai. A three-dimensional vertex dynamics cell model of space-filling polyhedra simulating cell behavior in a cell aggregate. *J. Theor. Biol.*, 226(4):439–53, 2004.

[71] H. Honda and H. Yamanaka. A computer simulation of geometrical configurations during cell division. *J. Theor. Biol.*, 106(3):423–435, 1984.

[72] S.D. Howison. Fingering in Hele-Shaw cells. *J. Fluid Mech.*, 167:439–453, 2006.

[73] A. Humphries and N.A. Wright. Colonic crypt organization and tumorigenesis. *Nat. Rev. Cancer*, 8(6):415, 2008.

[74] M. Ilyas. Wnt signalling and the mechanistic basis of tumour development. *J. Pathol.*, 205(2):130–144, 2005.

[75] J.R. Jass, J. Young, and B.A. Leggett. Evolution of colorectal cancer: change of pace and change of direction. *J. Gastroenterol. Hepatol.*, 17(1):17–26, 2002.

[76] M. D. Johnston, C. M. Edwards, W. F. Bodmer, P. K. Maini, and S. J. Chapman. Mathematical modeling of cell population dynamics in the colonic crypt and in colorectal cancer. *Proc. Nat. Acad. Sci. U.S.A.*, 104(10):4008–4013, 2007.

[77] A.F. Jones, H.M. Byrne, J.S. Gibson, and J.W. Dold. A mathematical model of the stress induced during avascular tumour growth. *J. Math. Biol.*, 40(6):473–499, 2000.

[78] D.A. Kessler and H. Levine. Stability of finger patterns in Hele-Shaw cells. *Phys. Rev. A*, 32(3):1930–1933, 1985.

[79] J. R. King and S. J. Franks. Mathematical analysis of some multi-dimensional tissue-growth models. *Eur. J. Appl. Math.*, 15(03):273–295, 2004.

[80] N. L. Komarova and L. Wang. Initiation of colorectal cancer: where do the two hits hit? *Cell Cycle*, 3(12):1558–1565, 2004.

[81] O. Kubota and I. Kino. Minute adenomas of the depressed type in familial adenomatous polyposis of the colon. A pathway to ordinary polypoid adenomas. *Cancer*, 72(4):1159–64, 1993.

[82] E. Kuhl and G.A. Holzapfel. A continuum model for remodeling in living structures. *J. Mater. Sci.*, 42(21):8811–8823, 2007.

[83] K. Kullander and R. Klein. Mechanisms and functions of eph and ephrin signalling. *Nat. Rev. Mol. Cell Biol.*, 3(7):475–486, 2002.

[84] G. Lal and S. Gallinger. Familial adenomatous polyposis. *Semin. Surg. Oncol.*, 18(4):314–323, 2000.

[85] S. A. Lamprecht and M. Lipkin. Migrating colonic crypt epithelial cells: primary targets fortransformation. *Carcinogenesis*, 23(11):1777–1780, 2002.

[86] K.A. Landman and C.P. Please. Tumour dynamics and necrosis: surface tension and stability. *Math. Med. Biol.*, 18(2):131–158, 2001.

[87] P.M. Lansdorp. Immortal Strands? Give Me a Break. *Cell*, 129(7):1244–1247, 2007.

[88] E. Lee, A. Salic, R. Kruger, R. Heinrich, and M. W. Kirschner. The roles of APC and Axin derived from experimental and theoretical analysis of the Wnt pathway. *PLoS Biol.*, 1(1):116–132, 2003.

[89] G. Lemon, J.R. King, H.M. Byrne, O.E. Jensen, and K.M. Shakesheff. Mathematical modelling of engineered tissue growth using a multiphase porous flow mixture theory. *J. Math. Biol.*, 52(5):571–594, 2006.

[90] A. Leslie, F.A. Carey, N.R. Pratt, and R.J.C. Steele. The colorectal adenoma-carcinoma sequence. *Brit. J. of Surg.*, 89(7):845–860, 2002.

[91] J.Q. Li, H. Miki, M. Ohmori, F. Wu, and Y. Funamoto. Expression of cyclin E and cyclin-dependent kinase 2 correlates with metastasis and prognosis in colorectal carcinoma. *Hum. Pathol.*, 32(9):945–953, 2001.

[92] L. Li and T. Xie. Stem cell niche: structure and function. *Annu. Rev. Cell Dev. Biol.*, 21:605–631, 2005.

[93] L.A. Loeb, K.R. Loeb, and J.P. Anderson. Multiple mutations and cancer. *Proc. Nat. Acad. Sci. U.S.A.*, 100(3):776–781, 2003.

[94] M. Loeffler, C.S. Potten, U. Paulus, J. Glatzer, and S. Chwalinski. Intestinal crypt proliferation. II. Computer modelling of mitotic index data provides further evidence for lateral and vertical cell migration in the absence of mitotic activity. *Cell Tissue Kinet.*, 21(4):247–58, 1988.

[95] M. Loeffler, R. Stein, HE Wichmann, CS Potten, P. Kaur, and S. Chwalinski. Intestinal cell proliferation. I. A comprehensive model of steady-state proliferation in the crypt. *Cell Tissue Kinet.*, 19(6):627–45, 1986.

[96] C.Y. Logan and R. Nusse. The Wnt signalling pathway in development and disease. *Annu. Rev. Cell Dev. Bi.*, 20(1):781–810, 2004.

[97] S.R. Lubkin and T. Jackson. Multiphase Mechanics of Capsule Formation in Tumors. *J. Biomech. Eng.*, 124:237, 2002.

[98] Brittan M. and Wright N. A. Stem cell in gastrointestinal structure and neoplastic development. *Gut*, 53:899–901, 2004.

[99] B.D. MacArthur and C.P. Please. Residual stress generation and necrosis formation in multi-cell tumour spheroids. *J. Math. Biol.*, 49(6):537–552, 2004.

[100] P. Macklin and J. Lowengrub. Evolving interfaces via gradients of geometry-dependent interior Poisson problems: application to tumor growth. *J. Comput. Phys.*, 203(1):191–220, 2005.

[101] J.V. Maher. Development of Viscous Fingering Patterns. *Phys. Rev. Lett.*, 54(14):1498–1501, 1985.

[102] M. Malumbres and M. Barbacid. To cycle or not to cycle: a critical decision in cancer. *Nat. Rev. Cancer*, 1(3):222–231, 2001.

[103] E. Marshman, C. Booth, and C.S. Potten. The intestinal epithelial stem cell. *BioEssays*, 24(1):91–98, 2002.

[104] F. Martini. *Fundamentals of Anatomy and Physiology*. Prentice Hall Englewood Cliffs, NJ, 1998.

[105] A. P. Maskens. Histogenesis of adenomatous polyps in the human large intestine. *Gastroenterology*, 77(6):1245–51, 1979.

[106] J.H. Mathews and K.D. Fink. *Numerical Methods Using MATLAB Fourth Edition*. Prentice-Hall, 2004.

[107] R.M. May. Uses and Abuses of Mathematics in Biology. *Science*, 303(5659):790, 2004.

[108] S. A. McDonald, S. L. Preston, L. C. Greaves, S. J. Leedham, M. A. Lovell, J. A. Jankowski, D. M. Turnbull, and N. A. Wright. Clonal Expansion in the Human Gut: Mitochondrial DNA Mutations Show Us the Way. *Cell Cycle*, 5(8), 2006.

[109] F. A. Meineke, C. S. Potten, and M. Loeffler. Cell migration and organization in the intestinal crypt using a lattice-free model. *Cell Prolif.*, 34(4):253–266, 2001.

[110] G. R. Mirams. *Subcellular Phenomena in Colorectal Cancer*. PhD thesis, University of Nottingham, 2008.

[111] P.J. Morin. Beta-catenin signaling and cancer. *Bioessays*, 21(12):1021–30, 1999.

[112] T. Nagai and H. Honda. A dynamic cell model for the formation of epithelial tissues. *Philos. Mag. B*, 81(7):699–719, 2001.

[113] T. Nagai and H. Honda. Wound Healing Mechanism in Epithelial Tissues Cell Adhesion to Basal Lamina. *WSEAS Transactions on Biology and Biomedicine*, 3(6):389, 2006.

[114] T. Nagai, K. Kawasaki, and K. Nakamura. Vertex Dynamics of Two-Dimensional Cellular Patterns. *J. Phys. Soc. Japan*, 57(7):2221–2224, 1988.

[115] I. Nathke. Cytoskeleton out of the cupboard: colon cancer and cytoskeletal changes induced by loss of APC. *Nat. Rev. Cancer*, 66, 2006.

[116] I.S. Nathke. The Adenomatous Polyposis Coli Protein: The Achilles Heel of the Gut Epithelium. *Annu. Rev. Cell Dev. Biol.*, 20(1):337–366, 2004.

[117] W.J. Nelson and R. Nusse. Convergence of Wnt, β-Catenin, and Cadherin Pathways. *Science*, 303(5663):1483–1487, 2004.

[118] M.A. Nowak, N.L. Komarova, A. Sengupta, P.V. Jallepalli, I.M. Shih, B. Vogelstein, and C. Lengauer. The role of chromosomal instability in tumor initiation. *Proc. Nat. Acad. Sci. U.S.A.*, 99(25):16226–16231, 2002.

[119] University of Leeds. Faculty of biological sciences. website, 2007. `http://www.bmb.leeds.ac.uk/teaching/icu3/mdcases/ws3/`.

[120] A. Okabe, B. Boots, K. Sugihara, and S. Nok Chiu. Spatial Tessellations: Concepts and Applications of Voronoi Diagrams (Second Edition), 1992.

[121] R. Okamoto and M. Watanabe. Molecular and clinical basis for the regeneration of human gastrointestinal epithelia. *J Gastroenterol*, 39(1):1–6, 2004.

[122] N.B. Ouchi, J.A. Glazier, J.P. Rieu, A. Upadhyaya, and Y. Sawada. Improving the realism of the cellular Potts model in simulations of biological cells. *Physica A*, 329(3-4):451–458, 2003.

[123] E. Palsson. A three-dimensional model of cell movement in multicellular systems. *Fut. Gen. Comp. Sy.*, 17(7):835–852, 2001.

[124] P. Pathmanathan, J. Cooper, A. Fletcher, G. R. Mirams, L. Momtahan, P. Murray, J. Osborne, J. Pitt-Francis, A. C. Walter, and S. J. Chapman. A computational study of discrete mechanical tissue models. *Phys. Biol.*, 2009. To be Published.

[125] P. Pathmanathan, J. Cooper, A. Fletcher, I. M. M. van Leeuwen, G. R. Mirams, L. Momtahan, P. Murray, J. Osborne, J. Pitt-Francis, A. C. Walter, S. J. Chapman, P. K. Maini, J. P. Whiteley, H. M. Byrne, and D. J. Gavaghan. Chaste: Developing Computational Models of Cancer Using Agile Software Engineering Methods. *J. Theor. Biol.*, 2009. Submitted.

[126] D. Pinto and H. Clevers. Wnt, stem cells and cancer in the intestine. *Biol. Cell*, 97(3):185–196, 2005.

[127] D. Pinto, A. Gregorieff, H. Begthel, and H. Clevers. Canonical Wnt signals are essential for homeostasis of the intestinal epithelium. *Gene Dev.*, 17:1709–1713, 2003.

[128] C.S. Potten, C. Booth, and D. Hargreaves. The small intestine as a model for evaluating adult tissue stem cell drug targets 1. *Cell Prolif.*, 36(3):115–129, 2003.

[129] C.S. Potten and M. Loeffler. Stem cells: attributes, cycles, spirals, pitfalls and uncertainties. Lessons for and from the crypt. *Development*, 110(4):1001–20, 1990.

[130] C.S. Potten, G. Owen, and D. Booth. Intestinal stem cells protect their genome by selective segregation of template DNA strands. *J. Cell Sci.*, 115(11):2381–2388, 2002.

[131] S.L. Preston, W.M. Wong, A.O.O. Chan, R. Poulsom, R. Jeffery, R.A. Goodlad, N. Mandir, G. Elia, M. Novelli, W.F. Bodmer, I.P. Tomlinson, and N.A. Wright. Bottom-up Histogenesis of Colorectal AdenomasOrigin in the Monocryptal Adenoma and Initial Expansion by Crypt Fission. *Cancer Res.*, 63:3819–3825, 2003.

[132] H. Rajagopalan, M.A. Nowak, B. Vogelstein, and C. Lengauer. The significance of unstable chromosomes in colorectal cancer. *Nat. Rev. Cancer*, 3(9):695–701, 2003.

[133] I. Ramis-Conde, D. Drasdo, A.R.A. Anderson, and M.A.J. Chaplain. Modelling the influence of the E-Cadherin-β-Catenin pathway in cancer cell invasion: A multi-scale approach. *Biophys. J.*, 2008.

[134] T. Reya and H. Clevers. Wnt signalling in stem cells and cancer. *Nature*, 434(7035):843–850, 2005.

[135] B. Ribba, T. Colin, and S. Schnell. A multiscale mathematical model of cancer, and its use in analyzing irradiation therapies. *Theoretical Biology and Medical Modelling*, 3(1):7, 2006.

[136] E.K. Rodriguez, A. Hoger, and A.D. McCulloch. Stress-dependent finite growth in soft elastic tissues. *J. Biomech.*, 27(4):455–67, 1994.

[137] L. Roncucci, A. Scalmati, and M. Ponz de Leon. Pattern of cell kinetics in colorectal mucosa of patients with different types of adenomatous polyps of the large bowel. *Cancer*, 68(4):873–878, 1991.

[138] T. Roose, P.A. Netti, L.L. Munn, Y. Boucher, and R.K. Jain. Solid stress generated by spheroid growth estimated using a linear poroelasticity model small star, filled. *Microvasc. Res.*, 66(3):204–12, 2003.

[139] W.S. Samowitz, M.D. Powers, L.N. Spirio, F. Nollet, F. van Roy, and M.L. Slattery. β-Catenin Mutations Are More Frequent in Small Colorectal Adenomas Than in Larger Adenomas and Invasive Carcinomas 1, 1999.

[140] P.A. Sanford. *Digestive System Physiology*. Arnold, 1992.

[141] O.J. Sansom, K.R. Reed, A.J. Hayes, H. Ireland, H. Brinkmann, I.P. Newton, E. Batlle, P. Simon-Assmann, H. Clevers, I.S. Nathke, A.R Clarke, and D.J. Winton. Loss of Apc in vivo immediately perturbs Wnt signaling, differentiation, and migration. *Genes and Development*, 18:1385–1390, 2004.

[142] K. Satake and H. Honda. Evolution towards the Solution of a Shape Optimization Problem. *Forma*, 17(3):253–274, 2002.

[143] R.A. Sausedo, J.L. Smith, and G.C. Schoenwolf. Role of nonrandomly oriented cell division in shaping and bending of the neural plate. *The Journal of Comparative Neurology*, 381(4):473–488, 1997.

[144] N.J. Savill and P. Hogeweg. Modelling morphogenesis: from single cells to crawling slugs. *J. Theor. Biol*, 184:229–235, 1997.

[145] G. Schaller and M. Meyer-Hermann. Kinetic and Dynamic Delaunay tetrahedralizations in three dimensions. *Arxiv preprint physics/0302018*, 2003.

[146] G. Schaller and M. Meyer-Hermann. Epidermal homeostasis control in an off-lattice agent-based model. *Arxiv preprint physics/0507059*, 2005.

[147] G. Schaller and M. Meyer-Hermann. Multicellular tumor spheroid in an off-lattice Voronoi-Delaunay cell model. *Phys. Rev. E*, 71(5):51910, 2005.

[148] G. Schaller and M. Meyer-Hermann. A modelling approach towards epidermal homoeostasis control. *J. Theor. Biol.*, 247(3):554–573, 2007.

[149] S. Schnell, R. Grima, and P.K. Maini. Multiscale modeling in biology. *Am. Sci.*, 95(2):134–142, 2007.

[150] L.W. Schwartz. Instability and fingering in a rotating Hele–Shaw cell or porous medium. *Phys. Fluids A-Fluid*, 1:167, 1989.

[151] Jonathan Richard Shewchuk. Triangle: A two-dimensional quality mesh generator and delaunay triangulator. website, 2009. `http://www-2.cs.cmu.edu/ ~quake/triangle.html`.

[152] J.R. Shewchuk. Triangle: Engineering a 2D Quality Mesh Generator and Delaunay Triangulator. *Lect. Notes Comput. Sci.*, pages 203–222, 1996.

[153] I.M. Shih, T.L. Wang, G. Traverso, K. Romans, S.R. Hamilton, S. Ben-Sasson, K.W. Kinzler, and B. Vogelstein. Top-down morphogenesis of colorectal tumors. *Proc. Nat. Acad. Sci. U.S.A.*, 98(5):2640–2645, 2001.

[154] M. Shtutman, J. Zhurinsky, I. Simcha, C. Albanese, M. D'Amico, R. Pestell, and A. Ben-Ze'ev. The cyclin D1 gene is a target of the beta-catenin/LEF-1 pathway. *Proc. Nat. Acad. Sci. U.S.A.*, 96(10):5522–7, 1999.

[155] SR Sipcic and G. Zajicek. Kinetic analysis of epithelial cell migration in the colon on a massively parallel processor (CM-2). *Comput. Biomed. Res.*, 26(4):393–412, 1993.

[156] R. Skalak, S. Zargaryan, R.K. Jain, P.A. Netti, and A. Hoger. Compatibility and the genesis of residual stress by volumetric growth. *J. Math. Biol.*, 34(8):889–914, 1996.

[157] E. L. Stott, N. F. Britton, J. A. Glazier, and M. Zajac. Stochastic Simulation of Benign Avascular Tumour Growth Using the Potts Model. *Math. Comput. Model.*, 30(5):183–198, 1999.

[158] J.P. Sunter, D.R. Appleton, M.S.B. Dé Rodriguez, N.A. Wright, and A.J. Watson. A comparison of Cell Prolif. at different sites within the large bowel of the mouse. *J Anat.*, 129(Pt 4):833–842, 1979.

[159] M. Swat, A. Kel, and H. Herzel. Bifurcation analysis of the regulatory modules of the mammalian G1/S transition. *Bioinformatics*, 20(10):1506–1511, 2004.

[160] M. Takeichi. Cadherins: A Molecular Family Important in Selective Cell-Cell Adhesion. *Annu. Rev. Biochem*, 59(1):237–252, 1990.

[161] R. W. Taylor, M. J. Barron, G. M. Borthwick, A. Gospel, P. F. Chinnery, D. C. Samuels, G. A. Taylor, S. M. Plusa, S. J. Needham, L. C. Greaves, T. B. Kirkwood, and D. M. Turnbull. Mitochondrial DNA mutations in human colonic crypt stem cells. *J. Clin. Invest.*, 112(9):1351–1360, 2003.

[162] O. Tetsu and F. McCormick. Beta-catenin regulates expression of cyclin D1 in colon carcinoma cells. *Nature*, 398(6726):422–6, 1999.

[163] I.P.M. Tomlinson and W.F. Bodmer. Failure of Programmed Cell Death and Differentiation as Causes of Tumors: Some Simple Mathematical Models. *Proc. Nat. Acad. Sci. U.S.A.*, 92(24):11130–11134, 1995.

[164] R.Y. Tsien. The Green Fluorescent Protein. *Annual Reviews in Biochemistry*, 67(1):509–544, 1998.

[165] S. Turner and J.A. Sherratt. Intercellular adhesion and cancer invasion: a discrete simulation using the extended Potts model. *J. Theor. Biol*, 216(1):85–100, 2002.

[166] S. Turner, J.A. Sherratt, K.J. Painter, and N.J. Savill. From a discrete to a continuous model of biological cell movement. *Phys. Rev. E*, 69(2):21910, 2004.

[167] J.J. Tyson and B. Novak. Regulation of the Eukaryotic Cell Cycle: Molecular Antagonism, Hysteresis, and Irreversible Transitions. *J. Theor. Biol*, 210(249):263, 2001.

[168] Cancer Research UK. Uk bowel cancer statistics. website, 2009. `http://info.cancerresearchuk.org/cancerstats/types/bowel/`.

[169] M. van de Wetering, E. Sancho, C. Verweij, W. de Lau, I. Oving, A. Hurlstone, K. van der Horn, E. Batlle, D. Coudreuse, A.P. Haramis, et al. The β-Catenin/TCF-4 Complex Imposes a Crypt Progenitor Phenotype on Colorectal Cancer Cells. *Cell*, 111(2):241–250, 2002.

[170] I. M. M. van Leeuwen, G. R. Mirams, A. C. Walter, J. Cooper, A. Fletcher, L. Momtahan, P. Murray, J. Osborne, J. Pitt-Francis, P. Pathmanathan, S. Varma, J. P. Whiteley, S. J. Chapman, D. J. Gavaghan, O. E. Jensen, J. R. King, P. K. Maini, and H. M. Byrne. An Integrative Computational Model for Intestinal Tissue Renewal. *Cell Prolif.*, 2009. To be Published.

[171] I.M. van Leeuwen, H.M. Byrne, O.E. Jensen, and J.R. King. Crypt dynamics and colorectal cancer: advances in mathematical modelling. *Cell Prolif.*, 39(3):157–81, 2006.

[172] IM van Leeuwen, HM Byrne, OE Jensen, and JR King. Elucidating the interactions between the adhesive and transcriptional functions of beta-catenin in normal and cancerous cells. *J. Theor. Biol.*, 247(1):77–102, 2007.

[173] W.C. Wake. *Extreme programming explored*. Addison Wesley Boston, 2002.

[174] DC Walker, G. Hill, SM Wood, RH Smallwood, and J. Southgate. Agent-based computational modeling of wounded epithelial cell monolayers. *IEEE T. Nanobiosci.*, 3(3):153–163, 2004.

[175] DC Walker, J. Southgate, G. Hill, M. Holcombe, DR Hose, SM Wood, S. Mac Neil, and RH Smallwood. The epitheliome: agent-based modelling of the social behaviour of cells. *Biosystems*, 76(1-3):89–100, 2004.

[176] C. Wang and L. Schubert. An optimal algorithm for constructing the Delaunay triangulation of a set of line segments. *Proceedings of the third annual symposium on Computational geometry*, pages 223–232, 1987.

[177] J. P. Ward and J. R. King. Mathematical modelling of avascular-tumour growth. *Math. Med. Biol.*, 14(1):39, 1997.

[178] H.S. Wasan, H.S. Park, K.C. Liu, N.K. Mandir, A. Winnett, P. Sasieni, W.F. Bodmer, R.A. Goodlad, and N.A. Wright. APC in the regulation of intestinal crypt fission. *J. Pathol.*, 185(3):246–255, 1998.

[179] G. A. Watson. Approximation in normed linear spaces. *J. Comput. Appl. Math.*, 121(1-2):1–36, 2000.

[180] G. A. Watson. Some robust methods for fitting parametrically defined curves and surfaces to measured data. *Advanced Mathematical and Computational Tools in Metrology l Series on Advances in Mathematics for Applied Sciences*, 53:256–272, 2000.

[181] M. Weliky. The mechanical basis of cell rearrangement. I. Epithelial morphogenesis during Fundulus epiboly, 1990.

[182] M. Weliky. Notochord morphogenesis in Xenopus laevis: simulation of cell behavior underlying tissue convergence and extension, 1991.

[183] M. Weliky and G. Oster. Modeling and simulation of morphogenesis by cell rearrangement. *Lect Notes Comput. Sc.*, pages 41–48, 1990.

[184] M.F. Wheeler. An elliptic collocation-finite element method with interior penalties. *SIAM J. Numer. Anal*, 15(1):152–161, 1978.

[185] W. M. Wong, S. B. Garcia, and N. A. Wright. Origins and morphogenesis of colorectal neoplasms. *APMIS*, 107(6):535–44, 1999.

[186] N. A. Wright and R. Poulsom. Top down or bottom up? Competing management structures in the morphogenesis of colorectal neoplasms. *Gut*, 51:306–308, 2002.

[187] N.A. Wright. Epithelial stem cell repertoire in the gut: clues to the origin of cell lineages, proliferative units and cancer. *Int. J. Exp. Pathol.*, 81(2):117–143, 2000.

[188] Y. Yatabe, S. Tavare, and D. Shibata. Investigating stem cells in human colon by using methylation patterns. *Proc. Nat. Acad. Sci. U.S.A.*, page 191225998, 2001.

[189] S. Zhang, J. Zhang, F. Li, and R. Cropp. Vector analysis theory on landscape pattern (VATLP). *Ecol. Modell*, 193(3-4):492–502, 2006.